A PROJECT OF
SUPER C-τ FACTORY IN NOVOSIBIRSK

Budker Institute of Nuclear Physics
Novosibirsk - 2011

DRAFT

BUDKER INSTITUTE OF NUCLEAR PHYSICS

Super Charm–Tau Factory

CONCEPTUAL DESIGN REPORT

Novosibirsk – 2011

This document is focused on a project of the Super Charm–Tau Factory (CTF) in the Budker Institute of Nuclear Physics (Novosibirsk, Russia). An electron-positron collider will operate in the range of center-of-mass energies from 2 to 5 GeV with unprecedented peak luminosity of about 10^{35} cm^{-2}s^{-1} and longitudinally polarized electrons at interaction point. To achieve this extremely high luminosity we are going to apply a novel idea of a Crab Waist collision scheme. The main goal of experiments at Super Charm-Tau Factory is a study of the processes with c quarks or τ leptons in the final state using data samples, which are by 3–4 orders of magnitude higher than collected by now in any other experiments. We expect that these experiments will be sensitive to effects of new physics not described by the Standard Model.

V.V. Anashin, V.M. Aulchenko, E.M. Baldin, A.K. Barladyan, A.Yu. Barnyakov, I.Yu. Basok, O.L. Beloborodova, A.E. Blinov, V.E. Blinov, A.V. Bobrov, V.S. Bobrovnikov, A.G. Bogdanchikov, A.V. Bogomyagkov, A.E. Bondar, A.A. Borodenko, A.V. Bragin, A.R. Buzykaev, V.L. Chernyak, V.Ya. Chudaev, I.N. Churkin, N.S. Dikansky, T.V. Dimova, A.M. Dolgov, V.P. Druzhinin, F.A. Emanov, S.I. Eidelman, Yu.I. Eidelman, D.A. Epifanov, L.B. Epshteyn, E.S. Ershov, V.S. Fadin, N.I. Gabyshev, A.Yu. Garmash, S.A. Glukhov, V.B. Golubev, D.N. Grigoriev, V.R. Groshev, S.V. Karpov, P.V. Kasyanenko, V.F. Kazanin, E.K. Kengebulatov, B.I. Khazin, S.V. Khruschev, V.A. Kiselev, V.I. Kokoulin, V.V. Kolmogorov, S.A. Kononov, I.A. Koop, A.A. Korol, E.A. Kravchenko, A.A. Krasnov, P.P. Krokovny, V.N. Kudryavtsev, A.S. Kuzmin, V.F. Kulikov, G.N. Kulipanov, E.A. Kuper, G.Ya. Kurkin, A.E. Levichev, E.B. Levichev, R.N. Li, P.V. Logachev, D.V. Matvienko, A.S. Medvedko, N.A. Mezentsev, A.I. Milstein, A.A. Morozov, N.Yu. Muchnoi, S.A. Nikitin, I.B. Nikolaev, I.N. Okunev, A.P. Onuchin, S.B. Oreshkin, A.A. Osipov, A.S. Osipov, A.V. Otboev, A.V. Petrenko, M.V. Petrichenkov, V.V. Petrov, P.A. Piminov, A.O. Poluektov, A.V. Polyanski, V.G. Prisekin, Yu.A. Pupkov, V.A. Rodiakin, G.A. Savinov, Yu.M. Schatunov, S.I. Serednyakov, D.N. Shatilov, V.E. Shebalin, L.I. Shekhtman, S.V. Shiyankov, S.N. Shmakov, D.A. Shtol, A.I. Shusharo, B.A. Shwartz, I.V. Sidorov, S.V. Sinyatkin, K.Yu. Skovpen, A.N. Skrinsky, V.V. Smaluk, A.V. Sokolov, E.V. Starostina, A.M. Sukharev, A.A. Talyshev, V.I. Telnov, Yu.A. Tikhonov, V.M. Titov, Yu.V. Usov, A.N. Vinokurova, P.D. Vobly, G.V. Vodnev, K.V. Zolotarev, A.I. Vorobiov, V.S. Vorobiev, Yu.V. Yudin, A.N. Yushkov, A.S. Zaytsev, V.N. Zhilich, V.V. Zhulanov
Budker Institute of Nuclear Physics, *pr. Lavrentieva 11, Novosibirsk 630090, Russia*

A.F. Danilyuk
Boreskov Institute of Catalysis, *pr. Lavrentieva 5, Novosibirsk 630090, Russia*

N.N. Achasov, I.F. Ginzburg, G.N. Shestakov
Sobolev Institute of Mathematic, *av. Acad. Koptyug 4, Novosibirsk 630090, Russia*

A.G. Kharlamov, G.L. Kotkin, I.B. Logashenko, D.A. Maksimov, O.I. Meshkov, I.O. Orlov, V.G. Serbo, Yu.I. Skovpen
Novosibirsk State University, *st. Pirogova 2, Novosibirsk 630090, Russia*

M.Yu. Barnyakov, S.G. Pivovarov
Novosibirsk State Technical University, *pr. K.Marksa 20, Novosibirsk 630090, Russia*

A.V. Arefiev, T.A. Aushev, K.A. Chilikin, R.N. Chistov, M.V. Danilov, D.R. Liventcev, R.V. Mizuk, G.V. Pakhlova, P.N. Pakhlov, V.Yu. Rusinov, E.I. Solovyeva, E.I. Tarkovsky, I.N. Tikhomirov, T.V. Uglov
State Scientific Center of the Russian Federation – Institute for Theoretical and Experimental Physics, *st. Bolshaya Cheremushkinskaya 25, Moscow 117218, Russia*

I.R. Boyko, D.V. Dedovich, Yu.A. Nefedov, A.S. Zhemchugov
Joint Institute for Nuclear Research, *st. Joliot-Curie 6, Dubna, Moscow region 141980, Russia*

V.A. Chtchegelsky, V.L. Golovtsov, N.V. Gruzinsky, V.I. Iatsura, V.A. Nikonov, A.V. Sarantsev, L.N. Uvarov
Petersburg Nuclear Physics Institute, *Gatchina, Leningrad district 188300, Russia*

A.Yu. Loginov, V.N. Stibunov
Tomsk Polytechnic National Research University of Resourse-Efficient Technology, *av. Lenin 30, Tomsk 634050, Russia*

D.A. Finogeev, T.L. Karavicheva, E.V. Karpechev, A.B. Kurepin, A.N. Kurepin, V.I. Razin, A.I. Reshetin, N.S. Topilskaya, E.A. Usenko
Institute for Nuclear Research, *pr. 60th October Anniversary prospect 70, Moscow 117312, Russia*

V. Smakhtin
Weizmann Institute of Science, *PO Box 26, Rehovot 76100, Israel*

M. Bracko, S. Korpar
University of Maribor, *Smetanova 17, SI-2000 Maribor, Slovenia*

B. Golob, R. Pestotnik, M. Staric
Jozef Stefan Institute, *P.O.B. 3000, SI-1001, Ljubljana, Slovenia*

P. Krizan
University of Ljubljana, *Jadranska 19, SI-1000, Ljubljana, Slovenia*

D. Babusci, G. Venanzoni, M. Zobov
Lab. Nazionali di Frascati dell'INFN, *CP 13, via E. Fermi 40, I-00044, Frascati Roma, Italy*

A. Lusiani
Scuola Normale Superiore e INFN, *Piazza die Cavalieri 7, I-56126, Pisa, Italy*

M. Mascolo, D. Moricciani
University of Rome Tor Vergata, *via della Ricerca Scientifica, 1, I-00133, Roma, Italy*

H. Czyz
Institute of Physics, University of Silesia in Katowice, *Uniwersytecka 4, PL-40-007 Katowice, Poland*

F. Jegerlehner
A.Humboldt University, DESY, *Platanenallee 6, D-15738, Zeuthen, Germany*

Contents

Chapter 1

Introduction

In the nineties of the past century several projects of $c\tau$ factories were discussed in high energy physics laboratories around the world. All these facilities were planned to work with beam energy of $1 \div 3$ GeV and a peak luminosity of about 10^{33} cm^{-2}s^{-1} [1, 2, 3, 4, 5, 6, 7] with exception of a round beam Novosibirsk option with 10^{34} cm^{-2}s^{-1} [8]. Different variants of monochromatization of the energy of particle collision were considered in order to study narrow resonances as well as the possibility of the production of transversely polarized particles (for precise energy calibration).

The only project from the "family" of those $c\tau$ factories which has been realized is the BEPC II collider commissioned at the IHEP laboratory (Beijing) in 2009 [9]. Its designed peak luminosity is 10^{33} cm^{-2}s^{-1}.

The revival of the interest in these subjects and the beginning of work on the project of $c\tau$ factory at Budker Institute of Nuclear Physics (BINP) is caused, first, by the outstanding results which were achieved at the B Factories, KEKB (KEK, Japan) and PEP-II (SLAC, US). These works culminated in the 2008 Nobel Prize in Physics to M. Kobayashi and T. Maskawa. Though the high luminosity of the B Factories allowed obtaining some interesting results at low energies with the ISR method, that is proposed and developed at BINP, creation of a highly productive factory specially intended to study the physics of charmed particles and τ lepton is still a topical issue.

Second, the growing interest in the creation of the next-generation $c\tau$ factory resulted from the discovery of a new and promising method of beam collision in electron-positron colliders which allows the luminosity to be raised by two orders of magnitude as compared with the existing factories without a significant increase of the beam intensity or the facility size or reduction of the bunch length. The idea was proposed by an Italian physicist, Pantaleo Raimondi, in 2006 when he studied the possibility of creating a high-luminosity B factory [10]. Later the method was justified in joint works by P. Raimondi, M. Zobov (INFN/LNF, Frascati), and D. Shatilov (BINP, Novosibirsk) [11, 12] with simulation of the collision effects using the LIFETRAC software developed by D. Shatilov. The new approach, described in detail below, was called *"Crab-Waist Collision with Large Piwinski Angle"*. For brevity's sake, we will refer to the new approach as the Crab Waist or CW collision method. Besides the $c\tau$ factory in Novosibirsk, the CW collision method is used in the projects of the Super$B$ factory in Italy and the Super$KEKB$ factory (without the CW sextupoles at the moment) in Japan. In other words, all the projects of future electron-positron circular super-colliders are based on this new approach.

In 2008–2009 the new beam collision method was tried at the ϕ factory DAΦNE; the experiment results confirm the method to be promising and are in good agreement with the theory [13].

The following scientific goals can be formulated for the new project: the precision study of the processes with c quarks and τ leptons in the final states, the search of four- and five-quark states, glueballs, hybrid, other exotic states and study of their properties. That requires data samples of D mesons, τ leptons and data collected on- and off-range of charmonium resonances that are 3–4 orders of magnitude higher than collected today. This allows studying such new phenomena as CP violation in D meson system, τ leptons and lepton flavor violation in τ decays.

This program requires a development of a universal magnetic detector with an extremely high momentum resolution for charged particles and high energy resolution for photons, with record parameters for the particle identification system. Extremely high luminosity demands a unique trigger, which can select physics events under very high detector load, as well as digitizing hardware and data acquisition system which is able to read out events at a rate of 300–400 kHz.

On the basis of the scientific tasks, which are discussed in detail in the section of the physics program of the $c\tau$ factory, the following main requirements to the accelerator complex were stipulated:

- The beam collision energy in the center-of-mass system must vary from 2 to 5 GeV, which allows experiments spanning from the nucleon-antinucleon production energy to the region of ψ mesons and charmed baryons. Besides, such an energy range will allow us to use the results obtained with the VEPP–2000 and VEPP–4M colliders at BINP.
- The luminosity of the factory shall be not less than 10^{35} cm^{-2}s^{-1} in the high energy region and $\geq 10^{34}$ cm^{-2}s^{-1} in the low energy one.
- The electron beam shall be polarized longitudinally at the interaction point [14, 15].
- Beams shall collide with equal energies; asymmetry is not required.
- Since no schema for collision monochromatization without a significant decrease in the luminosity had been found, it was decided to abandon energy monochromatization, all the more so because the high luminosity allows effective exploration of the narrow resonance states without complicated monochromatization solutions.
- It was decided to abandon the need to have transversely polarized beams for precise calibration of energy. The energy will be measured by means of Compton back scattering of laser radiation on the particles of the circulating beam. This technique has been implemented recently on VEPP–4M [16] and shown a relative accuracy better than $\sim 10^{-4}$, which seems sufficient for the tasks of the new $c\tau$ factory.

It is worth to mention among other requirements to the project the possibility of using, after a modernization that will increase the positron production, the BINP injection complex being now under commission. To reduce the cost of the facility its design relies on the existing BINP infrastructure, tunnels, buildings and premises. It was decided to employ in the complex the technical and technological solutions available at BINP (electro- and superconducting magnets, the source of polarized electrons, elements of vacuum chamber and beam diagnostics etc).

Bibliography

[1] C-Tau in Novosibirsk: Conceptual Design Report, BINP, Novosibirsk, 1995

[2] E. Perelshtein et al. Proc. of the 3rd Workshop on the TC Factory, Marbella, Spain, 1-6 Jun 1993, 557-570

[3] M.V. Danilov et al. Int. J. Mod. Phys. A, Proc. Suppl. 2A (1993) 455-457

[4] E.Berger et al. ANL-HEP-TR-94-12, Feb 1994. 28pp

[5] Yu.Aleksahin, A.Dubrovin, A.Zholents. In EPAC 90 Proc., vol. 1, 398-400

[6] He-Sheng Chen. Nucl. Phys. Proc. Suppl. 59: 316-323, 1997

[7] A. Faus-Golfe and J. Le Duff. Nucl. Instr. and Meth. A372:6-18, 1996

[8] A.N.Skrinsky Studies for a Tau-Charm Factory, SLAC-Report-451, October, 1994

[9] J.Q. Wang, L. Ma, Q. Qin, C. Zhang. Status and performance of BEPC II, Proceedings of IPAC'10, Kyoto, Japan, 2010, WEXMH01, p. 2359.

[10] P. Raimondi, Status of the Super*B* Effort, presentation at the 2nd Workshop on Super B Factory, LNF-INFN, Frascati, March 2006

[11] P. Raimondi and M. Zobov, DAΦNE Technical Note G-58, April 2003;

[12] D. Shatilov and M. Zobov, ICFA Beam Dyn. Newslett. 37, 99 (2005)

[13] M.Zobov (INFN LNF), for DAFNE Collaboration Team, DAFNE Operation Experience With Crab Waist Collision, arXiv:0810.2211v1

[14] Ya.S.Derbenev, A.M.Kondratenko, A.N.Skrinsky. On the spin motion of particles in storage rings with arbitrary field. INP preprint, № 2-70 (1970).

[15] Ya.S.Derbenev, A.M.Kondratenko, A.N.Skrinsky. Soviet Doklady (Physics) v. 192, № 6, pp. 1255-1258 (1970) (In Russian). Soviet Physics "Doklady", 15, pp 583-586 (1970) (translation)

[16] N.Yu. Muchnoi, S. Nikitin, V. Zhilich. Proc. of EPAC 2006, Edinburg, Scotland

Chapter 2

Physics

2.1 Introduction

A Super $c\tau$ factory is an electron-positron collider operating in the range of center-of-mass (c.m.) energies from 2 to $5\div6$ GeV with a high luminosity of about $10^{35}\,\mathrm{cm}^{-2}\mathrm{s}^{-1}$. In this energy range practically all states with charm can be produced including charmonium-mesons, which are bound states of c and $\bar{c}$ quarks, charmed mesons comprising one c ($\bar{c}$) quark, and charmed baryons comprising one c quark. In addition, at the c.m. energy above $2m_\tau \approx 3.6$ GeV τ-lepton pairs can be produced. Because of its extremely high luminosity such a collider will be a copious source of charmed particles and τ leptons. This brings us to the name Super $c\tau$ factory (CTF).

The main goal of experiments at CTF is a study of the processes with c quarks or τ leptons in the final state using data samples that are 3-4 orders of magnitude higher than collected today at CLEO*c* and BESII detectors. To understand opportunities provided by CTF we show in Table 2.1 a possible distribution of an integrated luminosity of 1 ab^{-1} in different energy ranges. At CTF with a luminosity of $10^{35}\,\mathrm{cm}^{-2}\mathrm{s}^{-1}$ such an integrated luminosity can be collected during half a year producing thereby 10^9 τ leptons, 10^9 D mesons and a fantastic number (10^{12}) of J/ψ mesons. These statistics will allow a systematic study of all states of quarks of the two first generations (u, d, s and c) as well as searches for states of exotic nature.

A theory of strong interactions, quantum chromodynamics (QCD), in addition to standard mesons and baryons consisting of 2 and 3 quarks, respectively, cannot rule out the existence of four- and five-quark states as well as bound states of gluons, carriers of strong interactions [1]. Such states are possible because gluons, in contrast to a photon, an electrically neutral carrier of electromagnetic interactions, possess a strong or color charge. QCD predicts both hybrid quark-gluon states and states consisting of gluons only, glueballs. Hybrids and glueballs are a completely new form of matter that can be formed by strong interactions only. One of the tasks of CTF is to discover exotic states and study their properties.

Huge data samples of D mesons and τ leptons will allow a study of principally new phenomena, such as CP violation in the D meson system and in τ leptons as well as lepton flavor violation.

Table 2.1: Possible distribution of an integrated luminosity collected at CTF (1 ab^{-1}) in different energy ranges.

E, GeV	3.097	3.686	3.770	3.800–5.000
L, fb^{-1}	300	150	350	200

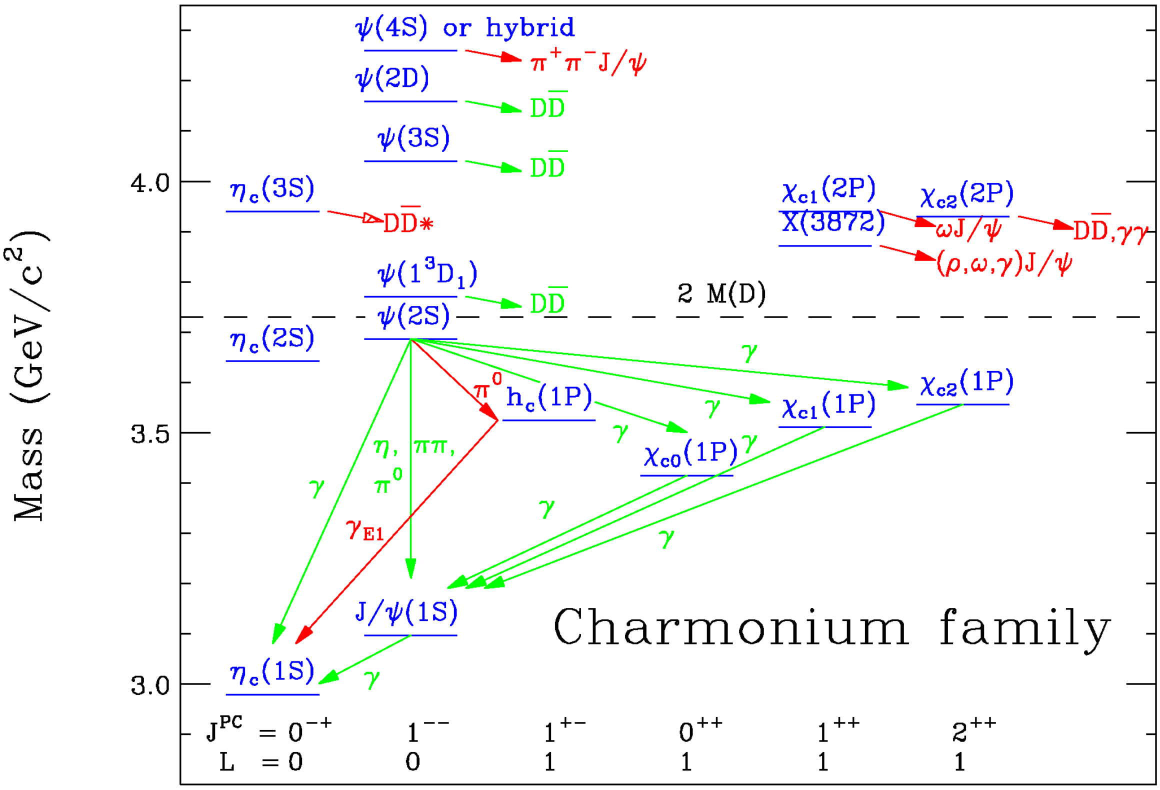

Figure 2.1: Charmonium system and transitions. Red (dark) arrows indicate recently discovered decays and transitions between the levels. The dashed line shows a production threshold for a pair of charmed mesons.

A physics program for CTF can be subdivided into the following subsections, which are discussed in more detail below:

1. charmonium,
2. spectroscopy of states of light quarks,
3. physics of D mesons,
4. physics of charmed baryons,
5. τ lepton physics,
6. measurement of the cross section of $e^+e^- \to$ hadrons,
7. two-photon physics.

2.2 Charmonium

A scheme of charmonium levels is shown in Fig. 2.1. All states lying below the threshold of D meson production and therefore decaying into hadrons consisting of the light u, d and s quarks (or into a lower mass charmonium) have been discovered. Vector mesons ($J^{PC} = 1^{--}$), i.e., J/ψ, $\psi(2S)$, $\psi(3770)$, etc. are directly produced in e^+e^- collisions. In Table 2.2 we list the numbers

Table 2.2: The number of $c\bar{c}$ mesons that can be produced at CTF with an integrated luminosity of 1 ab^{-1}. Estimates of physical cross sections are based on Refs. [2, 3, 4].

	J/ψ	$\psi(2S)$	$\psi(3770)$	$\psi(4040)$	$\psi(4160)$	$\psi(4415)$
M, GeV	3.097	3.686	3.773	4.039	4.153	4.421
Γ, MeV	0.093	0.304	27	80	103	62
σ, nb	$\sim$3400	$\sim$640	$\sim$6	$\sim$10	$\sim$6	$\sim$4
L, fb^{-1}	300	150	350	10	20	25
N	10^{12}	10^{11}	2×10^9	10^8	10^8	10^8

of 1^{--} mesons that can be produced at CTF with an integrated luminosity of 1 ab^{-1}. Estimates take into account the expected beam energy spread.

In radiative decays of J/ψ and $\psi(2S)$ mesons [2] about 10^{10} χ_{cJ} and η_c mesons each can be obtained. About 10^8 h_c mesons can be produced in the $\psi(2S) \to h_c\pi^0$ decay, which has a branching fraction of about 10^{-3} [5]. For observing $\eta_c(2S)$ one can use a rare, not yet discovered radiative transition $\psi(2S) \to \eta_c(2S)\gamma$ (its branching fraction is expected to be 5×10^{-4} [1]) or two-photon production (see Sec. 2.8). Such a data sample allows a systematic study of $c\bar{c}$-meson properties. The following items should be mentioned:

1. Precision measurement of probabilities for transitions between low-lying levels of charmonium, their masses, total and leptonic or two-photon widths. These parameters are calculated in potential quark models and can also be obtained within lattice QCD. In close future the accuracy of lattice calculations will reach a level of about 1% or better. At CTF one will be able to measure probabilities of rare, not yet discovered electric $\eta_c(2S) \to h_c\gamma$ (2.5×10^{-3}), $\psi(3770) \to \chi_{c0}\gamma$ (2×10^{-4}) and magnetic $\psi(2S) \to \eta_c(2S)\gamma$ (5×10^{-4}), $\eta_c(2S) \to J/\psi\gamma$ (3×10^{-5}), $h_c \to \chi_{c0}\gamma$ $(\sim 10^{-6})$ dipole transitions. Shown in parentheses are transition probabilities expected in the quark model [1]. From the analysis of angular distributions of photons in the $\chi_{cJ} \to J/\psi\gamma$ and $\psi(2S) \to \chi_{cJ}\gamma$ decays one can extract the amplitudes of $M2$ and $E3$ transitions interfering with the dominating $E1$ transition and determine an admixture of the D wave state in $\psi(2S)$ (see a review in [6] and references therein).

2. Information about decays of low-lying states of charmonium is very incomplete. For the best-studied J/ψ meson about 40% of hadronic decays only have been measured. For other states the situation is even worse. One of the tasks for CTF is a systematic study of all low-lying charmonium states. This program, in particular, includes a precision measurement of hadronic transitions between charmonium states with emission of one or two π mesons, η meson, $\psi, h_c \to 3\gamma$ decays, a photon spectrum in the reaction $\psi \to \gamma X$, where X is a hadronic state of light quarks, and direct measurement of the probabilities of $\eta_c, \chi_{c0}, \chi_{c1} \to 2\gamma$ decays.

3. During recent years considerable progress has been achieved in studies of states above the threshold of D meson production. New states $X(3872)$, $Z(3930)$, $X(3940)$, $Y(3940)$, $Y(4260)$ have been discovered (see reviews [6, 7] and references therein). There is serious evidence for three more resonances: $Y(4360)$ [8], $Y(4660)$ [9], and $Z^+(4430)$ [10]. Note that a charged charmonium state $Z^+(4430)$ obviously does not fit the two-quark model. Four new states with mass below 4 GeV have a positive C-parity and can be associated with excited $c\bar{c}$

mesons, $\eta_c(3S)$ and $\chi_{cJ}(2P)$, although some properties of the $X(3872)$ meson can hardly be explained within the two-quark assumption. At CTF, for identification and study of $\chi_{cJ}(2P)$ mesons one can use decays $\psi(4040)$, $\psi(4160)$, $\psi(4415) \to \chi_{cJ}(2P)\gamma$. To this end, considerable statistics should be accumulated at the $\psi(4040)$, $\psi(4160)$ and $\psi(4415)$ resonances (see Table 2.2). Probabilities of electric dipole transitions $\psi \to \chi_{cJ}(2P)\gamma$ are predicted at the 10^{-3} level [11].

The $Y(4260)$, $Y(4360)$, $Y(4660)$ states have quantum numbers 1^{--} and can be directly produced in e^+e^- collisions. Typical cross sections of their production are about 50 pb. For their detailed study a scan of the energy range 3.8 to 5.0 GeV with an integrated luminosity of about 100 fb^{-1} is needed. Such a program can be realized at CTF only.

4. A relatively small width of the J/ψ resonance and a huge data sample provided by CTF allow an observation of weak J/ψ decays. The total probability of weak decays of J/ψ via a $c \to sW^+$ transition is (2–4)$\times 10^{-8}$ [12]. Semileptonic $J/\psi \to D_s^* l\nu$, $D_s l\nu$ and hadronic $J/\psi \to D_s^+\rho^-$, $D_s^{*+}\pi^-$ modes have branching fractions of (3–4)$\cdot 10^{-9}$ [12, 13] and can be measured at CTF. In Standard Model (SM) decays with $\Delta S = 0$ are suppressed. For example, the branching fractions of $J/\psi \to D^0\rho^0$ and $J/\psi \to D^0\pi^0$ decays are predicted at the level of 2×10^{-11} and 0.6×10^{-11} [13], respectively. This makes such decays sensitive to effects of new physics not described by SM, in particular, to the existence of a flavor-changing neutral current (a $c \to u$ transition) [14].

   Another type of weak processes ($c\bar{c} \to s\bar{s}$ with W boson exchange) results in decays violating C parity, such as, e.g., $J/\psi \to \phi\phi$. The expected branching fraction of this decay is sufficiently high ($\sim 10^{-8}$ [15]) for its observation at CTF.

5. A large sample of ψ meson decays allows a search for phenomena not described by SM, such as violation of CP parity and lepton flavor conservation. Lepton flavor violation can be observed in $J/\psi \to l\bar{l}'$ decays, where $l, l' = e, \mu, \tau$. Branching fractions of such decays can be related in a model-independent way to branching fractions of μ and τ decays to three leptons [16]. From the limits $B(\mu \to ee^+e^-) < 10^{-12}$ [2] and $B(\tau \to \mu e^+e^-) < 2.7 \times 10^{-8}$ [17] one obtains $B(J/\psi \to \mu e) < 2 \times 10^{-13}$ and $B(J/\psi \to \tau l) < 6 \times 10^{-9}$. A limit on the decay $\tau \to \mu e^+e^-$ has been set with a data sample of 5×10^8 τ lepton pairs. Thus at CTF J/ψ decays can be more sensitive to lepton flavor violation than those of τ leptons.

One of physical effects beyond SM is the existence of the non-zero electric dipole moment (EDM) of quarks or leptons leading, in particular, to CP violation. J/ψ decays provide the best opportunity to obtain information about the c-quark EDM. To search for CP violation one can use three-body decays, e.g., $J/\psi \to \gamma\phi\phi$. In this case, one can compose a CP-odd combination of momenta of final particles and an initial electron and determine a parameter describing CP asymmetry which is proportional to EDM. With 10^{12} J/ψ mesons, using the $J/\psi \to \gamma\phi\phi$ decay one can obtain a sensitivity to the c-quark EDM at the 10^{-15} e·cm level [18]. A two-body $J/\psi \to \Lambda\bar{\Lambda}$ decay, in which polarizations of final baryons can be measured from the $\Lambda \to p\pi^-$ decay, can be also used for a search for CP violation. With 10^{12} J/ψ mesons, this decay can be used to set a limit on the Λ-hyperon EDM at the 5×10^{-19} e·cm level [19], two orders of magnitude more stringent than the existing limit.

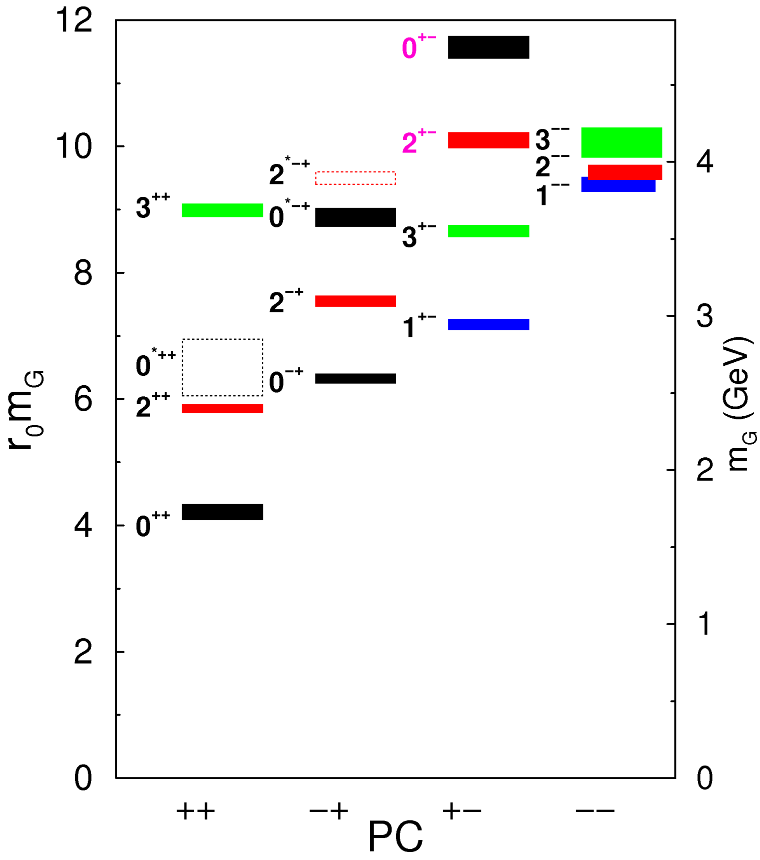

Figure 2.2: Spectrum of glueball masses [20].

2.3 Spectroscopy of states of light quarks

Charmonium states with a mass smaller than two D-meson masses decay into hadrons consisting of light u, d and s quarks. Selecting special decay modes of $c\bar{c}$ mesons one can select and study states with practically any quantum numbers. Therefore, CTF is a unique laboratory to study properties of mesons consisting of u, d, and s quarks with mass lighter than 3 GeV.

Of special interest is a search for bound states of two gluons, glueballs, and hybrid states, $q\bar{q}g$. With a $\sim 9\%$ probability the J/ψ meson decays into γgg followed by hadronization of two gluons. Thus, the J/ψ radiative decays are the best sources of glueball production. Lattice QCD calculations [20, 21] predict that the lightest glueballs with the quantum numbers $J^{PC} = 0^{++}$, 2^{++}, and 0^{-+} have masses smaller than 3 GeV. The glueball spectrum obtained in Ref. [20] is shown in Fig. 2.2.

One of the characteristic features allowing to distinguish a glueball from a regular two-quark meson is anomalously small two-photon width. Therefore, a search for glueballs in J/ψ decays should be complemented by a study of two-photon meson production. (see section 2.8). Previous searches for glueballs failed to give an unambiguous result. Most probably, glueballs are mixed with two-quark mesons. To determine a glueball fraction in a meson, one should study in detail meson properties in different processes and decay modes. For example, for a family of scalars (f_0, a_0, K_0^*), one should measure with high precision the processes $J/\psi \to f_0\gamma$, $f_0\phi$, $f_0\omega$, $a_0\rho$, $K^*(892)K_0^*$, and $\gamma\gamma \to f_0$, a_0 in different scalar decay modes $f_0, a_0, K_0^* \to PP$, VP, VV, $V\gamma$, where V and P

Table 2.3: The maximum values of the $e^+e^- \to D\bar{D}^{(*)}$ and $e^+e^- \to D_s\bar{D}_s^{(*)}$ cross sections [22, 23] and the energies where the cross sections are maximal.

	D^+D^-	$D^0\bar{D}^0$	$D\bar{D}^*$	$D_s^+D_s^-$	$D_s^+D_s^{*-}$
E, GeV	3.77	3.77	4.02	4.01	4.17
σ, nb	2.9	3.7	∼6.7	∼0.25	∼0.9

are vector and pseudoscalar mesons, respectively. A gluon component will reveal itself as a ratio of decay probabilities unusual for two-quark mesons and appearance of an extra f_0 meson not fitting the scheme of two-quark states. It is worth noting that in addition to gluonic and two-quark states, QCD predicts existence of exotic four-quark mesons and molecular states of two mesons. Existence of such states and their mixing with two-quark states makes even more complicated the pattern of levels of scalar mesons. Detailed systematization of mesons requires very large data samples of J/ψ decays and two-photon events that can be accumulated at CTF only.

A search for hybrid states is facilitated by the fact that such a state with a smallest mass of 1.3–2.2 GeV/c^2 should have exotic quantum numbers $J^{PC} = 1^{-+}$, impossible in the quark model (see review [7] and references therein). At the present time there are two candidates for the light-quark hybrid: $\pi_1(1400)$ and $\pi_1(1600)$. Properties of these states are badly investigated and even their existence should be confirmed. The π_1 states were observed primarily in diffractive experiments $\pi^-N \to \pi_1^-N$. CTF allows a study of completely different production mechanisms: S-wave decay $\chi_{c1} \to \pi\pi_1$ and P-wave decay $J/\psi \to \rho\pi_1$. One should study main decay modes expected for a hybrid: $\rho\pi$, $b_1\pi$, $f_1\pi$, $\eta\pi$, $\eta'\pi$. It is expected that the lightest state of a hybrid with non-exotic quantum numbers 0^{-+} is also in the mass region around 2 GeV. This state can be searched for in the decay $\chi_{c0} \to \pi\pi_1$ as well as in ψ meson decays.

2.4 Physics of D-mesons

In Table 2.3 the values of the D-meson production cross sections are listed. With the luminosity distribution given in Table 2.1, about 10^9 pairs of charged and neutral D mesons, and about 2×10^7 pairs of D_s mesons can be produced at CTF.

These numbers do not exceed the numbers of D mesons produced at existing B-factories at the e^+e^- c.m. energy of 10.58 GeV. There are, however, crucial differences between D-meson events at 10.58 and 3.77 GeV, which make low energy measurements preferable and allow to obtain more precise results with lower statistics:

- The multiplicity of charged and neutral particles is about two times lower at $\psi(3770)$ than at $\Upsilon(4S)$.
- In contrast to $\Upsilon(4S)$, where D meson production is accompanied by many other particles, at the threshold pure $D\bar{D}$ events are produced. This allows to use additional kinematic constraints for the event reconstruction. In particular, in events with leptonic or semileptonic decay of one of the D mesons, the neutrino is reconstructed with the additional constraint of zero missing mass. Use of the double-tag method, when one of the D mesons is fully reconstructed, while the other is studied, strongly reduces background and allows to perform precise measurements of absolute decay probabilities.

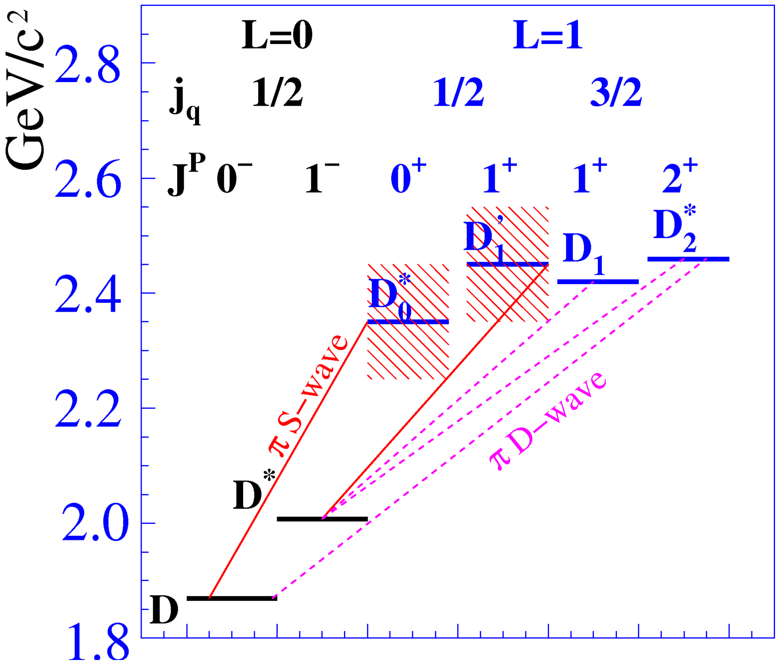

Figure 2.3: The D-meson states and transitions between them.

- D and $\bar{D}$ mesons are produced in a quantum-coherent state, for example, with $J^{PC} = 1^{--}$ in the reaction $e^+e^- \to D\bar{D}$ or $J^{PC} = 0^{++}$ in the reaction $e^+e^- \to D\bar{D}\gamma$. The coherence allows to use simple techniques for a study of $D\bar{D}$ mixing, search for CP violation, measurement of strong phases, and probabilities of decays to CP states.

At CTF a systematic study of D-meson properties will be performed.

2.4.1 Spectroscopy of D mesons

There are three types of charmed mesons: charged $D^\pm$ mesons with the quark structure $(c\bar{d})$ or $(\bar{c}d)$, neutral D^0 and $\bar{D}^0$ mesons with the structure $(c\bar{u})$ or $(\bar{c}u)$, and $D_s^\pm$ mesons with the structure $(c\bar{s})$ or $(\bar{c}s)$. The classification if D-meson excited states is demonstrated in Fig. 2.3. From the six states shown, the two lowest have $L = 0$, while the four others have $L = 1$. For the heavy-light quark system, in the heavy-quark limit, the total angular momentum (j_q) of the light quark is a conserved quantum number. This leads to decomposition of the P-wave states (D_J) into two multiplets with $j_q = 1/2$ and $j_q = 3/2$. The D_J states transit into the D and D^* states with π meson emission. Mesons with $j_q = 3/2$ decay in the D-wave and are therefore relatively narrow. Such a classification is applicable to all three types of D mesons. The known low-lying states of D and D_s mesons [2] are listed in Table 2.4. Experimental information about the D_J and D_{sJ} mesons is not complete. The quantum numbers for most of them are not established. Almost no information exists about their decay modes. Moreover, the masses of the D_{sJ} mesons lie well below the predictions of the quark model [24]. To explain this discrepancy, the hypotheses, for example, of six-quark or molecular D_{sJ} structure are suggested. At CTF D_J and D_{sJ} mesons can be produced in the reactions $e^+e^- \to D_0^*\bar{D}^*$, $D_1^{(\prime)}\bar{D}^{(*)}$, $D_2^*\bar{D}^{(*)}$, which have thresholds in the energy range of 4.3–4.7 GeV. The cross sections of these reactions are about 1 nb [25, 26]. So, the integrated luminosity of about 50 fb^{-1}, collected in the 4.3–5.0 GeV energy range, will be sufficient to perform a careful study of D_J and D_{sJ} properties. Detailed measurement of exclusive charm-production cross sections up to the 5–6 GeV will allow to observe production of the known

Table 2.4: The parameters of D and D_s mesons. The masses and widths are given in MeV.

Charge		D	D^*	D_0^*	D_1'	D_1	D_2^*
$\pm$	M	1869.60 ± 0.16	2010.25 ± 0.14	2403 ± 38		2423.4 ± 3.1	$2460.1^{+2.6}_{-3.5}$
	Γ	1040 ± 7 fs	0.096 ± 0.022	283 ± 40		25 ± 6	37 ± 6
0	M	1864.83 ± 0.14	2006.96 ± 0.16	2318 ± 29	2427 ± 36	2422.0 ± 0.6	$2462.8 \pm 1.$
	Γ	410.1 ± 1.5 fs	< 2.1	267 ± 40	384^{+130}_{-105}	20.4 ± 1.7	42.9 ± 3.1
Charge		D_s	D_s^*	D_{s0}^*	D_{s1}'	D_{s1}	D_{s2}^*
$\pm$	M	1968.47 ± 0.33	2112.3 ± 0.5	2317.8 ± 0.6	2459.5 ± 0.6	2535.29 ± 0.20	2572.6 ± 0.9
	Γ	500 ± 7 fs	< 1.9	< 3.8	< 3.5	< 2.3	20 ± 5

higher excited states, $D_{sJ}(2632)$ [27], $D_{sJ}(2708)$ [28], and $D_{sJ}(2860)$ [29], and find new states of this family.

2.4.2 Charmed-meson decays

Charmed-meson decays are a unique source for studying the dynamics of strong interactions. CTF allows to perform a detailed study of D and D_s decays including high precision measurements of decay probabilities, Dalitz plot analyses for three-body decays, and analyses of four-body decay distributions. It is expected that in close future many parameters extracted from D and D_s decays, such as the decay constants, f_D and f_{D_s}, and form factors of semileptonic decays, will be calculated with high accuracy in the framework of the lattice QCD (LQCD). Precision measurements of D decays will allow to control these calculations and extrapolate them to the B-meson region. As a result, a significant decrease of the theoretical uncertainties in extracting the CKM matrix elements V_{cd}, V_{cs}, V_{td}, V_{ts}, V_{ub} and V_{cb} from the precision measurements of various B meson decays is expected. For a precise measurement of the angle γ (ϕ_3) of the unitarity triangle at a super-B factory, neutral D-meson data are required, such as $D^0 - \bar{D}^0$ mixing parameters, the ratio of the amplitudes for D^0 and $\bar{D}^0$ decays into $K^+\pi^-$, the strong phase difference between these amplitudes, Dalitz distributions for the three-body hadronic decays, for example, into the $K_S\pi^+\pi^-$ final state [30]. All these data can be obtained at CTF. Below, the current status of leptonic and semileptonic D decays and CTF possibilities for their measurements are discussed in more detail.

In SM the width of a leptonic D decay is given by

$$\Gamma(D^+ \to l^+\nu) = \frac{G_F^2}{8\pi} f_D^2 m_l^2 M_D \left(1 - \frac{m_l^2}{M_D^2}\right)^2 |V_{cd}|^2.$$

A similar formula with the substitution of V_{cs} for V_{cd} is used for a D_s leptonic decay. The data on leptonic decays of the D and D_s mesons obtained by the CLEO Collaboration [31, 32] are listed in Table 2.5. The probabilities of the decays $D^+(D_s^+) \to e^+\nu$ are expected to be about $10^{-8}(10^{-7})$ and can hardly be measured even at CTF. The expected branching fraction for the $D^+ \to \tau^+\nu$ (about 1.2×10^{-3}) is at the level of the CLEO upper limit.

In SM the unitarity constraints allow to determine the CKM matrix elements V_{cd} and V_{cs} from experimental data with high precision: $|V_{cd}| = 0.2251(8)$, $|V_{cs}| = 0.9735(2)$ [33]. Therefore, the measured leptonic decay branching fractions can be used to extract the decay constants and their ratio. The experimental values of these parameters obtained using CLEO data from Table 2.5 are listed in Table 2.6.

Table 2.5: The data on leptonic decays of the D and D_s mesons obtained by the CLEO Collaboration.

	D^+	D_s^+
$e^+\nu_e$	$< 8.8 \times 10^{-6}$ [31]	$< 1.2 \times 10^{-4}$ [32]
$\mu^+\nu_\mu$	$(3.82 \pm 0.32 \pm 0.09) \times 10^{-4}$ [31]	$(5.65 \pm 0.45 \pm 0.17) \times 10^{-3}$ [32]
$\tau^+\nu_\tau$	$< 1.2 \times 10^{-3}$ [31]	$(6.42 \pm 0.81 \pm 0.18) \times 10^{-2}$ [32]

Table 2.6: The experimental values of the D and D_s decay constants [31, 32] in comparison with the LQCD calculation [34].

	Experiment	Theory
f_D, MeV	$205.8 \pm 8.5 \pm 2.5$	208 ± 4
f_{D_s}, MeV	$259.5 \pm 6.6 \pm 3.1$	241 ± 3
f_{D_s}/f_D	$1.26 \pm 0.06 \pm 0.02$	1.162 ± 0.009

In the second column of Table 2.6 the results of the most accurate-to-date LQCD calculation [34] are listed. It is seen that the claimed accuracy of the theoretical calculations has reached 1–2%. The measured value of f_D agrees with the result of the calculation, whereas the difference between the measurement and the LQCD calculation for f_{D_s} is 2.3 standard deviations. It is obvious that an independent confirmation of the theoretical calculations [34] is required. Since SM relations are used for the extraction of the decay constants, the difference between the experiment and the SM calculation can indicate the presence of contributions beyond the Standard Model (BSM). An additional SM test in this case might be the lepton universality test, i.e., comparison of the D_s decay widths into the $\tau\nu$ and $\mu\nu$ final states. The current experimental value of this ratio 11.4 ± 1.7 [32] is consistent with the theoretical value 9.76.

At CTF the expected statistics of D and D_s mesons are about three orders of magnitude larger than in the CLEO experiment. This will allow to measure the decay constants with an accuracy not worse than 0.5%. The same accuracy will be achieved in the near future in theoretical calculations.

The total branching fractions of the semileptonic D decays measured by CLEO are $B(D^0 \to Xe^+\nu_e) = (6.46 \pm 0.17 \pm 0.13)\%$, $B(D^+ \to Xe^+\nu_e) = (16.13 \pm 0.20 \pm 0.33)\%$ [35]. For D_s the same branching fraction is measured with a poor accuracy and is about 8%. One of the goals of CTF is a high-statistics study of exclusive semileptonic decay modes, including Dalitz plot analyses, and extraction of the form factors describing the hadronization of the primary quarks produced in D decays.

The best studied are semileptonic D decays into π and K mesons. These decays are described well with a single form factor. For example, the width for the $D \to Ke\nu$ decay is proportional to

$$\frac{d\Gamma(q^2)}{dq^2} \propto |f_+(q^2)|^2 |V_{cs}|^2,$$

where q is the difference of the D and K four-momenta. From measurements, the q^2 dependence of the form factor and the product $f_+(0)|V_{cs}|$ are extracted. The value of the form factor $f_+(0)$

can be calculated theoretically, for example, in the framework of LQCD. The current accuracy of these calculations is about 10%. The theoretical values of the form factors, $f_+^\pi(0) = 0.64(3)(6)$ and $f_+^K(0) = 0.73(3)(7)$ [36], are consistent with experimental values. The most precise measurement of the form factors was performed by the CLEO Collaboration [37]: $f_+^\pi(0) = 0.666(19)(5)$, $f_+^K(0) = 0.739(7)(5)$. To obtain these experimental values, the elements of the CKM matrix satisfying the unitarity condition [2] are used. It is expected that the accuracy of theoretical calculations of the form factors will improve to a 1% level. In this case the semileptonic decays can be used for measurements of V_{cs} and V_{cd} and to test the unitarity relation.

Other semileptonic D and D_s decay modes, excluding $D \to K^*\ell\nu$, are measured with low accuracy. For their detailed study, large statistics are needed which can be collected only at CTF. For example, an integrated luminosity of 100 fb^{-1} is required to measure the $D \to \rho e\nu$ branching fraction with a 0.5% accuracy, and ten times more statistics are needed for the precise measurement of three form factors describing this decay.

2.4.3 D^0–$\bar{D}^0$ Mixing

One of the main goals of the CTF is a study of D^0–$\bar{D}^0$ mixing. The transitions $D^0 \Leftrightarrow \bar{D}^0$ are a result of the interaction which changes the internal quantum number charm by $\Delta C = 2$. Due to these transitions of D mesons, the eigenstates of the mass matrix are the following:

$$|D_1\rangle = \frac{1}{\sqrt{|p|^2 + |q|^2}}(p|D^0\rangle + q|\bar{D}^0\rangle),$$

$$|D_2\rangle = \frac{1}{\sqrt{|p|^2 + |q|^2}}(p|D^0\rangle - q|\bar{D}^0\rangle).$$

In case of the CP-invariant interaction $p = q$ and the eigenstates $|D_1\rangle$ and $|D_2\rangle$ have a definite internal CP-parity. As a rule, two non-dimensional parameters are used for a description of mixing:

$$x \equiv \frac{\Delta m}{\Gamma}, \quad y \equiv \frac{\Delta\Gamma}{2\Gamma},$$

where Δm and $\Delta\Gamma$ are the differences of masses and widths of the $|D_2\rangle$ and $|D_1\rangle$ states and Γ is the average width of a D^0 meson. In SM the values of these parameters result from long-distance interactions (due to intermediate-meson transitions) and, therefore, predictions for their values have poor precision [38]. It is predicted that x and y can reach the values of ~ 0.01. The most precise data for D-meson mixing were obtained in B factory experiments. Averaging the current data, which was done by HFAG [39] under the assumption of CP-invariance, gives the following results:

$$x = 0.0100^{+0.0024}_{-0.0026}, \; y = 0.0076^{+0.0017}_{-0.0018}.$$

In CTF experiments, D^0 and $\bar{D}^0$ mesons will be produced in a coherent state with the odd C-parity in the process $e^+e^- \to D^0\bar{D}^0(n\pi^0)$ and the even one in the process $e^+e^- \to D^0\bar{D}^0\gamma(n\pi^0)$. This can be used for a measurement of mixing. In case of a symmetric CTF (the energies of colliding electrons and positrons are equal), a study of time evolution of the $D^0\bar{D}^0$ system is not possible due to a small lifetime of the D-mesons. Therefore, time integrated values will be analyzed below. The decays to the following final states will be considered as suggested in Ref. [40]:

- Hadron final states f and $\bar{f}$ which do not have a definite CP-parity, for example, $K^-\pi^+$, which is a Cabibbo-favored (CF) decay of D^0, or doubly Cabibbo suppressed (DCF) decay of $\bar{D}^0$;

Table 2.7: The ratios of decay probabilities of the $D^0\bar{D}^0$ state to various final states. Only leading-order terms in a power series expansion in r_f^2, x and y are given.

	$C=-1$	$C=+1$
$(1/4)\cdot(\Gamma_{lS_+}\Gamma_{S_-}/\Gamma_{lS_-}\Gamma_{S_+} - \Gamma_{lS_-}\Gamma_{S_+}/\Gamma_{lS_+}\Gamma_{S_-})$	y	$-y$
$(\Gamma_{fl^-}/4\Gamma_f)\cdot(\Gamma_{S_-}/\Gamma_{lS_-} - \Gamma_{S_+}/\Gamma_{lS_+})$	y	$-y$
$(\Gamma_{f\bar{f}}/4\Gamma_f)\cdot(\Gamma_{S_-}/\Gamma_{\bar{f}S_-} - \Gamma_{S_+}/\Gamma_{\bar{f}S_+})$	$y+r_fz_f$	$-(y+r_fz_f)$
$(\Gamma_f\Gamma_{S_+S_-}/4)\cdot(1/\Gamma_{fS_-}\Gamma_{S_+} - 1/\Gamma_{fS_+}\Gamma_{S_-})$	$y+r_fz_f$	0
$(\Gamma_{\bar{f}}/2)\cdot(\Gamma_{S_+S_+}/\Gamma_{\bar{f}S_+}\Gamma_{S_+} - \Gamma_{S_-S_-}/\Gamma_{\bar{f}S_-}\Gamma_{S_-})$	0	$y+r_fz_f$
$\Gamma_{ff}/\Gamma_{f\bar{f}}$	R_M	$2r_f^2+r_f(z_fy-w_fx)$
$\Gamma_{fl^+}/\Gamma_{fl^-}$	r_f^2	$r_f^2+r_f(z_fy-w_fx)$
$\Gamma_{l^\pm l^\pm}/\Gamma_{l^+l^-}$	R_M	$3R_M$

- Semileptonic and leptonic final states, l^+ and l^-, which, without mixing, uniquely determine the flavor of a D^0-meson;
- The states which are eigenstates of CP parity, S_+ and S_-.

Under the assumption of CP invariance, the probability of producing two D^0 mesons in various combinations in the final state depends on the following parameters: x, y, the amplitudes $A_f = \langle f|D^0\rangle$, $A_l = \langle l^+|D^0\rangle$, $A_{S_\pm} = \langle S_\pm|D^0\rangle$, the absolute value and phase of the ratio for the DCF and CF amplitudes $r_fe^{-\delta_f} = -\langle f|\bar{D}^0\rangle/\langle f|D^0\rangle$. One can also determine the following parameters: $R_M \equiv (x^2+y^2)/2$, $z_f \equiv 2\cos\delta_f$, $w_f \equiv 2\sin\delta_f$. The ratios of decay probabilities of the $D^0\bar{D}^0$ system to various final states are shown in Table 2.7. Γ_{jk} means D^0 decay to the j state and $\bar{D}^0$ to the k state. Γ_j means D^0 decay to the j state and $\bar{D}^0$ to any final state.

As shown in the Table 2.7, evidence of events $D^0\bar{D}^0 \to (K^-\pi^+)(K^-\pi^+)$ and $D^0\bar{D}^0 \to (K^-e^+\nu_e)(K^-e^+\nu_e)$ in $\psi(3770)$ decays is possible via mixing only. For 10^9 $D^0\bar{D}^0$ events and for $R_M = 0.8\times10^{-4}$ obtained using the measured x and y values, it is expected to detect about 150 of these events. Results of Ref. [40] were used for estimation of the detection efficiency which corresponds to CLEO performance. Thus, a statistical sensitivity for a measurement of R_M using these two decays only is about 5×10^{-6}. A systematic uncertainty will mainly depend on the quality of particle identification.

The probabilities of inclusive $D^0\bar{D}^0$ decays to the $S_\pm X$ final states are proportional to $(1\mp y)$ [40]. This allows to measure a y parameter. For double ratios shown in the first and second rows of Table 2.7, the substantial part of systematic errors, which originates from data-MC simulation difference in track reconstruction and particle identification, cancels. A statistical precision of y determined from the ratio $(1/4)\cdot(\Gamma_{lS_+}\Gamma_{S_-}/\Gamma_{lS_-}\Gamma_{S_+} - \Gamma_{lS_-}\Gamma_{S_+}/\Gamma_{lS_+}\Gamma_{S_-})$ was estimated in [41] to be $26/\sqrt{N_{DD}}$, where N_{DD} is the number of produced $D^0\bar{D}^0$ pairs. For $N_{DD} = 10^9$ it equals 0.0008, i.e., 2.5 times better than the current experimental precision.

The value of the strong phase δ_f in the $K^-\pi^+$ final state, which is important, for example, for a measurement of $D^0\bar{D}^0$ mixing at B-factories, can be measured using the relations listed in the third and fourth rows of Table 2.7. The expected statistical precision for a measurement of $\cos\delta_f$ is estimated as $444/\sqrt{N_{DD}} = 0.014$ [41], that corresponds to a precision of 0.05 for δ_f. At the present time the average value of this parameter is $0.39^{+0.17}_{-0.18}$.

Measurements, which can be performed with the $D^0\bar{D}^0$ system in the C-even state, have the best sensitivity for y. For a measurement of y with a precision of 0.0008 from the ratio $\Gamma_{fl^+}/\Gamma_{fl^-}$, 3×10^8 $D^0\bar{D}^0$ pairs are required. This number of C-even $D^0\bar{D}^0$ pairs can be produced in the process $e^+e^- \to D^0\bar{D}^{*0} \to D^0\bar{D}^0\gamma$ with an integrated luminosity of 250 fb^{-1} collected at an energy of 4.02 GeV. This measurement is also sensitive to the parameter x. However, as it is shown in Table 2.7, a sensitivity to x is worse than for y due to δ_f infinitesimality. As it was shown in a recent paper [42], this problem can be successfully solved in case of a three-particle decay of D^0, for example, to $K_S\pi^+\pi^-$ or $K^+\pi^-\pi^0$. An important feature of the suggested method is that for the C-odd $D^0\bar{D}^0$ state all effects of mixing, which have impact on the density of events on the Dalitz plot, cancel in the first order of x and y. In the case of the C-even one, the effects of mixing are doubled compared to a non-coherent D^0 decay. Thus, in this experiment there is a possibility to measure x and y by a direct comparison of the distribution of events on the Dalitz plot for the C-even and -odd $D^0\bar{D}^0$ states. As it was shown in Ref. [42], statistical errors for x and y are approximately equal. It is expected that many systematic errors in this measurement will cancel because the states with opposite charge parity will be produced simultaneously and in similar kinematic states during data taking. Furthermore, unlike other methods described above, this method does not require measuring absolute probabilities of D^0 decays. It can be estimated that for an integrated luminosity of about 1 ab^{-1}, a precision of measuring mixing parameters will be not worse than at the Super B factory for an integrated luminosity of 10 ab^{-1} [43].

2.4.4 Search for CP violation

A search for CP violation in D decays is one of the most interesting experiments to be performed at CTF. The Standard Model predicts a very small CP asymmetry in reactions with charmed particles. The maximum effect of about 10^{-3} is expected in the Cabibbo-suppressed (CS) D decays [38]. An observation of a CP asymmetry in CF and DCS decays at any level or an asymmetry higher than 10^{-3} in CS decays will clearly indicate the presence of new BSM physics. The exceptions are the decays to the final states containing K_S or K_L, for example, $D \to K_S\pi$, in which the CP asymmetry arises from the fact that a K_S meson is not a CP eigenstate. For the decay $D^\pm \to K_S\pi^\pm$, a CP asymmetry is predicted with a relatively high accuracy, $(3.32 \pm 0.06) \times 10^{-3}$ [38].

We can distinguish three types of CP violation:

- The direct CP violation in $\Delta C = 1$ transitions reveals itself as an inequality of the amplitude of D meson decay (A_f) and the corresponding CP-conjugate amplitude ($\bar{A}_{\bar{f}}$). CP violation can be observed when the decay amplitude is a sum of two amplitudes with different weak and strong phases:
$$A_f = |A_1|e^{i(\delta_1+\phi_1)} + |A_2|e^{i(\delta_2+\phi_2)}.$$
The weak phase changes its sign under the CP transformation ($\phi_i \to -\phi_i$), while the strong phase δ_i does not.

- CP violation in D^0–$\bar{D}^0$ mixing due to $\Delta C = 2$ transitions reveals itself in a deviation of the ratio $R_m = |p/q|$ from unity.

- In decays of neutral D mesons CP violation can be observed in the interference of decays with mixing ($D^0 \to \bar{D}^0 \to f$) and without it ($D^0 \to f$). This type of CP violation is described by the parameter
$$\varphi = \arg\lambda_f = \arg\left(\frac{q}{p}\frac{\bar{A}_f}{A_f}\right).$$

Table 2.8: The current values of the CP asymmetry measured in D decays.

$D^0 \to K^-\pi^+$	$0.005 \pm 0.004 \pm 0.009$ [44]		
$D^0 \to K_S\pi^0$	$+0.001 \pm 0.013$ [45]	$D^+ \to K_S\pi^+$	$-0.013 \pm 0.007 \pm 0.003$ [44]
$D^0 \to K^+K^-$	-0.0017 ± 0.0031 [2]		
$D^0 \to K_SK_S$	-0.23 ± 0.19 [45]	$D^+ \to K_SK^+$	$-0.002 \pm 0.015 \pm 0.009$ [44]
$D^0 \to \pi^+\pi^-$	0.002 ± 0.004 [2]		
$D^0 \to \pi^0\pi^0$	$+0.001 \pm 0.048$ [45]		
$D^0 \to K^-\pi^+\pi^0$	$+0.002 \pm 0.004 \pm 0.008$ [22]	$D^+ \to K^-\pi^+\pi^+$	$-0.005 \pm 0.004 \pm 0.009$ [22]
$D^0 \to K_S\pi^+\pi^-$	$-0.009 \pm 0.021^{+0.016}_{-0.057}$ [46]	$D^+ \to K_S\pi^+\pi^0$	$+0.003 \pm 0.009 \pm 0.003$ [22]
$D^0 \to K^+K^-\pi^0$	$-0.0100 \pm 0.0167 \pm 0.0025$ [47]	$D^+ \to K^+K^-\pi^+$	$+0.003 \pm 0.006$ [2]
$D^0 \to \pi^+\pi^-\pi^0$	$+0.0031 \pm 0.0041 \pm 0.0017$ [47]	$D^+ \to \pi^+\pi^-\pi^+$	-0.017 ± 0.042 [48]
$D^0 \to K^-\pi^+\pi^+\pi^-$	$+0.007 \pm 0.005 \pm 0.009$ [22]	$D^+ \to K^-\pi^+\pi^+\pi^0$	$+0.010 \pm 0.009 \pm 0.009$ [22]
$D^0 \to K^+\pi^-\pi^+\pi^-$	-0.018 ± 0.044 [49]	$D^+ \to K_S\pi^+\pi^+\pi^-$	$+0.001 \pm 0.011 \pm 0.006$ [22]
$D^0 \to K^+K^-\pi^+\pi^-$	$-0.082 \pm 0.056 \pm 0.047$ [50]	$D^+ \to K_SK^+\pi^+\pi^-$	$+0.001 \pm 0.011 \pm 0.006$ [50]

CP violation in mixing leads to the difference between the widths of semileptonic decays with a wrong sign of the decay lepton $\Gamma(\bar{D}^0 \to l^+X) \neq \Gamma(D^0 \to l^-X)$. For example, in $\psi(3770)$ decays the following asymmetry can be measured

$$A_{SL} = \frac{\Gamma_{l^+l^+} - \Gamma_{l^-l^-}}{\Gamma_{l^+l^+} + \Gamma_{l^-l^-}} = \frac{1 - |q/p|^4}{1 + |q/p|^4}.$$

For 10^9 $D^0\bar{D}^0$ pairs, about 60 $(K^\pm e^\mp\nu)(K^\pm e^\mp\nu)$ events are expected to be produced. With these statistics, the $|q/p|$ ratio will be determined with about 6% accuracy. The current value of the parameter $|q/p|$ is $0.86^{+0.17}_{-0.15}$.

Direct CP violation can be observed as a difference between the decay widths for charged D mesons:

$$A^{CP}_{\pm} = \frac{\Gamma(D^- \to f^-) - \Gamma(D^+ \to f^+)}{\Gamma(D^- \to f^-) + \Gamma(D^+ \to f^+)}.$$

For neutral D mesons, all three types of CP violation contribute to the same asymmetry parameter. The current values of the CP asymmetry measured in D decays are listed in Table 2.8.

In Ref. [22] the CP asymmetries were measured by the CLEO detector using a data sample of 10^6 D^+D^- pairs. At CTF, for many decays the statistical error of asymmetry can be decreased to a level of 10^{-3}-10^{-4}. The systematic error is dominated by uncertainties in track reconstruction and particle identification. The reconstruction and identification efficiencies are different for pions and kaons of different charges and are usually not reproduced in simulation with sufficient accuracy. At CTF a level of 10^{-3} for the systematic uncertainty seems achievable. For example, in the BaBar and Belle measurements of the asymmetries for the decays $D^0/\bar{D}^0 \to K^+K^-$, $\pi^+\pi^-$ [51, 52], the systematic uncertainty due to a difference in the detection efficiency for π^+ and π^- mesons used for D tagging was decreased to the 10^{-3} level. The thickness of material before and inside the tracking system of the CTF detector should be minimized to reduce the systematic uncertainty for charge asymmetry measurements.

The CP asymmetry in decays of neutral D mesons can be represented as a sum of three terms. For example, for the decay into the CP eigenstate $\eta^{CP}_f = \pm 1$ [53]

$$A^{CP}_f = a^d_f + a^m_f + a^i_f,$$

$$a_f^m = -\eta_f^{CP}\frac{y}{2}(R_m - R_m^{-1})\cos\varphi,$$

$$a_f^i = \eta_f^{CP}\frac{x}{2}(R_m + R_m^{-1})\sin\varphi,$$

where a_f^d is a CP asymmetry in the decay, φ is a relative weak phase between the amplitudes for the decays $D^0 \to f$ and $D^0 \to \bar{D}^0 \to f$. The magnitude of the second term a_f^m is determined mainly by CP violation in mixing. The third term a_f^i is dominated by CP violation in the interference. The mixing leads to a difference in the time dependencies of the D^0 and $\bar{D}^0$ decay probabilities. This allows to localize and measure the contribution of the second and third terms. In experiments at B-factories [54, 55] the value

$$\delta Y = a_f^m + a_f^i = (-0.12 \pm 0.25) \times 10^{-2}$$

was obtained for the final states K^+K^- and $\pi^+\pi^-$. The formula given above is valid for incoherent production of D^0 and $\bar{D}^0$ mesons. At CTF such an asymmetry will be studied for decays of D^0 mesons produced in the reaction $e^+e^- \to D^{*-}D^+ \to \pi^-D^0D^+$. For coherent $D^0\bar{D}^0$ production, the formula for A^{CP} is modified and becomes dependent on the decay used for tagging. This makes it possible to separate various contributions to the CP asymmetry without studying their time dependence. For example, the reaction $D^0\bar{D}^0 \to f_1 f_2$, where f_1 and f_2 are the states with the same CP parity, is forbidden at the $\psi(3770)$ resonance if CP is conserved. The probability of the decay is described by the following formula [56]:

$$\Gamma_{f_1 f_2} = \frac{1}{2R_m^2}\left[(2 + x^2 - y^2)|\lambda_{f_1} - \lambda_{f_2}|^2 + (x^2 + y^2)|1 - \lambda_{f_1}\lambda_{f_2}|^2\right]\Gamma_{f_1}\Gamma_{f_2}.$$

Since the terms corresponding to the contribution of mixing are proportional to the squares of x and y, the difference between direct CP violation for decays $D^0 \to f_1$ and $D^0 \to f_2$ is measured in this reaction.

At CTF with 10^9 $D^0\bar{D}^0$ pairs the sensitivity level of 10^{-3} can be reached for the asymmetry difference between, for example, the K^+K^- and $\pi^+\pi^-$ final states. A similar measurement can be performed using the reaction $e^+e^- \to D^{*0}\bar{D}^0 \to \gamma D^0\bar{D}^0$. In this case the difference between CP asymmetries for states with opposite CP parities is measured.

Another example is a measurement of the asymmetry

$$A_{fl}^{CP} = \frac{\Gamma(l^-X, f) - \Gamma(l^+X, f)}{\Gamma(l^-X, f) + \Gamma(l^+X, f)}.$$

Here one D meson decays semileptonically, while the other to a CP eigenstate. Neglecting direct CP violation [57]

$$A_{fl}^{CP} = (1 + \eta)(a_f^m + a_f^i),$$

where η is the C parity of the $D^0\bar{D}^0$ pair. It is seen that at $\eta = -1$, i.e., in $\psi(3770)$ decays, mixing does not contribute to the measured asymmetry, while for $\eta = 1$, i.e., in the reaction $e^+e^- \to D^{*0}\bar{D}^o \to \gamma D^0\bar{D}^0$ the mixing contribution to the asymmetry is two times larger than that for D^0 mesons produced incoherently. Measurements performed in these two reactions allow to separate the contributions of direct and indirect mixing.

There are other powerful methods to search for CP violation. In Ref. [58] it is proposed to use the difference between the probabilities of decays of untagged D^0 mesons to the charge-conjugate states, for example, $K^-\pi^+$ and $K^+\pi^-$, to extract the parameter $\sin\varphi$. The Dalitz analysis of three-body decays allows to measure CP asymmetries for different resonant intermediate states (see, for example, the results of Ref. [59]). An interference between the CP-conserving and CP violating amplitudes in the Dalitz-plot distributions can increase the sensitivity of a search for CP violation. In the four-body decays, a search for CP violation can use T-odd moments [60] or triple products of momenta [61]. Using these methods at CTF, one can measure the CP asymmetry in D decays with an accuracy of about 10^{-3} for both direct and indirect mechanisms of CP violation.

2.4.5 D-meson rare decays

Rare decays of D mesons are a tool for a search for new physics beyond the Standard Model [62]. The rare D decays most suitable for this purpose are:

1. flavor-changing neutral current (FCNC) decays via the weak neutral current, providing the transition between c and u quarks,
2. lepton-flavor-violating (LFV) decays,
3. lepton-number-violating (LV) decays.

Two latter types of decays are forbidden in the Standard Model. In SM decays via a $c \to u$ transition are described by loop diagrams and are strongly suppressed. For example, the probabilities for the $c \to ul^+l^-$ and $c \to u\gamma$ transitions are estimated to be of the order 10^{-8}. For specific exclusive D decays, however, the contributions of large-distance dynamics should be taken into account. For example, the dominant contribution to the decay $D^+ \to \pi^+l^+l^-$ comes from the transition via the intermediate $\pi^+\phi$ state followed by the decay $\phi \to l^+l^-$. As a result, the $D \to X\gamma$ and $D \to Xl^+l^-$ branching fractions, where X is a hadronic state, increase up to 10^{-5}–10^{-6}. Two of such decays have been measured and have the values of the branching fractions consistent with SM: $B(D^0 \to \phi\gamma) = (2.4^{+0.7}_{-0.6}) \times 10^{-5}$ [63] and $B(D^+ \to \pi^+\phi \to \pi^+\mu^+\mu^-) = (1.8 \pm 0.5 \pm 0.6) \times 10^{-6}$ [64].

Due to the large-distance contributions, which are difficult to calculate accurately in the framework of SM, decays like $D \to X\gamma$ become weakly sensitive to new physics effects. But even for these decays, observables having some "new physics" sensitivity can be found. For example, in Ref. [65] it is proposed to measure the difference $R = B(D^0 \to \rho^0\gamma)/B(D^0 \to \omega\gamma) - 1$, which is estimated to be $(6 \pm 15)\%$ in SM. In the Minimal Supersymmetric Standard Model (MSSM), with some choice of model parameters the probability of the transition $c \to u\gamma$ can reach 6×10^{-6} and the value of R can be of the order 1 [65].

In decays $D \to Xl^+l^-$ one can analyze the spectrum of the lepton-pair invariant mass and select mass regions sensitive to the small-distance contributions. In Fig.2.4 taken from Ref. [66] the lepton invariant mass spectra are shown for the decays $D^+ \to \pi^+e^+e^-$ and $D^0 \to \rho^0e^+e^-$ in SM and MSSM. Restrictions on the MSSM parameters can be obtained with a sensitivity to the decay at the level of 10^{-6}. The predictions for decays $D \to Xl^+l^-$ obtained in different SM extensions can be found in Refs. [62, 66, 67].

Another class of decays with the $c \to u$ transition includes decays of a neutral D meson into the lepton or photon pair. SM predicts $B(D^0 \to \gamma\gamma) \simeq 3.5 \times 10^{-8}$ and $B(D^0 \to \mu^+\mu^-) \sim 10^{-12}$ [66]. The $D^0 \to \mu^+\mu^-$ branching fraction can reach 3.5×10^{-6} in supersymmetric models with R-parity violation. These models give also large values for the branching fractions of the following LFV decays: $B(D^0 \to \mu^+e^-) < 10^{-6}$, $B(D^+ \to \pi^+\mu^+e^-) < 3 \times 10^{-5}$, $B(D^0 \to \rho^0\mu^+e^-) < 1.4 \times 10^{-5}$.

In Table 2.9 the current upper limits on the rare D and D_s decays are listed. At CTF a sensitivity of 10^{-8} to rare D decays can be reached.

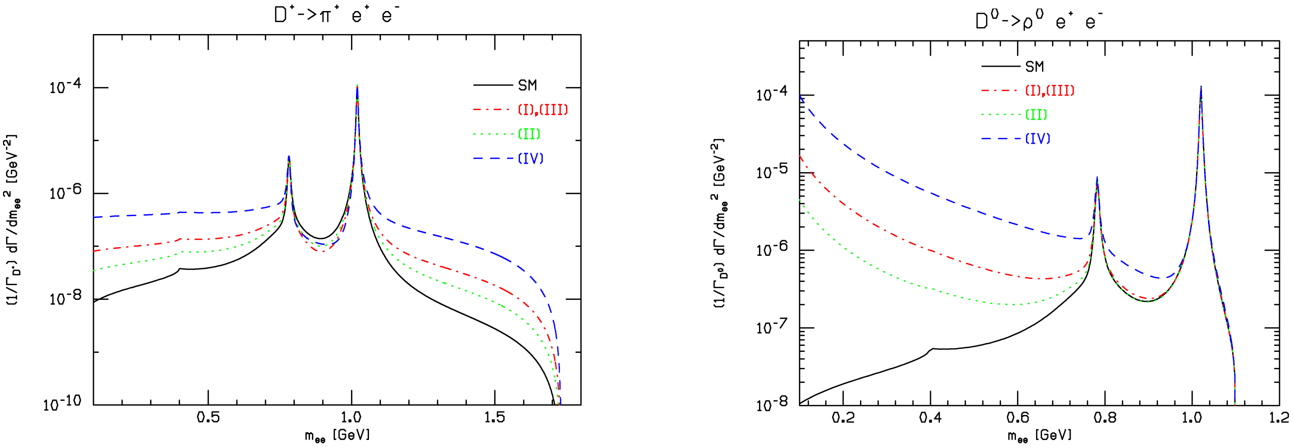

Figure 2.4: The spectra of the lepton-pair invariant mass for the decays $D^+ \to \pi^+ e^+ e^-$ (left) and $D^0 \to \rho^0 e^+ e^-$ (right). The solid curve represents the SM prediction, while the dashed curves indicate the MSSM predictions for different sets of model parameters.

Table 2.9: The experimental upper limits on the rare D and D_s decays in units of 10^{-6}.

$D^0 \to \gamma\gamma$	26 [68]	$D^+ \to \pi^+ e^+ e^-$	7.4 [71]
$D^0 \to e^+ e^-$	1.2 [69]	$D^+ \to \pi^+ \mu^+ \mu^-$	3.9 [64]
$D^0 \to \mu^+ \mu^-$	1.3 [69]	$D^+ \to \pi^+ e^+ \mu^-$	10.8 [72]
$D^0 \to \mu^+ e^-$	0.81 [69]	$D^+ \to \rho^+ \mu^+ \mu^-$	560 [73]
$D^0 \to \pi^0 e^+ e^-$	45 [70]		
$D^0 \to \rho^0 e^+ e^-$	100 [70]	$D_s^+ \to K^+ e^+ e^-$	6.6 [72]
$D^0 \to \pi^0 e^+ \mu^-$	86 [70]	$D_s^+ \to K^+ \mu^+ \mu^-$	25.4 [72]
$D^0 \to \rho^0 e^+ \mu^-$	49 [70]	$D_s^+ \to K^+ e^+ \mu^-$	3.6 [72]

Table 2.10: Parameters of the S-wave charmed baryons [2]

	Structure	J^P	Mass, MeV	Width,MeV	Decay
Λ_c^+	udc	$(1/2)^+$	2286.46 ± 0.14	(200 ± 6) fs	weak
Ξ_c^+	usc	$(1/2)^+$	$2467.8^{+0.4}_{-0.6}$	(442 ± 26) fs	weak
Ξ_c^0	dsc	$(1/2)^+$	$2470.88^{+0.34}_{-0.8}$	112^{+13}_{-10} fs	weak
Σ_c^{++}	uuc	$(1/2)^+$	2454.02 ± 0.18	2.23 ± 0.30	$\Lambda_c^+\pi^+$
Σ_c^+	udc	$(1/2)^+$	2452.9 ± 0.4	< 4.6	$\Lambda_c^+\pi^0$
Σ_c^0	ddc	$(1/2)^+$	2453.76 ± 0.18	2.2 ± 0.4	$\Lambda_c^+\pi^-$
$\Xi_c'^{+}$	usc	$(1/2)^+$	2575.6 ± 3.1	—	$\Xi_c^+\gamma$
$\Xi_c'^{0}$	dsc	$(1/2)^+$	2577.9 ± 2.9	—	$\Xi_c^0\gamma$
Ω_c^0	ssc	$(1/2)^+$	2695.2 ± 1.7	(69 ± 12) fs	weak
Σ_c^{*++}	uuc	$(3/2)^+$	2518.4 ± 0.6	14.9 ± 1.9	$\Lambda_c^+\pi^+$
Σ_c^{*+}	udc	$(3/2)^+$	2517.5 ± 2.3	< 17	$\Lambda_c^+\pi^0$
Σ_c^{*0}	ddc	$(3/2)^+$	2518.0 ± 0.5	16.1 ± 2.1	$\Lambda_c^+\pi^-$
Ξ_c^{*+}	usc	$(3/2)^+$	$2645.9^{+0.5}_{-0.6}$	< 3.1	$\Xi_c\pi$
Ξ_c^{*0}	dsc	$(3/2)^+$	2645.9 ± 0.5	< 5.5	$\Xi_c\pi$
Ω_c^{*0}	ssc	$(3/2)^+$	2765.9 ± 2.0	—	$\Omega_c^0\gamma$

2.5 Charmed baryons

Charmed baryons, which can be produced at CTF in the reaction $e^+e^- \to B_c\bar{B}_c$, consist of two light quarks (u, d, s) and a heavy c quark. A pair of light quarks forms two SU(3) multiplets: the antisymmetric antitriplet and the symmetric sextet. In S-wave low-lying baryons, the flavor symmetry and spin are related to each other: the total spin of light quarks is equal to 0 for the antitriplet and 1 for the sextet. In combination with the c quark, the antitriplet produces three states with spin 1/2 (Λ_c^+, Ξ_c^+, Ξ_c^0), while the sextet gives six states with spin 1/2 ($\Sigma_c^{++,+,0}$, $\Xi_c'^{+}$, $\Xi_c'^{0}$, Ω_c^0) and six states with spin 3/2 ($\Sigma_c^{*++,+,0}$, Ξ_c^{*+}, Ξ_c^{*0}, Ω_c^{*0}). All 15 S-wave charmed baryons have been observed. Their parameters are listed in Table 2.10.

Many excited charmed baryons are expected. In particular, the quark model predicts 63 P-wave states [74]. Sixteen of the excited states with masses in the range from 2.6 to 3.1 GeV have been observed [2, 75].

In recent years physics of charmed baryons has been studied mainly at B-factories. In spite of the large number of produced charmed baryons (B factories produced about 10^7 Λ_c), their properties are rather badly known. There is practically no experimental information about the quantum numbers of baryons and absolute branching fractions of their decays. The potential of CTF in a study of charmed baryons depends strongly on the cross sections for the reactions $e^+e^- \to B_c\bar{B}_c$. For the reaction $e^+e^- \to \Lambda_c\bar{\Lambda}_c$ the cross section was measured by Belle [76]. The cross section is maximal at the energy about 4.65 GeV. The maximal value is about 0.5 nb. Such a large cross section value can be explained by a possible presence of a $c\bar{c}$ resonance near the $\Lambda_c\bar{\Lambda}_c$ threshold. With an integrated luminosity of 200 fb^{-1} CTF will produce 10^8 $\Lambda_c\bar{\Lambda}_c$ pairs. This will allow to perform a detailed study of Λ_c properties with the use of the double-tag method. For other charmed baryons the experimental data on the reactions $e^+e^- \to B_c\bar{B}_c$ are absent. Without a resonance enhancement the expected cross section does not exceed 10 pb. The physics program for baryons depends on the maximum energy of CTF. The most interesting physics task is a detailed study of weak decays of the charmed baryons $\Lambda_c^+(2286)$, $\Xi_c^+(2468)$, $\Xi_c^0(2471)$, and $\Omega_c^0(2698)$. The required maximum energies of the factory are 4.7, 5.1 and 5.5 GeV.

2.6 τ lepton physics

At CTF τ leptons are produced in the process $e^+e^- \to \tau^+\tau^-$. Its cross section grows fast from 0.1 nb near threshold of $\tau^+\tau^-$ production ($2E = 3.55$ GeV) to 2.5 nb near threshold of D meson production ($2E \approx 3.7$ GeV) and reaches its maximum of 3.5 nb at $2E = 4.25$ GeV. During the CTF operation about 10^{10} pairs of τ leptons will be produced, an order of magnitude larger than at B factories, but smaller than statistics expected at Super B factories (about 5×10^{10}).

One should note that the existing accuracy of many τ lepton parameters, e.g., its decay widths, is currently limited by systematic effects. For precise measurements of decay probabilities and hadronic spectral functions, a dedicated near-threshold run is planned. At threshold τ leptons are produced at rest allowing to suppress background by applying an additional condition on kinematics of hadronic decays: $2m_\tau E_{had} = m_\tau^2 + m_{had}^2$, where E_{had} and m_{had} are energy and invariant mass of the hadronic system. Use of this condition allows to select τ events with the tagging method. The remaining background can be measured running below threshold of τ lepton production. With an integrated luminosity of 1 ab^{-1} collected near the $\tau^+\tau^-$ threshold about 10^8 τ lepton pairs will be produced.

Spectral functions measured in hadronic decays of the τ can be used to determine the strong interaction constant α_s [77] (see also Ref. [78]). Data from hadronic decays with $\Delta S = 1$ are used to determine the mass of the s-quark m_s and the CKM matrix element V_{us} [79]. Potentially τ lepton decays provide a source for the most precise measurements of α_s, m_s and V_{us}.

A high precision measurement of the probabilities of leptonic decays as well as decays $\tau^+ \to \pi^+\nu_\tau$ and $\tau^+ \to K^+\nu_\tau$ will result in a significant improvement of lepton universality tests in the charged lepton sector.

For precision tests of SM and lepton universality, knowledge of the τ lepton mass is mandatory. The most precise method of τ lepton mass determination is a measurement of the energy dependence of the cross section for the process $e^+e^- \to \tau^+\tau^-$ near threshold. Such measurements require high-precision energy calibration of the collider using resonance depolarization or Compton back scattering.

An important test of SM is a study of the Lorentz structure of the amplitude for the $\tau \to l\nu_l\nu_\tau$ decay. A near-threshold measurement will allow a determination of the lepton energy spectrum in this decay without background. The spectrum is parametrized using four Michel parameters [80], two of which require knowledge of τ lepton polarization. The polarization degree can be measured via the decay of the second τ, e.g., via the decay $\tau \to \rho\nu$. A longitudinal polarization of initial beams would allow a more efficient usage of the collected data samples and minimize a systematic uncertainty of polarization-dependent parameters.

LFV decays of τ lepton, such as $\tau \to l\gamma$, $\tau \to lll^{(\prime)}$ or $\tau \to lh$, where l, l' — electron or muon, and h is a hadronic system, are sensitive to effects of New Physics. Different models beyond SM predict probabilities of these decays at the level of 10^{-7}–10^{-10} (see, for example, Ref. [81]).

Experimental upper limits on the probabilities of LFV decays achieved at the B factories are in the range 10^{-7} to 2×10^{-8} [2] and already constrain the space of parameters of some models. For most of the decays, a much higher sensitivity is expected in future experiments at super-B factories. However, for some decays in which an upper limit on the decay probability is determined by background, the CTF sensitivity can be higher than at super-B factories. This is, in particular, true for $\tau \to \mu\gamma$ decay, very important in a search for New Physics. At B factories an upper limit for the probability of this decay is determined by the background from the process $e^+e^- \to \tau^+\tau^-\gamma$, not significant at CTF.

CP violation in the quark sector does not explain the observed baryon asymmetry of the universe. Therefore, it is reasonable to search for it in the lepton sector, in particular, in τ lepton decays. CP violation can be observed in hadronic τ decays, provided that there are two interfering amplitudes with different strong and weak phases. Under CP transformation, $e^{i\delta_w+i\delta_s}$ is transformed into $e^{-i\delta_w+i\delta_s}$, where δ_w and δ_s are relative strong and weak phases of two amplitudes. This results, for example, in the non-equality of the widths of CP conjugate decays. The asymmetry $A_{CP} = (\Gamma(\tau^+ \to f+) - \Gamma(\tau^- \to f-))/(\Gamma(\tau^+ \to f+) + \Gamma(\tau^- \to f-))$ is proportional to $\sin\delta_s \sin\delta_w$. In SM τ lepton decays are described by a single amplitude with a W boson exchange. Therefore, observation of CP asymmetry would be an explicit indication of physics beyond SM. An only exception is $\tau \to \pi K_{S(L)}\nu_\tau$ decay, in which the CP asymmetry at the level of 3×10^{-3} [82] arises in SM because of CP violation in kaons. Suggestions for using various decays for CP violation are considered in Refs. [83, 84, 85, 86, 87, 88]. The most promising decays are $\tau \to K\pi^0\nu_\tau$, $\tau \to \rho\pi\nu_\tau$, $\tau \to \omega\pi\nu_\tau$, $\tau \to a_1\pi\nu_\tau$. In addition to measuring the asymmetry in the decay width, A_{CP} defined above, it is also suggested to use a so called modified asymmetry, when experimental differential distributions of the final hadrons are integrated with a specially selected kernel over a limited range of phase space, and an asymmetry in the triple product $\boldsymbol{\sigma \cdot (p_1 \times p_2)}$, where $\boldsymbol{\sigma}$, $\boldsymbol{p_1}$, $\boldsymbol{p_2}$ are a τ polarization vector and momenta of two final hadrons, respectively. It is worth noting that the asymmetry in the triple product is proportional to $\cos\delta_s \sin\delta_w$, i.e., a non-zero difference of the strong phases is not needed for its observation.

A search for CP violation was performed in the CLEO experiment using 10^7 τ-lepton pairs for $\tau^\pm \to \pi^\pm\pi^0\nu$ [89] and $\tau^\pm \to K_S\pi^\pm\nu$ [90] decays. One can expect an increase of sensitivity after analysis of the data samples accumulated at the B factories and later at super-B factories and CTF. Longitudinal polarization of the initial beams will significantly increase sensitivity in searches for CP violation in τ lepton decays.

2.7 Measurement of $e^+e^- \to$ hadrons between 2 and 5 GeV

A measurement of the total cross section of e^+e^- annihilation into hadrons is usually referred to as an R measurement, where R is the hadronic cross section, corrected for initial state radiation and normalized to the lowest-order QED cross section of the reaction $e^+e^- \to \mu^+\mu^-$:

$$R = \frac{\sigma^{(0)}(e^+e^- \to \text{hadrons})}{\sigma^{(0)}(e^+e^- \to \mu^+\mu^-)}.$$

Measurements of R can be utilized to test perturbative QCD and measure α_s [92]. QCD sum rules provide a method of extracting from the values of R such important parameters as quark masses, quark and gluon condensates and the value of Λ_QCD [93]. Through dispersion relations R measurements give an input to the calculations of the hadronic corrections to various fundamental quantities: the anomalous magnetic moment of the muon or $(g_\mu - 2)/2$ [94], the running fine structure constant $\alpha(s)$ [95], superfine splitting in muonium [96] etc. Depending on the problem, different energy ranges are of importance. For example, for $(g_\mu - 2)/2$ the low energy range up to 2 GeV gives about 92% of the whole leading-order hadronic contribution. However, the region from 2 to 5 Gev also gives a non-negligible contribution, which is about 7%. For $\alpha(s)$ the corresponding contributions are about equal: 19.0% and 18.1%, respectively [97].

The c.m. energy range from 3 to 5 GeV is almost asymptotic for u-, d-, and s-quarks. There are no resonances made of light quarks at these energies, but for the c-quark the resonance region just starts here. Numerous R measurements exist in the c.m. energy range between 3 and 5 GeV, where many experimental groups studied various states just above the charmonium threshold: Crystal Ball [98], PLUTO [99], DASP [100], Mark-I [101, 102], and BES [103, 104]. In general, these measurements are consistent. Of them that of BES is the most precise: in their first measurement R was measured at 6 energy points from 2.6 to 5.0 GeV with a systematic uncertainty between 5.9% and 8.4% [103] while in the second one the energy range from 2 to 5 GeV was scanned allowing R determination at 85 energy points with an average systematic uncertainty of ~7% [104]. However, this accuracy is insufficient for high-precision tests of the Standard Model, which require knowledge of the cross section to at least 1%. To reach such accuracy, we need a detailed scan with a few-MeV step and integrated luminosity of 10 pb^{-1} per point or about 10 fb^{-1} in total in the whole energy range.

Despite a rather detailed information on R collected by BES, no data on the cross sections of exclusive channels or on the parameters of broad charmonia in this energy range are available from this experiment. As a result, until recently the properties of $\psi(4040)$, $\psi(4160)$, and $\psi(4415)$ were determined by the old DASP [100] and Mark-I [101] measurements. Some progress was achieved after fits of the old measurements by Crystal Ball [98] and those of BES [103, 104] appeared [105, 106]. A real breakthrough happened recently after CLEO scanned a c.m. energy range from 3.77 to 4.26 GeV [107] and Belle and BaBar used ISR to measure various exclusive cross sections with D, D^*, D_s, and D_s^* from 3 to 5 GeV, see the complete bibliography in [108]. An important conclusion that the total cross section is saturated by the contribution of the light quarks was achieved, see Fig. 2.5. A lot of efforts are still needed to understand the spectroscopy of the ψ family and pattern of their decays.

It is important to note that for various applications, e.g., for extracting quark masses from spectral moments, it is necessary to know the component of R coming from a specific quark flavor, particularly in the threshold energy range. Experimentally, it is a rather complicated problem. One of the theory-driven possibilities can be illustrated by a method used in a charm mass determination [109]. For the energy range from 3.73 to 4.8 GeV the authors employ the data for the total R, $R_{\rm tot}$, obtained by the BES collaboration [104]. To obtain the charm component of R, $R_{\rm cc}$, they first fit the non-charm R ratio, $R_{\rm nc}$, assuming its energy independence and using the last four data points below 3.73 GeV. Finally, $R_{\rm cc}$ is obtained by subtracting the fitted values of $R_{\rm nc}$ from $R_{\rm tot}$. Note that to estimate the final error of $R_{\rm cc}$ in this method a sophisticated analysis of various experimental uncertainties is needed. Another possibility is to reconstruct all exclusive final states containing particles with a corresponding quark flavor. For example, in the vicinity of the charm threshold one can assume that the corresponding R component, $R_{\rm cc}$, is saturated by the contributions from the $D^{(*)}\bar{D}^{(*)}, D^{(*)}\bar{D}^{(*)}$ final states. As discussed above, this assumption seems to account for the observed total cross section in the almost whole energy range. Clearly, this method crucially depends on the assumptions made and requires reliable reconstruction of various final states as well as huge integrated luminosities since the exclusive cross sections have small cross sections. In the future, substantial progress in the charmonium energy range can be expected from ISR measurements at Super$B$ factories and, first of all, direct scans of at CTF.

Below 3 GeV a 1% uncertainty for the total cross section can be achieved using ISR from the higher energies or in direct scans of the c.m.energy range from 2 to 3 GeV, where CTF will be

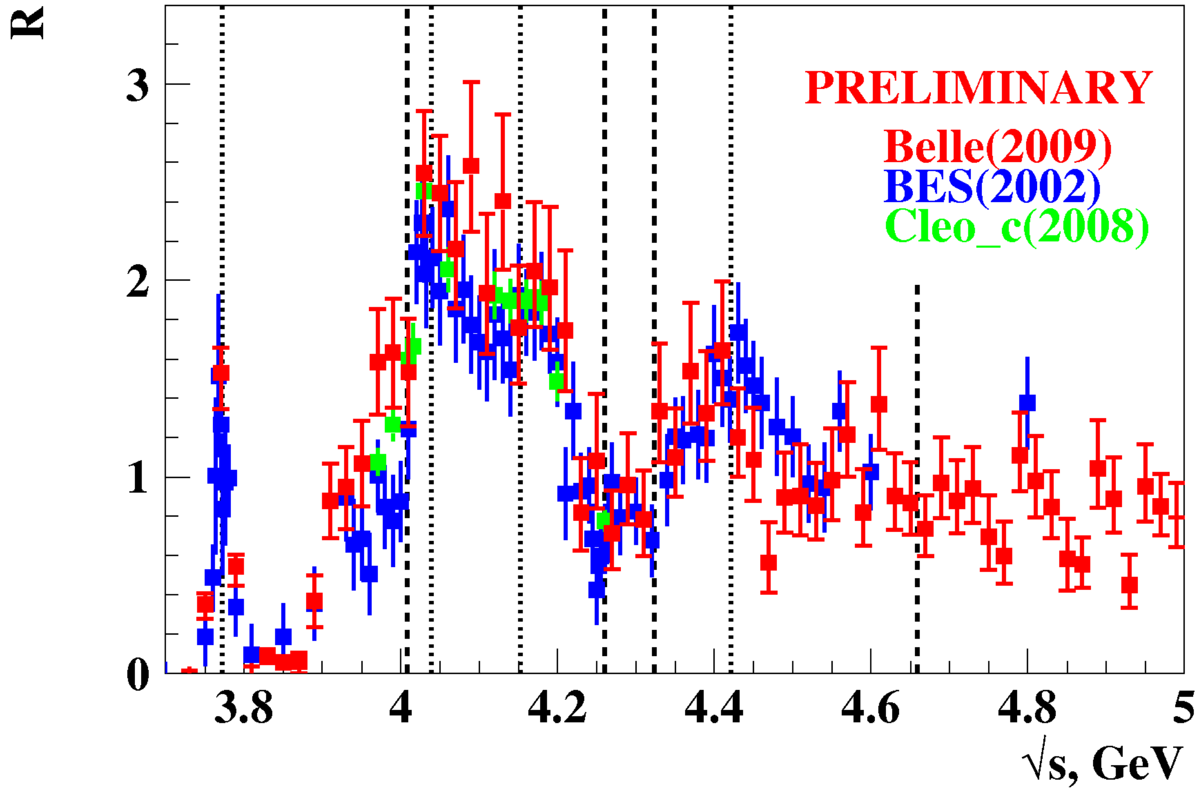

Figure 2.5: Comparison of BES, CLEO and Belle measurements of the total cross section due to charmed quarks

able to provide integrated luminosities at least two orders of magnitude higher than in all previous measurements [110, 111, 112, 103, 104]. Since in this energy range the number of possible final states in the process $e^+e^- \to$ hadrons is relatively small, the total cross section can be determined as a sum of cross sections for various exclusive channels. Such a method will also provide a natural way to study intermediate mechanisms for various final states of light quarks, searches for possible exotic states like tetraquarks, hybrids and glueballs, and a detailed study of the ρ, ω, and ϕ excitations.

Besides that, running at the threshold of a baryon-antibaryon pair production in a polarized mode of CTF will allow a study of the baryon form factors near threshold to be performed, including a unique chance of doing that for polarized baryons. Particularly important is an opportunity to obtain polarized antineutrons and antiprotons, and measure a polarization part of the cross section of their polarization[113].

2.8 Two-photon physics

Today two-photon physics is an important sector of particle physics. In principle, it is physics for photon colliders extensively discussed now. However, e^+e^- colliders as a source of two-photon collisions have one important advantage, one or two of the virtual colliding photons can be strongly off-shell. This provides additional possibilities compared to the collisions of real photons.

Physical tasks first of all include a study of C-even resonances consisting of both light and charm quarks with quantum numbers $J^{PC} = 0^{++}$, 0^{-+}, 2^{-+}, 2^{++}. When one of the photons is strongly off shell, particles with $J = 1$ can also be produced, including those with exotic quantum numbers $J^{PC} = 1^{-+}$. High luminosity of CTF will allow not only a determination of the two-photon widths of the resonances, but also a study of their rare decay modes. A separate problem also requiring high luminosity is a measurement of transition form factors in the processes $\gamma^* \to \gamma M$ and $\gamma^* \to \gamma^* M$, where M is a C-even resonance.

Note also the importance of measuring the total cross sections of $\gamma\gamma \to$ hadrons as well as the cross sections of separate channels like $\gamma\gamma \to \rho\rho$, $p\bar{p}$, $\phi\phi$, $f_0 f_0$ etc. CTF gives a chance for measuring cross sections with accuracy of about 1%.

In such studies, to suppress a background from e^+e^- annihilation into hadrons, one needs a high hermeticity of the detector as well as a low-angle tagger to detect scattered electrons.

2.9 Conclusions

An important difference of CTF compared to the existing B factories at SLAC and KEK and the ϕ factory at Frascati is its ability to run in the broad energy range whereas the colliders mentioned above run basically at a single c.m. energy. This complicates the experimental facilities, both a collider and a detector, but of course makes much broader a physical program.

And one more rather general conclusion. In the discussed energy range a predictive power of the existing theory is rather limited. Our recent experience shows that some particles, e.g., $Y(4260)$ or $X(2150)$, were discovered accidentally and their interpretation is still unclear. Therefore, an experimental study is still most important and one can hope that CTF will help to solve many of the existing problems.

Bibliography

[1] N. Brambilla *et al.* [Quarkonium Working Group], arXiv:hep-ph/0412158; N. Brambilla *et al.* [Quarkonium Working Group], arXiv:1010.5827; G.V. Pakhlova, P.N. Pakhlov and S.I. Eidelman, Phys. Usp. **53**, 219 (2010).

[2] K. Nakamura *et al.* [Particle Data Group], J. Phys. G **37**, 075021 (2010).

[3] D. Besson *et al.* [CLEO Collaboration], Phys. Rev. Lett. **96**, 092002 (2006) [arXiv:hep-ex/0512038].

[4] M. Ablikim *et al.* [BES Collaboration], Phys. Lett. B **660**, 315 (2008) [arXiv:0705.4500 [hep-ex]].

[5] J. L. Rosner *et al.* [CLEO Collaboration], Phys. Rev. Lett. **95**, 102003 (2005) [arXiv:hep-ex/0505073]; P. Rubin *et al.* [CLEO Collaboration], Phys. Rev. D **72**, 092004 (2005) [arXiv:hep-ex/0508037]; S. Dobbs *et al.* [CLEO Collaboration], Phys. Rev. Lett. **101**, 182003 (2008) [arXiv:0805.4599 [hep-ex]]; G. S.Adams *et al.* [CLEO Collaboration], Phys. Rev. D **80**, 051106 (2009) [arXiv:0906.4470 [hep-ex]].

[6] E. Eichten, S. Godfrey, H. Mahlke and J. L. Rosner, Rev. Mod. Phys. **80**, 1161 (2008) [arXiv:hep-ph/0701208].

[7] E. Klempt and A. Zaitsev, Phys. Repts. **454**, 1 (2007) [arXiv:0708.4016 [hep-ph]].

[8] B. Aubert *et al.* [BaBar Collaboration], Phys. Rev. Lett. **98**, 212001 (2007) [arXiv:hep-ex/0610057].

[9] X. L. Wang *et al.* [Belle Collaboration], Phys. Rev. Lett. **99**, 142002 (2007) [arXiv:0707.3699 [hep-ex]].

[10] K. Abe *et al.* [Belle Collaboration], Phys. Rev. Lett. **100**, 142001 (2008) [arXiv:0708.1790 [hep-ex]].

[11] T. Barnes, Int. J. Mod. Phys. A **21**, 5583 (2006) [arXiv:hep-ph/0608103].

[12] M. A. Sanchis-Lozano, Z. Phys. C **62**, 271 (1994).

[13] K. K. Sharma and R. C. Verma, Int. J. Mod. Phys. A **14**, 937 (1999) [arXiv:hep-ph/9801202].

[14] A. Datta, P. J. O'Donnell, S. Pakvasa and X. Zhang, Phys. Rev. D **60**, 014011 (1999) [arXiv:hep-ph/9812325].

[15] G. Goggi and G. Penso, Nucl. Phys. B **165**, 429 (1980).

[16] W. J. Huo, T. F. Feng and C. x. Yue, Phys. Rev. D **67**, 114001 (2003) [arXiv:hep-ph/0212211].

[17] Y. Miyazaki *et al.* [Belle Collaboration], Phys. Lett. B **660**, 154 (2008) [arXiv:0711.2189 [hep-ex]].

[18] J. P. Ma, R. G. Ping and B. S. Zou, Phys. Lett. B **580**, 163 (2004) [arXiv:hep-ph/0311012].

[19] X. G. He, J. P. Ma and B. McKellar, Phys. Rev. D **47**, 1744 (1993) [arXiv:hep-ph/9211276].

[20] C. J. Morningstar and M. J. Peardon, Phys. Rev. D **60**, 034509 (1999) [arXiv:hep-lat/9901004].

[21] A. Hart, C. McNeile, C. Michael and J. Pickavance [UKQCD Collaboration], Phys. Rev. D **74**, 114504 (2006) [arXiv:hep-lat/0608026].

[22] S. Dobbs *et al.* [CLEO Collaboration], Phys. Rev. D **76**, 112001 (2007) [arXiv:0709.3783 [hep-ex]].

[23] R. Poling, *In the Proceedings of 4th Flavor Physics and CP Violation Conference (FPCP 2006), Vancouver, British Columbia, Canada, 9-12 Apr 2006, pp 005* [arXiv:hep-ex/0606016].

[24] E. S. Swanson, Phys. Rept. **429**, 243 (2006) [arXiv:hep-ph/0601110].

[25] G. Pakhlova *et al.* [Belle Collaboration], Phys. Rev. Lett. **100**,062001 (2008) [arXiv:0708.3313 [hep-ex]].

[26] T. J. Burns, F. E. Close and C. E. Thomas, Phys. Rev. D **77**, 034008 (2008) [arXiv:0709.1816 [hep-ph]].

[27] A. V. Evdokimov *et al.* [SELEX Collaboration], Phys. Rev. Lett. **93**, 242001 (2004) [arXiv:hep-ex/0406045].

[28] J. Brodzicka *et al.* [Belle Collaboration], Phys. Rev. Lett. **100**, 092001 (2008) [arXiv:0707.3491 [hep-ex]].

[29] B. Aubert *et al.* [BaBar Collaboration], Phys. Rev. Lett. **97**, 222001 (2006) [arXiv:hep-ex/0607082].

[30] A. Bondar and A. Poluektov, Eur. Phys. J. C **47**, 347 (2006) [arXiv:hep-ph/0510246].

[31] B. I. Eisenstein *et al.* [CLEO Collaboration], Phys. Rev. D **78**, 052003 (2008) [arXiv:0806.2112 [hep-ex]].

[32] J. P. Alexander *et al.* [CLEO Collaboration], Phys. Rev. D **79**, 052001 (2009) [arXiv:0901.1216 [hep-ex]].

[33] CKM Fitter Group Home Page, http://www.slac.stanford.edu/xorg/ckmfitter

[34] E. Follana, C. T. H. Davies, G. P. Lepage and J. Shigemitsu [HPQCD Collaboration], Phys. Rev. Lett. **100**, 062002 (2008) [arXiv:0706.1726 [hep-lat]].

[35] N. E. Adam *et al.* [CLEO Collaboration], Phys. Rev. Lett. **97**, 251801 (2006) [arXiv:hep-ex/0604044].

[36] C. Aubin *et al.* [Fermilab Lattice Collaboration], Phys. Rev. Lett. **94**, 011601 (2005) [arXiv:hep-ph/0408306].

[37] D. Besson [CLEO Collaboration], Phys. Rev. D **80**, 032005 (2009) [arXiv:0906.2983 [hep-ex]].

[38] S. Bianco, F. L. Fabbri, D. Benson and I. Bigi, Riv. Nuovo Cim. **26**, 1 (2003) [arXiv:hep-ex/0309021].

[39] Heavy Flavor Averaging Group Home Page, http://www.slac.stanford.edu/xorg/hfag/

[40] D. M. Asner and W. M. Sun, Phys. Rev. D **73**, 034024 (2006) [arXiv:hep-ph/0507238].

[41] X. D. Cheng, K. L. He, H. B. Li, Y. F. Wang and M. Z. Yang, Phys. Rev. D **75**, 094019 (2007) [arXiv:0704.0120 [hep-ex]].

[42] A. Bondar, A. Poluektov, V. Vorobiev, Phys. Rev. D **82**, 034033 (2010) [arXiv:1004.2350].

[43] M. Bona *et al.*, arXiv:0709.0451 [hep-ex].

[44] H. Mendez *et al.* [CLEO Collaboration], Phys. Rev. D **81**, 052013 (2010) [arXiv:0906.3198 [hep-ex]].

[45] G. Bonvicini *et al.* [CLEO Collaboration], Phys. Rev. D **63**, 071101 (2001).

[46] D. M. Asner *et al.* [CLEO Collaboration], Phys. Rev. D **70**, 091101 (2004).

[47] B. Aubert *et al.* [BaBar Collaboration], Phys. Rev. D **78**, 051102 (2008) [arXiv:0802.4035 [hep-ex]].

[48] E. M. Aitala *et al.* [E791 Collaboration], Phys. Lett. B **403**, 377 (1997).

[49] X. C. Tian *et al.* [Belle Collaboration], Phys. Rev. Lett. **95**, 231801 (2005).

[50] J. M. Link *et al.* [FOCUS Collaboration], Phys. Lett. B **622**, 239 (2005).

[51] B. Aubert *et al.* [BaBar Collaboration], Phys. Rev. Lett. **100**, 061803 (2008) [arXiv:0709.2715 [hep-ex]].

[52] M. Staric *et al.* [Belle Collaboration], Phys. Lett. B **670**, 190 (2008) [arXiv:0807.0148 [hep-ex]].

[53] Y. Grossman, A. L. Kagan and Y. Nir, Phys. Rev. D **75**, 036008 (2007) [arXiv:hep-ph/0609178].

[54] B. Aubert *et al.* [BaBar Collaboration], Phys. Rev. D **78**, 011105 (2008) [arXiv:0712.2249].

[55] M. Staric *et al.* [Belle Collaboration], Phys. Rev. Lett. **98**, 211803 (2007) [arXiv:hep-ex/0703036].

[56] A. A. Petrov, arXiv:0711.1564 [hep-ph].

[57] D. s. Du, Eur. Phys. J. C **50**, 579 (2007) [arXiv:hep-ph/0608313].

[58] A. A. Petrov, Phys. Rev. D **69**, 111901 (2004) [arXiv:hep-ph/0403030].

[59] D. M. Asner *et al.* [CLEO Collaboration], Phys. Rev. D **70**, 091101 (2004) [arXiv:hep-ex/0311033].

[60] I. I. Bigi, arXiv:0710.2714 [hep-ph].

[61] A. Datta and D. London, Int. J. Mod. Phys. A **19**, 2505 (2004) [arXiv:hep-ph/0303159].

[62] G. Burdman and I. Shipsey, Ann. Rev. Nucl. Part. Sci. **53**, 431 (2003) [arXiv:hep-ph/0310076].

[63] K. Abe *et al.* [Belle Collaboration], Phys. Rev. Lett. **92**, 101803 (2004) [arXiv:hep-ex/0308037].

[64] V. M. Abazov *et al.* [D0 Collaboration], Phys. Rev. Lett. **100**, 101801 (2008) [arXiv:0708.2094 [hep-ex]].

[65] S. Prelovsek and D. Wyler, Phys. Lett. B **500**, 304 (2001) [arXiv:hep-ph/0012116].

[66] G. Burdman, E. Golowich, J. L. Hewett and S. Pakvasa, Phys. Rev. D **66**, 014009 (2002) [arXiv:hep-ph/0112235].

[67] S. Fajfer, N. Kosnik and S. Prelovsek, Phys. Rev. D **76**, 074010 (2007) [arXiv:0706.1133 [hep-ph]].

[68] T. E. Coan *et al.* [CLEO Collaboration], Phys. Rev. Lett. **90**, 101801 (2003) [arXiv:hep-ex/0212045].

[69] B. Aubert *et al.* [BaBar Collaboration], Phys. Rev. Lett. **93**, 191801 (2004) [arXiv:hep-ex/0408023].

[70] A. Freyberger *et al.* [CLEO Collaboration], Phys. Rev. Lett. **76**, 3065 (1996) [Erratum-ibid. **77**, 2147 (1996)].

[71] Q. He *et al.* [CLEO Collaboration], Phys. Rev. Lett. **95**, 221802 (2005) [arXiv:hep-ex/0508031].

[72] B. Aubert *et al.* [BaBar Collaboration], arXiv:hep-ex/0607051.

[73] K. Kodama *et al.* [E653 Collaboration], Phys. Lett. B **345**, 85 (1995).

[74] D. Pirjol and T. M. Yan, Phys. Rev. D **56**, 5483 (1997) [arXiv:hep-ph/9701291].

[75] R. Mizuk, arXiv:0712.0310 [hep-ex].

[76] G. Pakhlova *et al.* [Belle Collaboration], Phys. Rev. Lett. **101**, 172001 (2008) [arXiv:0807.4458 [hep-ex]].

[77] E. Braaten, S. Narison and A. Pich, Nucl. Phys. B **373**, 581 (1992).

[78] S. Bethke, arXiv:0908.1135 [hep-ph].

[79] E. Gamiz, M. Jamin, A. Pich, J. Prades and F. Schwab, JHEP **0301**, 060 (2003) [arXiv:hep-ph/0212230]; Phys. Rev. Lett. **94**, 011803 (2005) [arXiv:hep-ph/0408044].

[80] L. Michel, Proc. Phys. Soc. A **63**, 514 (1950); C. Bouchiat and L. Michel, Phys. Rev. **106**, 170 (1957).

[81] J. R. Ellis, J. Hisano, M. Raidal and Y. Shimizu, Phys. Rev. D **66**, 115013 (2002) [arXiv:hep-ph/0206110]; T. Fukuyama, T. Kikuchi and N. Okada, Phys. Rev. D **68**, 033012 (2003) [arXiv:hep-ph/0304190]; A. Brignole and A. Rossi, Phys. Lett. B **566**, 217 (2003) [arXiv:hep-ph/0304081].

[82] I. I. Bigi and A. I. Sanda, Phys. Lett. B **625**, 47 (2005) [arXiv:hep-ph/0506037].

[83] Y. S. Tsai, SLAC-PUB-5003

[84] Y. S. Tsai, Phys. Rev. D **51**, 3172 (1995) [arXiv:hep-ph/9410265].

[85] J. H. Kuhn and E. Mirkes, Phys. Lett. B **398**, 407 (1997) [arXiv:hep-ph/9609502].

[86] A. Datta, K. Kiers, D. London, P. J. O'Donnell and A. Szynkman, Phys. Rev. D **75**, 074007 (2007) [Erratum-ibid. D **76**, 079902 (2007)] [arXiv:hep-ph/0610162].

[87] D. Delepine, G. Faisl, S. Khalil and G. L. Castro, Phys. Rev. D **74**, 056004 (2006) [arXiv:hep-ph/0608008].

[88] K. Kiers, K. Little, A. Datta, D. London, M. Nagashima and A. Szynkman, Phys. Rev. D **78**, 113008 (2008) [arXiv:0808.1707 [hep-ph]].

[89] P. Avery *et al.* [CLEO Collaboration], Phys. Rev. D **64**, 092005 (2001) [arXiv:hep-ex/0104009].

[90] G. Bonvicini *et al.* [CLEO Collaboration], Phys. Rev. Lett. **88**, 111803 (2002) [arXiv:hep-ex/0111095].

[91] V. P. Druzhinin, arXiv:0710.3455 [hep-ex].

[92] J. Kühn and M. Steinhauser, Nucl. Phys. B **619** (2001) 588; Erratum-ibid, B640 (2002) 415.

[93] M.A. Shifman, A.I. Vainshtein and V.I. Zakharov, Nucl. Phys. B **147** (1979) 385.

[94] M. Davier, S. Eidelman, A. Höcker, Z. Zhang, Eur. Phys. J. C **31** (2003) 503.

[95] B. Pietrzyk and H. Burkhardt, Phys. Lett. B **513** (2001) 46.

[96] A. Czarnecki, S.I. Eidelman and S.G. Karshenboim, Phys. Rev. D **65** (2002) 053004.

[97] M. Davier *et al.*, Eur. Phys. J. C **71** (2004) 127.

[98] A. Osterheld *et al.*, SLAC-PUB-4160, 1986.

[99] J. Burmeister *et al.*, Phys. Lett. **66B** (1977) 395.

[100] R. Brandelik *et al.*, Phys. Lett. **76B** (1978) 361.

[101] J.L. Siegrist *et al.*, Phys. Rev. Lett. **36** (1976) 700.

[102] J.L. Siegrist *et al.*, Phys. Rev. D **26** (1982) 969.

[103] J.Z.Bai *et al.*, Phys. Rev. Lett. **84**, 594 (2000).

[104] J.Z.Bai *et al.*, Phys. Rev. Lett. **88**, 101802 (2002).

[105] K.K. Seth *et al.*, Phys. Rev. D **72**, 017501 (2005).

[106] M. Ablikim *et al.*, Phys. Lett. B **660**, 315 (2008).

[107] D. Cronin-Hennessy *et al.*, Phys. Rev. D **80**, 072001 (2009).

[108] N. Brambilla *et al.*, Eur. Phys. J. C **71** (2011) 1534.

[109] A.H. Hoang and M. Jamin, Phys. Lett. **B594** (2004) 127.

[110] G. Cosme *et al.*, Nucl. Phys. B **152**, 215 (1979).

[111] A. Antonelli *et al.*, Phys. Lett. B **365**, 427 (1996).

[112] C. Bacci *et al.*, Phys. Lett. B **86**, 234 (1979).

[113] A. Bondar *et al.*, Phys. Lett. B **697**, 159 (2011).

Chapter 3

Detector

3.1 Overview

The physics program of experiments at the Super $c\tau$ factory with a peak luminosity of $10^{35}\,\text{cm}^{-2}\text{s}^{-1}$ in the region $2E = 2 \div 5\,\text{GeV}$ is dedicated to studies of rare decays of D mesons, τ lepton, $D^0\bar{D}^0$ oscillations and searches for yet unobserved lepton-flavor-violating decays of τ, in particular, $\tau \to \mu\gamma$. This program requires a construction of a universal magnetic detector with the field of about 1 T. The detector should feature:

- an excellent momentum resolution for charged particles and a good energy resolution for photons;
- a particle identification system with nearly record parameters among existing detectors or those under construction. For selection of rare D decays, K/π separation higher than 3σ is needed. In addition, for selection of $\tau \to \mu\gamma$ decay and suppression of high background from π mesons a robust μ/π separation up to $1.2\,\text{GeV}/c$ momentum is required;
- a digitizing hardware and data acquisition system, which is able to read events at a rate of 300–400 kHz with an average event length of about 30 kB;
- a unique trigger, which is able to select physics events and suppress background under a very high detector load.

To achieve a high efficiency of data taking and to minimize time for detector maintenance, the detector design should satisfy the following requirements:

- digitizing hardware should reside inside the detector, 10 Gbit optical links will be used to transmit the data;
- a detector design should provide fast access to detector subsystems for repair and hardware replacement, a typical disassembling–repair–assembling period should not exceed 12 – 24 hours;
- input (output) of the detector's magnetic field should not take more than two-three hours;
- fast access to detector subsystems using a movable radiation shield enabling personnel to work on the detector and its technological entresols of the detector while beams are in the collider.

The design of the universal magnetic detector for CTF is based on the experience of the Budker Institute as well as that coming from the BaBar and Belle experiments.

The detector (see Fig. 3.1) contains a standard set of subsystems:

- a vacuum chamber,
- a vertex detector,
- a drift chamber,
- a particle identification system based on a Cherenkov detector with a multilayer aerogel radiator (*Focusing Aerogel RICH – FARICH*),
- an electromagnetic calorimeter based on pure CsI crystals,
- a superconducting coil produced by traditional technology,
- an iron yoke with a muon system inside.

3.2 Vacuum chamber

The beams collide in the center of a beryllium vacuum chamber with the radius of 20 mm and the length of 600 mm. The wall thickness is 1 mm. To suppress the background from synchrotron radiation, the inside of the chamber is coated with a copper layer 0.05 mm thick. Such a design provides a small amount of material, about 0.6% of the radiation length at normal incidence.

3.3 Vertex detector

The Vertex detector (VD) is placed between the vacuum chamber and the drift chamber and increases a solid angle of the detector up to 98 %. The VD represents a cylinder with the length of 60 cm and the inner and outer diameters equal 50 mm and 400 mm, respectively. Its task is to detect secondary vertices from the decays of short-lived particles such as K^0_S or Λ. Furthermore, the VD complements the drift chamber in measuring momenta of charged particles. Since the VD is placed in the vicinity of the beam pipe, it should handle a high particle flux when the collider operates at its maximum luminosity of $10^{35}\mathrm{cm}^{-2}\mathrm{s}^{-1}$.

Information from the VD can be processed either together with the drift chamber to improve the momentum resolution and alone, to reconstruct secondary vertices.

Two options of the VD are foreseen at the moment — a time projection chamber (TPC) or a stack of silicon strip layers.

3.3.1 Time projection chamber

A time projection chamber [1] is a combination of the drift and proportional chamber (see Fig. 3.2). An axial electric field in the drift volume filled with a gas mixture, e.g., $\mathrm{Ar/CO_2}$ 80/20, is created by two endcap anode planes and a mesh cathode in the middle of the chamber. The field uniformity is preserved using a special field cage.

A charged particle traversing the sensitive volume leaves a track as a chain of clusters of the ionized gas. The linear cluster density depends on the gas. For example, for argon at normal

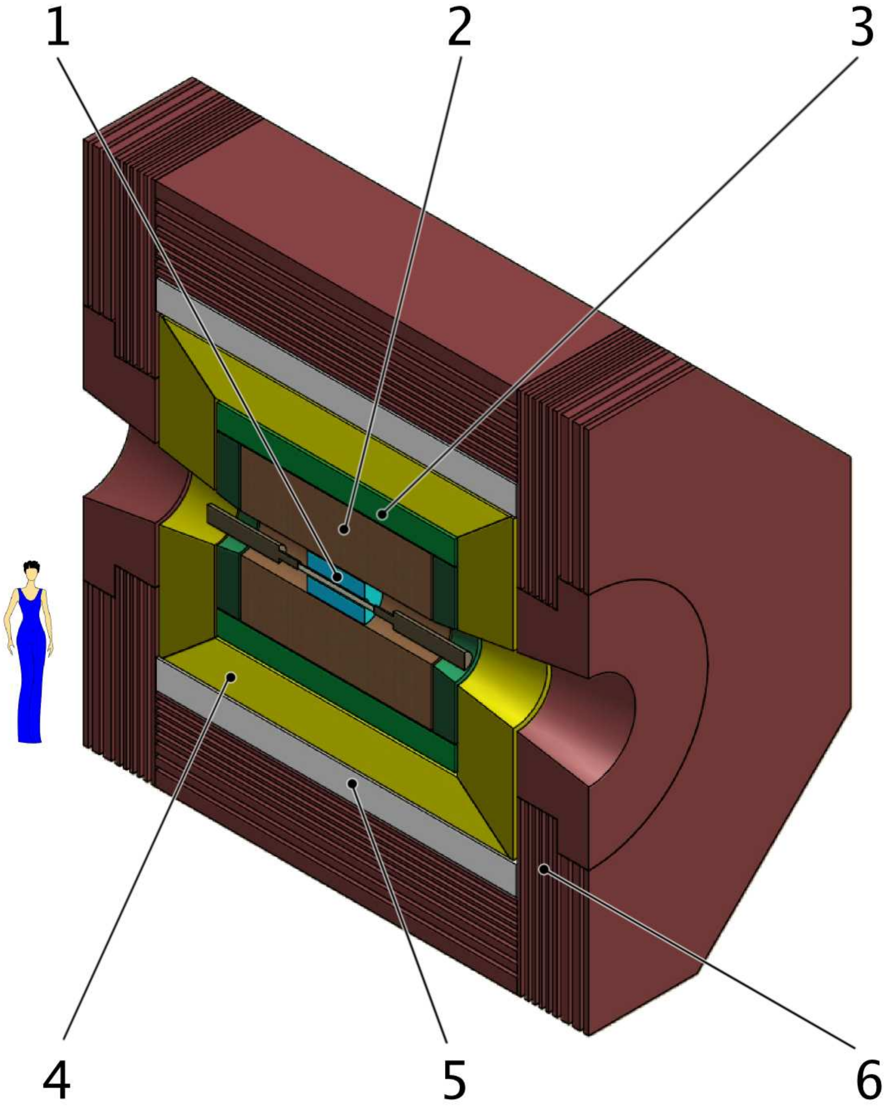

Figure 3.1: Universal magnetic detector: 1 – vertex detector; 2 – drift chamber; 3 – identification system based on FARICH; 4 – calorimeter; 5 – superconducting coil; 6 – yoke with a muon system.

temperature and pressure it is about 30 clusters per cm. Electrons drift with a constant velocity towards the anode planes and create avalanches detected by a sensitive pad plane providing information about two coordinates. The third coordinate of the track is a product of the drift time of each primary electron cluster and the drift velocity. Despite the relatively large drift distance of about 30 cm, a transverse diffusion is relatively small due to the longitudinal magnetic field of 1 T (see Fig. 3.3). Because of that the transverse spatial resolution can achieve 50–100 μm depending on the drift path. In the longitudinal direction the resolution is somewhat worse — about 300 μm because of larger diffusion.

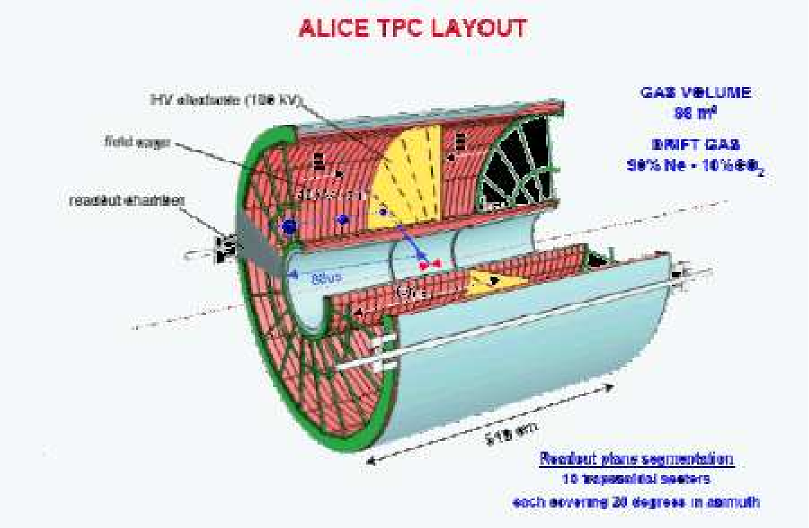

Figure 3.2: ALICE time projection chamber (CERN).

At the present time the multiwire proportional chamber (MWPC) is used in TPCs for detection of ionization clusters. Such chambers cannot work in the continuous mode because of a backflow of ions resulting in a space charge accumulation which leads to an electric field distortion. In its turn it deteriorates the spatial resolution. Therefore, a special protection mesh is used to prevent such an effect. This mesh opens access to the MPWC in accordance with the external trigger signal. This inavoidably leads to a large dead time after each event which leads to a loss of physics events.

A new generation of colliders including the CTF will have a very small time between consequent events, thus a standard TPC cannot be used. To overcome this problem, several new readout schemes based on the novel micropattern gas technologies were suggested. For example, the $\overline{P}ANDA$ Collaboration is developing a TPC [2] with the continuous readout using gas electron multipliers (GEM) [3]. A similar chamber is being designed for a detector for the international linear collider by the LC TPC Collaboration [4]. Besides the GEM option, the LC TPC Collaboration also studies a possibility of using Micromegas for signal amplification (see Fig. 3.4). It should be noted that both amplification principles reduce the backflow of ions by more than three orders of magnitude. Therefore, a TPC equipped with such a device can work in the continuous mode.

A very good spatial resolution, close to the theoretical limit, has been achieved during tests of the prototypes with different readout schemes. The tests have been done with the "hot" gas mixture — $Ar/CF_4/C_4H_{10}$ in the proportion 95/3/2. The spatial resolution of the prototypes with GEM and Micromegas in the 1 T magnetic field parallel to electric field lines at 5 cm from the readout plane was equal to 52 μm and 55 μm, respectively (see Figs. 3.5 and 3.6).

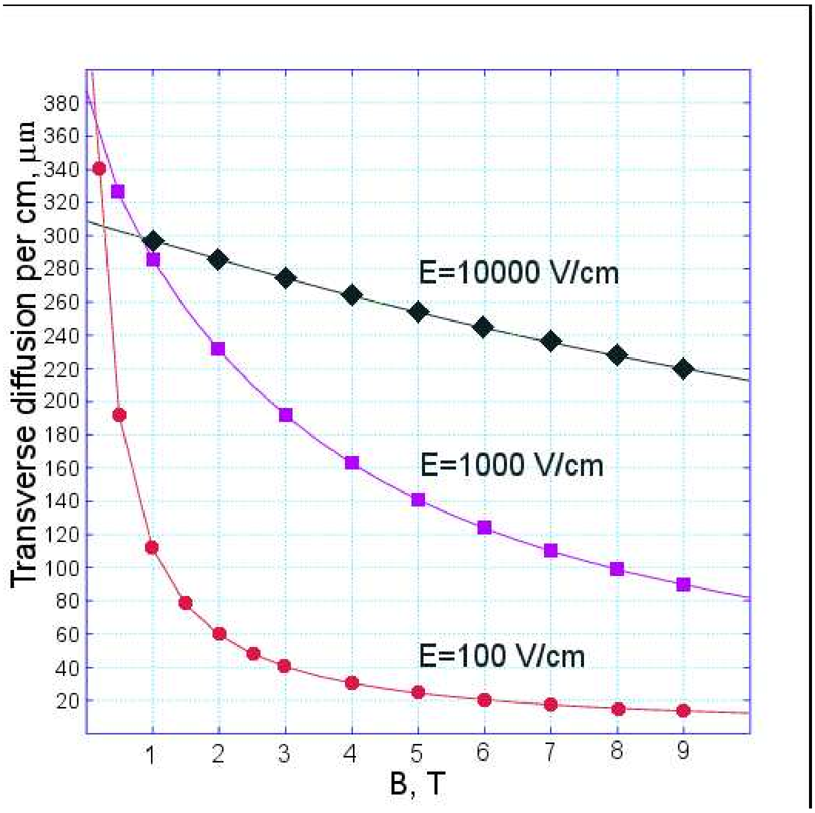

Figure 3.3: Diffusion variation as a function of a magnetic field intensity for the gas mixture Ar/C_2H_4 80/20 for different electric field values.

Further improvement of the spatial resolution is possible due to a decrease of a sensitive pad size. In the examples above pad sizes were $1.2 \times 5.4\,\mathrm{mm}^2$ for the GEM version and $3.2 \times 7\,\mathrm{mm}^2$ for the Micromegas one. It should be noted that in the latter case (Micromegas) sensitive pads were covered by a special resistive layer to spread a charge over a larger area and improve the spatial resolution. At the present time an experiment is in progress to directly detect a signal in the silicon pixel detector with a pixel size of $50 \times 50\,\mu\mathrm{m}^2$. It is anticipated that the spatial resolution in this case will be about $40\,\mu$m in the vicinity of the detection plane.

Apart from a position information, the TPC can be used for particle identification based on the energy loss in gas. Indeed, at the typical pad size of 2 mm each particle crossing the chamber along the radius will produce about 70 fired pads. That should provide the $\mathrm{d}E/\mathrm{d}x$ resolution at the level of a few per cent.

Another important problem is a minimization of the chamber wall thickness, which should keep an electric potential difference at the level of a few tens of kilovolts. Such a high potential is required to provide the electric field of the order of $200 - 300\,\mathrm{V/cm}$, allowing an electron drift velocity of about $5\,\mathrm{cm}/\mu\mathrm{s}$.

At the present time a design of the detector is studied using a dedicated computer simulation.

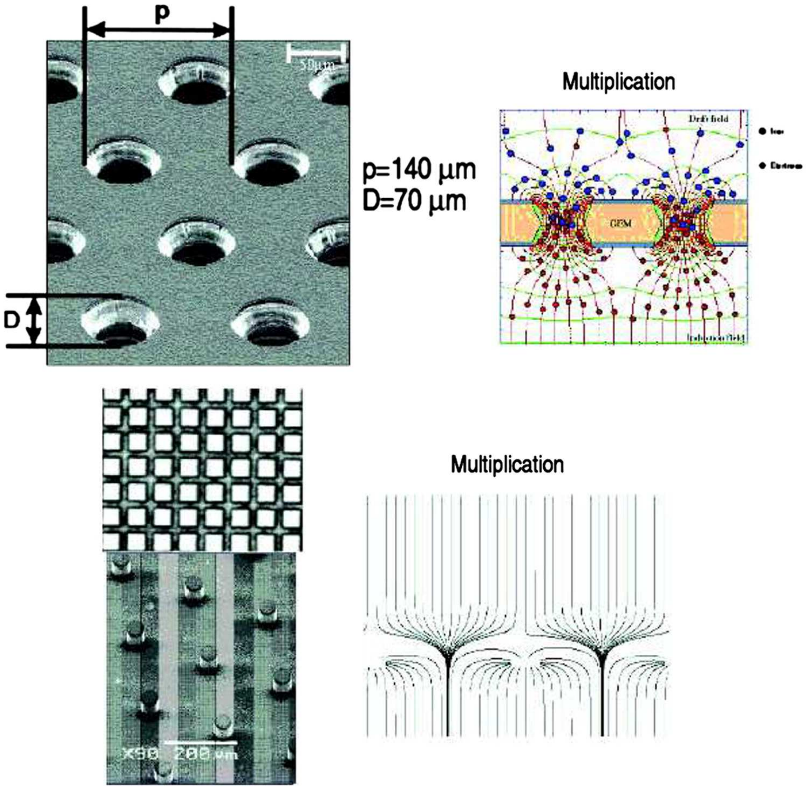

Figure 3.4: Layout and principle of operation of GEM (upper row) and Micromegas (lower row). The figure is taken from [5].

3.4 Drift chamber

3.4.1 Introduction

The drift chamber (DCH) is the main tracking and momentum-measuring system. It provides precision momentum measurements as well as a good particle identification for low momentum tracks. The DCH design is based on the BaBar drift chamber described in detail in [6].

3.4.2 Drift chamber design

The drift chamber has conventional cylindrical design, is 2.0 m long and 1.8 m in diameter. The endplates, which carry an axial load of about 32,000 N, are made of 24 mm thick aluminum to hold plastic and metal feedthroughs for the wires. The maximum total deflection of the endplates under loading is small, about 2 mm or 28% of the 7 mm wire elongation under tension. The inner cylinder is made of 1.5 mm carbon fiber. The outer cylinder is 5 mm thick fiber glass. The inner cylindrical wall of DCH carries 40% of the wire load, while the outer wall bears 60%. To simplify its installation, this external wall was constructed of two half-cylinders with longitudinal and circumferential joints. The main structural element consists of 5 mm fiber glass. The outer shell is capable of withstanding a differential pressure of 30 mbar and temperature variations as large as $\pm 20^{o}$C, conditions that could be encountered during shipping or installation. The aluminum foil, 25 μm thick on the internal surface and 100 μm on the external one, is in good electric contact with the endplates, thereby completing an RF shield for the chamber. The total thickness of DCH

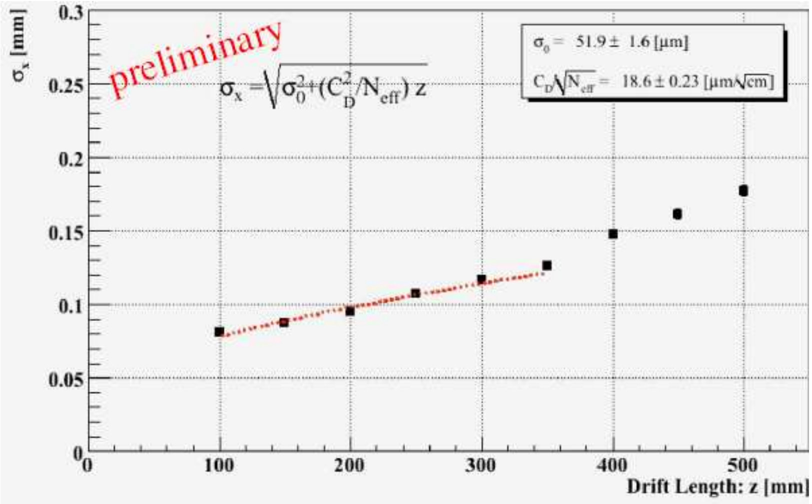

Figure 3.5: Spatial resolution of the TPC prototype with the GEM readout.

at normal incidence is $1.08\%X_0$, of which the wires and gas mixture contribute $0.2\%X_0$, and the inner wall — $0.28\%X_0$.

The drift system of the chamber consists of 40 layers of close-packed 7,104 small hexagonal cells, each with a single sense wire surrounded by field-shaping wires. Each hexagonal cell is approximately 1 cm in radius.

3.4.3 Drift cells

3.4.3.1 Layer arrangement

The layers are grouped by four into ten superlayers with the same wire orientation and equal numbers of cells in each layer of a superlayer. Sequential layers are staggered by half a cell. This arrangement enables local segment finding and left-right ambiguity resolution within a superlayer, even if one out of four signals is missing. The stereo angles of the superlayers alternate between axial (A) and stereo (U,V) pairs, in the order AUVAUVAUVA, as shown in Fig. 3.7.

To provide three-dimensional track reconstruction, the superlayers alternate between axial (wires parallel to the z axis) and small-angle stereo (wire endpoints offset by 7 to 12 cells, in alternate directions). The stereo angles vary between ±32 mrad and ±56 mrad; they have been chosen so that the drilling patterns are identical for the two endplates. The hole pattern has a 16-fold azimuthal symmetry, which is well suited to the modularity of the electronic readout and trigger system.

3.4.3.2 Cell Design and Wires

The drift cells are hexagonal in shape, 11.9 mm by approximately 19.0 mm along the radial and azimuthal directions, respectively. The hexagonal cell configuration is desirable because approximate circular symmetry can be achieved over a large portion of the cell. The choice of aspect ratio has a benefit of decreasing the number of wires and electronic channels, while allowing a 40-layer chamber in a confined radial space. Each cell consists of one sense wire surrounded by six field wires.

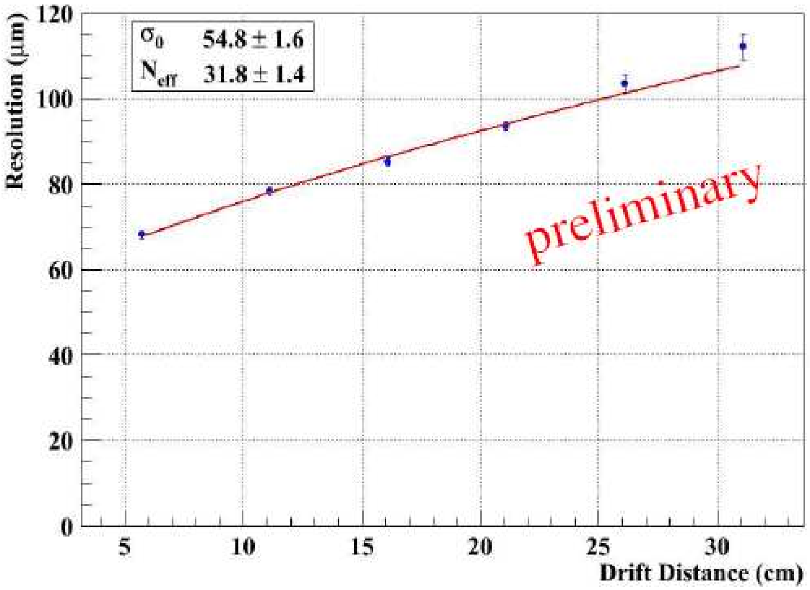

Figure 3.6: Spatial resolution of the TPC prototype with the Micromegas readout.

The sense wires are made of tungsten-rhenium alloy, 20 μm in diameter and tensioned with a weight of 30 g. The deflection due to gravity is 200 μm at midlength. Tungsten-rhenium has a substantially higher linear resistivity (290 Ω/m) compared to pure tungsten (160 Ω/m), but is considerably stronger and has better surface quality.

While the field wires are at ground potential, a positive high voltage is applied to the sense wires. An avalanche gain of approximately $5 \cdot 10^4$ is obtained at a typical operating voltage of 1960 V and a 80/20 helium/isobutane gas mixture.

The relatively low tension on the approximately 2 m-long sense wires was chosen so that the aluminum field wires have a matching gravitational sag and are tensioned well below the elastic limit. A simulation of the electrostatic forces shows that the cell configuration has no instability problems. At the nominal operating voltage of 1960 V, the wires deflect by less than 60 μm.

The tension of the field wires is 155 g to match the gravitational sag of the sense wires to within 20 μm. This tension is less than half the tensile yield strength of the aluminum wire. For cells at the inner or outer boundary of a superlayer, two guard wires are added to improve the electrostatic performance of the cell and to match the gain of the boundary cells to those of the cells in the inner layers. At the innermost boundary of layer 1 and the outermost boundary of layer 40, two clearing wires have been added per cell to collect charges created through photon conversions in the material of the walls.

A total of three different types of feed-throughs were required for the chamber to accommodate the sense, field, and clearing field wires. The three types are illustrated in Fig. 3.8. They incorporate crimp pins of a simple design which fasten and precisely locate the wires. The choice of pin material (gold-plated copper for the signal wires and gold-plated aluminum for the field wires) and wall thickness in the crimp region was optimized to provide an allowable range of almost 150 μm in crimp size as a primary means to avoid wire breakage.

3.4.3.3 Drift Isochrones

The calculated isochrones and drift paths for ions in adjacent cells of layer 3 and 4 of an axial superlayer are presented in Fig. 3.9. The isochrones are circular near the sense wires, but deviate

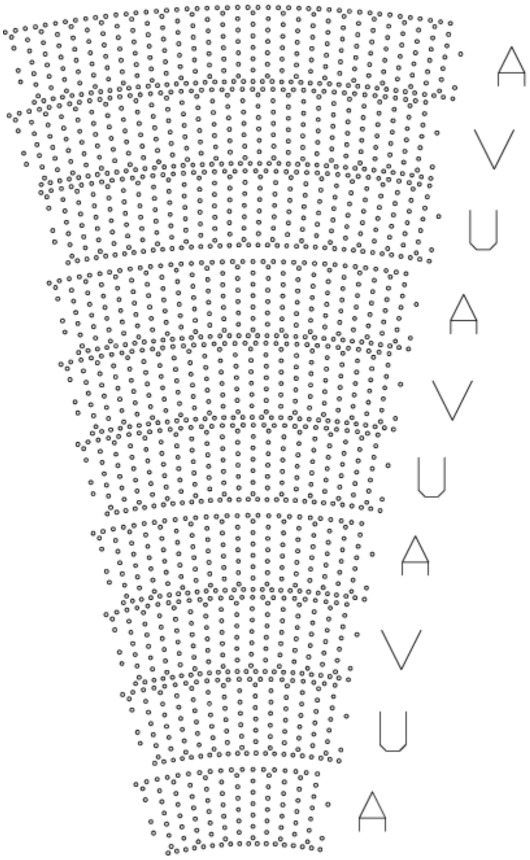

Figure 3.7: Arrangement of drift chamber wires. One sixteenth sector of the full chamber is shown, with axial (A) and small-angle stereo (U and V) superlayers indicated.

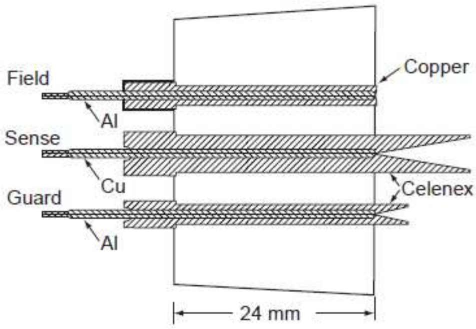

Figure 3.8: Design of three DCH wire feedthroughs for the 24 mm-thick endplates. The copper jacketed feedthrough is for grounded field wires, the other four are for sense wires (4.5 mm diameter), and guard and clearing field wires (2.5 mm diameter), all made of a Celenex insulator surrounding the crimp pins.

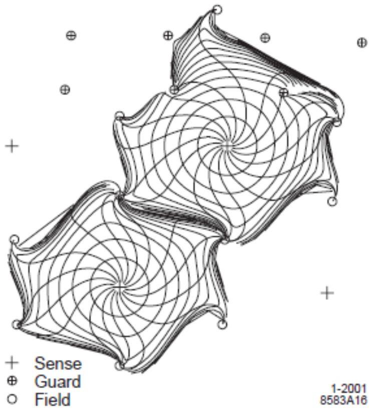

Figure 3.9: Drift cell isochrones, i.e., contours of equal drift times of ions in cells of layers 3 and 4 of an axial superlayer. The isochrones are spaced by 100 ns. They are circular near the sense wires, but become irregular near the field wires, and extend into the gap between the superlayers.

strongly from circles near the field wires. Ions originating in the gap between superlayers are collected by cells in the edge layers after a delay of several μs. These lagging ions do not affect the drift times measurements, but they contribute to the dE/dx measurement.

3.4.3.4 Cross Talk

A signal on one sense wire produces oppositely charged signals on neighboring wires due to capacitive coupling. The cross talk is largest between adjacent cells of adjacent layers, ranging from -0.5% at a superlayer boundary to -2.7% for internal layers within the superlayers. For adjacent cells in the same layer, the cross talk ranges from -0.8 to -1.8%, while for cells separated by two layers it is less than 0.5%.

3.4.3.5 Gas system

The drift chamber is operated with a gas mixture of 80% helium and 20% isobutane, passed through a bubbler to introduce 3500 ppm of water vapor. The bubbler also introduces approximately 100 ppm of oxygen into the gas mixture, which has a small effect on the avalanche gain. The chamber is maintained at 4 mbar over atmospheric pressure with a recirculating pump; freshly mixed gas is introduced when necessary to compensate for losses.

3.4.3.6 Drift chamber performance

The performance of the BaBar drift chamber during six years of operation has been excellent. The momentum resolution is determined by reconstructing through-going cosmic ray events as two separate "tracks" and taking the difference in the fitted transverse momentum (inverse curvature in the XY plane) at the center of the chamber as a resolution. The result is

$$\frac{\sigma(p_T)}{p_T} = (0.13 \pm 0.01)\% \cdot p_T + (0.45 \pm 0.03)\%$$

The single-hit position resolution is determined for all tracks by comparing the fitted trajectory excluding each measured hit with the position of the hit determined from the readout timing and

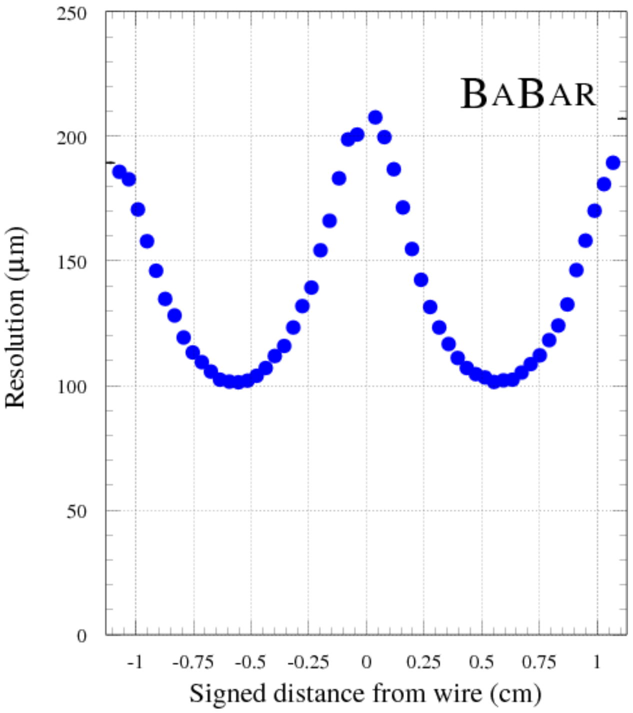

Figure 3.10: BaBar single-hit resolution vs. distance from the sense wire. Resolution is computed from the residual of the hit position compared with the fitted track excluding that hit. The sign of the distance is positive (negative) for tracks passing to the right (left) of the radial vector to the sense wire.

the calibration time-to-distance relation for that cell. The result (Fig. 3.10) is a weighted-average resolution of 125 μm over all cells; in the region of each cell with the most uniform electric field, the resolution is 100 μm.

The drift chamber readout system includes both timing, with 1 ns precision and integrated charge information. The detector is calibrated for the electronics gain of each channel, normalized to the charge deposition and avalanche gain as a function of the track trajectory in each layer of the chamber. With these calibrations, the integrated charge from each hit can be used to compute a relative energy loss; the $\mathrm{d}E/\mathrm{d}x$ for each track is computed from an 80% truncated mean of the hits assigned to a track, as shown in Fig. 3.11. For electrons from radiative Bhabha events $\sigma(dE/dx)/(dE/dx) \leq 7.5\%$ is obtained.

3.5 FARICH system

3.5.1 Introduction

An excellent particle identification (PID) for hadrons and leptons over the full momentum range for particles coming from charm and τ decays is essential to achieve the physics objectives of the experiment. In particular, a search for lepton flavor violation in the decay channel $\tau \to \mu\gamma$ with a sensitivity to the branching fraction of 10^{-9} requires a good μ/π separation around 1 GeV/c momentum. Another example is a search for CP violation in D decays that needs full particle identification to reconstruct exclusive final states and tag the flavor of the other D meson in the

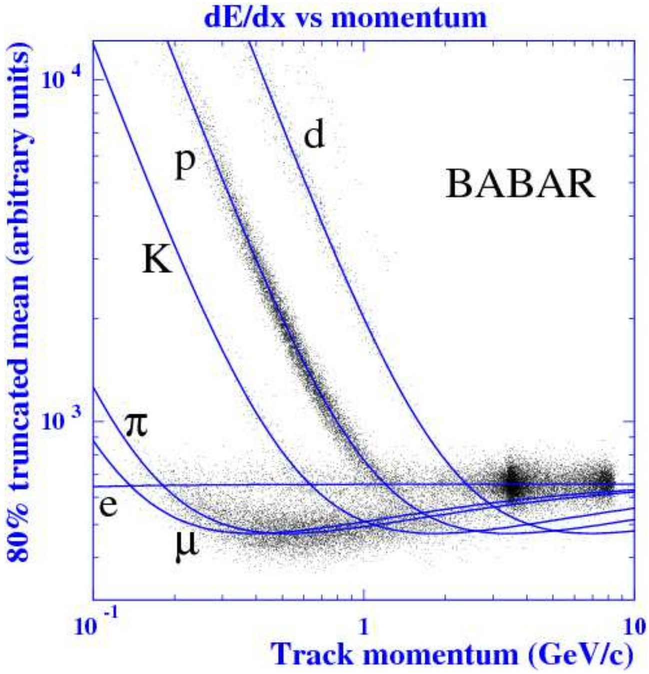

Figure 3.11: dE/dx distribution vs momentum for particle samples.

event.

Identification of leptons is performed by the electromagnetic calorimeter and the muon system, while energy losses in the drift chamber (dE/dx) can be used to identify charged hadrons. However, the latter technique cannot discriminate between pions and kaons with momenta above 0.7 GeV/c. Identification of muons with momenta below 1 GeV/c is a hard task for existing muon range detectors. For example, the efficiency of the BaBar detector for muons of 1 GeV/c momentum was 64% while pion misidentification rate was 2% (2.4σ separation) [7]. The KLM system of the Belle detector has a somewhat better performance with a 78% muon efficiency and 2% pion misidentification rate (2.8σ separation) at 1 GeV/c momentum [8].

For particle identification in the experiments at CTF a novel Ring Imaging Cherenkov counter with a *focusing* aerogel radiator (FARICH) is proposed. It is able to provide a high μ/π separation below and about 1 GeV/c, as well as excellent $\pi/K/p$ separation for high momenta not covered by dE/dx measurements. Section 3.5.4 reports the results of MC simulation of FARICH performance.

Silica aerogel is a porous silicon dioxide with a variable index of refraction ($1.006 \div 1.2$) that is applicable in Cherenkov detectors for particles with a few GeV/c momentum.

A first RICH detector using silica aerogel as a Cherenkov radiator was successfully employed in the HERMES experiment [9]. It was followed by RICH1 of the LHCb detector [10]. Both RICH detectors use gas as a second radiator and focusing mirrors to form Cherenkov ring images on a photon detection plane.

A RICH with proximity focusing uses a gap between a layer of radiator medium and photon detector to make a ring image. This allows one to construct more compact RICH detectors as compared to RICH with focusing mirrors. Such a design was implemented in the RICH with the dual aerogel-NaF radiator for the upcoming ISS-born experiment AMS-02 [11].

3.5.2 FARICH concept

In a proximity focusing RICH, one of the main factors limiting Cherenkov angle resolution is a finite thickness of a radiator. In [12, 13, 14] it was proposed to use a radiator consisting of several layers of aerogel with different refractive indices to overcome this limitation. An index of refraction and a thickness of each layer are chosen so that rings from all layers coincide on the photon detection plane. Another possibility is to have several separate rings (Fig. 3.12). Both options allow one to diminish the photon emission point uncertainty. We call a detector employing this technique a Focusing Aerogel RICH (FARICH).

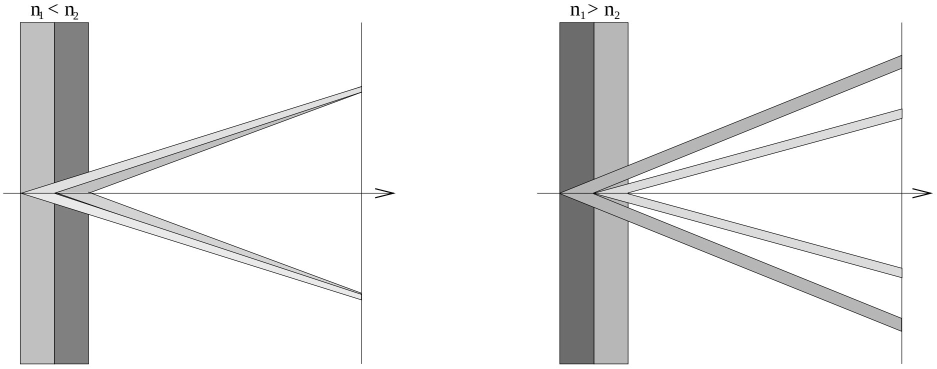

Figure 3.12: FARICH in single-ring (left) and multi-ring (right) alternatives.

In 2004 in Novosibirsk the first multilayer aerogel sample was obtained [13]. Four layers of that aerogel had indices of refraction and thicknesses that match designed ones with a good precision. At present, we have several aerogel tiles in a single-ring option with 2–4 layers with dimensions up to 115 × 115 × 40 mm^3.

3.5.3 Design

The FARICH for CTF should cover almost a 4π solid angle and identify muons and hadrons with momenta up to approximately 2 GeV/c. The FARICH will work in the magnetic field of 1 T that imposes a serious limitation on the photon detector choice. Presently, the only existing single photon detector sensitive to visible spectrum that is able to work in a strong magnetic field of arbitrary direction is a multipixel Geiger-mode avalanche photodiode (MPGM-APD or SiPM) [15]. SiPM is almost insensitive to magnetic field, has a gain of the order 10^6, a high photon detection efficiency (PDE) in the visible region, a low voltage bias and a size of a few mm. A main disadvantage of SiPMs is a high dark counting rate at the room temperature ($\sim$ 1 MHz/mm^2). These devices are readily available from a number of Russian and foreign producers: CPTA (Moscow), MEPhi/Pulsar (Moscow), Hamamatsu Photonics (Japan), Zecotek (Canada-Singapore), FBK-irst (Italy) etc.

The suggested FARICH layout is shown in Fig. 3.13. It consists of the barrel and endcap parts. A solid angle of the system is 98% of 4π. The radiator has the area of 17 m^2, photon detectors — 21 m^2. The number of SiPMs and electronics channels is about one million.

The very large number of channels and their high density will require a development of dedicated front-end electronics based on ASICs. The digitizing part (TDC) should be located right in the detector.

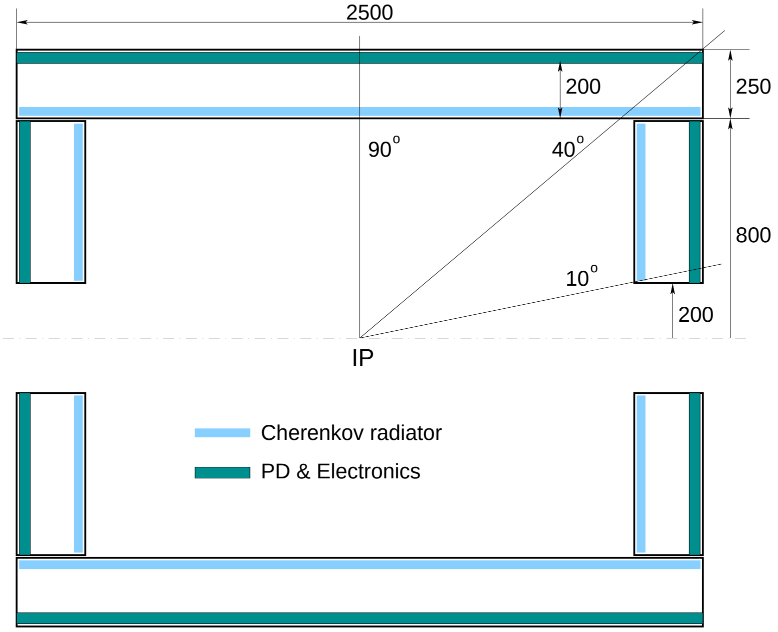

Figure 3.13: FARICH PID system for the Super $c\tau$ factory.

3.5.4 MC performance

The following configuration of the FARICH is considered and studied using a Geant4-based Monte Carlo simulation program:

- a distance between the radiator and photon detector — 200 mm,
- a single-ring four-layer aerogel radiator with a total thickness of 35 mm and $n_{\max} = 1.07$,
- a photon detector — MPPC (Hamamatsu Photonics) with a 3×3 mm^2 active area, PDE(500nm)=30%, packing density — 53%.

Simulation takes into account the processes of radiation, absorption and scattering of the Cherenkov light. Interactions of charged particles with matter were proved to be negligible (except for multiple scattering at momenta below 0.5 GeV/c) and not simulated. A magnetic field of 1 T is included in simulation. Effects of the SiPM dark noise and detector background are currently not taken into account.

Simulation shows that the number of photoelectrons for a relativistic particle is about 25 (Fig. 3.14a) that is enough for a robust ring reconstruction. The velocity resolution reaches $5 \cdot 10^{-4}$ (Fig. 3.14b). Figures 3.14c,d demonstrate π/K and μ/π separation levels derived from the velocity resolution. π/K separation is very good beginning from the kaon Cherenkov threshold in aerogel (1.3 GeV/c) and up to a few GeV/c momenta. In real situation the π/K separation will be determined by other processes such as kaon decays, noises of photon detectors, detector backgrounds etc. μ/π separation is possible at the level $\geq 3\sigma$ from 0.4 to 1.7 GeV/c and is 5.5 to 8 σ at 1 GeV/c momentum.

The development of DIRC upgrade with a focusing mirror and chromaticity correction is ongoing at SLAC [16]. π/K separation of the Focusing DIRC is shown along with the FARICH performance in Fig. 3.14c. We calculated from these data the corresponding velocity resolution

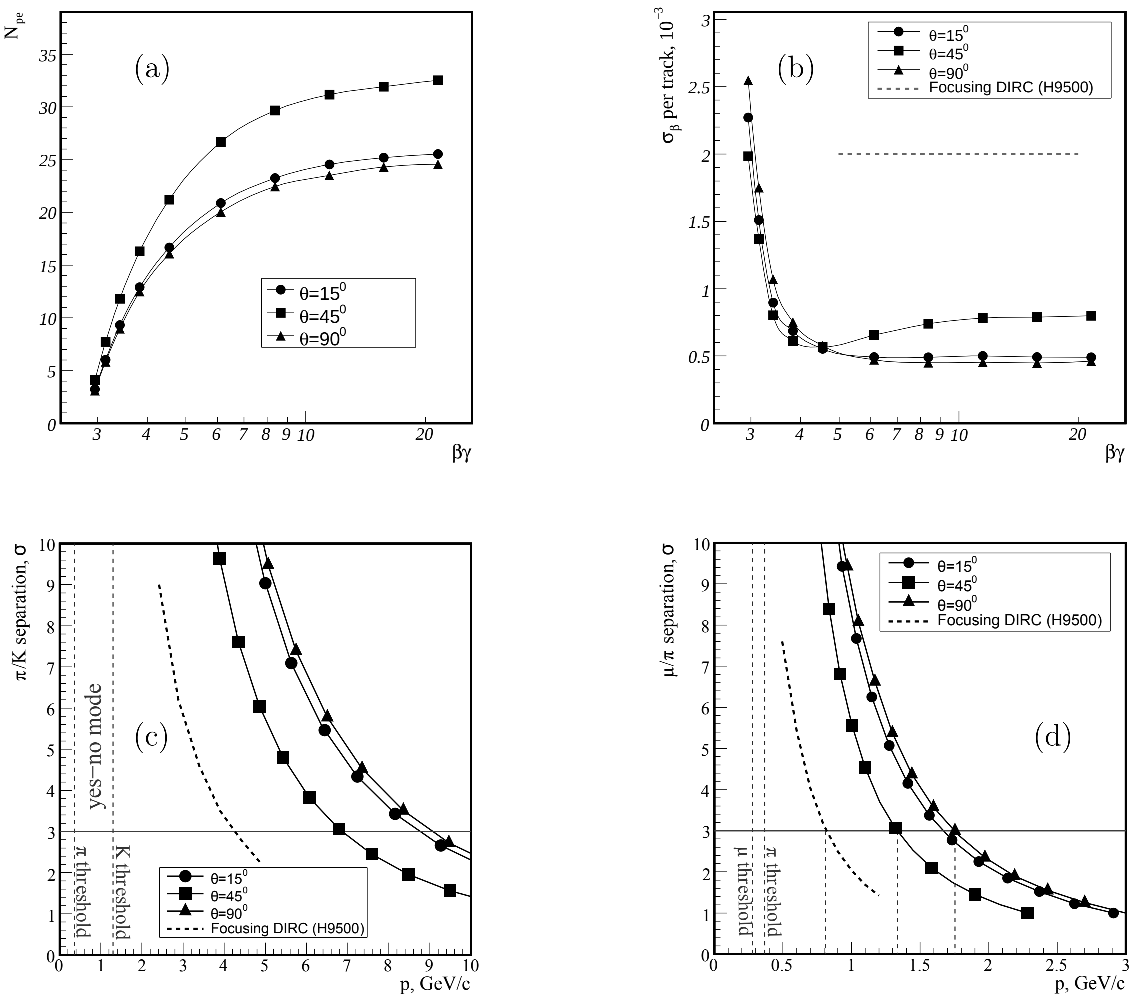

Figure 3.14: FARICH simulation results for three polar angles: the number of photoelectrons (a), velocity resolution (b), π/K (c) and μ/π (d) separations. Focusing DIRC performance is shown for comparison.

that is $\sim 2 \cdot 10^{-3}$ (Fig. 3.14b) and μ/π separation (Fig. 3.14d) that amounts to 2σ at 1 GeV/c momentum.

Methods of coverage of lower momenta is currently discussed and can be either a threshold mode of operation ("yes-no mode") or an employment of an additional radiator of higher index of refraction such as crystal NaF ($n = 1.33$). Both approaches demand reducing the effect of the SiPM dark noise. It is possible with a high timing resolution of the order 100 ps, but would require an application of rather complicated and expensive electronics with a high power consumption. Another possibility is to cool down photon detectors to the temperatures that decrease the dark counting rate below 1 MHz/channel. A development of an efficient cooling system with low material budget is needed in this case.

3.5.5 Status of prototype development

Presently, the prototype of the FARICH is being constructed. It will be tested at the electron beam with energy $\sim$ 1 GeV at the ROKK-1M facility at the VEPP-4M collider. It is planned to measure single-photon Cherenkov angle resolution and number of photoelectrons for several focusing aerogel tiles and compare the results with the simulation. Also a possibility to read out and reject the high SiPM noise rate will be tested.

In the prototype 32 MRS APDs 2.1×2.1 mm^2 from CPTA company, custom made 16-channel discriminator boards with built-in preamplifiers and multi-hit 64-channel TDC from CAEN with 100 ps discrete are used. The first run of the beam test is scheduled for November 2010–February 2011.

3.6 Electromagnetic calorimeter

An electromagnetic calorimeter of the CTF detector has the following functions:

- detection of γ–quanta and measurement of their energy in the broad energy range from 1 MeV to 2 GeV;
- determination of photon coordinates;
- separation of electrons and hadrons;
- formation of a signal for a neutral trigger.

In these experiments the main fraction of photons arising in hadron decays has energy of a few hundred MeV. Therefore, an important characteristic of a calorimeter is energy resolution in this energy region. At the present time the best energy resolution for photons with energy up to 1 GeV is obtained at calorimeters based on scintillation crystals CsI(Tl) [17, 6], $\sigma_E/E \approx 1.8\%$ at 1 GeV and about 3% at 100 MeV. Space resolution of such calorimeters is about $6\,\text{mm}/\sqrt{E(\text{GeV})}$. It is also worth noting that Budker Institute has big a experience of working with calorimeters based on scintillation alkali-halide crystals.

One more advantage of scintillation calorimeters is their high stability and low maintenance costs. CsI(Tl) crystals have a high light output (up to 50,000 photons/MeV) and emission spectrum with a maximum at about 550 nm well matching the region of high sensitivity of silicon photodetectors.

Maintenance of CsI(Tl) crystals in the B factory experiments showed that their radiation hardness is sufficiently high for conditions of e^+e^- colliders. For example, at the Belle detector the total absorbed dose for crystals closest to the beampipe is about 300 rad during 7 years of operation. At CTF with luminosity of $10^{35}\,\text{cm}^{-2}\text{s}^{-1}$, the absorption dose can reach about 1 krad after 5 years of experiments that results in about 20% loss of the light output only.

However, the emission time for such crystals is about 1 μs that can lead to a high probability of the pile-up of a background and useful signals at high background counting rates (about 100 kHz or more per crystal). A natural solution of this problem is to use faster crystals of non-activated (pure) CsI with the emission time of about 30 ns. Note, however, that the light output of these crystals is one order of magnitude lower than that of CsI(Tl) crystals necessitating use of vacuum photodetectors with gain, capable of operating in magnetic field. Thus, taking into account a higher cost of pure CsI crystals, a calorimeter based on such crystals is more expensive and have a more complicated structure. A reasonable trade-off is to use pure CsI in the calorimeter endcaps, where the background counting rate is high, and Cs(Tl) crystals in the barrel part where the background is one order of magnitude lower.

A length of the crystals and, correspondingly, a thickness of the active material is selected in such a way that about 95% of photon energy is absorbed in the calorimeter. A length necessary to reach good energy resolution is 16–18 radiation lengths or 26–34 cm. A transverse size of the crystals is determined by a transverse size of an EM shower and is usually chosen between 4 and 7 cm. A lower transverse size improves position resolution, but increases the number of electronics channels and the total number of gaps between the crystals. The total number of crystals in the calorimeter and its total mass depend on the specific detector design, but as experience of operation of existing calorimeters shows, the total mass of crystals should be 42 tons at the total number of calorimeter channels of about 10 thousand.

Note that in recent years new crystal scintillators with high light output and short emission time have been actively developed, e.g., lutecium ortosilicate (LSO) and lantane bromide ($LaBr_3$) activated by cerium. Despite their high promise, the cost of such crystals is rather high (5–10 times more expensive than CsI(Tl)) making the mass use of these crystals problematic. At the same time, active R&D studies of new crystals and their use in high energy physics in close cooperation with crystal producers can improve technology of their growth and make it cheaper as it happened in the past with NaI and CsI crystals.

3.7 Muon system

The muon system consists of nine layers of coordinate detectors in the barrel and eight layers at the endcap. The barrel part covers a solid angle of $64\%\times4\pi$ ($50^\circ < \Theta < 130^\circ$), while the endcap — $30\%\times4\pi$($20^\circ < \Theta < 50^\circ$ and $130^\circ < \Theta < 160^\circ$). Coordinate detectors are alternated with layers of a steel absorber, which also serves as the yoke of the magnet.

The main task of the muon system is to separate muons from a large number of hadrons produced in e^+e^- annihilation. Muons are identified by measuring their penetration depth (range) in the absorber. The ranges of muons and hadrons in matter are determined by two main processes: energy loss of a charged particle through ionization and nuclear interactions of hadrons with atoms of the absorber. At the same momentum muons have larger kinetic energy compared to pions and kaons, so they could lose more energy on ionization and their path is longer. Nuclear interactions of hadrons with the medium lead to additional absorption and further decrease of their range.

Due to bending of the particle track in the magnetic field of the detector, the detection threshold of the muon system is at the momentum of 0.4–0.5 GeV/c. In reality it is difficult to obtain reliable identification of muons at the momenta below 0.8 GeV/c. A pion can imitate a muon due to range fluctuations and as a result of the decay into muon and neutrino, particularly when a decay muon is emitted in the direction of the initial pion. Above 0.8 GeV/c the muon detection efficiency reaches 95–98 % and the level of pion misidentification is $\sim$5%, this corresponds to a pion suppression factor of $\sim$20. To achieve the main goals of the research program of the CTF the pion suppression at the level of 100 or better is desirable. To attain it, the muon system will work in combination with the FARICH identification system. The information from the FARICH can be also used to calibrate the muon system.

In modern experiments, coordinate detectors of different types are used in muon systems: counters with the localized discharge [18], streamer mode gas detectors [19], scintillation counters [20]. The choice of the detection technology of coordinate chambers requires a study of their long-term stability and resistance to the backgrounds under the experimental conditions of the CTF. One should also take into account the cost of the production of detectors. The total area of the coordinate detectors is more than 1000 m^2.

Currently, as a "working" option of the coordinate detectors for the muon system it is proposed to use coordinate detectors similar to the streamer tubes used in the KEDR detector [21]. Streamer tubes in a single block are arranged in two layers and are shifted relative to each other by half of the diameter. With this arrangement, a particle track always crosses one or more tubes at any incidence angle. Tubes of one electronic channel are connected sequentially in a row and alternated with the other channel tubes to reduce a probability of simultaneous triggering of several tubes in one channel by a single particle.

The basis of the block are two flanges made of duraluminum holding thin-wall stainless steel tubes. At the ends of the tubes kapronit made plugs with two holes are pressed. One hole in the center is for pin fixation, the second — for a gas inlet or outlet. In the center of the tube an anode wire is stretched with a force of 300 g and fixed in pins. The wire material is gold-plated molybdenum with a diameter of 100 μm.

The scheme of the readout electronics of one channel is shown in Fig. 3.15. A measurement of the longitudinal coordinate is based on the difference between the arrival times of signals on the opposite ends of the tube row. Two amplifiers with variable threshold discriminators are connected to both ends of the row. To prevent reflections at the ends of the row, the load resistors are used. The "start" and "stop" signals from both discriminators are transmitted to the expander. The "stop" signal is delayed to come later than "start" regardless of the hit position along the row. The expander gives a paraphase signal with the duration equal to the interval between "start" and "stop" multiplied by a coefficient of expansion about 40. Signals from the outputs of expanders are transmitted via shielded twisted-pair cables to the inputs of TDCs.

The duration of the output pulse from the expander depends on a particle hit location. Reconstruction of the hit longitudinal coordinate is done using a linear approximation taking into account the length of the wires connecting the tubes. The typical resolution of longitudinal coordinate is about 4 cm. The transverse coordinate is given by the number of the fired tube. A more accurate measurement of the transverse coordinate using a drift time of ionization is possible but not necessary because of the strong multiple scattering in the absorber.

To operate in the streamer mode, a gas mixture should contain a component with strong photon absorption in the UV spectrum. The working gas in the muon system is a nonexplosive mixture of $70\%\mathrm{Ar} : 23\%\mathrm{CO}_2 : 7\%$n-pentane.

3.8 Superconducting solenoid

3.8.1 Main demands

The superconducting solenoid is intended to produce an axial magnetic field in the detector volume. The solenoid's coil will be placed between the EM calorimeter and the muon system. Such a placement does not impose strong constrains on the thickness of the solenoid.

The main parameters of the solenoid are listed in the Table 3.1.

3.8.2 Original approach

Analogous superconducting solenoids were produced in the last decade by Japanese and European companies. For their production a technology based on superconducting cable with aluminum stabilizer was developed. The stabilizer made of 99.999% Al with the price \$1000/kg dominates the cost of the solenoid. The main purpose of the stabilizer is a quench protection. The stabilizer

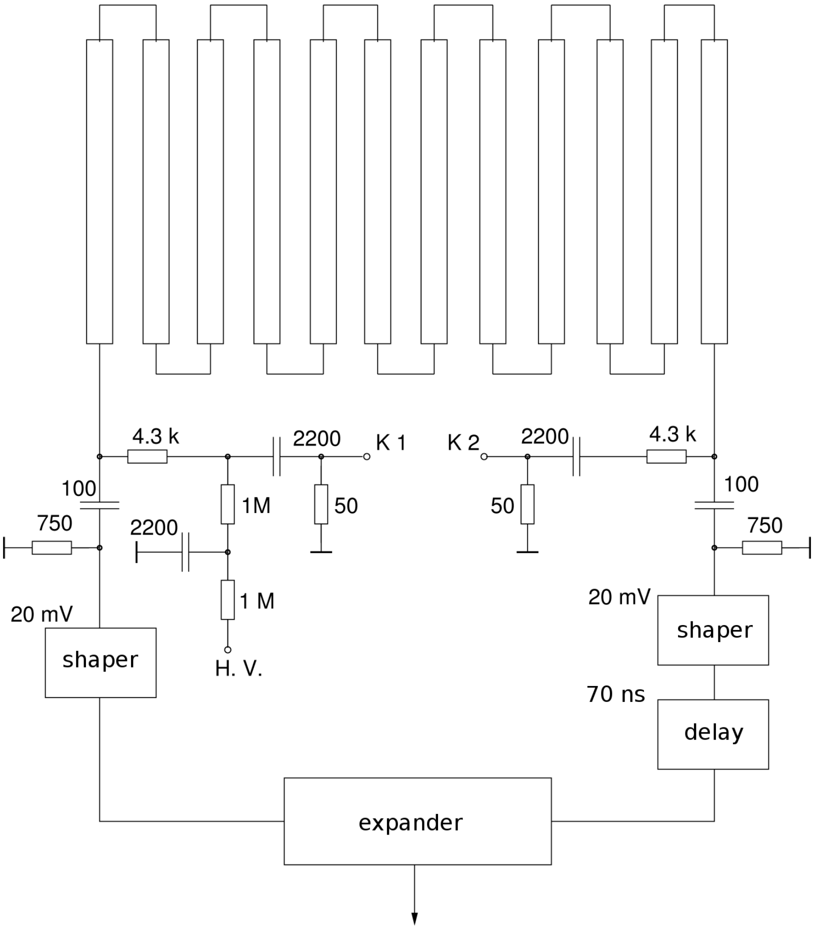

Figure 3.15: Readout electronics of the muon system.

Table 3.1: Main parameters of the solenoid.

Length	4 m
Internal diameter	3.2 m
Magnetic field	1 T
Stored energy	12.9 MJ
Charging time	< 4 h

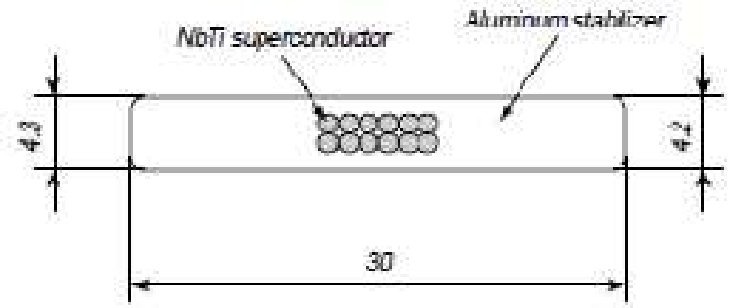

Figure 3.16: SC cable used in the ATLAS central solenoid.

drastically minimizes heat generation inside the solenoid, i.e. ρJ^2, where J — current density, ρ — electrical resistivity of the stabilizer. This circumstance was considered from three following points of view:

1. the electrical and thermal properties of 99.999% Al and 99.99% Al differ by factors from 2 to 5, while the cost of the 99.99% Al is less by factor of > 100;
2. the heat generation can be also minimized by increasing the amount of the stabilizer;
3. in the modern solenoids employed at LHC active quench protection is used.

The solenoid design for the Super $c\tau$ factory is based on the superconducting cable with the stabilizer of 99.99% Al. Active quench protection with heaters will be used for the quench propagation. The proposed approach allows $1–2 millions to be saved for the solenoid production.

Preliminary calculations show that the size of superconducting cable can be the same as for the ATLAS central solenoid that is shown in the Fig. 3.16. The cable for ATLAS was produced by Hitachi Co, Japan.

3.8.3 Cryogenics

The cryogenics of the detector should provide the operation of the detector solenoid and the final focus quadrupoles of the collider at the temperature of 4.5 K. The cryogenics will be based on a refrigerator with 100 W cooling performance at 4.5 K.

3.9 Trigger

Trigger of the CTF detector will be based on the concept of the “open-trigger”, which can select and save up to 100% of useful events. This concept implies that event selection is based on the universal criteria such as: the presence and the topology of the tracks in the coordinate system, the total energy deposition in the calorimeter, the topology of the energy deposition and the number of clusters in the calorimeter, the response of the muon system. “Open trigger” is not specially tuned for the selection of the particular predefined processes. This approach is conditioned by a very wide and diverse physics program of CTF and the task of finding “new physics” that is impossible to predict in advance. A disadvantage of this approach is that it is impossible to separate useful events from the events of nonresonant hadron production based on the trigger.

Useful event rates and rates of Bhabha events at different energies as well as rates from cosmic events are presented in Table 3.2. The cross section of the nonresonant hadron production at

Table 3.2: Luminosity, physical cross section, rates of useful events, Bhabha events at different energies and cosmic event rate.

	J/ψ	$\psi(2S)$	$\tau\bar{\tau}$	$\psi(3770)$	$\tau\bar{\tau}$	$\Lambda_c\bar{\Lambda}_c$
E_{cm}, MeV	3097	3686	3700	3770	4250	4650
L, 10^{34} cm^{-2}s^{-1}	7.7	9.2	9.2	9.4	10	10
σ, nb	~3400	~640	2.5	~6	3.5	0.5
f, kHz	260	60	2.3	5.6	3.5	0.5
Bhabha, kHz	~90	~80	~80	~80	~60	~50
Cosmics, kHz	~2					

these energies is ~20 nb, which corresponds to the counting rate of 20 kHz at the luminosity of 10^{35} cm^{-2}c^{-1}. At present it is difficult to estimate the trigger counting rate from the background events associated with the beam loss and beam interaction with the residual gas. Working conditions at the B factories at KEK and SLAC and the current development of the Super$B$ factory in Italy indicate that this counting rate will be at the level of several tens of kHz.

As follows from the data in Table 3.2, the maximum readout rate of useful events will reach 300–400 kHz. The average size of a single event is estimated at 30 kB.

To achieve so high event readout rate, it is expected to use the methods and approaches developed at the BaBar detector and for the Super$B$ project.

- All signals from the detector systems are continuously digitized in the electronics located directly on the detectors. The data are stored in digital pipelines for a few microseconds. The storage time is determined by the decision-making time of the L1 (L1) trigger.

- The electronics of the drift chamber, calorimeter and muon system give an additional "fast" signals, which are transmitted directly to the L1 trigger.

- After receiving the signal from the L1 trigger, data from the onboard electronics are transmitted over the high-speed optical links (10 Gbps) into the readout processors (ROP), which are located outside the detector. The preprocessing is performed in the ROPs (actual signal amplitudes and times are computed) in order to reduce the amount of data. An additional filtering based on the topology and timing information is also performed at this stage.

- Data from the ROPs of each system come into the "event builder" computer farm where they are synchronized and then processed by the high level trigger.

- The L1 trigger uses "fast" signals from the detector systems for a search of "useful" events . It is based on a specialized pipelined processor with the programmed logic of the event search. This logic uses the topology of tracks in the coordinate system, the total energy deposition, the topology of energy deposition and the number of clusters in the calorimeter as well as data from the muon system. The maximum frequency of the decision making is 500 kHz, the effective "dead time" of the L1 trigger should not exceed 100 ns. The decision making time of the L1 trigger is a few microseconds.

- The high level trigger is software based. The fast preliminary reconstruction of the events to get information about coordinates, momentum and energy of all secondary particles is

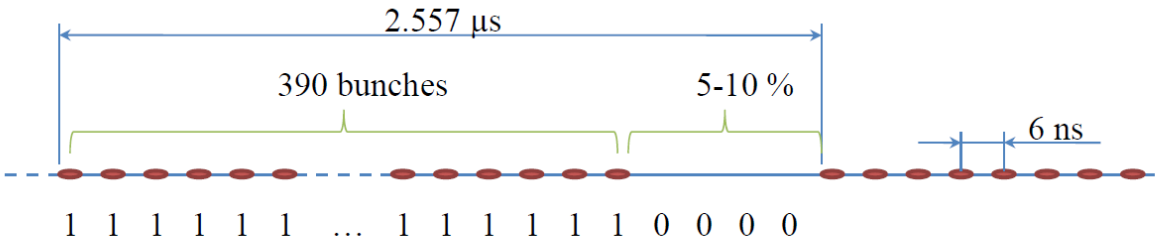

Figure 3.17: The bunch distribution and the corresponding binary map.

performed. At this stage, the effective rejection of the background events from the beam interactions and cosmics is done. To reduce the amount of the recorded information, prescaling of the Bhabha scattering events could be implemented. The high level trigger will be organized on the basis of a specialized computer farm, consisting of several hundred processors.

3.10 Electronics

Electronics together with computers and telecommunication equipment of the detector is one of the key elements of the CTF detector.

Collider parameters, which are important for the electronics, are below.

- The RF frequency is about 508 MHz.
- The period of bunch circulation is 2.557 μs.
- The quantity of separatrixes is 1300.
- Each third separatrix is filled, so the time gap between bunches is around 6 ns.
- The mode with filling each fourth separatrix is under discussions.
- The maximum quantity of bunches is 390.
- The gap of 5–10% (130 separatrixes) in a bunch train is necessary for suppression of the ion instability.

For a precise time measurement of several detector subsystems it will be necessary to know the bunch distribution in a train. Therefore, the binary map of the bunches will be used (Fig. 3.17). The synchronizing “phase” pulse for the bunch circulation will be also necessary.

All analog-to-digit conversions will be performed inside the detector in the front–end (FE) electronics. The information from a large group of channels will be sent through 10 Gbps optical links. Wide usage of ASICs is mandatory to reach a needed channel density and power consumption. The water cooling system with a negative pressure for the front-end electronics will be applied. The electronics should employ a maximum unification.

Table 3.3 lists the quantity of electronics channels for different subsystems of the detector, the geometrical size of channels, an estimate of the power consumption, participation of subsystems in the trigger and a type of required information (A — amplitude, T — time, P — position).

Table 3.3: Limitations and demands of the susbsystems' electronics.

Detector	Channel quantity	Channel size	Power consumption	Trigger participation	Information
VD–GEM	56 K	$2 \times 2\,\mathrm{mm}^2$	1 kW	Possible	A, T, P
VD–Pixel	10 M	$150 \times 150\,\mu\mathrm{m}^2$			
DC	7.1 K	$12 \times 20\,\mathrm{mm}^2$	2 kW	Yes	A, T, P
FARICH	1 M	$4.5 \times 4.5 \times 50\,\mathrm{mm}^3$	100 kW (21 m^2)	No	T, P
Calorimeter	7.5 K	$(40-70)^2\,\mathrm{mm}^2$	2 kW	Yes	A, T, P
Mu	4–44 K	diameter 20 mm	1–9 kW	Yes	T, P

Table 3.4: Parameters of subsystems' electronics.

Detector	Channel load	Duration of signals	Rate of digitization	Bit quantity of ADC (TDC)	Time meas. precision
VD	33 kHz	Rising edge 25 ns	from 20 to 80 MHz	10–12 bit ADC	1 ns
DC	50 kHz	Rising edge 100–200 ns, Follow edge 300 ns	50 MHz (ordinary mode) 200–300 MHz (cluster mode)	10 bit ADC 10 bit ADC	1 ns 1 ns
FARICH	10 MHz	5–10 ns	—	6 bits (for 8 ns) TDC	200 ps
Calorimeter	15 kHz	30 ns for pure CsI	40–50 MHz	18 bit ADC	1 ns
Mu	100 kHz	30–200 ns	—	11–12 bit TDC	60 ps

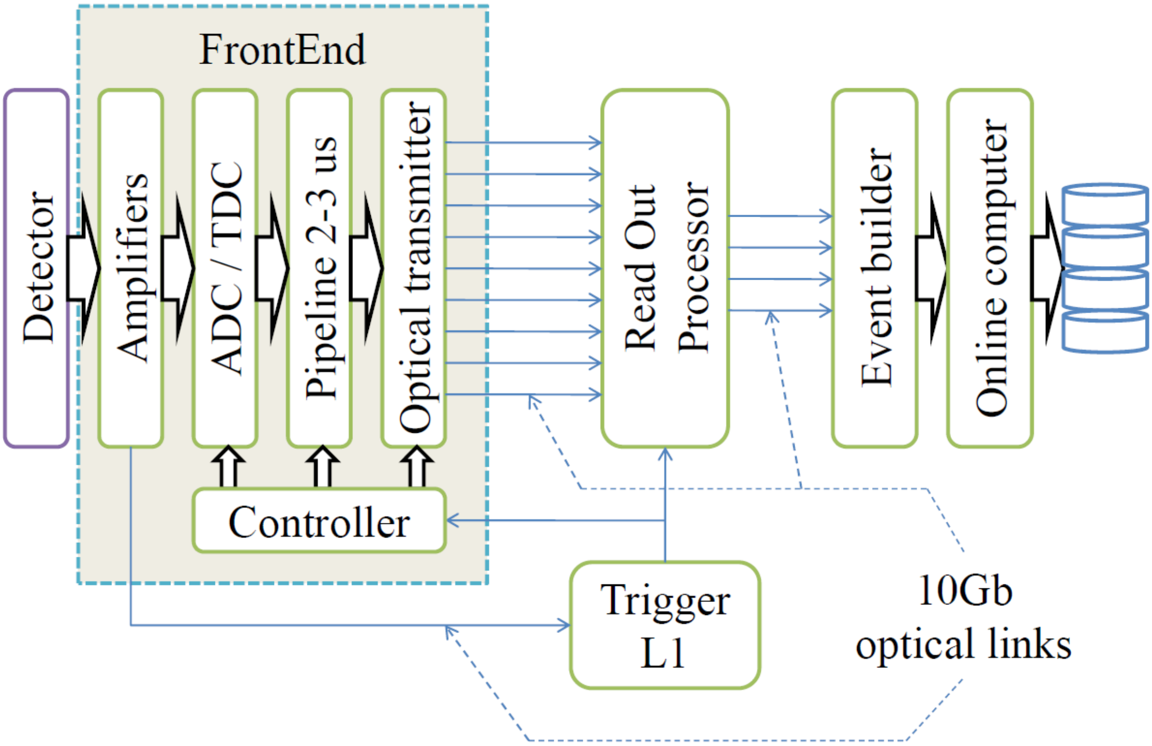

Figure 3.18: Block diagram of electronics.

Table 3.4 shows the maximal channel load, the time characteristics of the pulses, the required rates of digitization, the bit quantity of ADC and TDC and the necessary precision of time measurements.

Figure 3.18 shows the common block diagram of readout electronics. The FE electronics contains amplifiers, ADC and TDC, an obligatory pipeline for the working time of the L1 trigger, controller, which manages a board and optical transmitters, 10 Gbps optical links connecting the FE electronics and the readout processors (ROP), which are located near the detector. ROPs get raw data and perform calculations of amplitude and time of pulse. Additional selection of information based on the L1 trigger data is possible in ROPs. Results are sent to EventBuilders and on-line computers located in the data storage hall.

The L1 trigger is located near the detector. It gets fast information from the FE electronics by 10 Gbps optical links.

It is planned to make a modular FE electronics in order to enable a fast replacement of broken elements. This approach has been successfully working in the drift chamber of BaBar (Fig. 3.19 and Fig. 3.20). All electronics of the BaBar drift chamber is divided into 16 sectors in φ and 3 rings in radius. Therefore there are 48 assemblies of the FE electronics. All boards of an assembly are placed into an aluminum frame, which serves not only as a shield but also as a heat sink. All microchips have a thermal contact with a frame. The assemblies are firmly screwed to the radial bars that carry water cooling. The total power of about 1.5 kW is removed from the detector.

The drift chamber FE electronics (Fig. 3.21) will have 48 modules of 3 types. Each module will have from 128 to 192 channels, from 2 to 4 FE boards and one readout board. The FE board will contain from 48 to 64 channels of amplifiers and ADCs. The readout board will hold a common pipeline and controller in FPGA which will send information to a ROP upon a signal arrival from the L1 trigger.

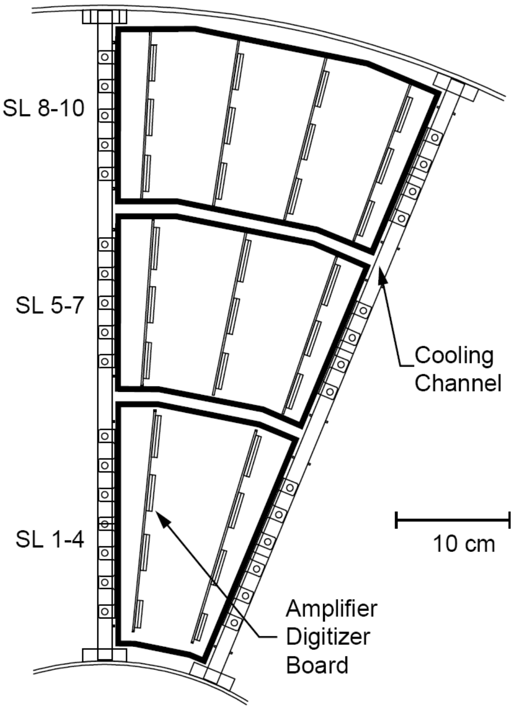

Figure 3.19: FrontEnd Assembly of the drift chamber of BaBar.

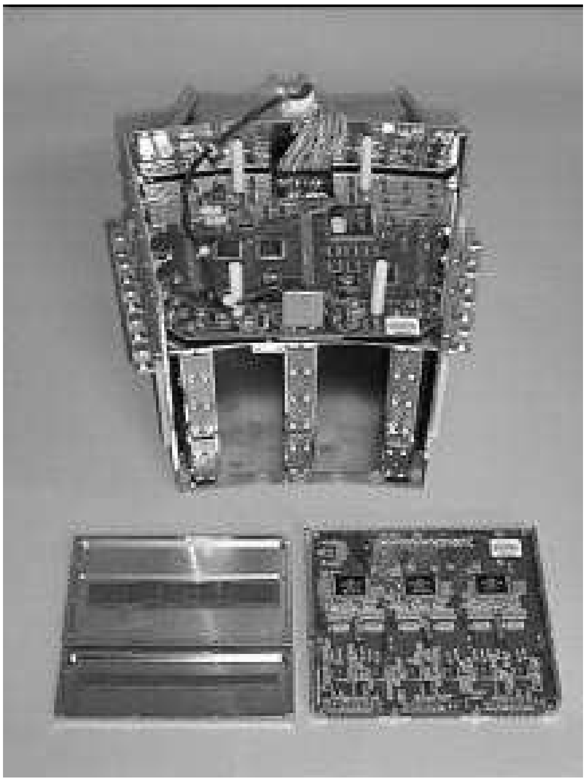

Figure 3.20: Photo of FrontEnd Assembly of the BaBar drift chamber.

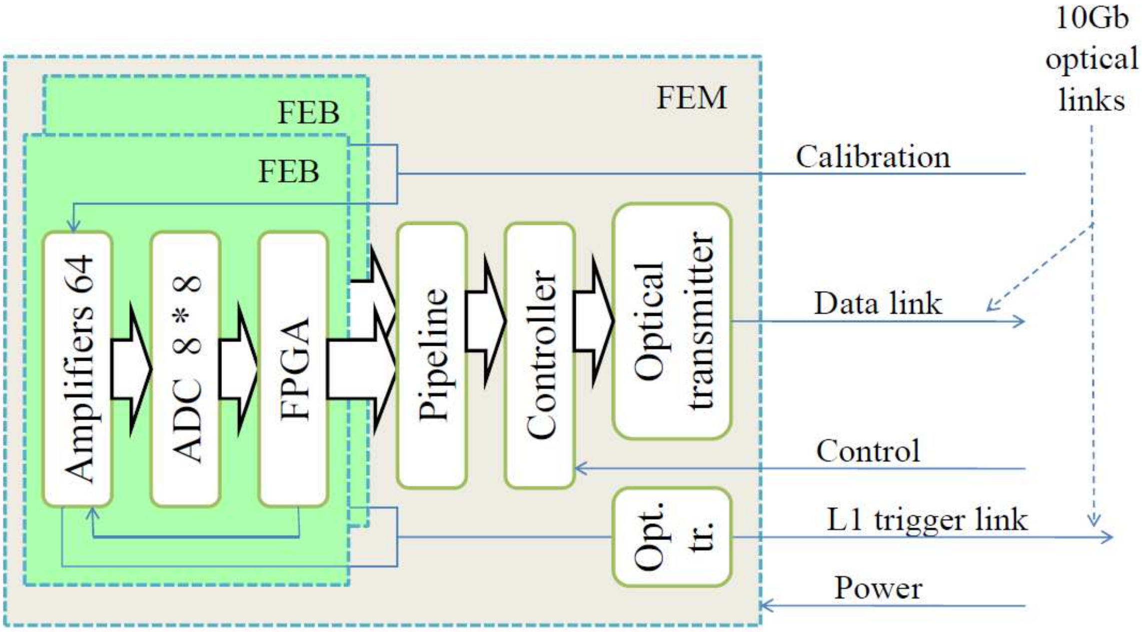

Figure 3.21: Block diagram of the drift chamber FE module.

Table 3.5 was created after estimating the data flows from the detector subsystems and convenience of mounting. It shows the supposed quantity of optical links for data and trigger information. The quantity of 10 Gbps links is redundant for all subsystems except FARICH. In total, there are 1168 data links and 168 trigger links.

The ROP gets data via 8 optical links (Fig. 3.22). Therefore 146 ROPs will be necessary for 1168 data links. This unit calculates the amplitude and time of pulses from raw data of the FE electronics. It uses L1 trigger information to process so called “field of interests” — the places of the detector where the channels are triggered. This approach reduces the processing time and amount of the output data.

146 ROPs will occupy 10 VME crates, which will be located in 5 racks. The preliminary power consumption of one crate is about 900 W, so one rack will consume 1.8–2.7 kW. The racks with ROPs will be located near the detector (Fig. 3.23).

Table 3.5: Number of electronics channels, data and trigger links.

Detector	Number of channels	Number of data links	Number of trigger links
VD–GEM	56 K	56	56
VD–Pixel	10 M	n/a	n/a
DC	7.1 K	48	48
FARICH	1 M	1000	0
Calorimeter	7.5 K	32	32
Mu	4 – 44 K	32	32

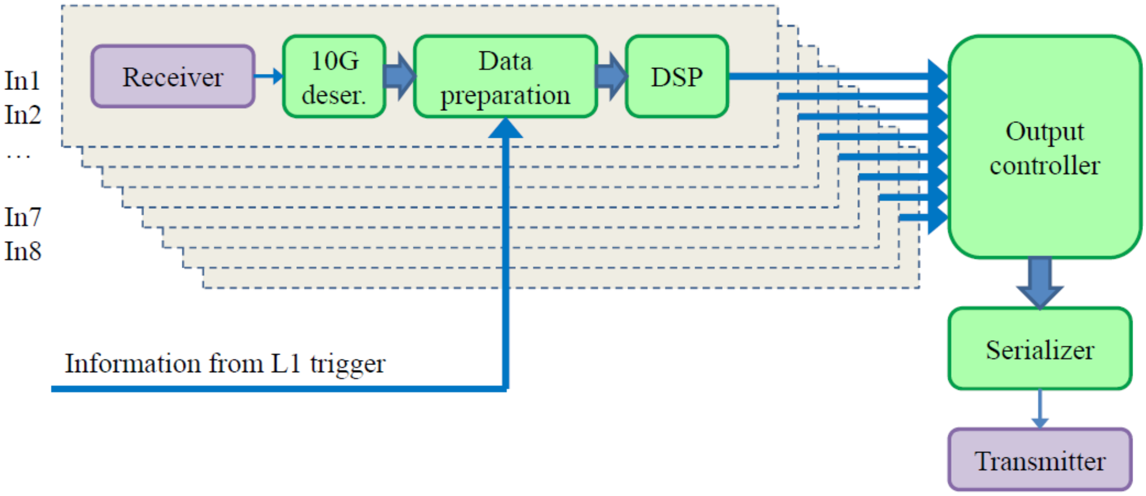

Figure 3.22: Block diagram of the ReadOut processor.

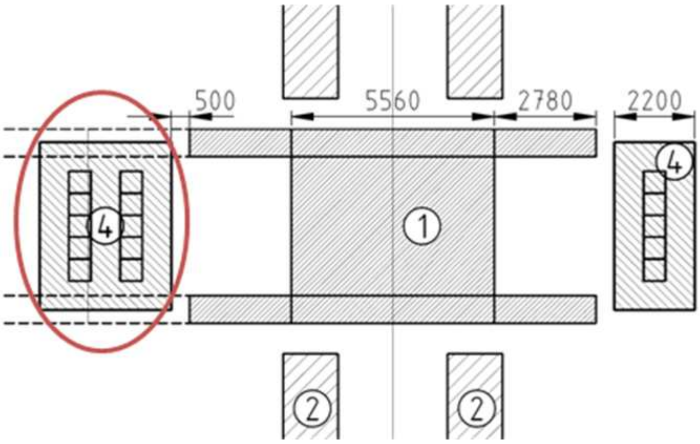

Figure 3.23: Location of racks with ROPs near the detector.

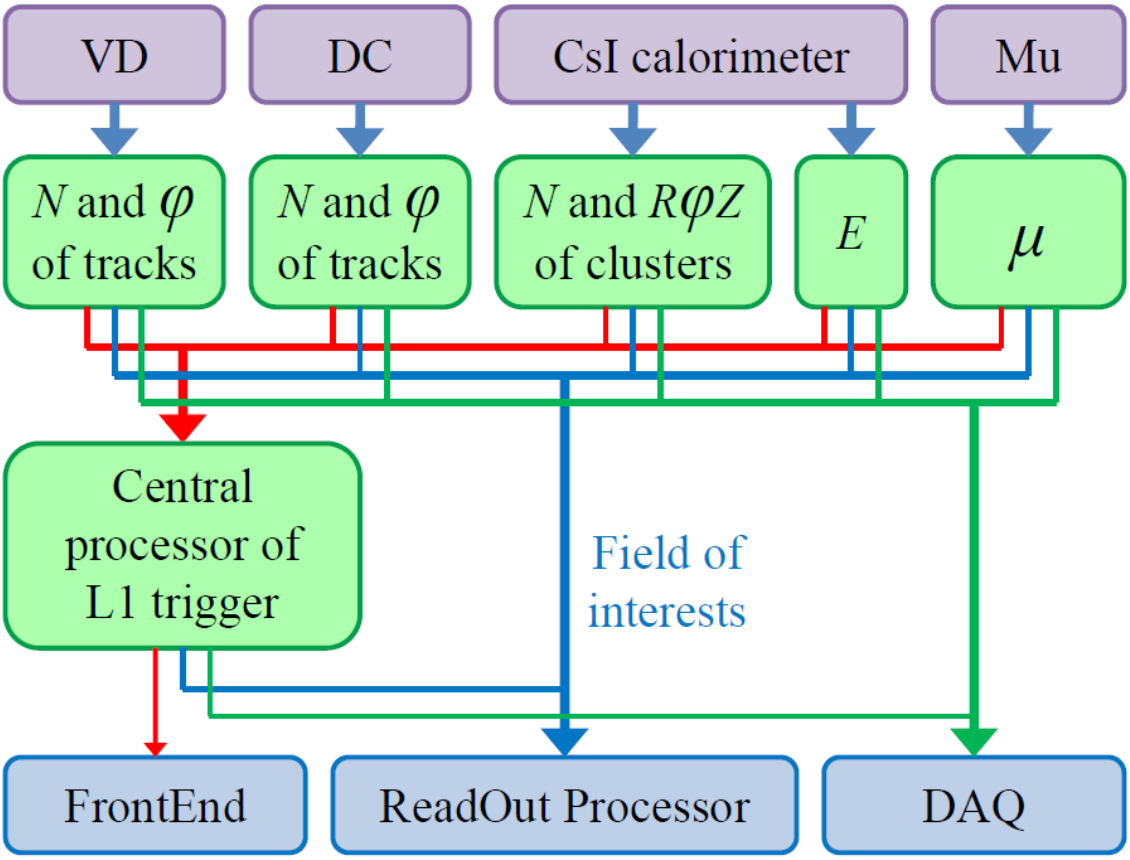

Figure 3.24: Block diagram of the Level 1 trigger.

The L1 trigger has a pipelined structure. It gets information from the drift chamber, the calorimeter, the muon system and possibly from the vertex detector (Fig. 3.24). Preprocessors of the tracking systems calculate the number of tracks and their topology. Preprocessors of the calorimeter determine the topology and number of clusters and energy level. Also the information about triggering of the muon system is present. The preprocessors transfer the information to the central trigger processor which makes a decision.

The L1 trigger decision pulse goes to the FE electronics. The fields of interests are transferred to ROPs. And the intermediate information about the trigger is transmitted to the Data Acquisition system. The L1 trigger will occupy two racks that will be located near the detector together with ROP racks.

3.11 Networking and computing systems

3.11.1 Introduction

Networking and computing infrastructure is going to play one of the key roles in operating the experiment at the CTF detector. Below we give a thorough overview of designing, building and operating the computing infrastructure for this experiment.

Section 3.11.2 contains a brief introduction to the prospected organization of trigger and DAQ, offline data processing and data storage systems of the detector. It also gives an insight into the architecture and hardware requirements for the systems involved.

More details related to the data processing and storage systems of the experiment are given in Section 3.11.3. Some specific technical questions such as choosing the architecture of software execution environment for the experiment and ways of distributing the data processing activities of the detector experiment across local and remote computing facilities are also discussed here.

Section 3.11.4 is devoted to hardware and financial resource estimation for the proposed computing and networking solutions for the experiment. In addition, it contains plans for prototyping the key components of the detector computing systems and hardware deployment plans for the computing facilities supporting the experiment during the period of 2014–2025.

3.11.2 Brief Overview of TDAQ and Offline Data Processing Systems

The following three functional groups of components are forming the computing environment of the CTF experiment:

1. Trigger and DAQ systems (TDAQ):
    (a) a two-level hardware and software trigger system with a maximum trigger rate of 0.5 MHz for the average event size of approximately 30 kB, thus capable of generating the stream of output data with the rate up to 120 Gbps,
    (b) an event building system,
    (c) a storage buffer used for exporting data to the offline data processing systems.
2. Detector monitoring and control systems:
    (a) detector information system,
    (b) detector slow control system,
    (c) detector safety and access control systems,
    (d) engineering infrastructure and environment conditions monitoring systems,
    (e) dedicated control rooms for the continuous operation of the detector, its TDAQ systems and their computing infrastructure.
3. Detector offline data processing farm and its multilevel heterogeneous data storage system.

Data flow diagram between these functional groups is shown in Fig. 3.25.

The detailed diagram of the data flow originating from the detector and going through its TDAQ, offline data processing and storage system is shown in Fig. 3.26, which also displays the proposed capacities of the storage systems involved and the throughput values of network links interconnecting them. These values were derived by minimizing the price/performance ratio for the whole detector computing system with respect to the financial estimations discussed in Section 3.11.4.1.

It is essential that the proposed configuration of TDAQ and offline farm make it possible to capture the full flux of data generated by the first level trigger and store it for the long term analysis if needed. For more detail about the architecture of the computing systems discussed here we refer to Section 3.11.3.1.

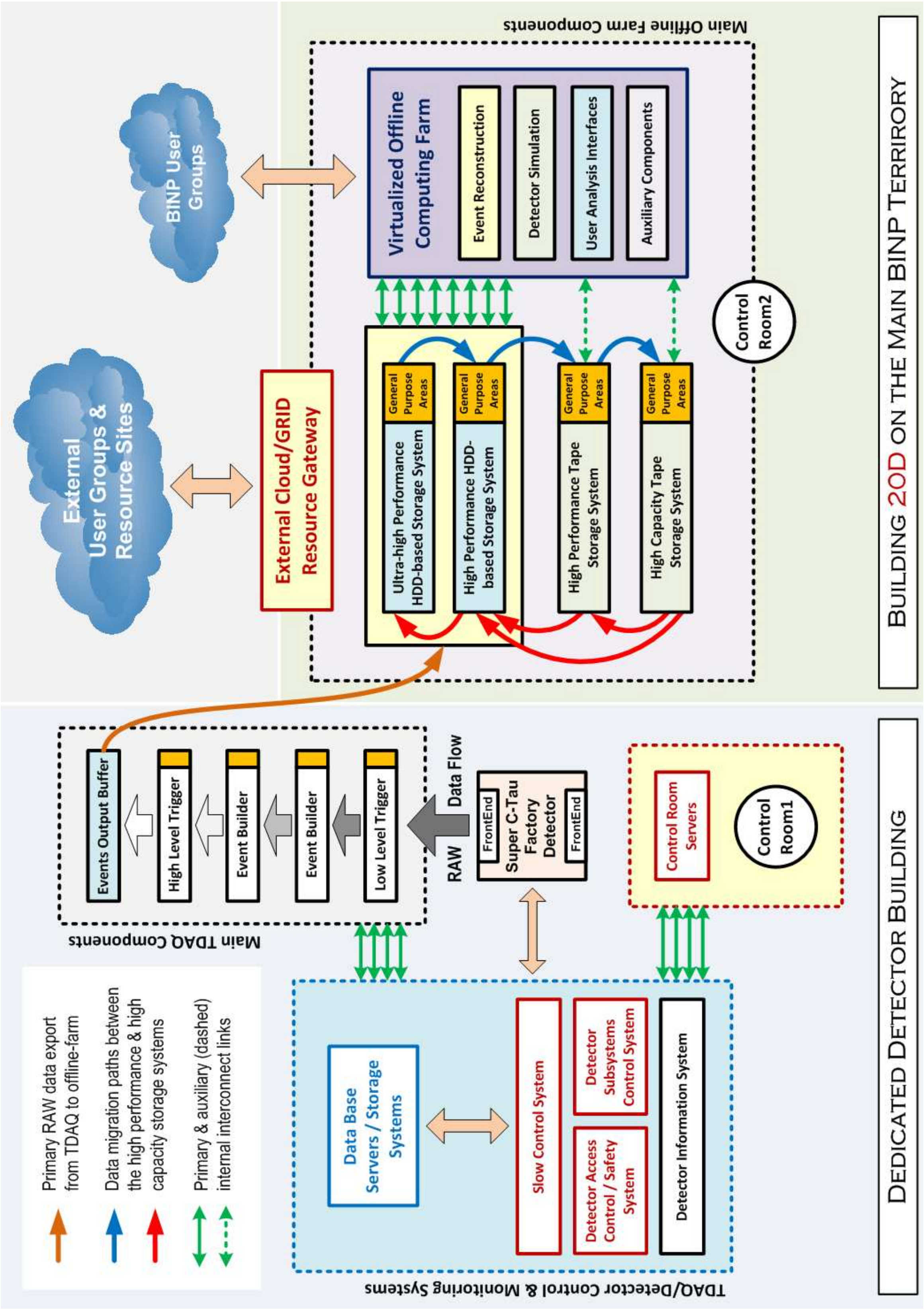

Figure 3.25: Generic data flow diagram for TDAQ and offline data processing systems of the detector.

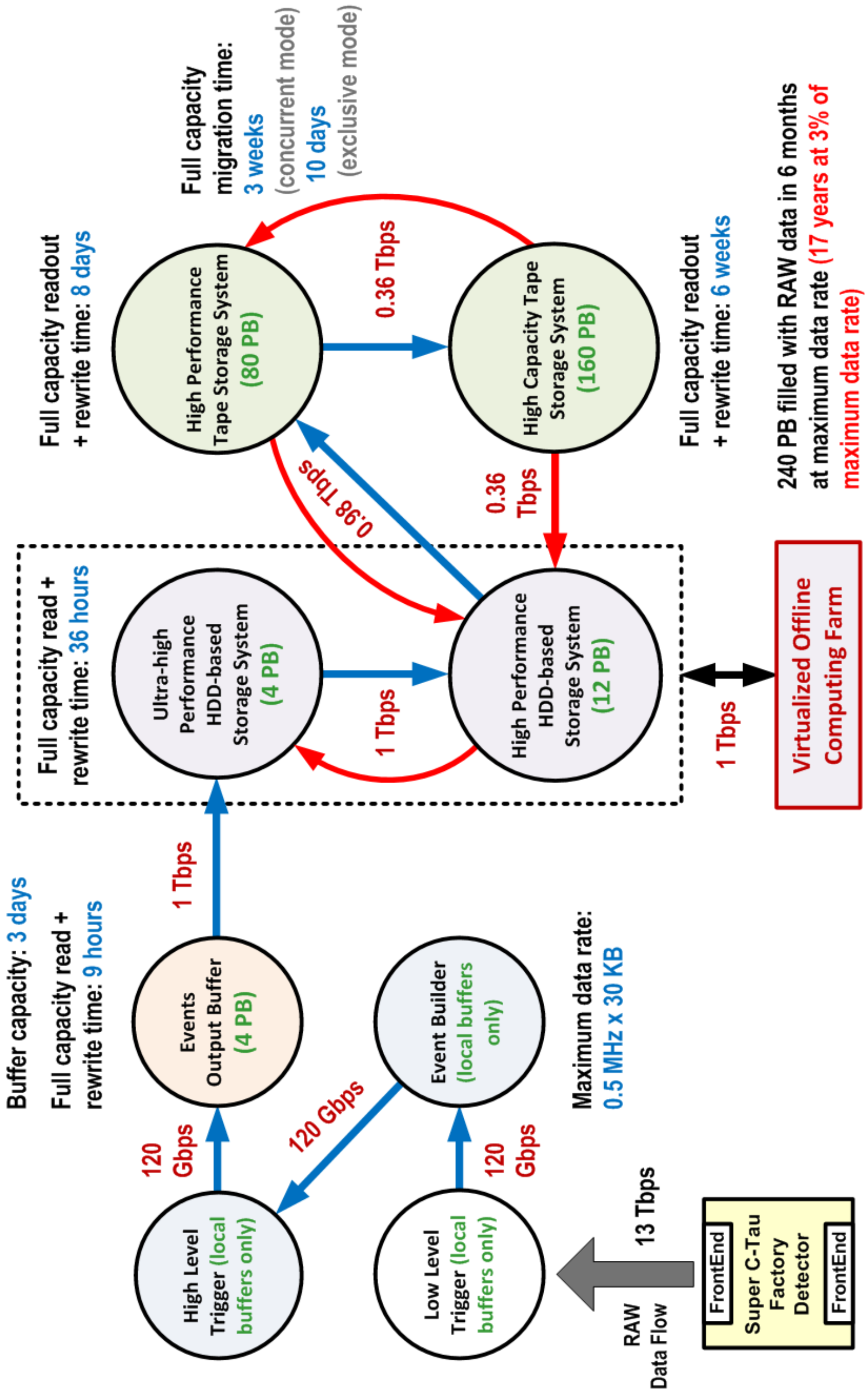

Figure 3.26: Detailed diagram of the data flow originating from the detector and going through its TDAQ, offline data processing and storage systems. Capacities of the storage systems involved and the expected data rates between them in a simultaneous read/write mode are displayed as well.

3.11.3 Architecture of the Data Processing and Storage Systems

3.11.3.1 Main Components

The following parts of networking and computing environment of the CTF experiment, which are listed below, do play an important role in the processes of accumulating experimental data, storing and processing. A short summary for each of them describes its functionality and interaction with other components in the list below and in addition provides with unique ID for future references.

1. **[FrontEnd1,2]** Modules of the front-end electronics installed within the volume of the detector located 17 m below the ground level in the dedicated detector building.

2. **[ReadOut1,2]** The following electronics equipment, which is installed in the dedicated racks in the vicinity of the detector and mechanically attached to it:

   (a) front-end electronics' power supplies,

   (b) detector subsystems' readout equipment,

   (c) Low Level Trigger (LLT) of the detector,

   (d) aggregation systems for experimental event fragments and output buffers for transferring the data aggregated to the Event Builder installed in the **[DataCenter1]** facility for further processing.

3. **[FiberTray1(a,b)]** Optical-fibers communication line connecting passive optical crossing **[FiberCross1(a,b)]**, placed on the ground level near the detector cavern with the **[ReadOut1,2]** modules, consisting of three parts:

   (a) fixed vertical section going down to the detector cavern within the dedicated cable trays (providing mechanical protection and tension control for fibers) attached to one of the walls of the cavern;

   (b) horizontal movable and retractable section which is capable of automatically adjusting itself to the position of the detector in the experimental cavern, supporting the fibers on their path from the wall of the detector cavern to **[ReadOut1,2]** modules;

   (c) fixed section provided with radiation resistant fibers (discussed below in Section 3.11.3.2) going over the multiple paths from **[ReadOut1,2]** to **[FrontEnd1,2]** modules installed within the detector volume.

   The optical line consists of sixteen 24-core multichamber optical fiber cables (192 cores of SMF 9/125 optical fiber in total) subdivided into two equal sets of cables running over the physically independent paths within the detector cavern (at least 1 m separation along the path is required).

4. **[FiberTray2(a,b)]** Optical-fibers communication line connecting passive optical crossings **[FiberCross1(a,b)]** and **[FiberCross2]**, respectively (the total length is approximately 200 m over the fiber).

   The optical crossing consists of 8 optical patch panels supporting 24 pairs of fibers each distributed among four racks within the **[DataCenter1]** facility.

5. **[DataCenter1]** Computing facility located in the area number 114 of the dedicated detector building and hosting the following components:

    (a) passive optical crossing **[FiberCross2]**,
    (b) Event Fragment Input (EFI) and Event Builder (EB) subsystems,
    (c) High Level Trigger (HLT) of the detector experiment,
    (d) buffer storage systems used for exporting data between **[DataCenter1,2]** facilities,
    (e) passive optical crossing **[FiberCross3]** of the **[FiberTray3]** optical communication line linking **[DataCenter1,2]** facilities,
    (f) servers supporting detector control systems,
    (g) servers supporting environmental monitoring and detector safety systems,
    (h) servers supporting the main control room **[ControlRoom1]**,
    (i) terminal servers providing external access to the **[DataCenter1]** facility.

   Location of the **[DataCenter1]** facility and its engineering infrastructure within the dedicated detector building is shown in Fig. 3.28. The detailed equipment installation plan for the **[DataCenter1]** facility is given by Fig. 3.29. A list of basic specifications for the **[DataCenter1]** facility is given in Table 3.6.

6. **[DataCenter1Inf]** Engineering infrastructure of the **[DataCenter1]** computing facility deployed in the areas number 113, 113a, 115, 115a, and 116 of the dedicated detector building and its vicinity:
    (a) 10 kV power cables inlets,
    (b) dedicated transformed plant,
    (c) group of chiller modules serving the external cooling circuit of the **[DataCenter1]** facility,
    (d) external cargo bays for the areas number 113 and 115 of the detector building.
7. **[ControlRoom1]** Main detector control room constructed in the area number 112 of the detector building which holds control over the
    (a) detector subsystems and their engineering infrastructure,
    (b) entire **[DataCenter1]** computing facility including its safety and access control systems.
8. **[FiberTray3]** Optical-fibers communication line with the length not exceeding 2 km over the fiber linking the **[DataCenter1,2]** computing facilities. The optical line consists of four 48-core multichamber shielded optical fiber cables (192 cores of SMF 9/125 optical fiber in total).
9. **[DataCenter2]** Computing facility built within the existing BINP centralized IT facility hosting the following components:
    (a) passive optical crossing **[FiberCross4]** of the **[FiberTray3]** optical communication line linking **[DataCenter1,2]** facilities,
    (b) BINP general purpose internal networking core,
    (c) offline data processing farm of the experiment,
    (d) long term robotic tape storage system (several groups of tape robots),

   (e) central database servers of the experiment,
   (f) central backup system serving both **[DataCenter1,2]** facilities,
   (g) terminal servers providing external access to the **[DataCenter1]** facility.

   The prospected layout of the **[DataCenter2]** facility by 2020, assuming the major upgrade of its engineering infrastructure and deployment of all the equipment related the detector experiment is shown in Fig. 3.30. List of basic specifications for the **[DataCenter2]** facility is given in Table 3.6.

10. **[DataCenter2Inf]** Engineering infrastructure of the **[DataCenter2]** computing facility deployed in the vicinity of its main IT area.

11. **[ControlRoom2]** Dedicated control room of the **[DataCenter2]** computing facility holding control of the IT equipment deployed within the **[DataCenter2]** facility and its engineering infrastructure, including safety and access control systems.

The generic layout of the key components of TDAQ, data processing and storage systems of the detector experiment listed above is shown in Fig. 3.27.

Possible extensions of the basic organizational scheme of the network and computing infrastructure of the experiment summarized here are discussed in Section 3.11.3.3.

3.11.3.2 Fiber-optics Communication Lines Deployed in the Vicinity of the Detector

As it was mentioned earlier in Section 3.11.3.1, the fiber-optics communication lines deployed in the vicinity of the detector, especially some subsections of **[FiberTray1]** must be provided with means of radiation protection in order to keep the lifetime of fibers at a reasonable level and minimize the rate of permanent fiber failures encountered over the detector lifetime.

The radiation protection of the fiber-optics communication lines is proposed to be achieved in one of the following ways:

1. identifying the spots with high radiation loads within the detector volume by using the full detector simulation, which are to be avoided while tracing the paths of optical cables,

2. shielding the bunches of optical cables by using the custom design cable trays (for the cables deployed outside the detector volume),

3. using the radiation resistant optical fibers shielded with the special covers such as described in [37]–[41] to be deployed in the places where two previous solutions cannot be applied.

The optimal solution for the radiation resistant fiber-optics lines deployed within the detector is expected to be found while building and evaluating prototypes of the **[FiberTray1]** communication line which are proposed in Section 3.11.4.2.

3.11.3.3 External Connectivity of [DataCenter1,2] Facilities and Discussion of the Possible Involvement of the Remote Computing Centers

All the network equipment providing the external connectivity for BINP and the detector in particular will be hosted at the **[DataCenter2]** computing facility, thus it will be playing a role of an external network gateway for the entire computing infrastructure of the experiment.

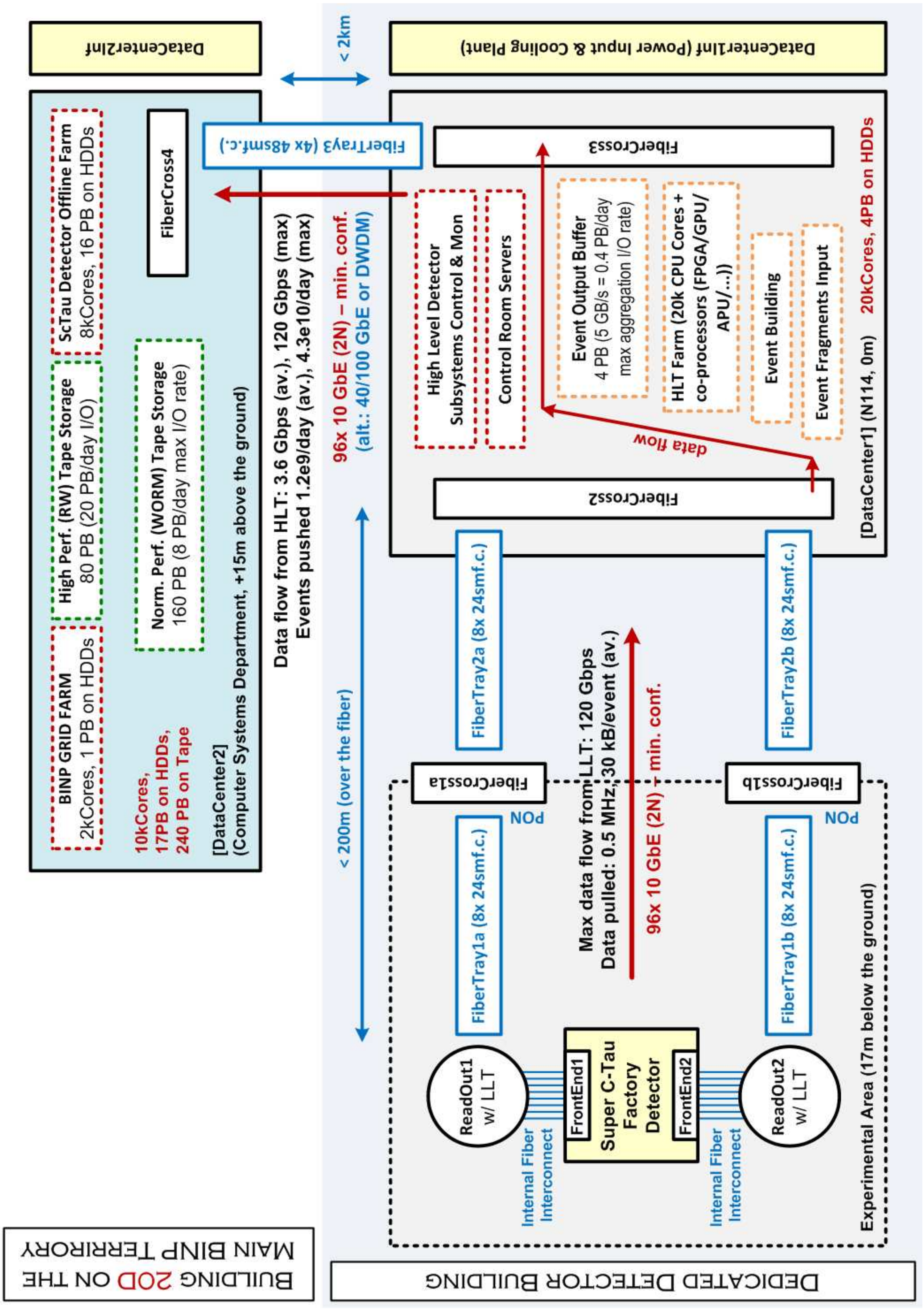

Figure 3.27: Generic layout of the key components of TDAQ, data processing and storage systems of the experiment located both in the dedicated detector building and the existing computing facility on the main BINP territory.

The prospected internal and external networking layout for all the HEP experiments carried out at BINP at early stages of building the networking and computing infrastructure for the detector is shown in Fig. 3.31.

So, even at the early stages of commissioning of the experiment and its networking and computing infrastructure, it will be provided with connectivity to Supercomputer Network of Novosibirsk Scientific Center (NSC/SCN) [42] via the dedicated 10 Gbps optical network which is in production since 2009. In a more distant future BINP may be getting direct access to the remote scientific networks such as Geant3 (GN3) [43] and international GRID systems such as WLCG [44] by means of the dedicated 1 Gbps optical links which would significantly enrich the list of data processing scenarios available for the CTF experiment and increase the peak amount of computing power available for BINP significantly.

If the capacity of external network links available to BINP is sufficient, the following extensions of the detector experiment network and computing design described earlier in Section 3.11.3.1 might be taken into consideration:

1. building an additional tape storage system on the geographically remote site in order to store a full copy of RAW data aggregated while doing experiments with the detector thus reducing the risks of data loss due to a catastrophic event on one of the sites,
2. building a geographically distributed group of computing sites merged into a single data processing entity by means of GRID technology or using the capacity of the existing regional and worldwide GRID infrastructure.

Use of the resources provided by the commercial cloud computing systems such as Amazon EC2 [45] for the purposes of the data processing and experimental events simulation for the CTF experiment is not considered as an option, at least at the present moment, as the prices for the resources offered by the commercial cloud systems remain at the level which makes the ownership of the dedicated computing farm a more preferable solution in our case.

3.11.3.4 Prospected Architecture of the Software Execution Environment

The standard execution environment designed to support all types of software related to events reconstruction, detector simulation, monitoring and control of the detector subsystems and other tasks is proposed to be virtualized, in order to gain the following advantages which hardware virtualization technology provides:

1. high reliability and rapid recovery of the virtualized services,
2. low level isolation of different types of services from each other,
3. ability to reproduce freezing the configuration execution environment over the periods of time such as the entire lifetime of detector experiment,
4. natural way of supporting heterogeneous computing systems, including cloud computing enabled environments.

Scientific Linux [46] is proposed to be used as a standard OS for the detector experiment while XEN [47] or KVM [48] (both are non-commercial products) would be the most preferable choice for the standard virtualization platform to be deployed over the offline farm computing resources. The virtualized environment of the offline farm is intended to be supplied with the custom design high level control tools, implemented privately.

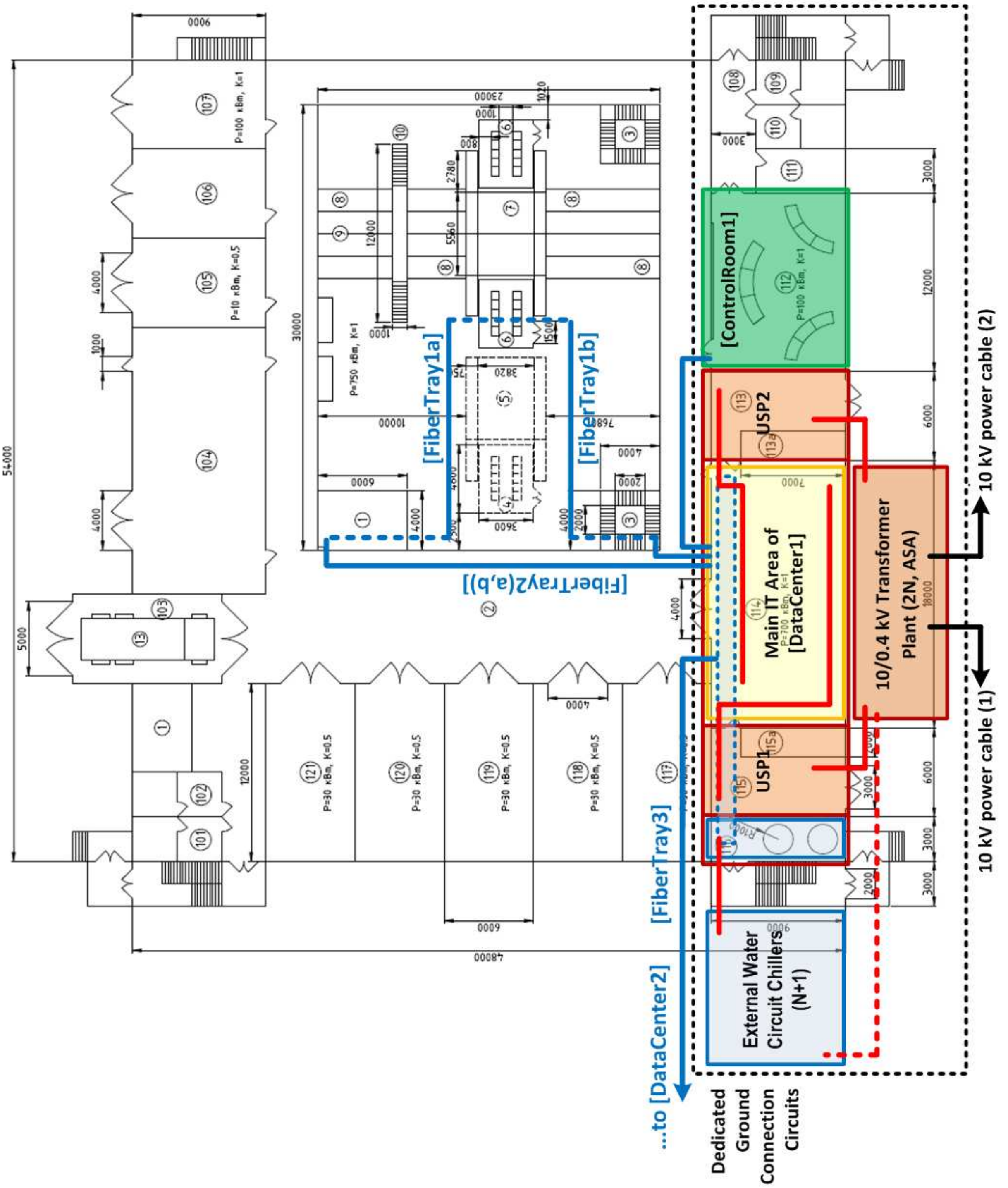

Figure 3.28: Location of the **[DataCenter1]** facility and its engineering infrastructure within the dedicated detector building. The main control room of the experiment **[ControlRoom1]** is also shown.

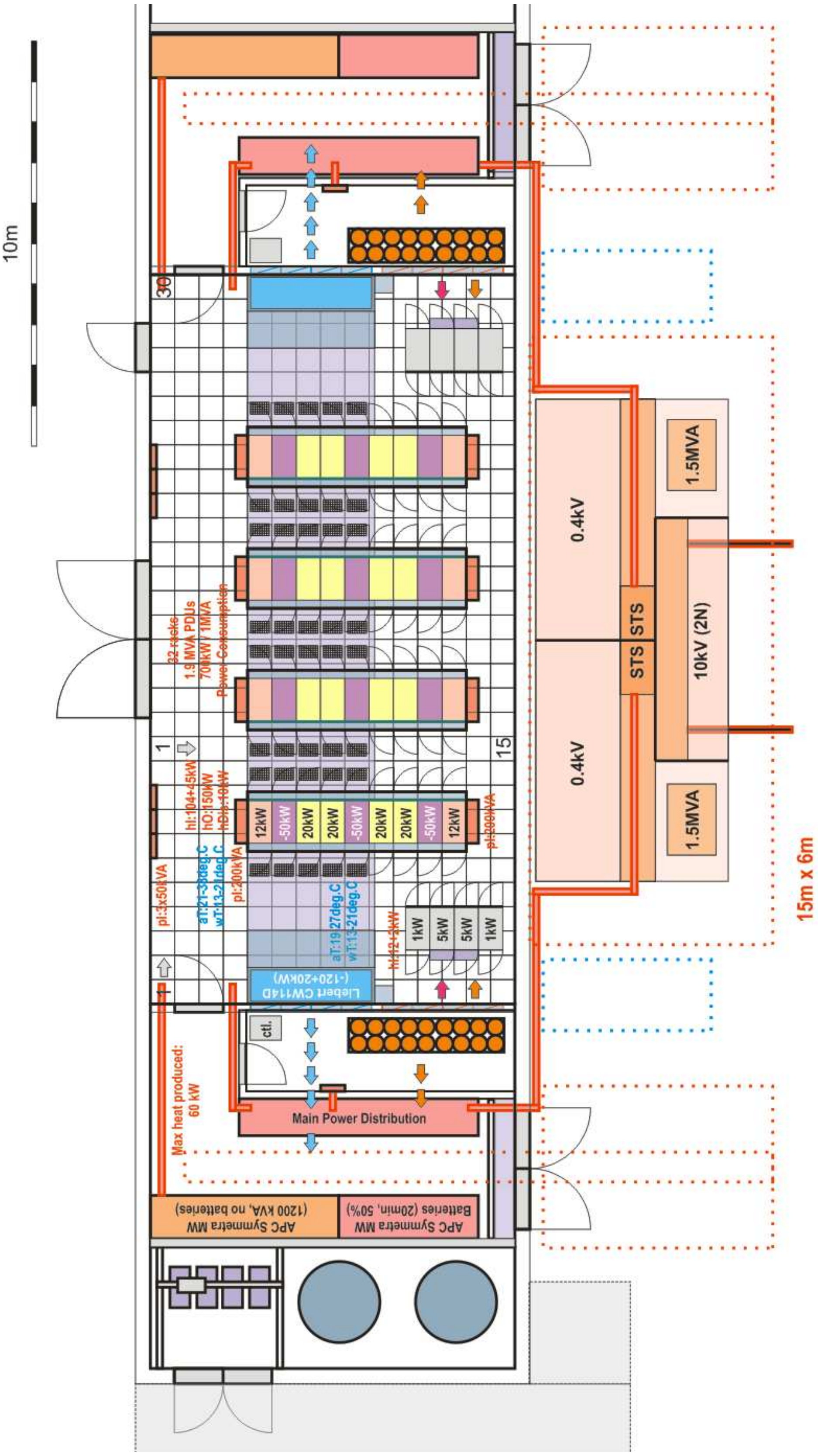

Figure 3.29: Closer look on the hardware installation layout of the **[DataCenter1]** facility (cooling and electrical power capacities indicated).

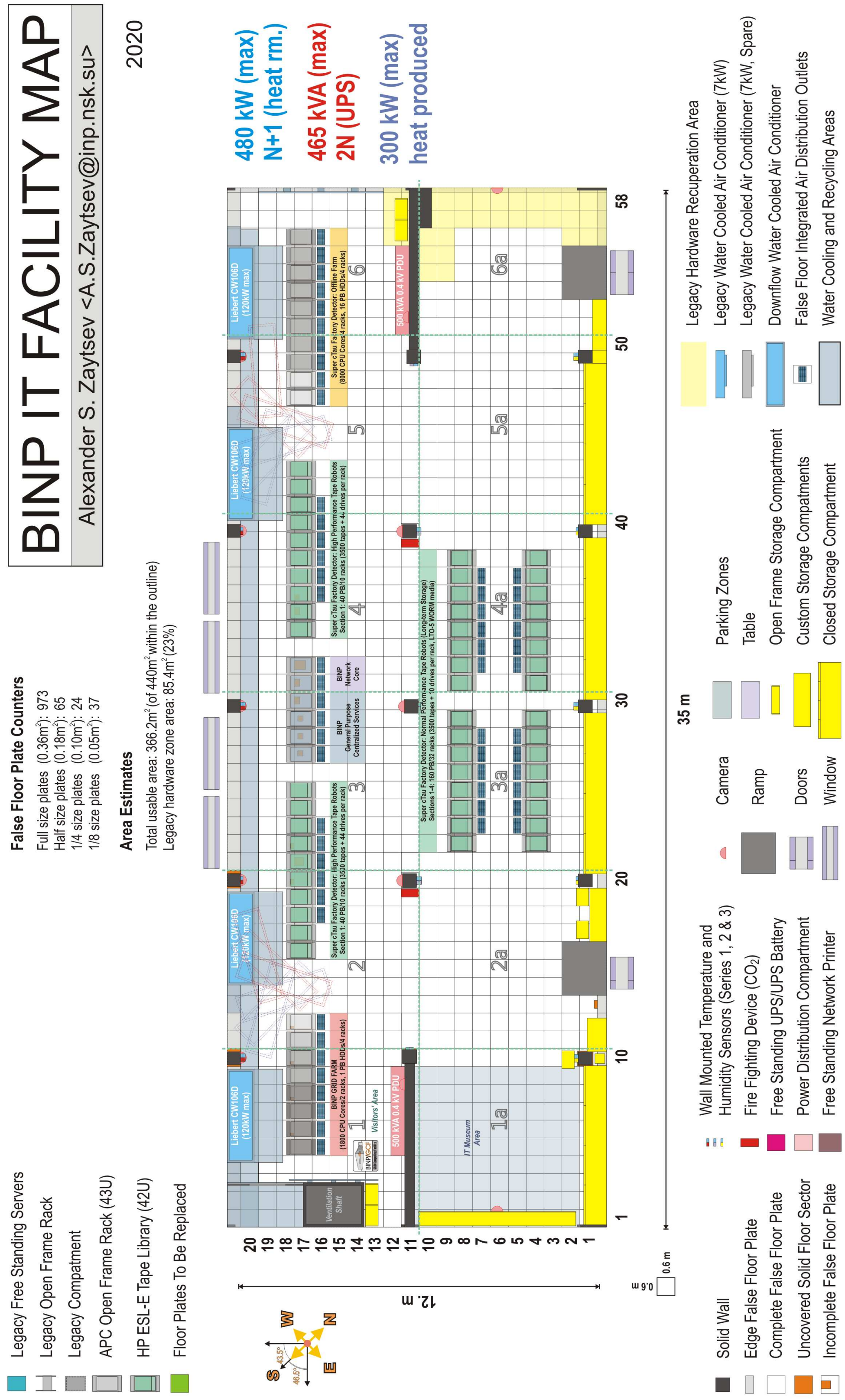

Figure 3.30: Prospected layout of the **[DataCenter2]** facility by 2020, assuming the major upgrade of its engineering infrastructure and deployment of all the equipment related to the detector.

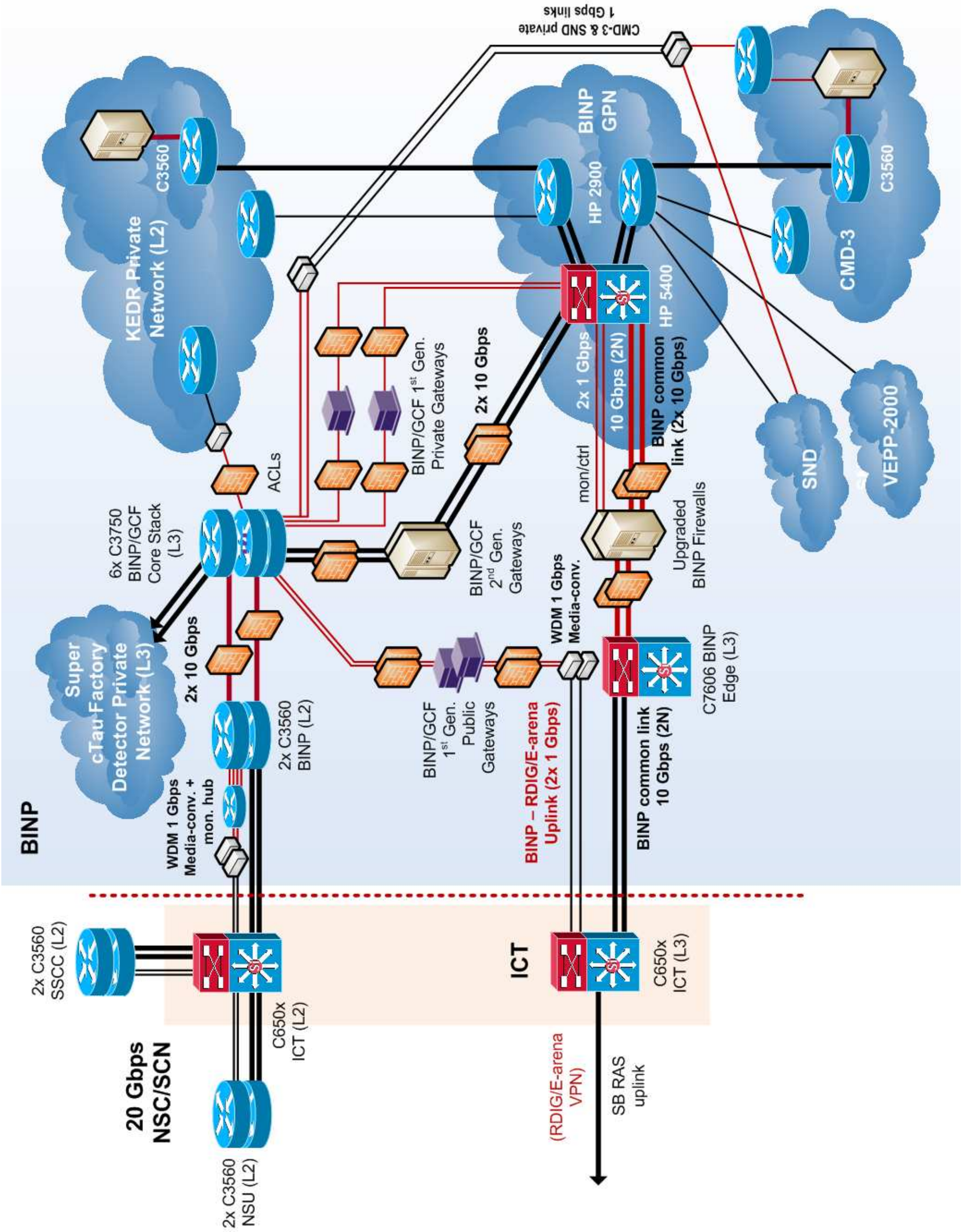

Figure 3.31: Prospected internal and external networking layout for all the HEP experiments carried out at BINP at early stages of building the networking and computing infrastructure for the CTF experiment.

Table 3.6: List of basic specifications for the **[DataCenter1,2]** computing facilities.

Feature	[DataCenter1]	[DataCenter2]
Total area (IT area), m^2	300 (160)	360 (220)
False floor load carrying capacity, ton/m^2	≤ 2	≤ 2
Number of racks (total rackmount capacity, 1U)	32 (1344)	76 (2432)
Maximum heat dissipation within a single rack, kW	20	12
Maximum heat dissipation within the IT area, kW	600	300
Maximum cooling capacity of the internal cooling circuit of the data center, kW (redundancy schema implemented)	800 (N+1)	480 (N+1)
Maximum cooling capacity of the external cooling circuit of the data center, kW (redundancy schema implemented)	1500 (N+1)	600 (N+1)
Time of running on the chilled water stored in the redundant water tanks of the internal cooling circuit of the data center, min	15	Unavailable
Maximum electrical power supported by the external power lines, kVA (redundancy scheme implemented)	1500 (2N)	500 (2N)
Maximum load supported by the centralized UPS system, kVA (redundancy scheme implemented)	1200 (2N)	465 (2N)
Centralized UPS capacity for 100% / 50% / 10% of nominal power consumption by the IT equipment, min	20 / 40 / 150	
Data center external connectivity, Gbps (redundancy scheme implemented for the external uplinks)	Unavailable	40 (2(2N))
Capacity of the internal communication lines between the [DataCenter1,2] facilities, Gbps (redundancy scheme implemented for the internal links)	960 (2N)	
Monitoring and maintenance services by the local personnel	365 × 24 × 7	

In case the offline data processing scheme for the detector is extended in order to include GRID computing technology support and the data processing within the geographically distributed environment, gLite middleware [52] should be considered as a preferable choice of the standard GRID middleware for the experiment.

3.11.4 Roadmap for Building the Offline Computing and Storage Systems

3.11.4.1 Hardware Commissioning Plan

As it was mentioned earlier in Section 3.11.2, the maximum trigger rate of the first level trigger (LLT) of the detector is equal to 0.5 MHz while the average experimental event size is estimated to be around 30 kB. The TDAQ and offline data processing systems of the detector are designed in such a way that the whole flux of data generated by the LLT could be saved on the storage systems of the offline farm for the long-term analysis. Thus the maximum output data rate of the detector TDAQ system is estimated to be 15 GBps = 120 Gbps (which is equivalent of 1.24 PB/day = 470 PB/year), so the maximum amount of data which could be generated by the TDAQ system over the 5 years of constant operation (assuming 100% efficiency) is equal to 2.4 EB.

If the period of running at maximum luminosity with the CTF experiment is going to be 2018–2023, then the optimal period for hardware deployment for the offline farm is estimated to be 2015–2017, and for the HDD and tape based storage systems — 2016–2021 (assuming linear growth of the amount of data aggregated on the detector storage systems with time). Therefore the detailed specifications for the hardware components needed for implementing networking and computing system of the detector is to be prepared first in 2014 and then reevaluated in 2017.

In order to estimate the amount of financial resources required for building and operating the solutions for the networking and computing systems of the detector experiment over the designated period of time, let us make the following assumptions taken as valid over the whole period of 2015–2021 for the cost estimates given below.

1. The optimal ratio of the total computing powers aggregated within the HLT trigger farm to the capacity of the HDD based storage system (both high performance and high capacity HDD based storage systems combined) available within the online and offline data processing farms is equal to 25 TFlops/PB and fixed over the whole period.
2. Ratio of capacities of the high performance tape storage system to all the HDD based storage systems within the detector TDAQ and offline data processing farm is equal to 4.0 and fixed.
3. Ratio of prices per unit of storage system capacity for high performance tape storage systems and HDD based storage systems is equal to 0.45 and fixed.

The computing infrastructure is prospected to go though the following stages in its deployment and operation over the lifetime of the detector experiment:

1. prototyping, testing and approval of the concepts implied by the design of the system plus engineering infrastructure deployment for the IT centers involved (2011–2014),
2. main deployment period of the IT and networking equipment (2015–2017),
3. production and scheduled maintenance period, devoted mainly to the experimental data taking, processing and archiving for future analysis (2018–2026).

Table 3.7: Cost estimation of the detector TDAQ and offline data processing IT infrastructure as a function of the beginning of the main deployment period in time, with cost of engineering infrastructure of detector computing facilities taken into account and the total cost of ownership (TCO) excluded.

Deployment period							
Beginning	2013.5	2014	2014.5	**2015**	2015.5	2016	2016.5
End	2015.5	2016	2016.5	**2017**	2017.5	2018	2018.5
SUM, MEuro	**15.9**	**14.3**	**12.8**	**11.6**	**10.6**	**9.8**	**8.9**

The total cost of the detector experiment computing system and its engineering infrastructure consisting of

- computing nodes with 0.5 PFlops of combined performance (to be deployed in 2013–2017),
- high performance HDD based storage system for the offline data processing farm and TDAQ with total capacity of 20 PB (to be deployed in 2013–2017 as well),
- high performance tape storage with total capacity of 80 PB (to be deployed in 2015–2021),

is estimated to be approximately 12 MEuro and its combined heat dissipation in the final configuration is to be up to 0.95 MW. An ambiguity of these values is assumed to be no better than 15–20%.

Once the high performance tape storage systems is filled up to 70–80% of its capacity (presumably by 2018–2020) the deployment of the second stage (high capacity) tape storage system on the IT area of **[DataCenter2]** facility is to be done, thus increasing the tape storage capacity available for the experiment by 160 PB (by the end of deployment period in 2026). The cost estimation for this particular subsystem is not evaluated yet.

Table 3.7 shows how the total cost estimation varies as the beginning of the main deployment period is shifted in time within the range of 3 years around the prospected optimal value (2015) reflecting the anticipated advances in the underlying computer hardware and the tape storage technology over the next 15 years.

Building the offline farm and the data storage system in such a configuration would make it possible to store 3% of maximum integral data flow generated by the detector's LLT over the 5 years (2.4 EB) in the average. In this case the average trigger rate is going to be around 20 kHz which delivers approximately $3 \cdot 10^{12}$ experimental events over the 5 years at maximum designed TDAQ system data aggregation rate.

3.11.4.2 Building the Prototypes for the Key Components of Data Processing and Storage Systems

Validation of the solutions proposed above for various components of networking and computing infrastructure of the detector experiment is to be done via building and testing the prototypes for each and every critical part of the infrastructure.

A list of the components which are to be evaluated by building the prototypes is given below.

1. HDD/SSD-based high performance storage systems:
    (a) fault-tolerant data storage systems based on redundant groups of RAID arrays,

    (b) distributed and parallel file systems (Lustre [49], PVFS2 [50], Hadoop [51], etc.),
    (c) multilevel I/O buffers for the storage system head nodes based on high performance SSD devices [33], [34].

2. Robotic tape libraries and tape media: studying the existing solutions for scalable modular robotic tape libraries [35]–[36].

3. High performance computing modules based on general purpose CPUs [28]–[30].

4. Hybrid computing architectures making use of GPU/FPGA based solutions [22]–[27], [31], [32]:
    (a) finding ways to maximize performance of EB and HLT subsystems (TDAQ),
    (b) studying feasibility of increasing performance of event reconstruction/simulation jobs running on the offline data processing farm.

5. Advanced networks:
    (a) 40/100 Gigabit Ethernet and IPoIB technologies,
    (b) Fiber Channel and FCoE technologies,
    (c) DWDM technology.

6. Radiation resistant optical fiber communication lines (Chapter 3.11.3.2).

7. Environmental control systems for industrial and IT applications, industrial process control systems:
    (a) groups of compact localized sensors similar to the solution [53],
    (b) distributed optical fiber based sensor systems with the readout performed from one of the endpoints, similar to the ones described in [54],
    (c) hybrid optical fiber based sensor systems supporting both distributed and localized information gathering along the path of the fiber, similar to those described in [55], [56].

Bibliography

[1] W. Lepeltier, "Review on TPC's," J. Phys.: Conf. Ser. 65 012001 (2007).

[2] W. Erni, I. Keshelashvili, B. Krusche *et al.*, "Physics Performance Report for PANDA," http://arxiv.org/abs/0903.3905v1 (2009).

[3] F. Sauli, Nucl. Instr. and Meth. A **386**, 531 (1997).

[4] M. Dixit *et al.*, "Micromegas TPC studies at high magnetic fields using the charge dispersion signal," Nucl. Instr. and Meth., A **581**, 254 (2007).

[5] Klaus Dehmelt for LP TPC Collaboration, "A large prototype of a time projection chamber for a linear collider detector," Nucl. Instr. and Meth. A, in press, 2010.

[6] B. Aubert *et al.* [BaBar Collaboration], Nucl. Instr. and Meth. A **479**, 1 (2002).

[7] C.O. Vuosalo, A.V. Telnov, K.T. Flood, BaBar Analysis Document #1853, 2010.

[8] A. Abashian *et al.*, Nucl. Instr. and Meth. A **491**, 69 (2002).

[9] N. Akopov *et al.*, Nucl. Instr. and Meth. A **479**, 511 (2002) [arXiv:physics/0104033].

[10] [LHC-b Collaboration], CERN-LHCC-2000-037, LHCb TDR 3, 7 September 2000.

[11] M. Buenerd [AMS RICH Collaboration], Nucl. Instr. and Meth. A **502**, 158 (2003) [arXiv:astro-ph/0211645].

[12] T. Iijima *et al.*, Nucl. Instr. and Meth. A **548**, 383 (2005),
S. Korpar *et al.*, Nucl. Instr. and Meth. A **553**, 64 (2005),
P. Krizan, S. Korpar, T. Iijima, Nucl. Instr. and Meth. A **565**, 457 (2006).

[13] A.Yu. Barnyakov *et al.*, "Focusing aerogel RICH (FARICH)," Nucl. Instr. and Meth. A **553**, 70 (2005).

[14] A.Yu. Barnyakov *et al.*, Nucl. Instr. and Meth. A **595**, 100 (2008).

[15] G. Bondarenko, B. Dolgoshein, V. Golovin, A. Ilyin, R. Klanner, E. Popova, Proc. of the 5th Int. Conf. on Advanced Technology and Particle Physics, Nucl. Phys. B — Proc.Suppl. **61** (1998) 3 pp. 347.
G. Bondarenko *et al.*, Nucl. Instr. and Meth. A **442**, 187 (2000).
Z. Sadygov *et al.*, Nucl. Instr. and Meth. A **504**, 301 (2003).

[16] J. Benitez *et al.*, Nucl. Instr. and Meth. A **595**, 104 (2008).

[17] A. Abashian *et al.* [Belle Collaboration], Nucl. Instr. and Meth. A **479**, 117 (2002).

[18] Y. Yusa, Nucl. Instr. and Meth. A **598**, 183 (2009).

[19] V. Smakhtin *et al.*, Nucl. Instr. and Meth. A **598**, 196 (2009).

[20] MINIOS collaboration, TDR on scintillator, ch.5, http://www-numi.fnal.gov/minwork/info/tdr/mintdr_5.pdf

[21] V.M. Aulchenko *et al.*, Nucl. Inst. and Meth. A **265**, 137 (1988).

[22] NVidia Fermi Architecture: http://www.nvidia.ru/object/fermi_architecture_ru.html

[23] Xilinx 7th series FPGA Products: http://www.xilinx.com/technology/roadmap/7-series-fpgas.htm

[24] Convey Hybrid Computing Platform:
http://www.conveycomputer.com/products.html

[25] Convey HC-1 Family Products:
http://www.conveycomputer.com/Resources/Convey_HC1_Family.pdf

[26] Nallatech PCI Express Cards: http://www.nallatech.com/pci-express-cards.html

[27] AMD Fusion Family of APUs: http://sites.amd.com/us/fusion/APU/Pages/fusion.aspx

[28] Intel Product Roadmap: http://download.intel.com/products/roadmap/roadmap.pdf

[29] List of Intel Microprocessors: http://en.wikipedia.org/wiki/List_of_Intel_microprocessors

[30] List of AMD Microprocessors: http://en.wikipedia.org/wiki/List_of_AMD_microprocessors

[31] SKIF-4 Supercomputer Platform: http://skif.pereslavl.ru/psi-info/rcms-skif/index.en.html

[32] SKIF-4 Architecture: http://skif.pereslavl.ru/psi-info/rcms-skif/skif-ppt.rus/2009/2009-04-01-pavt2009.ppt

[33] FusionIO ioDRIVE DUO Products: http://www.fusionio.com/products/iodriveduo/

[34] FusionIO ioXTREME Products: http://www.fusionio.com/products/ioxtreme/

[35] HP StorageWorks ESL E-series Products:
http://h10010.www1.hp.com/wwpc/ru/ru/sm/WF25a/12169-304612-304631-304631-304631-392031.html

[36] Fujitsu Scalar 10K Series Modular Tape Libraries:
http://ts.fujitsu.com/products/storage/tape/scalar/scalar_10k.html
https://globalsp.ts.fujitsu.com/dmsp/docs/ds_scalar10k.pdf

[37] http://www.optolink.ru/ru/catalog/p5/

[38] http://www.optolink.ru/pdf/fiber_ru.pdf

[39] http://www.optolink.ru/pdf/RSF.pdf

[40] http://fotonexpress.ru/pdf/st/004-010.pdf

[41] http://fotonexpress.ru/pdf/st/011-019.pdf

[42] A. Zaytsev et al., “Building a High Performance Computing Infrastructure for Novosibirsk Scientific Center” (contribution presented at CHEP2010 conference: 18-22/10/2010, Taipei, Taiwan): http://indico2.twgrid.org/MaKaC/materialDisplay.py?contribId=29&sessionId=110&materialId=slides&confId=3

[43] Geant3 Network (GN3): http://www.geant.net

[44] WLCG Project: http://cern.ch/lcg

[45] Amazon Elastic Compute Cloud (EC2): http://amazon.com/ec2/

[46] https://www.scientificlinux.org

[47] http://www.xen.org

[48] http://www.linux-kvm.org

[49] http://www.lustre.org

[50] http://www.pvfs.org

[51] http://hadoop.apache.org

[52] gLite Middleware: http://cern.ch/glite

[53] APC NetBotz Sensors: http://www.apc.com/products/family/index.cfm?id=400

[54] “Optical Fibre based Distributed Sensor for Temperature Measurement” http://www.igcar.ernet.in/benchmark/Tech/19-tech.pdf

[55] F. Rodríguez-Barrios et al., “Distributed Brillouin Fiber Sensor Assisted by First-Order Raman Amplification”: http://infoscience.epfl.ch/record/150155/files/JLT_28_2162_2010_1st

[56] L. Zou et al., “Distributed fiber Brillouin strain and temperature sensor with centimeter spatial resolution by coherent probe-pump technique”: http://net04.isis.umanitoba.ca/activeshm/ReferencePage/Reference/Bao/spie5855_zou_a.pdf

[57] S. Kolos et al., “Online Remote Monitoring Facilities for the ATLAS Experiment” (contribution presented at CHEP2010 conference: 18-22/10/2010, Taipei, Taiwan): http://indico2.twgrid.org/MaKaC/materialDisplay.py?contribId=174&sessionId=51&materialId=slides&confId=3

Chapter 4

Accelerator

4.1 Crab waist collision method

When two flat beams collide, a small vertical beta function β_y at the IP is one of the major conditions for high luminosity. However, due to the divergence of the beam, β_y is limited by the longitudinal size of the particle bunch σ_z (so-called *hour-glass* effect), which can not be made very small because of the growth of the collective effects. The electron bunch length achieved by now for characteristic beam currents of 1÷2 A is ~6÷10 mm, which limits the minimum vertical beta function at the IP and consequently the luminosity of the traditional electron-positron colliders.

This problem can be solved with the recently proposed Crab Waist scheme for collision of two bunches, which can significantly (up to two orders of magnitude) increase the luminosity of e+e- colliders without reducing the bunch length or increasing its intensity [1].The new approach involves two basic ideas.

The first idea is to arrange a collision of two beams at an angle in the horizontal plane θ so that the so-called Piwinski parameter

$$\phi = \frac{\sigma_z}{\sigma_x}\tan\frac{\theta}{2} \approx \frac{\sigma_z}{\sigma_x}\frac{\theta}{2} \tag{4.1.1}$$

be large enough, where σ_z is the bunch length and σ_x is its rms size in the transverse direction. The schematic of such a collision is shown in Fig. 4.1.1.

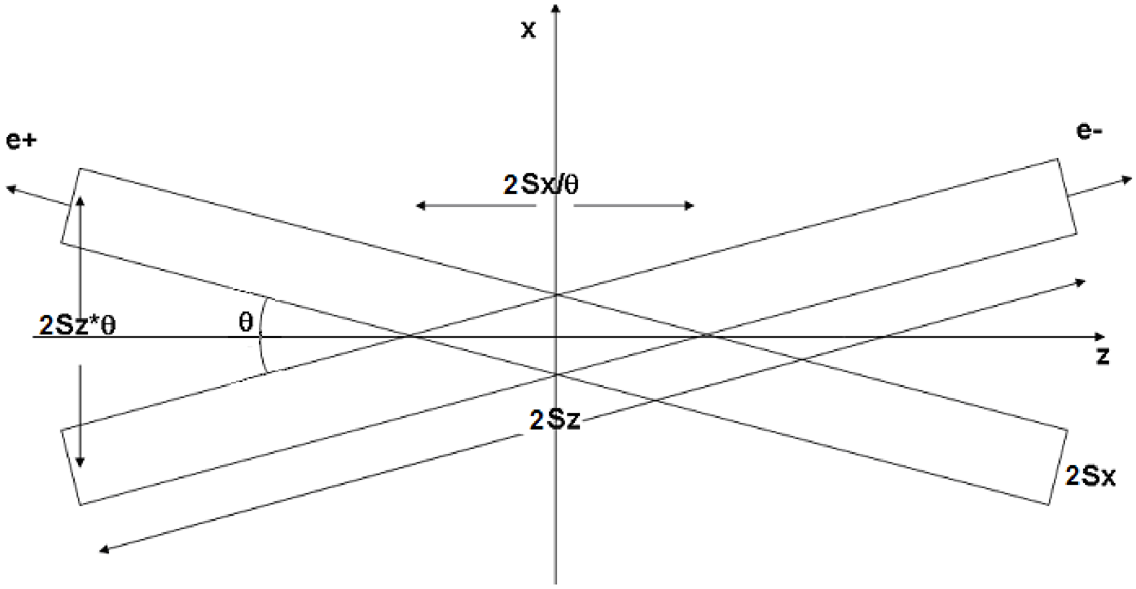

Fig.4.1.1 Beam collision with a large Piwinski parameter

One can see from Fig.4.1.1 that now the vertical betatron function is limited not by the bunch length σ_z but by the size of the beam interaction region: $\beta_y \approx \sigma_x / 2\theta$; and if the transverse beam size σ_x is small, the vertical betatron function can also be made very small.

In the general case, the luminosity and the parameters of the space charge can be written as [2]

$$L \propto \frac{N\,\xi_y}{\beta_y}, \qquad \xi_y \propto \frac{N\,\beta_y}{\sigma_x \sigma_y \sqrt{1+\phi^2}} \quad \text{и} \quad \xi_x \propto \frac{N}{\varepsilon_x\,(1+\phi^2)}. \tag{4.1.2}$$

From these formulas we can see that at $\phi=0$ we cannot increase the luminosity through reducing the vertical beta function (the *hour-glass* limitations) or increasing the number of particles per bunch N (restrictions on the collision parameter $\xi_y \sim 0.1$). If $\phi >> 1$, first, the region of beam interaction (and thus β_y) may become very small (fractions of millimeter), and the reduction in the beam size is compensated with a large ϕ so that the ξ_y value remains in the required limits. Moreover, the horizontal parameter of the space charge ξ_x, decreases as ϕ^{-1}, which is also a positive factor.

Note that luminosity expression (4.2) looks the same as for a head-on collision of beams, and the dependence on the intersection angle enters only the parameters of the space charge. Fig. 4.1.2 depicts beam collision at a small Piwinski angle and a large one.

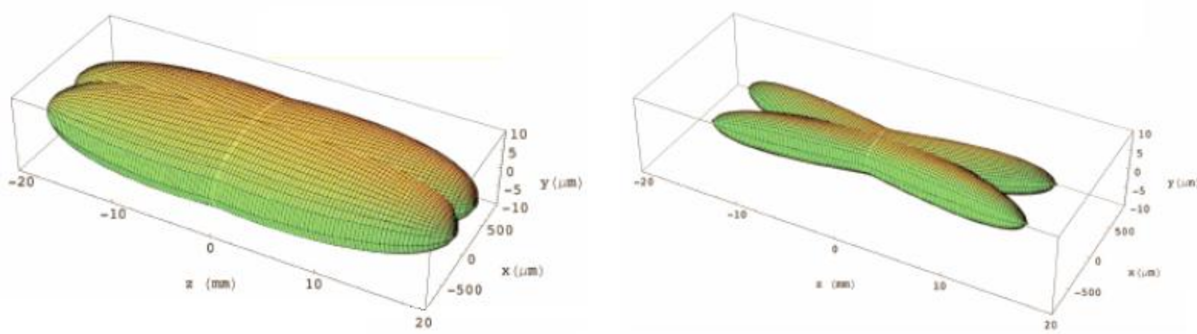

Fig. 4.1.2 Beams colliding with a small (left) and large Piwinski parameter. For the sake of clarity the transverse scale was increased much as compared with the longitudinal one.

At a CW collision, the increase in the Piwinski parameter occurs due to the increase in the angle of intersection and the reduction in the transverse beam size. Therefore, it is clear that for this approach, unlike the traditional facilities for colliding beams, the horizontal emittance must be small, which allows applying the well-developed methods of designing low-emittance synchrotron radiation sources.

Let us estimate the characteristics of a collider with energy E = 2 GeV and a circumference of about 800 m, which is determined by the convenience of the setup accommodation in the BINP area. Let the beam intersect at the angle 2θ = 60 mrad, then a luminosity of 10^{35} cm^{-2}s^{-1} requires parameters as listed in Table 4.1.1

Table 4.1.1 Beam parameters

Beam current, I	A	1.7
Number of particles in the beam, N		2.7×10^{13}
Number of bunches, n_B		390
Bunch current, I_b	mA	4.4
Bunch length, σ_z	mm	10
Emittance, $\varepsilon_x/\varepsilon_y$	nm-rad	8 / 0.04
β at the IP, β_x^*/β_y^*	mm	40/0.8
Beam size at the IP, σ_x/σ_y	μm	17.9/0.179
Piwinski parameter, Φ		15.1

Space charge parameter, ξ_x/ξ_y		0.0044/0.13
Luminosity, L	cm^{-2}s^{-1}	1.0×10^{35}

It should be mentioned that none of the parameters listed in the table limits (in the technical sense) the creation of the facility. Such (and even higher) currents were obtained at the B-factories (KEK and SLAC) and the F-factory (Frascati); such emittances have long been common for the modern synchrotron radiation sources, and a bunch length of ~ 6 ÷ 10 mm has been achieved at both colliding beam facilities and SR sources.

Various authors have long considered the problem of beam collision at an angle and shown (e.g. [3, 4]) that in such a scheme modulation of the vertical motion by horizontal betatron oscillations leads to a large (as compared with a frontal collision) number of coupled resonances which impede the realization of the above advantages. To solve this problem and correct the betatron coupling, the Crab Waist transformation of beam at the IP (Fig.4.1.3) was suggested.

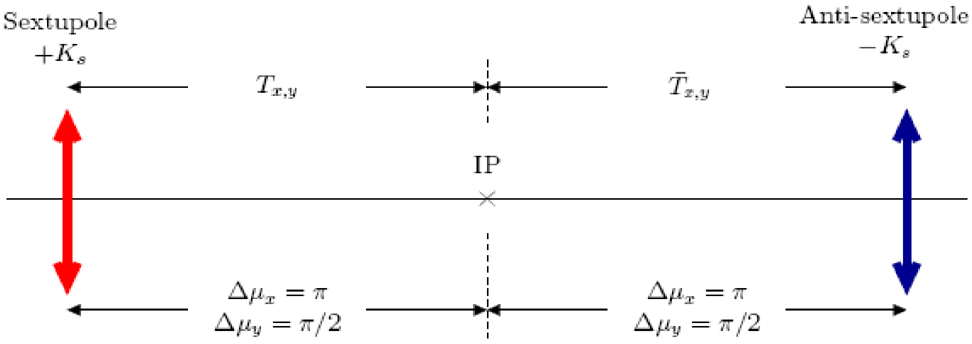

Fig. 4.1.3 Schematic arrangement of the CW sextupole magnets

For this purpose, two sextupole magnets are placed from two sides of the IP. The transformation of the vertical coordinate and the pulse through the first (along the beam) "thin" sextupole magnet with the integrated strength (ml)

$$y = y_0\,, \qquad y' = y'_0 + (ml)\cdot x_0 y_0$$

can be formally considered as vertical focusing of the beam with the focal length depending on the horizontal coordinate:

$$y' = y'_0 + K(x_0)\cdot l\cdot y_0\,, \quad \text{где} \quad K(x_0) = m\cdot x_0\,.$$

Then the position of the minimum of the vertical betatron function varies depending on the horizontal coordinate of the particle. In other words, the minimum of the vertical betatron function (waist) rotates as in Fig.4.1.4.

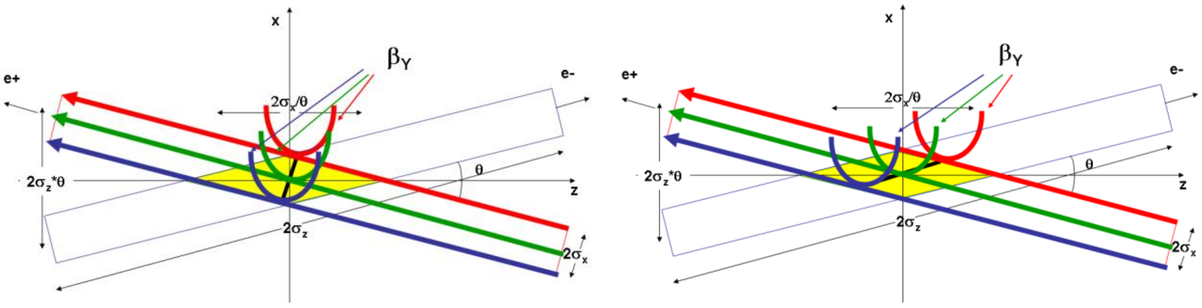

Fig. 4.1.4 Position of the minimum of the vertical betatron function before (left) and after (right) the CW transformation.

At a certain betatron phase advance between the CW sextupoles and the IP ($\Delta\mu_x = n \cdot \pi$, $\Delta\mu_y = (2m+1) \cdot \pi / 2$, where n and m are integers) and a certain integral strength of the lens

$$(m \cdot l) = \frac{1}{2\theta} \frac{1}{\beta_y^* \beta_y} \sqrt{\frac{\beta_x^*}{\beta_x}}, \tag{4.1.3}$$

where β^* and β denote the beta-function at the IP and in the azimuth of the "crab" sextupole, correspondingly, the minimum of the vertical betatron function rotates so that the dependence of the vertical betatron phase at the IP on the horizontal coordinate of the test particle gets suppressed, which efficiently kills both the betatron coupling resonances and their synchrobetatron satellites.

Fig.4.1.5 shows a luminosity scan in dependence on the position of the nonperturbed betatron tune for the case when the "crab" transformation is off (right) or on (left). One can see that in the latter case many coupling resonances are killed and the "good" luminosity region is much bigger.

The Crab Waist concept of collision was experimentally verified at the Φ-factory DAΦNE in Italy [5]. Through relatively small modifications, the beams were made to collide at a large Piwinski angle, and sextupole magnets were placed around the IP to provide the CW map. However, it was impossible to obtain a small vertical betatron function, because of the insufficient flexibility of the ring lattice. Nevertheless, the suppression of the collision effects due to the "crabbing" of the vertical beta waist alone increased the luminosity ~ 3 times as compared with the best results of the previous collider configuration (the green dots in Fig. 4.1.6 should be compared with the yellow and red ones). Turning the "crab" sextupoles off (the blue dots in the graph in Fig. 4.1.6) decreased the luminosity and made it impossible to work with large currents, because of the collision effects. The experiment clearly demonstrated the validity and potential of the Crab Waist collision concept.

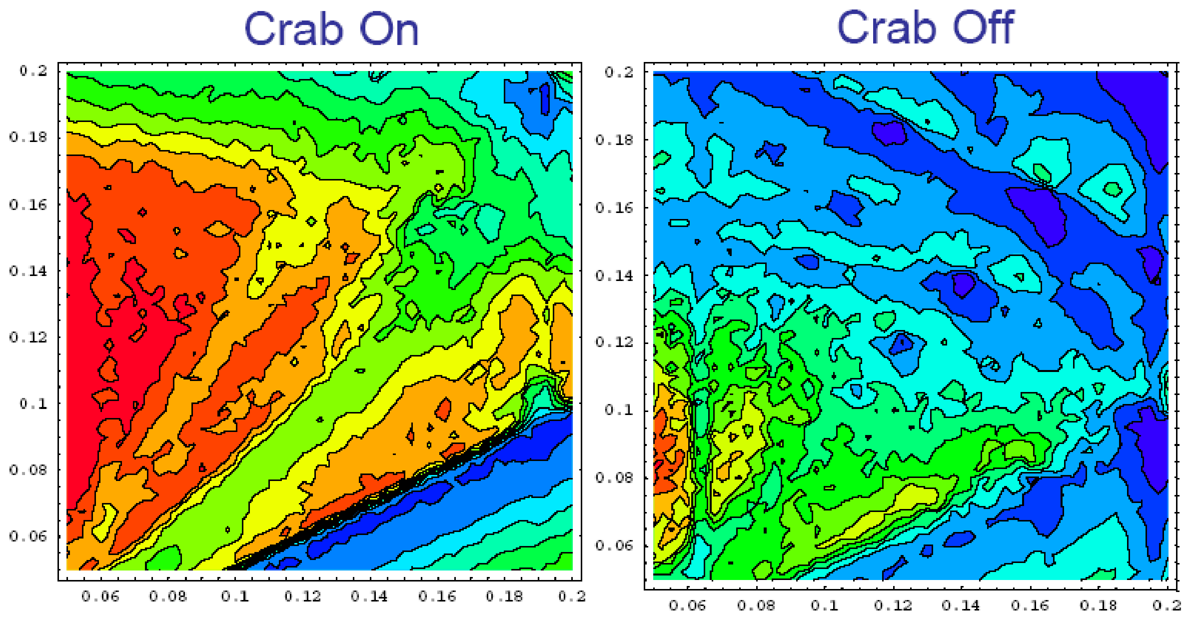

Fig. 4.1.5 Luminosity as a function of the working point of the betatron tunes (the horizontal and vertical axes correspond to the tune fractional part part). The red and blue colors show large and small luminosity.

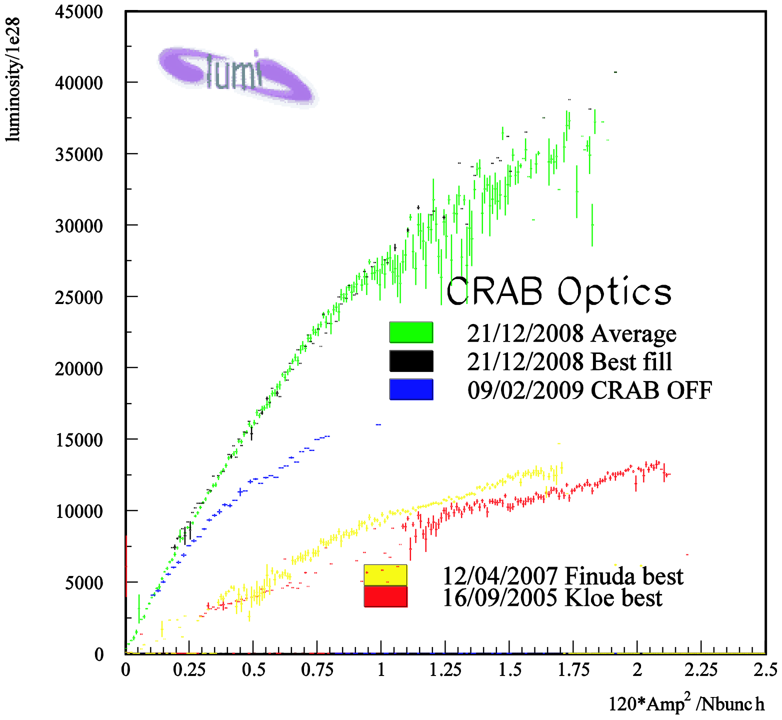

Fig. 4.1.6 Measured DAΦNE luminosity in peak in dependence on the colliding beam intensity. The red and yellow points indicate the best results in the previous configuration (without CW optics); the green and blue points are for the CW sextupoles on and off, correspondingly.

REFERENCES

1. P. Raimondi, Status of the SuperB Effort, presentation at the 2nd Workshop on Super B Factory, LNF-INFN, Frascati, March 2006
2. D. Shatilov and M. Zobov, ICFA Beam Dyn. Newslett. 37, 99 (2005)
3. D.V.Pestrikov, NIM Phys. Res., Sect. A 336, 427 (1993)
4. K. Ohmi et al., Phys. Rev. ST Accel. Beams 7, 104401 (2004)
5. M.Zobov (INFN LNF), for DAFNE Collaboration Team, DAFNE Operation Experience With Crab Waist Collision, arXiv:0810.2211v1

4.2 Collider parameters definition

There is one collision point in the collider, where, depending on the experimental program, one or two disposable detectors can be placed:

(1) An universal detector will operate throughout the energy range. The main luminosity integral will be gained at fixed points of 1.5 GeV (J/ψ-meson) to 2.5 GeV (charmed baryons) in the beam. At every such point, the collider collects statistics duirng a long time, and the luminosity must be maximum possible. The largest integral is estimated to be gained at the ψ(3770) point. Besides that, a few scannings over energy from 1 GeV to 2.5 GeV will be carried out.

(2) A detector with a dense polarized target. The high luminosity at the nucleon production threshold and the longitudinal polarization of electron beam make the *cτ*-factory the only possible source of polarized antinucleons. The experiment consists in the examination of the spin-dependent characteristics in the process of annihilation of nucleons and antinucleons. For this, the polarized target should to be placed as close to the place of particle production as possible. Unlike the universal detector, this architecture looks more compact and simple, including the simplification of the superconducting winding that forms the longitudinal field in the detector, which can be used to increase the luminosity at the expense of another final doublet with large aperture and another angle of beam collision.

So, the efficiency of the facility operation should be optimized for energies of 1.5 GeV to 2.5 GeV, the maximum efficiency (as to the luminosity, life time, operation time, etc.) reached at energy of 1.88 GeV, where a suppressing luminosity integral gain is predicted. This task is solved subject to the following considerations:

- High single-bunch luminosity, which is reached due to the application of the Crab Waist conception and the sub-millimeter vertical beta-function at the IP.
- The multi-bunch mode, which implies the application of the two-ring scheme.
- A high bunch charge at a small length (~10 mm).
- Efficient control of the damping parameters (emittance, damping time, etc.) to provide high luminosity over the entire energy range.
- The final focus that ensures obtaining an ultimately small beta-function at the beam IP; placement of the “crab” sextupoles; correction of the high chromaticity of the lenses of the final focus; etc.
- Provision of high-level longitudinal polarization of electron beam over the entire energy range.
- Continuous injection at the experimental energy with the positron current intensity providing achievement of high luminosity.

Luminosity. High luminosity in the single-bunch mode is achieved due to the Crab Waist scheme. The beam collision at a large Piwinski angle makes the interaction region significantly smaller than that at a frontal collision, when this region is equal to the length of the bunch. Thus, with no fear of the *hour-glass* effect, we can reduce the vertical beta function at the IP. Another positive moment also worth noting is that there is no problem of parasitic IPs in the scheme with a large Piwinski angle as the beams are moved several transverse dimensions apart already at the distance of the bunch length.

The ultimate value of the collision parameter ξ_y when the CW technology is applied is 2 to 3 times higher than at a head-on collision of beams. This is achieved due to the two “crab” sextupoles placed near the IP so that they do not perturb motion over the entire ring and rotate the vertical size at the IP in dependence on the transversal coordinate. Thus, the phase modulation induced by the beam-beam effects is suppressed as well as the betatron and synchrobetatron coupling resonances.

The maximum ξ_y value depends on the time of betatron oscillation damping in the storage ring, τ_x. Analysis of the parameters of electron-positron colliders shows that the ξ_y parameter is inversely proportional to the cube root of the damping time. Simulation of the beam-beam (BB) effects suggests that for $\xi_y \approx 0.15$ the damping time should be ~ 30 ms. To maintain a high ξ_y value throughout the energy range it is necessary to keep the damping time constant.

On the one hand, when the energy decreases, the luminosity will decrease proportionally to the energy itself. On the other hand, the influence of the BB effects will increase, which is expressed as the dependence of the ξ_y parameter on the energy. Exceeding the maximum ξ_y value leads to a decrease in the lifetime of the beam. Accordingly, to maintain a high luminosity it is necessary to compensate the energy change with other values entering ξ_y. The angle of beam intersection as well as the horizontal and vertical beta functions at the IP depends on the design of the final focus. So, it would be better to keep these values constant as the energy varies. It is proposed to optimize the luminosity via changing the bunch length: when the energy decreases, the bunch length increases, the maximum ξ_y value remains constant, while the luminosity decreases linearly. Increasing the bunch length is useful for reducing the role of collective effects and intra-bunch scattering.

The final focus design. Compact superconducting two-aperture magnets are planned to be used as the final doublet of quadrupole lenses. The distance from the IP to the cut of the yoke of the first (defocusing) quad is 60 cm and the gradient is 10.7 kG/cm. The application of two-aperture magnets allows passing beams along the magnet axis, reducing the unwanted background load of the detector from the synchrotron radiation. An additional complication of the final focus system is associated with the need to compensate the longitudinal field of the detector, which leads to the transversal rotation of the beams and introduces the betatron coupling.

Damping time and beam emittance. The phase-space volume and the damping time should remain constant throughout the energy range.

$$\alpha_x = \tau_x^{-1} = C_\alpha E^3 \frac{I_2}{\Pi}, \tag{4.2.1}$$

where C_α = 2115.1 m^2/GeV^3/s, Π is the storage ring circumference, I_2 is the second radiation integral (it is taken that the dimensionless damping decrement $J_x = 1$), which includes the contribution from the magnetic structure of the ring, I_{20}, and the wigglers, i_2:

$$I_2 = I_{20} + i_2, \qquad i_2 = \frac{1}{2} h_w^2 L_w, \tag{4.2.2}$$

where $h_w = B_w/BR$, B_w is the maximum field in the wiggler, BR is the magnetic rigidity, $L_w = \lambda_w N_w$ is the total length of the wiggler, λ_w is the field period, N_w is the number of periods. In order to keep the damping time constant throughout the energy range, there are superconducting wigglers mounted in the magnetic structure of the storage ring, which allows efficiently tuning the integral I_2.

Note that the energy loss by radiation per turn is unambiguously associated with the damping time:

$$U_0 = C_\alpha \gamma^2 \frac{\Pi}{\tau_x}.$$

A decrease in the damping time will lead to an increase in the power of the energy loss by radiation, which should be compensated by the accelerating RF system:

$$P = U_0 I,$$

where I is the total beam current.

Besides, the superconductive snakes allow monitoring the horizontal phase-space volume (I_{50} and i_5 denote the contribution from the storage ring and the snakes, correspondingly):

$$\varepsilon_x = C_q \frac{\gamma^2}{J_x}\frac{I_5}{I_2}, \qquad I_5 = I_{50} + i_5, \qquad i_5 = \frac{1}{15\pi^3} h_w^5 \lambda_w^2 L_w \left(\bar{\beta}_x + \frac{20\pi^2 \eta_0^2}{\bar{\beta}_x h_w^2 \lambda_w^2} \right), \tag{4.2.3}$$

where $\bar{\beta}_x$ is the horizontal beta function value averaged over the snake length; η_0 is the dispersion function at the center of the snake. The last expressions have been obtained for the sinusoidal model of snake. It is desirable to install the superconducting snakes in places with low beta function in order to minimize their influence on the beam.

Number of particles and bunch length. The maximum number of particles per bunch is determined by the *fast head-tail instability*. The threshold current of this effect is proportional to the bunch length and should be taken into account when choosing the latter. A large bunch charge distorts the potential well of the accelerating RF field and increases the bunch length. In addition, the microwave instability may lead to increase in the energy spread of the beam as well as in the bunch length. This effect has a threshold nature and it is efficient to work at beam current values below the threshold. Nevertheless, it is necessary to have a reserve in the accelerating voltage because the only way to overcome the bunch stretching due to the current is to reduce the bunch length at the zero current. The beam current and bunch length values for the *cτ*-factory are selected basing on the experience with the values already achieved at the present B-factories.

The number of bunches. The number of bunches (total current) depends on the power of the high-cost accelerating RF system. The number of bunches determines the system for suppression of multi-bunch instabilities. Suppressing the multi-turn ion instability in the electron ring requires a 5-10% gap in the bunch repetition. Fast ion instability may lead to increase in the vertical dimension of bunches at the end of the train. A vertical size increase can also occur in the positron ring as a result of the interaction with the electron clouds that are formed from the secondary particles near the beam axis. The point of the instability is proportional to the beam current and inversely proportional to the inter-bunch distance.

Loss of particles. Two effects leading to loss of particles dominate at the *cτ*-factory: the intrabeam scattering (Touschek effect) and the single bremsstrahlung, the latter being almost independent of the particle energy and determined by the single-bunch luminosity, which will fall with decreasing energy. Correspondingly, the loss due to the single bremsstrahlung will also fall. On the other hand, the Touschek loss will increase with decreasing beam energy. However, this dependence is not very strong, because the total phase-space volume increases with decreasing energy: the transverse emittance is preserved and the beam length increases.

Injection. To ensure a high integrated luminosity it is necessary to maintain an appropriate average current, for which the “continuous” injection mode is suggested. The choice of the injection frequency is determined by the efficiency of data recording (the ratio between the detector dead time and the background loading). The maximum frequency is determined by the repetition rate of the positron injection complex and equals 50 Hz. To reduce the dead time of the detector we suggest simultaneous injection of electrons and positrons, which requires their simultaneous acceleration in the linear accelerator with a shift of λ/2. Such a method has been implemented at KEKB.

Polarization. The longitudinal polarization of electron beam at the IP is one of the key issues of the *cτ*-factory. For this purpose a source of polarized electrons is allowed for in the design, at the exit from which one can get any spin direction and thus with all future rotations at the point of injection, the beam will have a correct spin direction. Two alternatives for obtaining the longitudinal polarization at the IP of the base ring were considered: (1) a scheme with polarization recovery, and (2) a scheme using the "Siberian snakes". In the first case, two spin rotators are used, which are located near the IP and perform spin rotation in a small region, the spin motion staying unperturbed over the rest of the ring. In this case, the spin rotators occupy a relatively small space and the integral of the longitudinal field is small, which is a positive moment in terms of the betatron coupling. A significant drawback of this scheme is the presence of (three) spin resonances in the working energy range, one of which falls on the point of τ-lepton production, and the other, on the Λ-baryon region. That is why the second scheme was chosen. However, to obtain a high degree of polarization throughout the energy range, there must be five or more Siberian snakes. To reduce the spin-orbit coupling the Siberian snakes must alternate with superconducting damping snakes. In this regard, the parameters under which the design luminosity is calculated are chosen for a relatively large (by modern standards) betatron coupling of 0.5%.

General arrangement of the setup. Subject to the above, the *cτ*-factory consists of the following facilities

- Injector of positrons
- Polarized electrons injector
- Full-energy linear pre-accelerator
- Double-ring collider

Two independent (electron and positron) injectors can effectively produce particles without losing time for changing the polarity of the magnets and implement a scheme of simultaneous acceleration of two bunches. The linear accelerator (unlike the synchrotron) allows accelerating the polarized particles without losing the degree of polarization as well as accelerating large charges of particles with smaller loss and higher frequency.

The main ring of the *cτ*-factory is a racetrack storage ring consisting of arcs, the technical straight section for injection and the experimental section (shown schematically in Fig. 4.2.1).

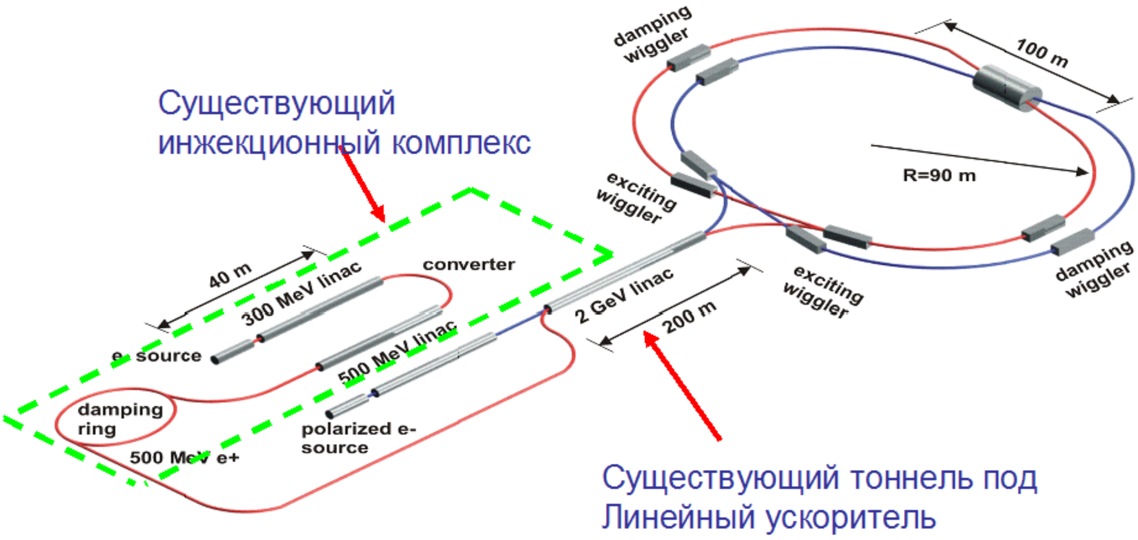

Fig. 4.2.1 Schematic of the complex

The arcs comprise four Siberian snakes alternating with four superconducting wigglers. The parameters of the arcs were chosen so as to obtain the required dimensions and the radiation parameters of the beam. The dipole magnet is selected subject to the requirement to the damping time. The optics of the periodicity elements must ensure the expected beam emittance. At 2.5

GeV the damping time should be 30 ms and the beam emittance should be 8 nm·rad with the wigglers turned off. The technical straight section accommodates the accelerating RF system, the fifth Siberian snake, and the injection equipment. In the midpoint of the technical straight section a vertical separation of the beams is arranged.

The experimental straight section is intended to focus the beams at the IP. The first quadrupole doublet is placed inside the detector. The lenses are to be superconducting and placed in one cryostat. The next lens system is designed to match the optical functions of the final doublet with the rest of the structure and correct the chromatic and geometric aberrations. The experimental straight section also comprises a system of collimators to reduce the halo of lost particles and improve the background situation for the detector. Since the energy loss per turn is rather large, it would be reasonable to place the energy calibration system near the IP, in one of the drifts.

The main parameters of the collider are presented in Table 4.2.1.

Table 4.2.1 Main parameters of the $c\tau$-factory

Energy	**1.0**	**1.5**	**2.0**	**2.5**	**GeV**
Circumfernce, Π	813.4				M
Revolution frequency, f_0	368.73				kHz
Revolution time, τ_0	2.712				μs
Orbit compaction factor, α	9.740	10.1		9.974	$\times10^{-4}$
Wiggler field, B_w	64	48	32	0	kGs
Accelerating voltage, V_{RF}	0.34	1.25	1.25	1.23	kV
Energy loss per turn, U_0	181	272	361	477	keV
Damping time, $\tau_x / \tau_z / \tau_s$	30/30/15				ms
Coupling factor, k	0.5				%
Horizontal emittance, ε_x	8				nm·rad
Vertical emittance, ε_y	40				πm·rad
Energy spread, σ_E	8.196	10.42	8.68	7.686	$\times10^{-4}$
Bunch length, σ_z	1.65	1.10	1.00	1.00	cm
Particles per bunch, N_0	$7.2\cdot10^{10}$				
Bunch current, I_0	4.24				mA
Number of bunches, N_b	390				
Total number of particles, N	$2.8\cdot10^{13}$				
Total current, I	1.65				A
Beta functions at the IP, β_x / β_y	4/0.08				cm
Beam size at the IP, σ_x / σ_y	17.9/0.18				μm
Intersection angle, 2θ	60				mrad
Piwinski angle, φ	26.91	18.50	16.82	16.82	
Hour-glass effect	0.906	0.906	0.906	0.906	
Collision parameter, ξ_y	0.15	0.15	0.12	0.10	
Single-bunch luminosity, L_0	1.56	2.33	2.57	2.57	$\times10^{32}$ cm^{-2}s^{-1}
Luminosity L	**0.61**	**0.91**	**1.00**	**1.00**	**$\times10^{35}$ cm^{-2}s^{-1}**

4.3 Magnetic lattice

4.3.1 General description

The magnetic lattice of the $c\tau$-factory is designed subject to the following main points:

- Provision of small beam emittance throughout the energy range (ε_x = 8 nm-rad, ε_y = 0.04 nm-rad).
- Ensuring high productivity of the collider at E = 1.0 – 2.5 GeV
- Optimization of the setup parameters is carried out in the region of the largest luminosity integral $E \approx 1.9$ GeV; the maximum luminosity at this energy must be 10^{35} cm^{-2}s^{-1} or more.
- The magnetic lattice shall allow placing the "crab" sextupoles in the azimuth with the required betatron phase advance.
- Ensuring high-degree longitudinal polarization of electron beam at the IP over the whole energy range.

To realize these conditions it is proposed to create the collider on the basis of two rings separated in the radial direction and having one main IP in the experimental section and a "parasitic" IP in the straight technical section (Fig. 4.3.1). The beams intersect in the radial direction in the technical section and are moved apart in the vertical direction by magnets that create a local orbit bump. This scheme of the rings allows accumulating sequences of large numbers of bunches and providing a total intersection angle of 60 mrad, which is required for the CW collision. For a luminosity of 10^{35} cm^{-2} s^{-1} the ring should accommodate 390 bunches with a total current of 1.65 A and a 10% gap in this sequence to prevent accumulation of ions in the electron beam potential. The facility perimeter required to accommodate the given number of bunches is about 813.4 m.

To obtain acceptable polarization throughout the energy range of the electron beam it is necessary to place five polarization insertiobs with superconducting solenoids in the ring with a bending angle between the devices of about 72º.

The implementation of the CW scheme with an angle of beam intersection at the main IP of 60 mrad imposes requirements on the beam emittance (ε_x = 8 nm-rad, ε_y = 0.04 nm-rad), which should not change throughout the energy range. Simulating the BB effects shows that ν_x = 0.54 and ν_y = 0.57 is the optimal choice for the operating point of the betatron tunes. The required damping time of transverse oscillations should not exceed 30 ms, and that of the longitudinal oscillations, 15 ms. To control the emittance and provide the necessary radiation damping, two inserts with superconducting damping wigglers are placed in each arcs of the collider. The systems of magnets and quadrupoles adjacent to the segment of the damping wigglers excite a dispersion function to correct the beam emittance.

The rings of the collider also contain matching sections to adjust the periodicity cells of the half-rings with the experimental section and the technical staright. The technical straight comprises the segment for moving the colliding beams apart.

A schematic view of the collider of the $c\tau$-factory is shown in Fig. 4.3.1. The collider lattice consists of two identical storage rings of the same circumference, which are spaced from each other in the horizontal plane. The rings are symmetrical with respect to the axis passing through the main and parasitic IPs. We can distinguish several functional sections in the electron and positron storage rings, denoted in Fig. 4.8 with the following numbers:

1. The IP, the detector and the superconducting lenses of the final focus that ensures the desired focusing of the beams at the IP. The building for assembling, maintaining and placing the detector systems is located over this site. The IP is in immediate adjacency to

the two long (70 m) collision segments, where the chromaticity correction sections and the "crab" sextupole lenses are located.

2. The technical section is intended to accommodate the injection system, the accelerating cavities and the beam separation drift. The building which will house the power supply system of the magnets, the RF generators, the control equipment, the power supplies for the vacuum pumps, the control room and other premises necessary for the functioning of the complex is planned to be built over the technical gap.
3. The big and small half-rings, consisting of the same elements but slightly differing in the length of the periodicity cell.
4. The spin rotators located uniformly over the angle of beam rotation in every ≈72^o and creating a longitudinally polarized electron beam at the IP with polarization sufficient for the experiments.
5. Four sections of the damping wigglers that ensure the required radiation parameters and control the emittance.
6. Four sections for matching the periodicity cells of the small and large half-rings with the experimental and technical sections; these sections also include the sections for zeroing the dispersion function.

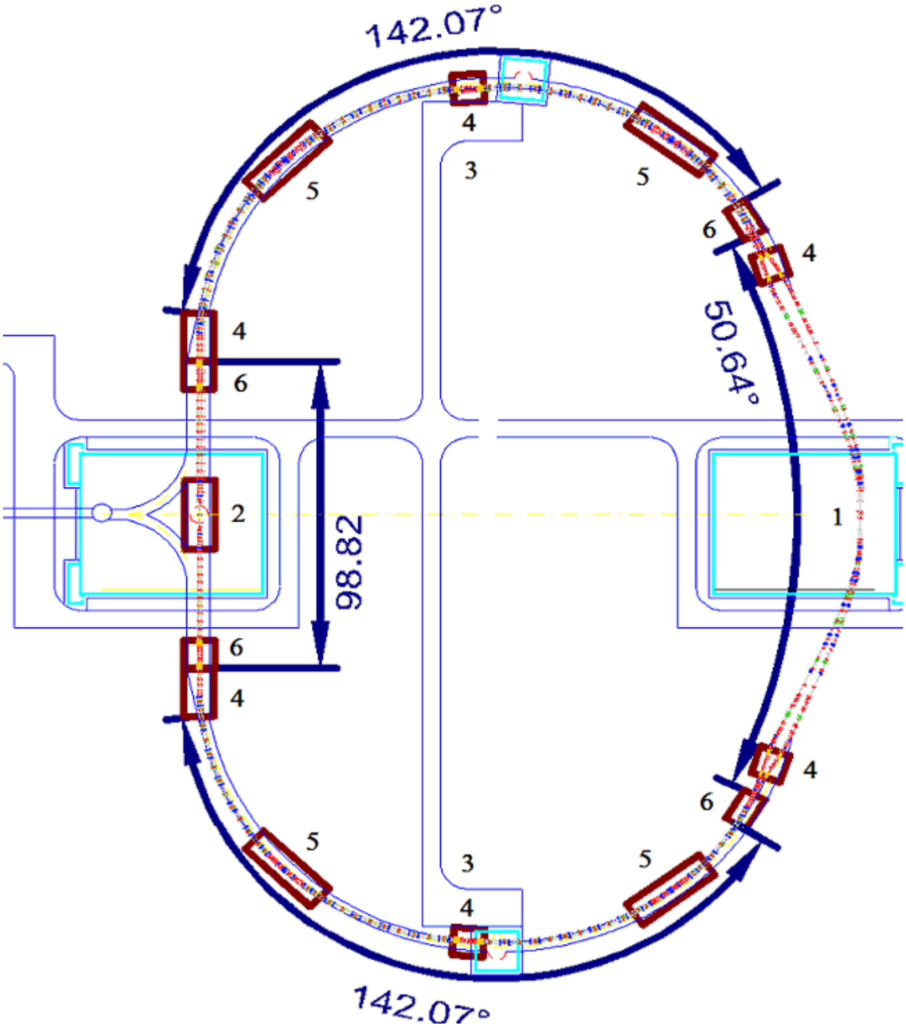

Fig. 4.3.1 Scheme of the collider of the cτ-factory. See the designations and explanations of the main components of the complex in the text.

4.3.2 Interaction region

Interaction region of $c\tau$-factory, which is a crucial issue for the collider, is designed to bring stored electron-positron beams into collision with luminosity of 10^{35} $\mathrm{cm}^{-2}\mathrm{sec}^{-1}$. In order to achieve that CW collision scheme is implemented, which requires cross-angle collision with high Piwinski parameter. The small values of the beta functions at the interaction point and distant final focus lenses are the reasons for high nonlinear chromaticity limiting energy acceptance of the whole ring. The present design allows correction of linear and nonlinear chromaticity of beta functions and of betatron tune advances, correction of second and third order geometrical aberrations from the strong sextupoles pairs, satisfies geometrical constraints, embraces realistic design of final focus quadrupoles and as close as possible positioning of crab sextupole to interaction point.

Having small beta functions generates high chromaticity in the final focus (FF) lenses, which at desired parameters is not linear. If it is not compensated locally, it limits energy acceptance of the collider leading to unacceptably small beam lifetime due to intra-beam scattering effect. Compensation of the FF system chromaticity is than performed by two pairs of sextupoles with $-I$ map in between to cancel geometrical aberrations.

The chosen solution works well for thin sextupoles, but consideration of real lengths sextupoles shows that only quadratic aberrations are cancelled, while higher order effects appear and deteriorate the dynamic aperture. Solution was found how to compensate these effects by additional sextupoles with strength lesser than 15% of the main ones.

Placement of sextupoles pairs in phase with corresponding quadrupole allows cancellation of the first order chromaticity of beta function and phase advance, the second and third order terms remain to be large and are the reasons for energy acceptance limitation. Introduction of octupoles and higher multipoles at places with high dispersion function does not allow compensation of the discussed terms. Therefore, introduction of additional sextupoles at places with high beta function chromaticity and linear dispersion function helps to solve the problem.

The size of the RF basket is $\Delta E/E \approx [1.0\%\text{-}1.5\%]$, in order to have satisfactory beam life time due to intrabeam scattering it is necessary to have energy acceptance of $\Delta E/E \geq 1.2\%$, introduction of insertions in the arcs (Siberian snakes, wigglers) decrease the energy acceptance, therefore the goal is to obtain energy acceptance about ± 2%.

The whole set of requirements to design of interaction region (IR) is summarized in the following list:

1. IR must provide small beta functions at IP
2. Chromaticity of FF doublet must be compensated locally
3. Geometrical aberrations from the strong sextupoles pairs must be cancelled in IR
4. Since accelerator is designed to operate at different energies there should be no longitudinal field integral over the FF lenses
5. Integral of the detector longitudinal field should be compensated before each final focus lens
6. The length of the IR must be less than 200 meters and IR geometry must comply with geometry of already dug tunnels
7. Crab sextupole should be placed as close as possible to IP and at the position with low chromaticity of beta functions and phase advances to minimize its influence on dynamic aperture
8. The band width should be about ±2%
9. The synchrotron radiation background should be minimized

Parameters of Super-$c\tau$-factory related to design of IR are presented in Table 4.3.1.

Table 4.3.1 Parameters of Super-ct-factory

Energy	GeV	2
Particles per bunch/bunches		$7 \cdot 10^{10}/390$
Beam current, *I*	A	1.65
β_x / β_z / σ_s	mm	40/0.8 /9
Emittance ε_x	nm·rad	8
Coupling $\varepsilon_y/\varepsilon_x$	%	0.5
Collision angle	mrad	60
Beam-beam tune shift ξ_y		0.12
IP beam size, σ_x/σ_y	μm	17.9/0.179
Piwinsky parameter	rad	16.8
Luminosity geometrical/hourglass	$cm^{-2}sec^{-1}$	$1.17/1.06 \cdot 10^{35}$

Obtaining small beta functions at IP requires placement of FF lenses as close to IP as possible. Since, detector solenoid coil envelops the FF doublet; the compensating solenoid is placed before the FF quadrupoles. Also, there is a solenoid covering both FF quadrupoles in order to screen the main detector field. The compensating solenoid and screening one provide uncoupled beam motion in the FF doublet.

The distance from IP to the first edge of FF quadrupole Q0 is 60 cm, and compensated solenoid with length of 20 cm is 40 cm away from IP. The next lens Q1 is 30 cm away from the first one. The distance is optimized to obtain maximum acceptance and minimum beta function in the lens. The FF quadrupole possess two apertures in order for incoming and out coming beams not to experience the bending field reducing the synchrotron radiation. The crossing angle is determined by the technical requirements of the FF lens design. Fig. 4.3.2 shows the placement of different elements around the IP and possible cones of detector opening.

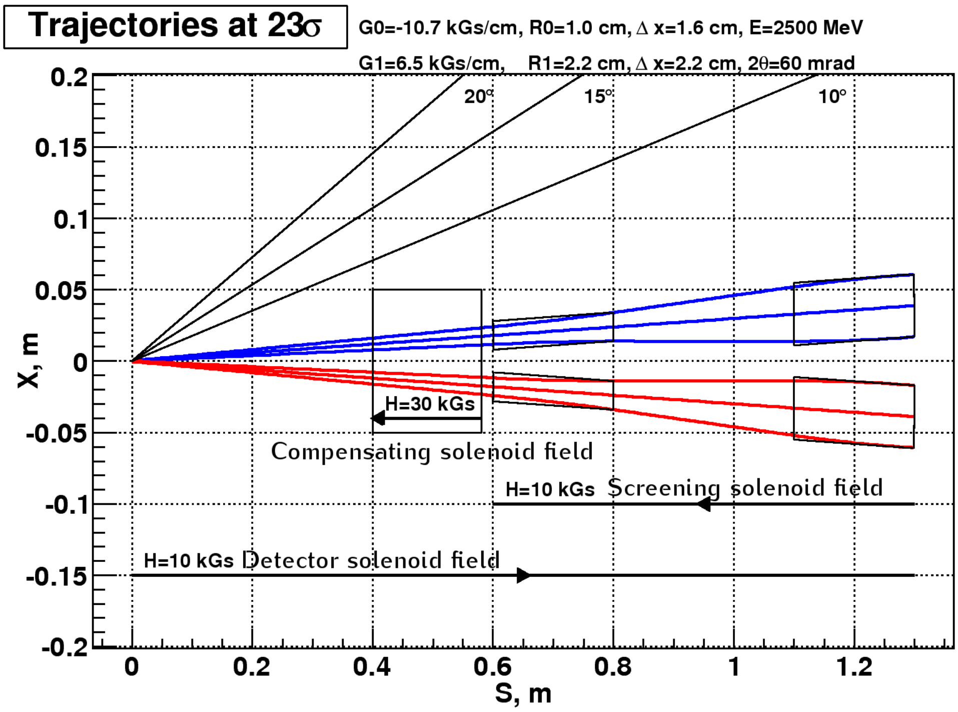

Fig. 4.3.2 The basic scheme of elements arangement around the interaction point. Shown are FF quadrupoles, place for compensating and screening solenoids, value of the detector field, and detector opening cones at 10, 15, 20 degrees.

The basic blocks of interaction region are FF telescope (FFT), chromaticity correction section (CCS) and CRAB sextupole section (CSS). All blocks are chosen to be telescopic transformations, to simplify optical and chromatical calculations. Map of the telescopic transformation with respect to momentum deviation (δ) expansion is represented as

$$R = \begin{pmatrix} R_{11} + T_{116}\delta + U_{1166}\delta^2 & 0 + T_{126}\delta + U_{126}6\delta^2 \\ 0 + T_{216}\delta + U_{2166}\delta^2 & R_{22} + T_{226}\delta + U_{2266}\delta^2 \end{pmatrix}.$$

Then relations between initial values of optical functions (subscript 1 and α_1=0, n is integer number) and final (subscript 2) in telescopic transformation, as well as chromatical expansion are given in simple expressions:

$$\mu_2 = n\pi + \frac{T_{126}}{\beta_1 R_{11}}\delta + \left[\frac{U_{1266}}{\beta_1 R_{11}} - \frac{T_{126}T_{116}}{\beta_1 R_{11}^2}\right]\delta^2 ,$$

$$\beta_2 = R_{11}^2\beta_1 + 2R_{11}T_{116}\beta_1\delta + \left[\left(T_{116}^2 + 2R_{11}U_{1166}\right)\beta_1 + \frac{T_{126}^2}{\beta_1}\right]\delta^2 ,$$

$$\alpha_2 = -\left[R_{11}T_{216}\beta_1 + \frac{T_{126}R_{22}}{\beta_1}\right]\delta - \left[\beta_1\left(R_{11}U_{2166} + T_{116}T_{216}\right) + \frac{\left(T_{126}T_{226} + U_{1266}R_{22}\right)}{\beta_1}\right]\delta^2 .$$

As it was shown in [1] element $T_{116} = 0$ could be zero in telescope system with certain symmetry properties and then the first order chromaticity of beta function vanishes. These formulas also give a recipe on how to tune sextupoles in order to cancel desired chromaticity, e.g. if sextupoles are tuned to provide $T_{126} = 0$ and $T_{346} = 0$ then linear chromaticity of betatron phase advances vanishes in both planes respectfully.

FFT consists of two quadrupole doublets and is tuned to match optical functions with CCS, and to minimize T_{116} and T_{336}, thereby minimizing linear chromaticity of the beta functions in horizontal and vertical planes respectfully, given zero chromaticity at IP.

CCS is built around two pairs of sextupoles with phase advance of multiple of π in appropriate plane from one quadrupole of FF doublet and with phase advance of multiple of π in other plane from corresponding second quadrupole of FF doublet. CCS provides such values of dispersion and beta functions that chromaticity of FF quadrupoles is compensated with reasonable strength sextupoles. The pairs are separated by *–I* transformation for cancelation of second order geometrical aberrations. Dispersion function is brought to zero at the end of the section, in order to decouple CRAB sextupole from chromatical functions.

CSS is designed to provide phase advances between IP and CRAB sextupole of $\Delta\mu_x = \pi m$, $\Delta\mu_y = \pi/2(2n+1)$, where m and n are integer numbers. Values of beta functions are optimized so sextupole strength $K_2 \cdot L$ is reasonable

$$K2 \cdot L = \frac{1}{2\theta}\frac{1}{\beta_y^*\beta_y}\sqrt{\frac{\beta_x^*}{\beta_x}} ,$$

where *L* is sextupole length, β^* and β denote beta functions at IP and in the place of CRAB sextupole respectfully, θ is half of crossing angle.

Optical functions from IP to the end of interaction region are shown on Fig.4.3.3.

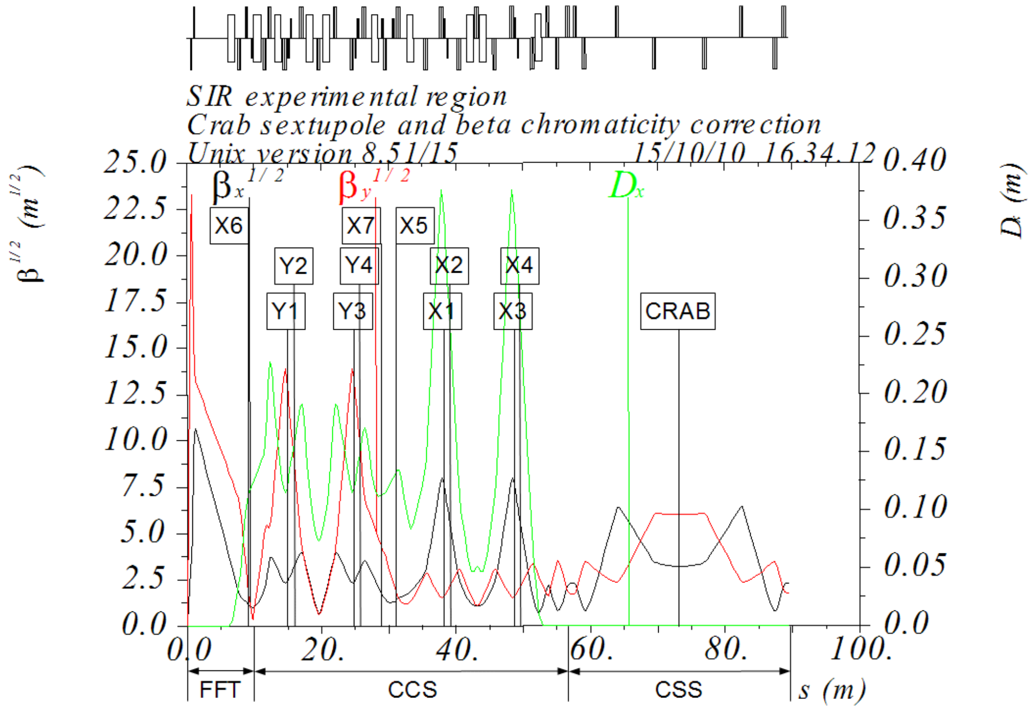

Fig.4.3.3 Optical functions and building blocks of IR. Names and positions of sextupoles are shown.

One of the essential tasks of IR is beta function chromaticity compensation, which is given by [2]

$$\frac{1}{\beta}\frac{d\beta}{d\delta} \propto \oint [K_2(s')D_0(s') - K_1(s')]\beta(s')\cdot\cos\left(\mu_0 - 2\left|\mu(s') - \mu(s)\right|\right)ds' .$$

where D_0 is a dispersion function, μ is phase advance, K_2 and K_1 are sextupole and quadrupole strengths respectfully. It is convenient to represent influence of each element as a complex vector

$Q = K_1 L\beta \exp(i2\mu)$ for quadrupoles,

$S = K_2 L\beta D_0 \exp(i2\mu)$ for sextupoles.

The beta function chromaticity will be compensated when summation of sextupole and quadrupole vectors will vanish, which requires that total sextupole vector must be parallel to quadrupole vector. In the structure where main sextupoles Y1 and Y3, X1 and X3 are matched to quadrupoles Q0 and Q1 respectfully the total sextupole vector is not parallel to quadrupole one in both planes and therefore beta function chromaticity is never completely compensated. The difference in phase advance is $\Delta\mu_x \approx 0.0043$ and $\Delta\mu_y \approx 0.00016$.

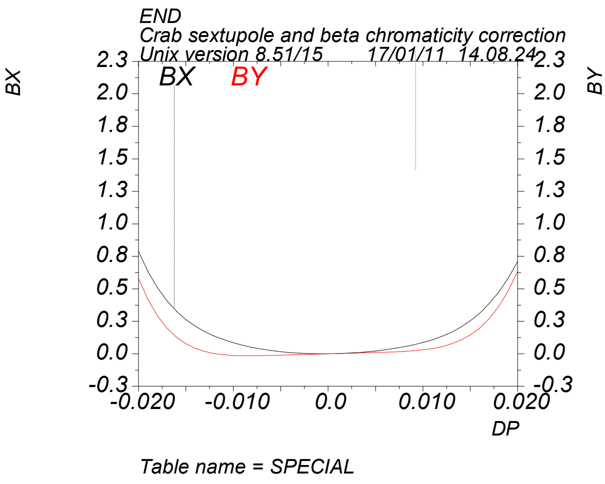

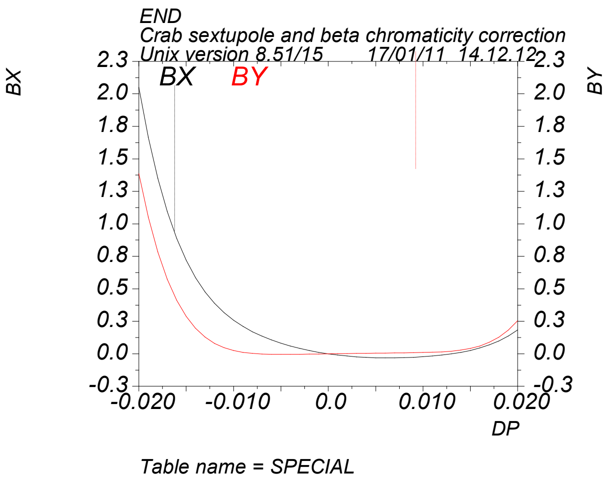

Fig.4.3.4 Beta function dependance on momentum deviation at the end of IR, sextupoles are in phase with quadrupoles of FF doublet (left), sextupoles adjusted $\Delta\mu_y \approx -1.65\cdot10^{-4}$ for Y pair, $\Delta\mu_x \approx -4.3\cdot10^{-3}$ for X pair (right).

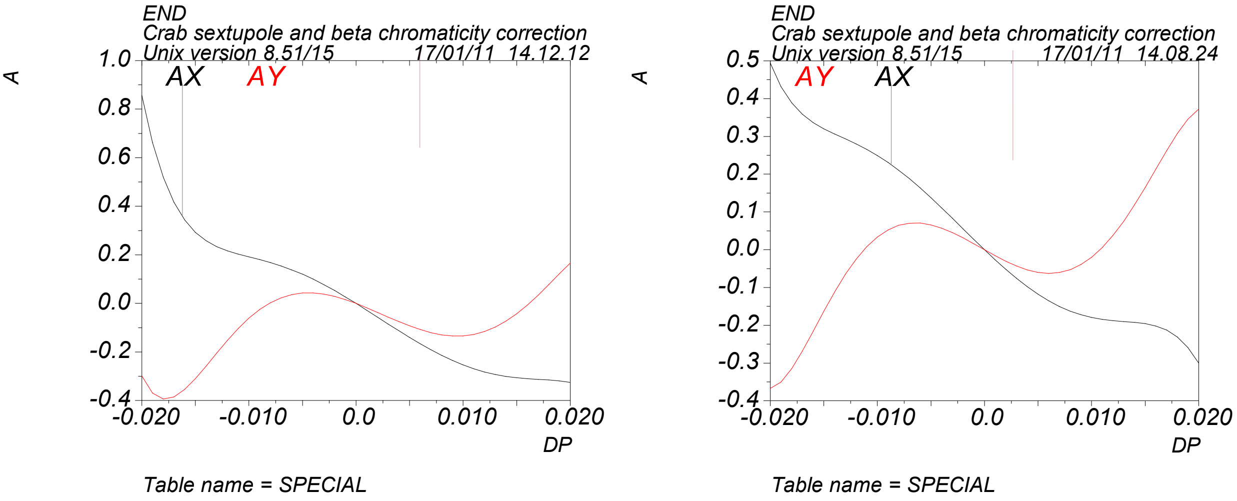

Fig.4.3.5 Alpha function dependance on momentum deviation at the end of IR, sextupoles are in phase with quadrupoles of FF doublet (left), sextupoles adjusted $\Delta\mu_y \approx -1.65\cdot10^{-4}$ for Y pair, $\Delta\mu_x \approx -4.3\cdot10^{-3}$ for X pair (right).

This happens because of influence of other quadrupoles in the IR. Therefore, the main sextupoles Y1 and Y3, X1 and X3 were displaced in phase advance in order to match the total quadrupole vector ($\Delta\mu_y \approx -1.65\cdot10^{-4}$ for Y pair, $\Delta\mu_x \approx -4.3\cdot10^{-3}$ for X pair). Obtained behavior of optical functions, beta and alpha functions dependence on energy deviation are shown on Figs.3.3.4 – 3.3.6.

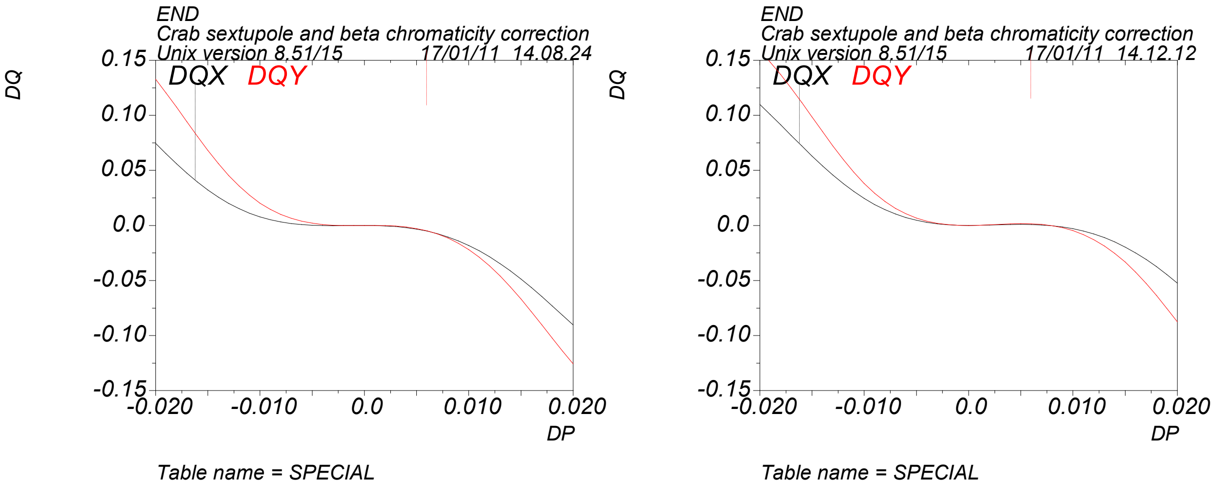

Fig.4.3.6 Phase advance dependance on momentum deviation from IP to the end of IR, sextupoles are in phase with quadrupoles of FF doublet (left), sextupoles adjusted $\Delta\mu_y \approx -1.65\cdot10^{-4}$ for Y pair, $\Delta\mu_x \approx -4.3\cdot10^{-3}$ for X pair.

As could be seen from Fig.4.3.4, odd order chromaticity of beta functions vanished. However, Fig.4.3.6 shows that phase advance chromaticity is mostly of 2nd and 3rd order. Usually it proposed to correct higher order chromaticity by appropriate multipoles, in particular 2nd order chromaticity should be corrected by octupole. However, required strength of the octupole in present structure is unrealistically large. Therefore, it is more efficient to use sextupole at the place with small on energy beta function and large first order chromaticity of beta function and dispersion to correct second order phase advance chromaticity [1]. Similar speculations give a solution for 2nd order compensation by sextupole with large second order beta function chromaticity. In the places with given conditions sextupoles X5, X6 and X7 have been introduced. Behavior of beta functions with respect to momentum deviation at the sextupoles is presented on Figs.3.3.7 and 3.3.8.

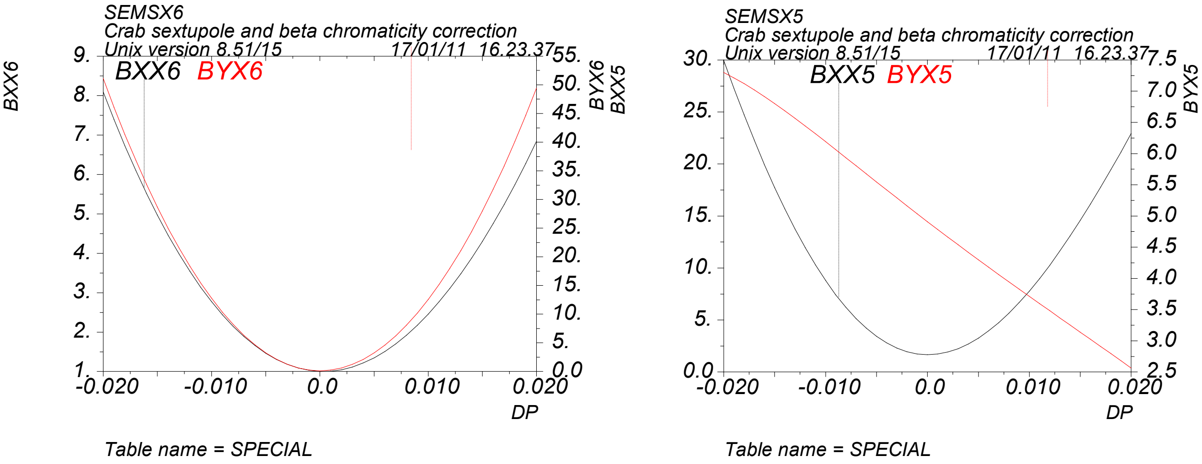

Fig.4.3.7 Left plot: beta function chromaticity at sextupole X6 (the end of FFT). Second order beta function chromaticity in vertical plane is larger than in horizontal, therefore sextupole is coupled to third order vertical phase chromaticity. Right plot: beta function chromaticity at sextupole X5. Second order beta function chromaticity in horizontal plane is larger than in vertical, therefore sextupole is coupled to third order horizontal phase chromaticity.

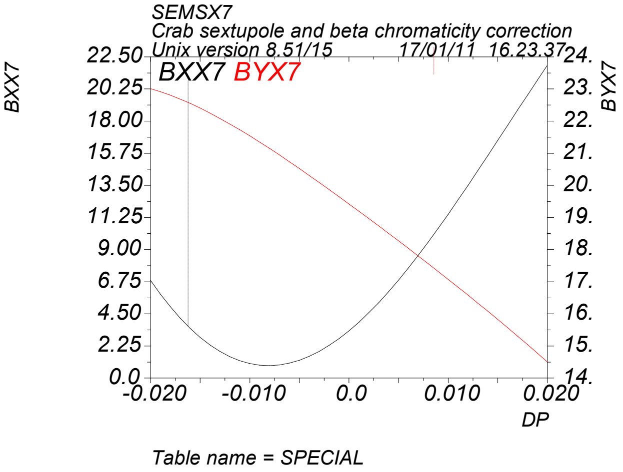

Fig.4.3.8 Beta function chromaticity at sextupole X7. First order beta function chromaticity in horizontal plane is larger than in vertical, therefore sextupole is coupled to second order horizontal phase chromaticity.

Tuning of additional sextupoles allows compensation of beta functions and phase advances chromaticities.

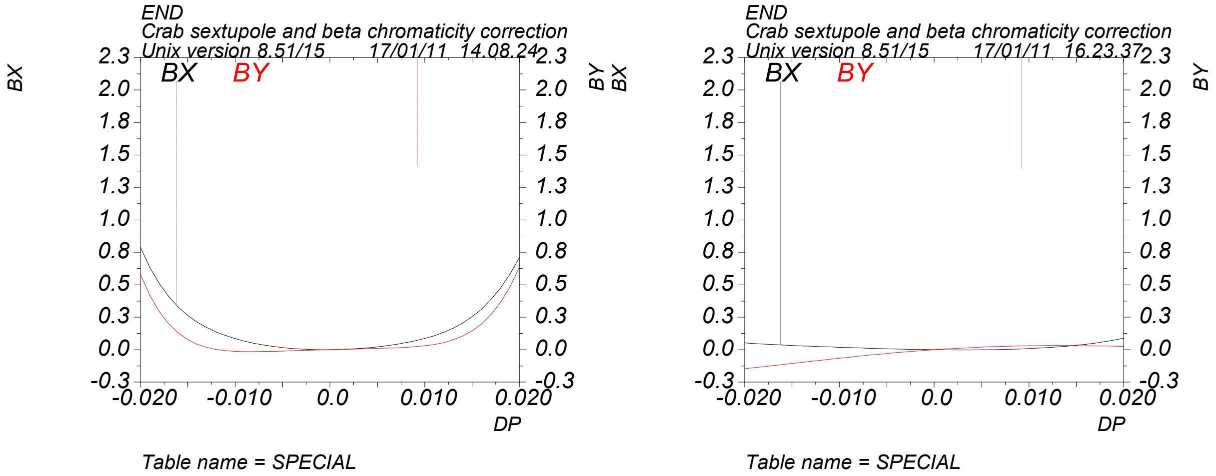

Fig.4.3.9 Beta function dependance on momentum deviation at the end of IR, only main sextupoles are on (left), main and additional sextupoles are on (right).

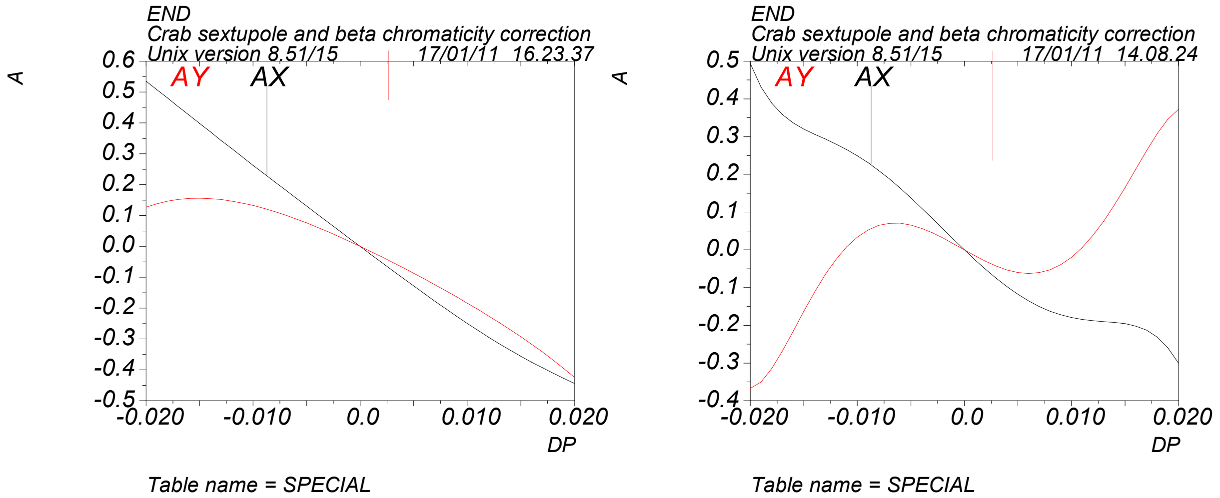

Fig.4.3.10 Alpha function dependance on momentum deviation at the end of IR, only main sextupoles are on (left), main and additional sextupoles are on (right).

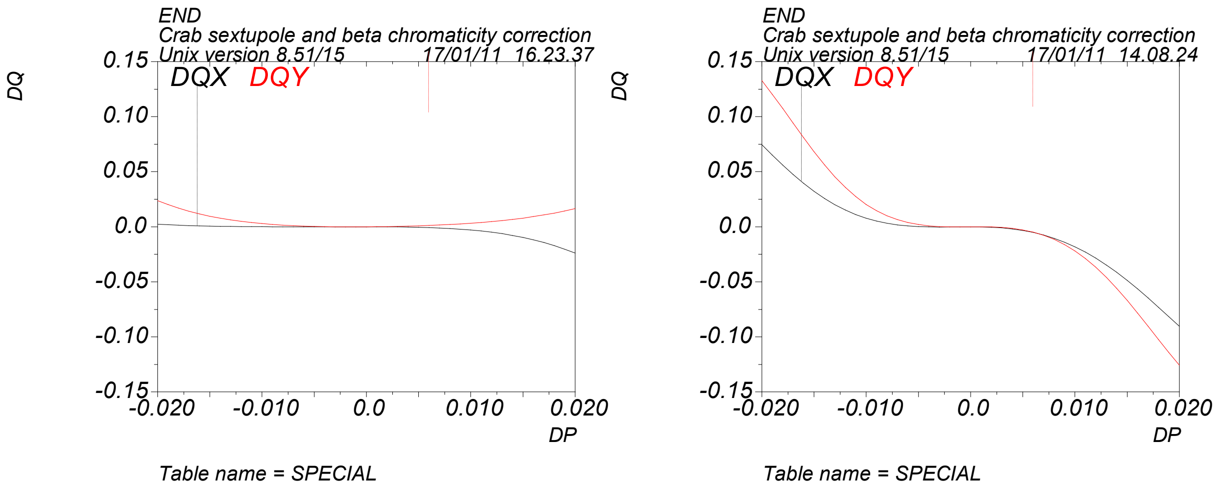

Fig.4.3.11 Phase advance dependance on momentum deviation from IP to the end of IR, only main sextupoles are on (left), main and additional sextupoles are on (right).

It has been shown by K.Brown [3] that all high order geometrical aberrations from sextupole can be cancelled exactly by another sextupole with the same strength placed at –*I* map. But it is correct only for thin sextupoles, in case of finite length magnets only second order vanishes, while the third order becomes large and limits dynamic aperture of present IR design. However, it was observed in [4] that placing additional sextupoles at the same distance from the main ones allows partial compensation of the third order geometrical aberrations, these are Y2 and Y4, X2 and X4 sextupoles (Fig.4.3.3). The strength of the additional sextupoles is about 13% of strength of the main ones. The map of such an interleaved sextupole pair is

$$\begin{aligned} x_1 &= -x_0 - \frac{B_1(K_{21}, K_{22}, r)}{12}\left(x_0^3 + x_0 y_0^2\right)L^4, \\ p_{x1} &= -\frac{B_2(K_{21}, K_{22}, r)}{6}\left(x_0^3 + x_0 y_0^2\right)L^3, \\ y_1 &= -y_0 - \frac{B_1(K_{21}, K_{22}, r)}{12}\left(y_0^3 + x_0^2 y_0\right)L^4, \\ p_{y1} &= -\frac{B_2(K_{21}, K_{22}, r)}{6}\left(y_0^3 + x_0^2 y_0\right)L^3, \end{aligned}$$

where K_{21} and K_{22} are main and additional sextupole strengths respectfully, r is distance between main sextupoles and additional ones in units of sextupole length L,

$$\begin{gathered} B_1(K_{21}, K_{22}, r) = (3 + 2r)K_{21}^2 + 6\left(2 + 3r + r^2\right)K_{21}K_{22} + K_{22}^2, \\ B_2(K_{21}, K_{22}, r) = K_{21}^2 + 6(1 + r)K_{21}K_{22} + K_{22}^2. \end{gathered}$$

Third order aberrations are connected with coefficients B_1 and B_2, setting one to zero decreases another one 3-5 times. Minimizing coefficients B_1 and B_2 in above relations gives a range of values for additional sextupole of 5%-15% of the main one. Numerical optimization gives 13%.

4.3.3 Magnetic lattice of the storage ring

The optical functions of the collider are shown in Fig.4.3.12. Since the beta functions are small at the point of beam collision, the the vertical betatron function reach values of 600 m in the final focus lenses (Fig.4.3.13).

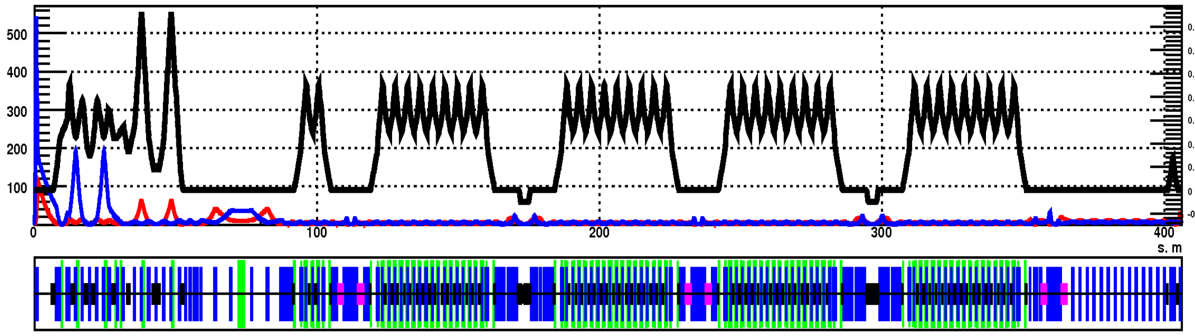

Fig.4.3.12 Optical functions of the $c\tau$ –factory half. Legend: the vertical beta is in blue, the horizontal beta is in red and the horizontal dispersion function is in black. The dispersion function behaviour clearly shows four periodic sections of the arc with the damping wigglers and siberian snake insertions in between

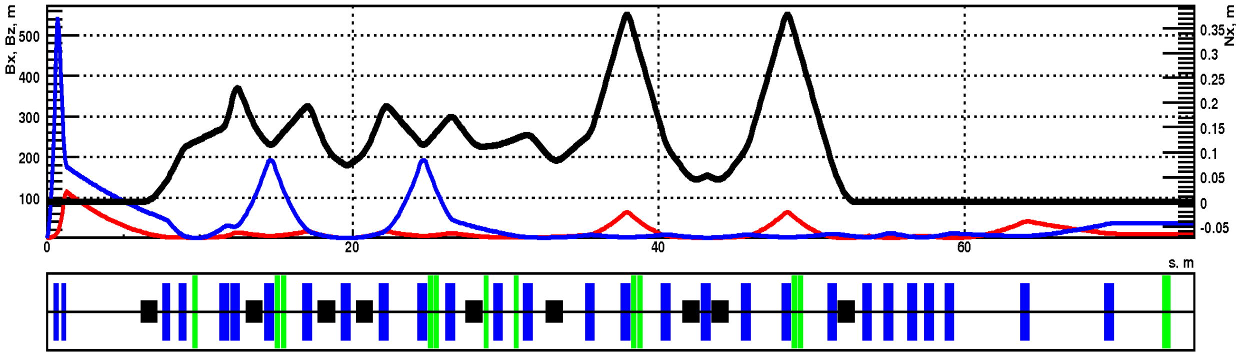

Fig.4.3.13 Optical functions of the $c\tau$ –factory Interaction Region. Cf. Fig.4.3.3 with explanation of the sextupoles arrangement. The element line legeng (in the bottom of the plot): dipole magnets for dispersion control are in black, quadrupole magnets are in blue and sextupole magnets are in green. Start point is the IP and the end point is the crab sextupole.

As a result, the final focus quadrupoles are a strong source of chromaticity (both of the betatron tunes and of the optical functions), the high chromaticity orders playing a significant role. Thus the influence of the field errors and the nonlinearities, including the edge ones, of the lenses of the final focus increases as well as the requirements to the manufacturing accuracy of such lenses.

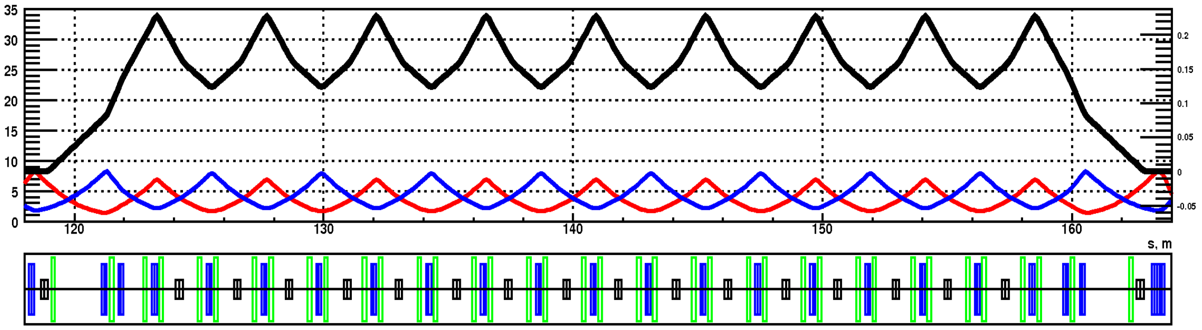

Fig.4.3.14 A regular arc section lattice functions. The legend is as for the previous plots.

The two arcs of each (electron and positron) storage ring are slightly different in size, for arrangement of the beam intersection. However, the periodicity cells of the small and large half-rings, which are intended to solve the problem of obtaining a small emittance, hardly differ from each other in the behavior of the optical functions, which are shown in Fig.4.3.14. The cell is a FODO lattice in which the short bending magnets (black in Fig.4.3.14) are placed between the focusing and defocusing lens (blue bars in Fig.4.3.14). Such a cell is still compact but tuned to a fairy low emittance. Pair of sextupoles provide chromatic correction in the cell.

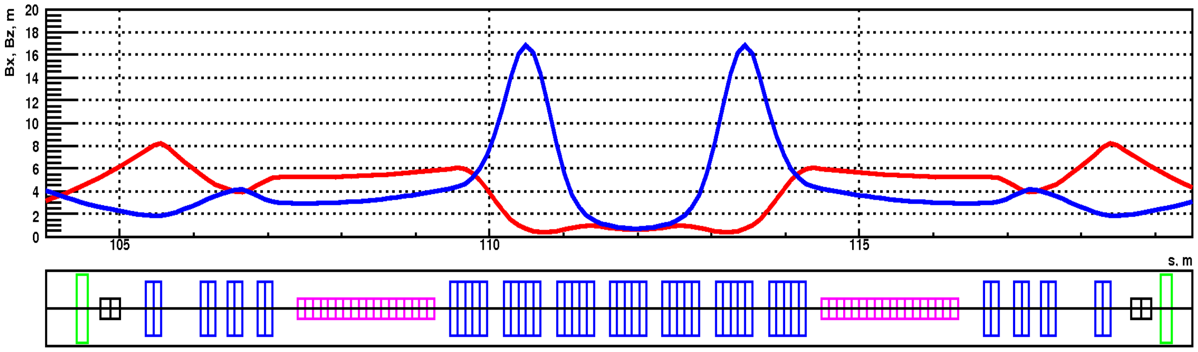

Fig.4.3.15 Siberian snake section. Two solenoids are colored in magenta while matching quadrupoles are in blue.

A required spin dynamics in the electron storage ring is provided by 5 spin rotators of Siberian Snake type. Each snake rotates the spin by 180^0 around the longitudinal axis of the accelerator reference frame. The snake consists of two superconducting solenoids separated by a mirror-symmetrical optical system of 7 quadrupole lenses, as it is shown in Fig.4.3.15. The total integral of the field of the two solenoids is 26 T-m at 2.5-GeV beam energy. A transport matrix of the spin rotator (including the solenoids) provides spin transparency together with the condition of zeroing of 2×2 off-disgonal blocks. Betatron coupling induced by solenoinds are compensated by the optical condition of $T_x = -T_y$ between the solenoids. This method does not require skew quadruples for the coupling compensation.

In this scheme the solenoid field may vary in a wide range (including complete switching off) without changing the quadrupoles current and the coupling vanishes in the whole range. Though, if one wants to leave the advance of the betatron phases unchanged throughout the insert, the field gradients in the lens still have to be slightly corrected.

With an odd number of the snakes the spin in the arcs of the ring lies in the median plane and takes exactly the longitudinal direction in the middle of the arcs between the snakes.

In details spin dynamics is described below.

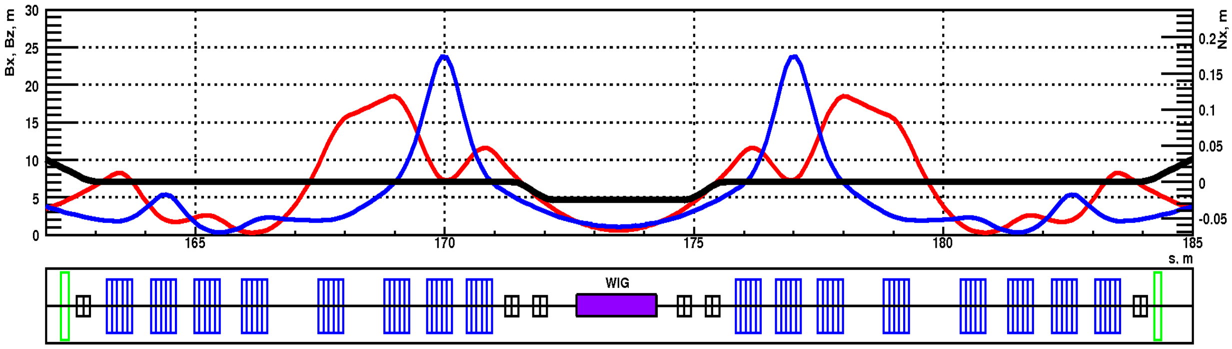

Fig.4.3.16 Damping wiggler section

For luminosity optimization in the whole energy range of the factory, damping parameters of the beams should be carefully controlled with energy. For this purpose we plan to use special system of superconducting damping wigglers. The wiggler field iz zero at the maximum energy (when the radiation damping is provided by the arc magnets) and gradually increases with the energy goes down reaching the maximum value of 4.5 T at 1 GeV.

Such strong wiggler field influences (especially at low energy) the ring optics and a system of quadrupole magnets shown in Fig.4.3.16 recovers the betatron function beating and betatron tune shift.

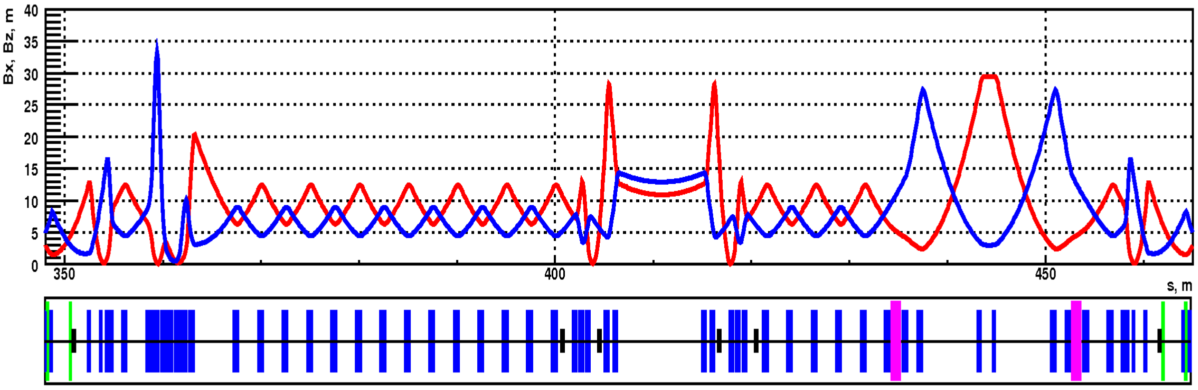

Fig.4.3.17 Lattice functions of the RF/injection section

At the opposite side of the interaction region there is a straight section accommodating the RF accelerating cavities and injection equipment. The lattice functions of this section are depicted in Fig.4.3.17. This part also provides the beams separation in vertical plane and contains the beam diagnostics equipment.

The list of collider (electron ring) magnets is given below.

Type	**No**	**Length, cm**	**Maximal strength**
Superconducting final focus doublet			
Anti-solenoid	2	10	45 kGs
Defocusing quadrupole	2	20	Gradient is 10.7 kGs/cm
Focusing quadrupole	2	20	Gradient is 6.6 kGs/cm
Superconducting magnets			
Damping wigglers	4	160	Field is 45 kGs
Siberian snake solenoids	10	185	60 kGs
Experimental section magnets			
Bending magnet	20	100	Angle is 3.5º
Quadrupole	4	40	Gradient is 1.0 kGs/cm
Quadrupole	56	50	Gradient is 2.3 kGs/cm
Sextupole	22	20	Gradient is 2.0 kGs/cm^2
Sextupole	6	40	Gradient is 1.0 kGs/cm^2
Regular magnets			
Bending magnet	152	27	Angle is 2º
Quadrupole	230	20	Gradient is 2.8 kGs/cm
Quadrupole	6	40	Gradient is 3.7 kGs/cm
Quadrupole	100	50	Gradient is 2.9 kGs/cm
Quadrupole	35	50	Gradient is 4.0 kGs/cm
Sextupole	324	15	Gradient is 0.3 kGs/cm^2

4.3.4 Controlling the emittance and the damping parameters

To obtain the maximum luminosity of the $c\tau$-factory in the required energy range it is necessary to effectively control the radiation damping parameters of the accelerator in order to maintain a constant horizontal emittance ($\varepsilon_x = 8$ nm-rad) (nm-rad) and the damping time ($\tau_{x,y} \approx$ 30 ms, $\tau_z \approx$ 15 ms). Superconducting wigglers are planned to be installed for this purpose on both rings. The wigglers parameters can be estimated from the following considerations.

The dependence of the damping time on the energy and the wigglers parameters has the following form:

$$\tau_{x,y,s} = \frac{const_{x,y,s}}{E^3(I_{20}+i_2)}, \tag{4.3.1}$$

where I_{20} and i_2 are the second radiation integral from the accelerator lattice and the wigglers, correspondingly. Varying i_2 with energy as

$$i_2(E) = I_{20}\left(\frac{E_0^3}{E^3}-1\right), \tag{4.3.2}$$

where $I_2(E_0) = I_{20} = 0.79\,\mathrm{m}^{-1}$ for $E_0 = 2.5\,\mathrm{GeV}$, it is possible to make the damping time (4.3.1) a constant function of the energy.

It follows from (4.3.2) that the maximum value of the damping integral the wigglers shall ensure for the minimum energy $E = 1.0\,\mathrm{GeV}$ must be $i_2(E) = 11.5\,\mathrm{m}^{-1}$. The second radiation integral from the wiggler field is written as

$i_2 = \frac{L_w}{\rho_w^2}$ for a piece-wise approximation of the poles, and

$i_2 = \frac{L_w}{2\rho_w^2}$ for a sinusoidal model of the wiggler field, where L_w is the total length of all the wiggler and ρ_w is the particle turning radius for the maximum field of the wiggler. It can be seen that the piecewise-constant approximation gives, for the same length and amplitude of the wiggler field, a twofold win in i_2. For such an approximation to be valid, the wiggler field period should exceed the pole gap by far. On the other hand, the longer the period, the greater the deviation of the beam orbit from the axis, and thus the requirements for the value of the horizontal aperture of the snake and the quality of the field tighten. Basing on the experience of fabrication of superconducting wigglers by BINP, a reasonable compromise is a wiggler with a pole gap of ≈ 40 mm and a period length of ≈ 200 mm. In this case, it is quite possible to use a piecewise constant model of the field.

Choosing (subject to the free space available) L_w = 6.4 m, we obtain the maximum field of the snakes $B_{w\max} = 4.5\,\mathrm{T}$ at $E = 1.0\,\mathrm{GeV}$ T, which seems quite acceptable for the chosen parameters of the wiggler.

To ensure the constancy of the damping time of the betatron and synchrotron oscillations throughout the beam energy range, the wiggler field amplitude should depend on the energy as follows:

$$B_w(E) = B\rho(E)\cdot\sqrt{\frac{I_{20}}{L_w}\left(\frac{E_0^3}{E^3}-1\right)}, \tag{4.3.3}$$

where $B\rho(E)$ is the rigidity of the magnetic system. The dependence of the wiggler field on the energy at our parameters is shown in Fig.4.3.18.

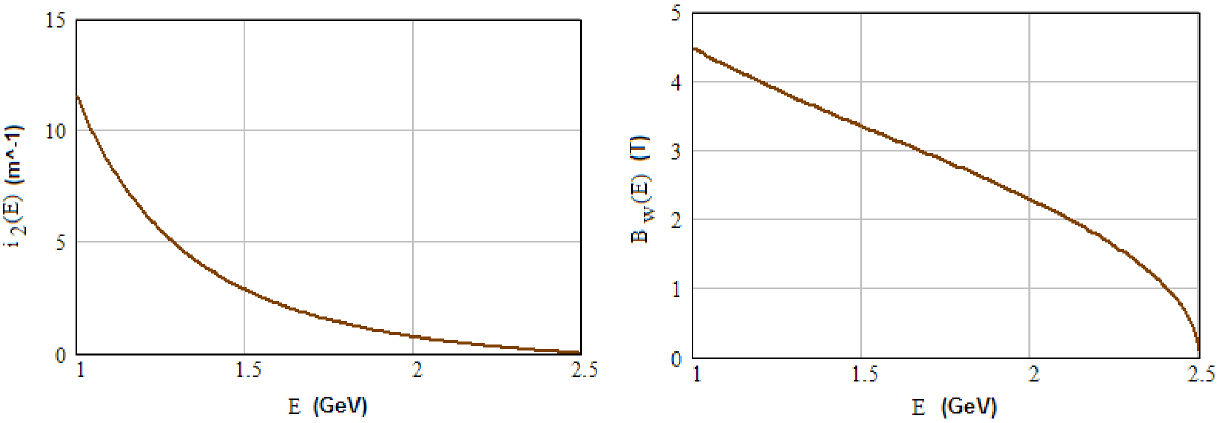

Fig.4.3.18 Dependence of the radiation integral (left) and the wiggler field amplitude on the beam energy.

The dependence of the emittance on the energy and the wiggler parameters is written as

$$\varepsilon_x(E) = const \cdot E^2 \frac{I_{50} + i_5}{I_{20} + i_2}. \tag{4.3.4}$$

Requiring the emittance to be constant at energy and substituting (4.3.2) into (4.3.4), we have

$$i_5(E) = I_{50}\left(\frac{E_0^5}{E^5} - 1\right), \tag{4.3.5}$$

where $I_5(E_0) = I_{50} = 6.8 \cdot 10^{-4}\,\text{m}^{-1}$ for $E_0 = 2.5\,\text{GeV}$, which together with the second radiation integral I_{20} ensures the horizontal emittance $\varepsilon_x = 8$ nm-rad at the maximum energy and the wiggler field off.

It follows from (4.3.**5)** that at $E = 1.0\,\text{GeV}$ the wiggler shall produce the integral $i_5(E) = 6.6 \cdot 10^{-2}\,\text{m}^{-1}$. For a sinusoidal model, the fifth radiation integral can be written as

$$i_5 = \frac{8}{15\pi}\frac{i_2}{\rho_w} \cdot \left(5\frac{\eta_0^2}{\overline{\beta}_x} + \overline{\beta}_x \theta_w^2\right), \tag{4.3.6}$$

where $\overline{\beta}_x$ is the horizontal beta function averaged over the wiggler length, η_0 is the «residual» dispersion function in the wiggler straight section, and the maximum angle of the beam orbit deviation in the wiggler field is computed as

$$\theta_w = \frac{\lambda_w}{2\pi\rho_w}. \tag{4.3.7}$$

To ensure the emittance constancy throughout the energy range, we have to equate (4.3.6) to (4.3.5) over this range. Since the condition of keeping of the damping time constant unambiguously determines the behavior of $i_2(E)$, $\rho_w(E)$ and $\theta_w(E)$, the only thing we can change in (4.3.6) is the structure function $\overline{\beta}_x$ or η_0. It is advantageous to fix a rather small $\overline{\beta}_x \approx 0.5 \div 1$ m in order to reduce the influence of the wiggler field on the beam dynamics. In this case, one can obtain the constancy of the emittance (together with that of the damping time) if the dispersion function of the wiggler segment depends on the energy as follows:

$$\eta_0^2(E) = \frac{3\pi}{8}\bar{\beta}_x \frac{I_{50}}{I_{20}} \frac{\rho_w(E)}{E^2} \frac{E_0^5 - E^5}{E_0^3 - E^3}\,. \qquad (4.3.8)$$

This expression takes into account that the second term in the brackets is much less than the first one:

$$\eta_{0\min} >> \frac{1}{\sqrt{5}}\bar{\beta}_x\theta_w$$

Here $\eta_{0\min} \approx 50$ mm corresponds to energy of 1 GeV, while $\bar{\beta}_x\theta_w/\sqrt{5} \approx 10$ m at the same energy.

In the region of high energies, $E \approx E_0$, there is practically no need in the wigglers because the magnetic structure of the storage ring ensures the required emittance and damping. In the region of small energies, $E < E_0$, estimate expression (4.3.8) can be written as

$$\eta_0^2(E) \approx \frac{3\pi}{8}\bar{\beta}_x \frac{I_{50}}{I_{20}} \rho_w(E)\frac{E_0^2}{E^2}\,,$$

taking into account that $\rho_w(E) \sim E$, $\eta_0 \sim 1/\sqrt{E}$.

Fig.4.3.19 shows the dependence of the dispersion function on the energy in the wiggler segment, calculated in accordance with (4.3.8). The minimum dispersion value is $\eta_{0\min} \approx 50$ mm at energy of 1 GeV, and then it grows up to ~150 mm at energy of 2.5 GeV.

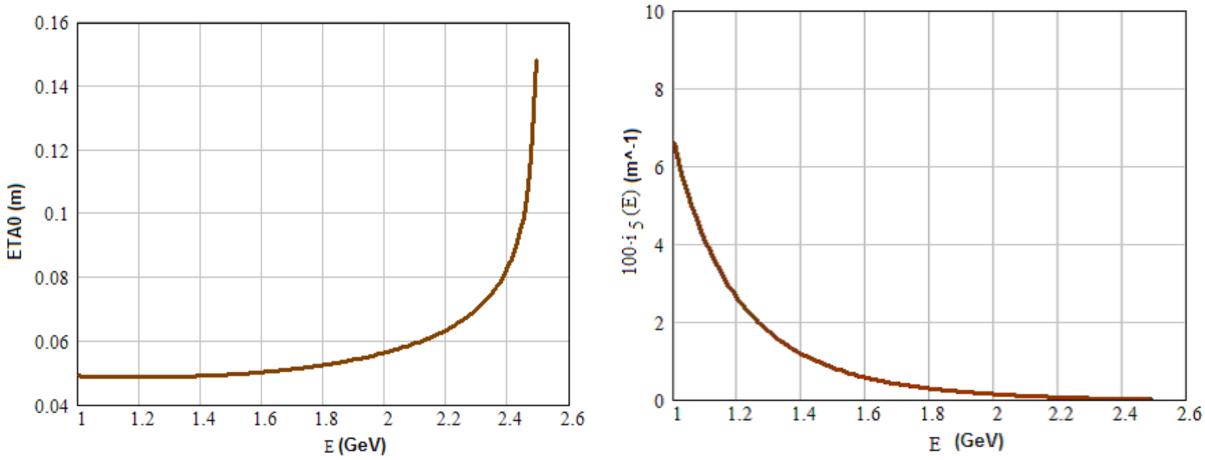

Fig.4.3.19 “Residual” dispersion function in the wiggler segment (left) and the fifth radiation integral produced by the wiggler to preserve the emittance over the operation energy range of the $c\tau$-factory.

For the above-chosen wiggler parameters, the maximum angle of deviation and the orbit drift in dependence on the energy are shown in Fig.4.3.20.

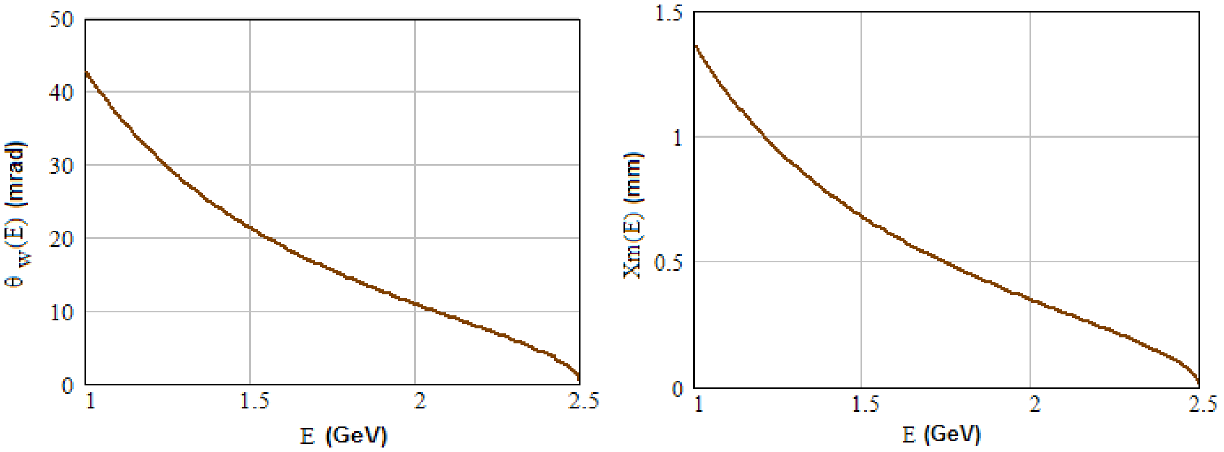

Fig.4.3.20 Maximum angle of deviation (left) and orbit drift in the wiggler field.

Since in real life a (small) change in the dispersion function in the “wiggler” segment will inevitably be accompanied by a change (also small) in the average horizontal beta function entering (4.3.6), the maximum luminosity should be set “in accordance with the effect”.

4.3.5 Correction of chromaticity and the dynamical aperture

For the $c\tau$-factory the study and optimization of the dynamical aperture have a number of features that are more or less identical for all projects of colliders with the Crab Waist (or “Nanobeam”) collision scheme.

Small values of the betatron functions (especially of the vertical one) at the IP result in large chromaticity values (of the tunes and the optical functions) generated by the final focus section:

$$\xi^* \approx -l/\beta^*,$$

where l is the distance from the IP to the quadrupole lens, and β^* is the corresponding betatron function at the IP. For $\beta_y^* < 1$ mm, the typical vertical chromaticity is $\xi_y^* \sim -10^3 \ldots -10^4$. The horizontal chromaticity is smaller but it may also be as high as a few hundreds. For the $c\tau$-factory the bulk of the vertical chromaticity is produced by the final focus quadrupole system (see Table 4.3.2).

Table 4.3.2 Parameters of the storage ring for dynamic aperture calculation and optimization

Parameter	**Value**	**Units**
Betatron tunes, ν_x/ν_z	43.54/34.57	
Synchrotron tune, ν_s	0.01	
Compaction factor, α	$9.97\cdot10^{-4}$	
Natural chromaticity	95.7/-256.7	
Beta functions, β_x/β_z	4/0.08	cm
Beam sigma, σ_x/σ_z	17.9/0.18	µm
Bunch length, σ_s	1	cm

Chromaticity	Expr	Ring	Total
Horizontal	-37.5	-58.2	-95.7
Vertical	-198.4	-58.3	-256.7

The IR chromaticity is corrected locally by the sextupole magnets located, if possible, close to the final focus lenses. The strengths of the sextupoles are large and the dynamical aperture turns out to be small. To avoid this, we place the magnets in pairs as in Fig.4.3.21.

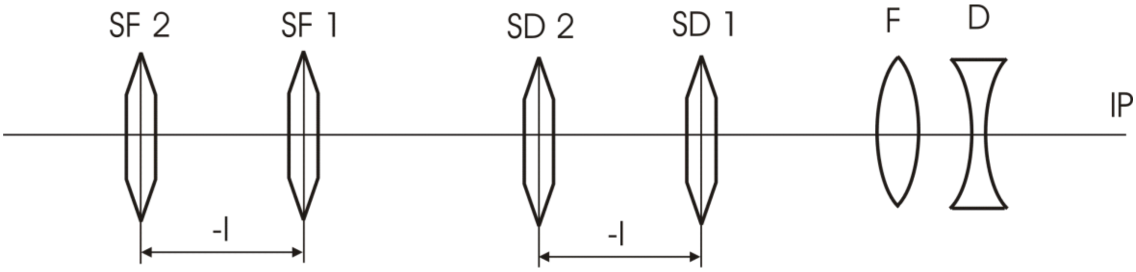

Fig.4.3.21 The beam IP, the doublet of the quadrupole lenses of the final focus (FD), and the two pairs of the sextupole magnets to correct the vertical (SD) and horizontal (SF) chromaiticity.

If the matrix of the optical transformation between the sextupole magnets of the pair is equal to minus unity, such a system does not generate higher-order aberrations outside the pair and therefore does not affect the dynamic aperture [1, 5].

However, this principle is true only for a model with infinitely thin (zero-length) sextupole lenses. Allowing for the finite length leads to the fact that only the quadratic aberrations are fully compensated, but the higher ones still stay, and in view of the large values of the betatron functions severely limit the dynamic aperture [4].

A method to correct this effect was proposed in [4]. The method consists in adding a pair of corrective sextupole lenses also located in phase with the *-I* transformation to the pair of the main chromatic sextupole lenses (Fig.4.3.22). Strength of the corrective lenses of 3-10% of the basic lenses turns out to be enough to significantly (several times) increase the dynamic aperture.

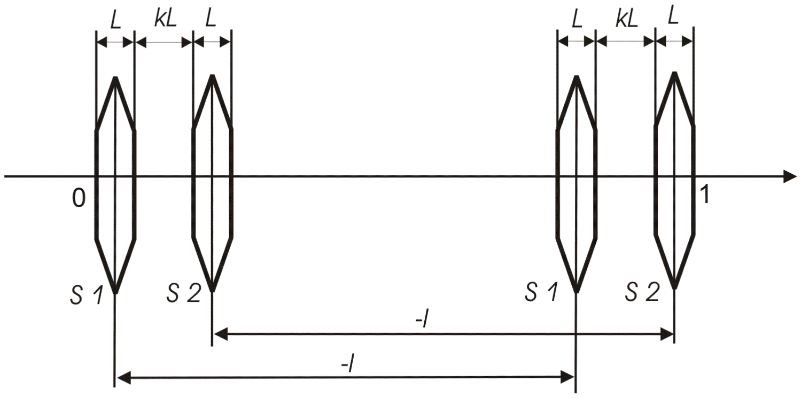

Fig.4.3.22 Addition of the corrective pair of sextupole lenses (*S2*) to the main ones (*S1*).

This approach was applied to the $c\tau$-factory interaction region and gave exelent results as it is shown in Fig.4.3.23.

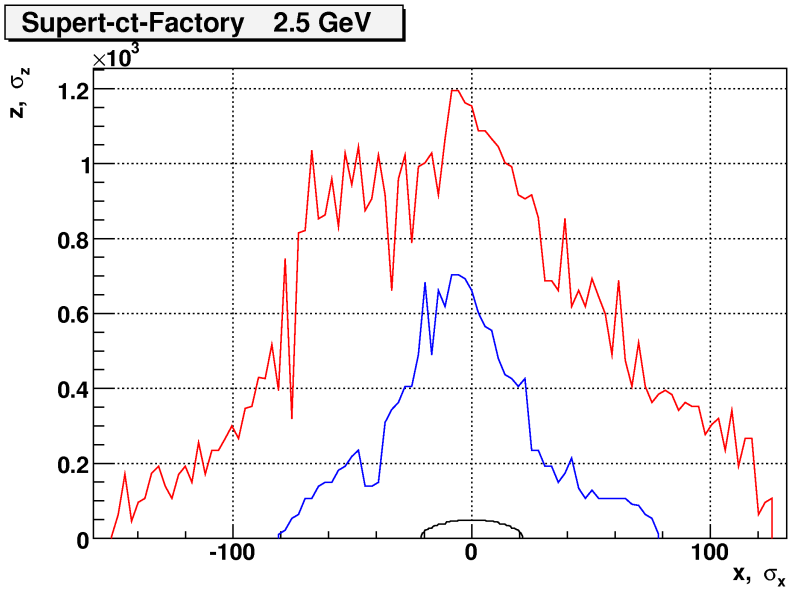

Fig.4.3.23 Transverse dynamic aperture of the interaction region with compensated chromaticity. Black curve indicates the DA with two pairs (vertical and horizontal) of main chromatic sextupoles, red curves shows the DA recovered by small correction sextupoles and blue curve depicts the resulting DA when the bandwidth increase sextupole correctors are inserted.

Besides the main and the transverse DA correcting sextupoles, the interaction region includes also a number of sextupole magnets to optimize a momentum dynamic aperture (related to the optical bandwidth). A resulting optimized transerse dynamic aperture is shown in Fig.4.3.23 in blue.

Since the condition of placing a pair of a "crab" sextupole lenses is essentially identical to a pair of chromaticity-correction lenses placed through the *-I* transformation and the strengths of the "crab" lenses are great, the same effect – reduction in the dynamic aperture if the non-zero length of the magnets is taken into account – is observed here too. Placing an extra pair of compensating lenses of small strength can also essentially increase the resulting aperture here.

When a nonlinear beam dynamics was optimized for the interaction region from the viewpoint of the maximum transverse/momentum dynamic aperture, the rest of the ring was added and the resulting dynamic aperture was re-optimized again. At this step we used the method of “the best sextupole pair” proposed in [6]. According to the algorithm, we correct the chromaticity by *N* small steps along the vector $\vec{\xi} = \left(\xi_{x0}, \xi_{y0}\right)$ as it is shown in Fig.4.3.24. At each step 1/*N*-th fraction of the horizontal and vertical chromaticity is compensated by a single (in some sense the best for this particular step) pair of focusing and defocusing sextupoles $\left(SF_i, SD_j\right)$.

To find the best pair of sextupoles, we try all possible $\left(SF, SD\right)$ - combinations and the pair demonstrating the largest dynamic aperture is fixed at this step. If N_{SF} and N_{SD} are the number of focusing and defocusing sextupoles, then $N_{SF} \times N_{SD}$ combinations have to be looked through at every step. At the next steps the procedure is repeated until the chromaticity will reach the desired value.

The algorithm may be naturally extended for increasing the off-momentum aperture: instead of a single DA with $\Delta p / p = 0$ several DAs with specified $\left(\Delta p / p\right)_i$ are optimized and no modifications are required.

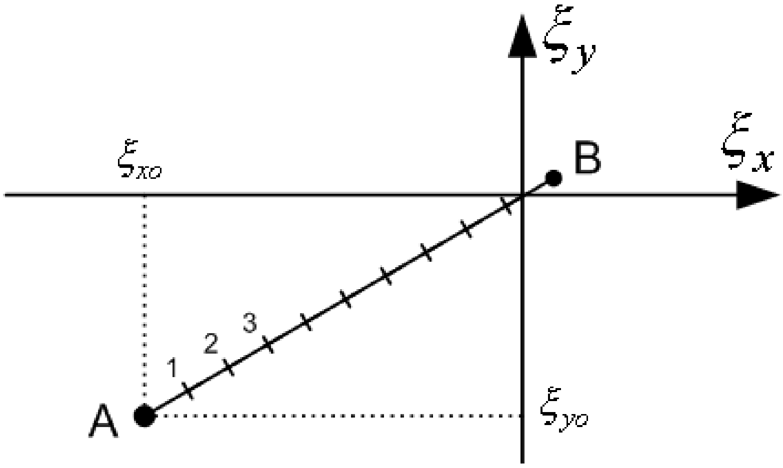

Fig.4.3.24 Step-by-step chromaticity compensation. A and B are initial and final points

The method of “the best sextupole pair” allowed optimizing the collider dynamic aperture up to ±40σ_x in horizontal direction and up to 430σ_z in vertical direction, which seems quite enough to get expected luminosity.

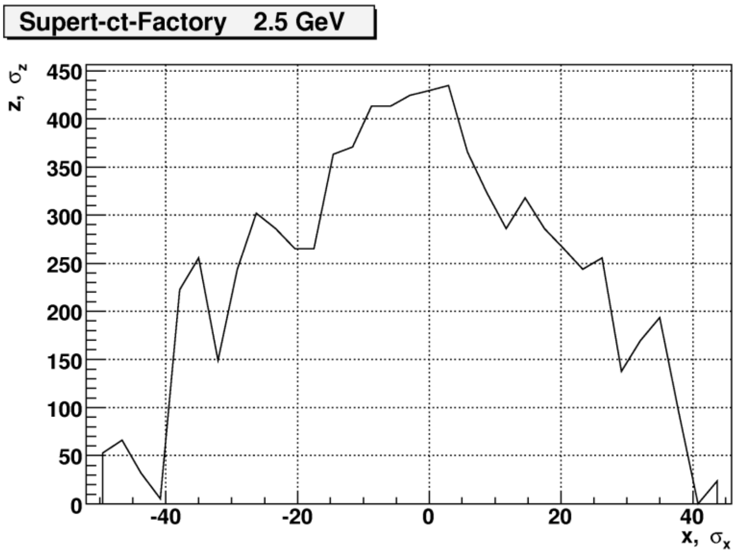

Fig.4.3.24 A transverse dynamic aperture with all main nonlinear perturbation included

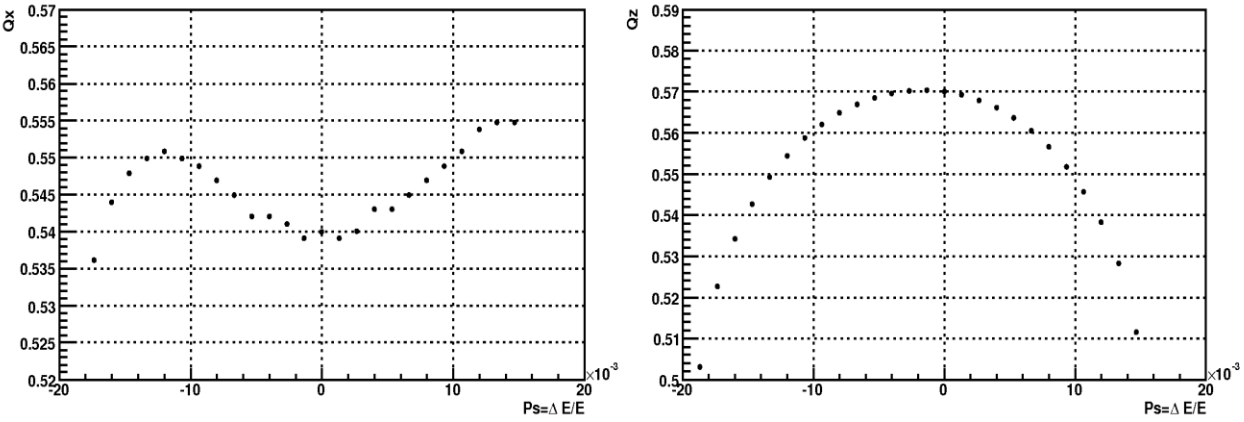

Fig.4.3.25 Betatron tune bandwidth

At the same time, a momentum dynamic aperture was opimized also and the tune bandwith of ~ ±1.9%, which seems adequate for the reasonable Touschek life time, was obtained (see Fig.4.3.26).

Tune-amplitude dependence for the optimized dynamic aperture is shown in Fig.4.3.26. It is seen clearly that the tunes tend to approach a half-integer resonance with the amplitude increase and the later yields the dynamic aperture limitation.

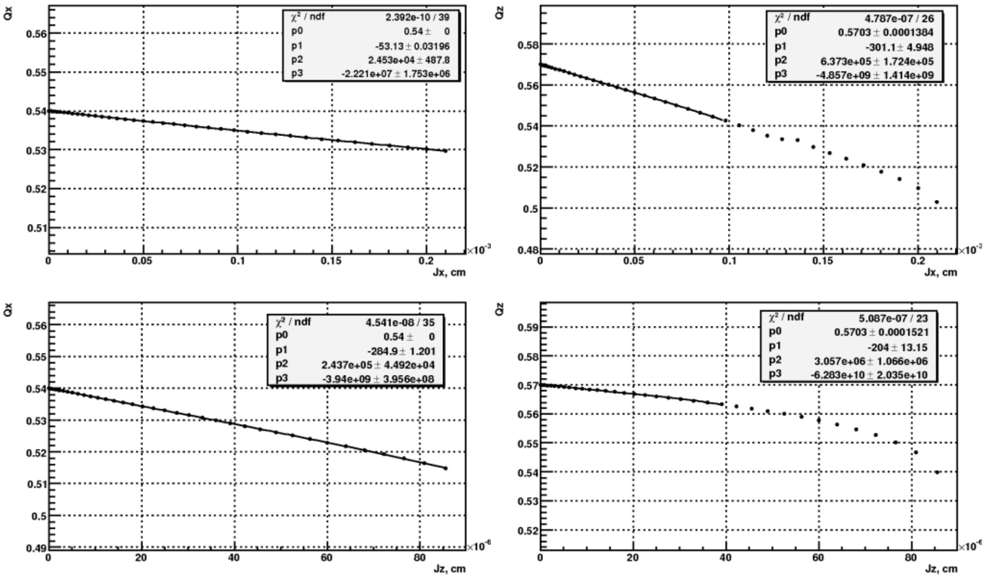

Fig.4.3.36 The tune dependence on amplitude

Besides the sextupole perturbation, kinematic terms and quadrupole fringe field high order terms were checked from a viewpoint of the dynamic aperture reduction. But as the simulation has shown, due to the fact of moderate values of the betatron function in the final focus quadrupoles (540 m in vertical and 120 m in horizontal direction respectively) these sources of perturbation do not influence the aperture much.

4.3.6 Final focus lenses

Fig.4.3.37 schematically shows the vacuum chamber of the final focus section. The vacuum chamber parameters determine the design of the final focus elements and other magnetic elements which are located here. The beryllium vacuum chamber of a vertex detector 300 mm long from one side (the total length of the chamber is 600 mm) begins from the IP. The following 100 mm are reserved for the detector electronics. In this region the inner diameter and the thickness of the vacuum chamber are 40 mm and 1 mm, correspondingly. The angle between the beams is 60 mrad here. Then goes a transition gap approximately 150 mm long, where the chamber bifurcates into two chambers, each 20 mm in diameter. This gap houses a superconducting (SC) solenoid compensating the detector field, the solenoid aperture repeating the vacuum chamber aperture.

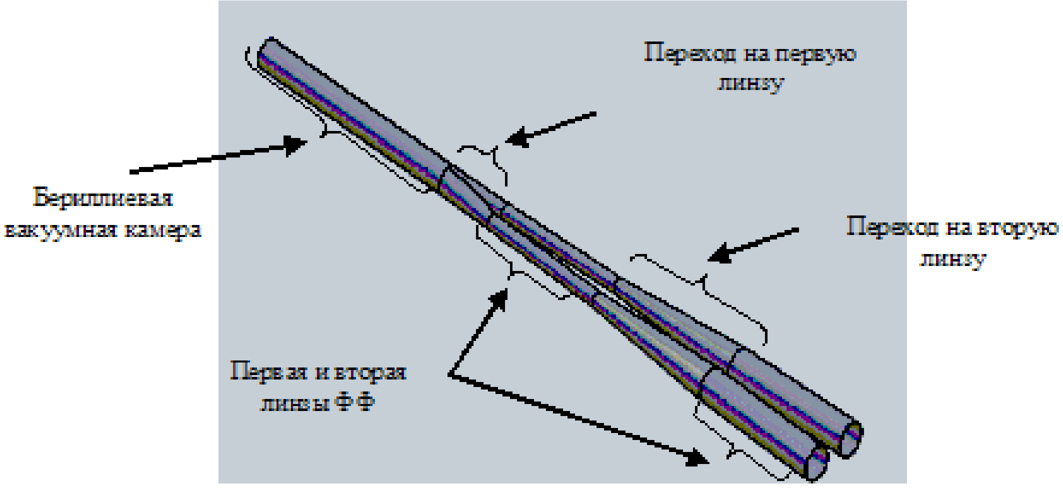

Fig.4.3.37 Vacuum chamber of the IP (schematic).

Further is the superconducting solenoid which ensures the absence of longitudinal field in the FF lens. The solenoid consists of two parts with different apertures (SSH1 and SSH2). The aperture of the solenoids is determined by the overall size of the lens and the vacuum chamber at the end of the solenoid. The first lens begins inside the shielding solenoid and is almost completely shielded from the longitudinal field of the compensating solenoid and the detector field. The first FF lens as well as the second one is 200 mm long. There is 300 mm of empty area between them. The first shielding solenoid covers the entire lens plus at least 50-100 mm of the empty area. This place requires careful and accurate elaboration since it determines the solid angle of the detector. The second shielding solenoid begins around the middle of the empty space between the FF lenses; the length of the solenoid is determined by the design of the yoke of the detector and also requires a detailed study.

The parameters of the magnetic elements of the FF section are presented in Table 4.3.3 while their schematic view is given in Fig.4.3.38.

Table 4.3.3 Parameters of the FF lenses and solenoids at energy of 2.5 GeV

Name	L_{eff} (mm)	*s* (mm)	B_{max} (kG), G_{max} (kG/)	R_{ap}, mm	ΔB/B, ΔG/G (%)	Type
L_0	0.595	0	10	40	1	IP
SC0	100	45	-45	45	1	SC compact solenoid
SSH1	350-600	55	-10	-	1	SC shielding solenoid
SEQ0 (NEQ0)	200	60	-10.7	10	0.01-0.05	2-aperture SC quadrupole lens
SSH2	700-900	85	-10	-	1	SC shielding solenoid
SEQ1 (NEQ1)	200	110	6.5	22	0.01-0.05	2-aperture SC quadrupole lens

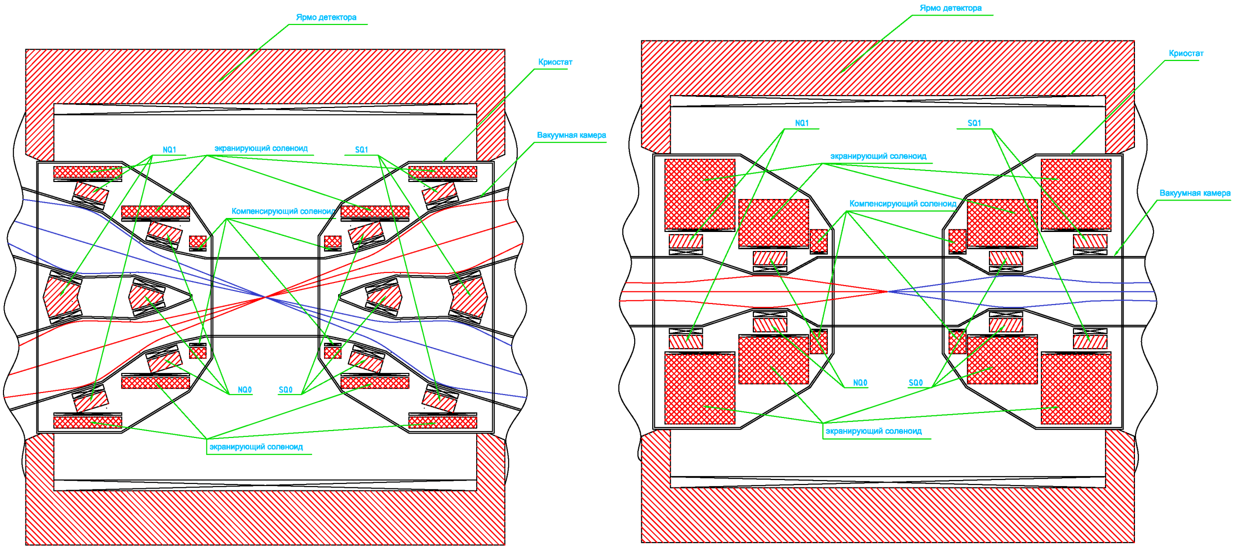

Fig.4.3.38 Top view (left) and the side view (right).

One of the most important elements in the final focus section are the first (defocusing) and second (focusing) quadrupole lenses that provide beam focusing at the IP.

The yoke of the first lens *SEQ0* (*NEQ0*) is located at a distance of 600 mm from the IP (the distance is indicated along the trajectory). The effective length of the lens is 200 mm; the overall length with the coils is less than 300 mm. The general view of the lens is shown in Fig.4.3.39. Calculations of the magnetic field (two-dimensional model) show that the accuracy of the gradient $\Delta G / G_0 \leq 4 \cdot 10^{-4}$ is achieved over the whole range of energy (Table 4.3.4, Fig.4.3.40) in the working aperture of the lens R = 10 mm. The field expansion harmonics listed in Table 4.5 have the following form:

$$B(x) = \sum_n A_n \cdot x^{n-1} .$$

The calculations also show that the dependence of the gradient on the energy is, with good accuracy, linear, despite the fact that the magnetic field induction in the yoke of the lens reaches 21-23 kG. The yoke of the lens is made of vanadium permendure with the magnetization curve shown in Fig.4.3.41.

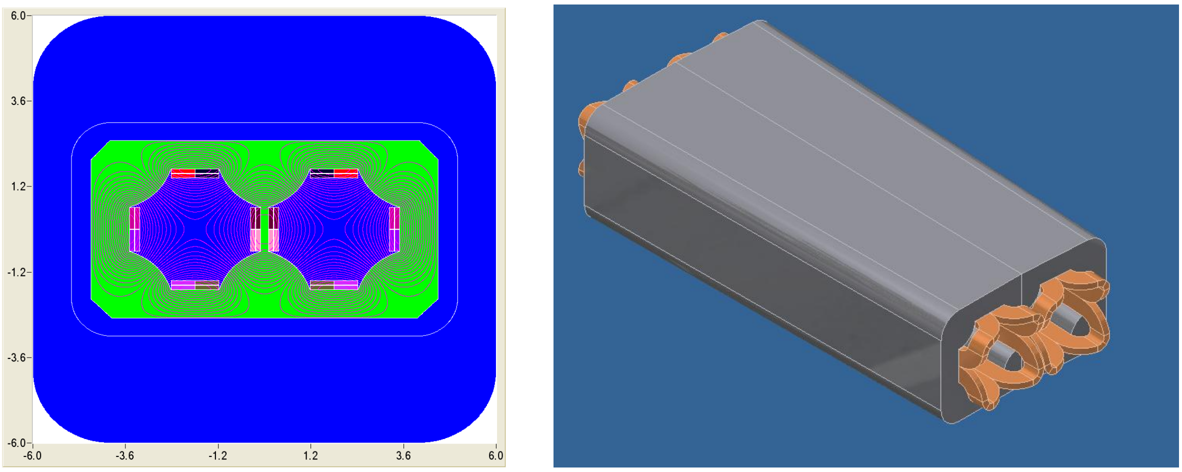

Fig.4.3.39 FF lens *SEQ0* (*NEQ0*). The cross section and the flux paths (left) and the general view (right).

Table 4.3.4 Main harmonics of the lens *SEQ0* (*NEQ0*)

	2.5 GeV	2 GeV	1.2 GeV
n	A_n, (kG/cm^{n-1})	A_n, (kG/cm^{n-1})	A_n, (kg/cm^{n-1})
2	-10.97	-9.08	-5.32
6	-0.0038	-0.0031	-0.0019
10	0.0021	0.0018	0.0011
14	0.0006	0.00046	0.00027
18	-2.2E-05	-1.8E-05	-1.1E-05

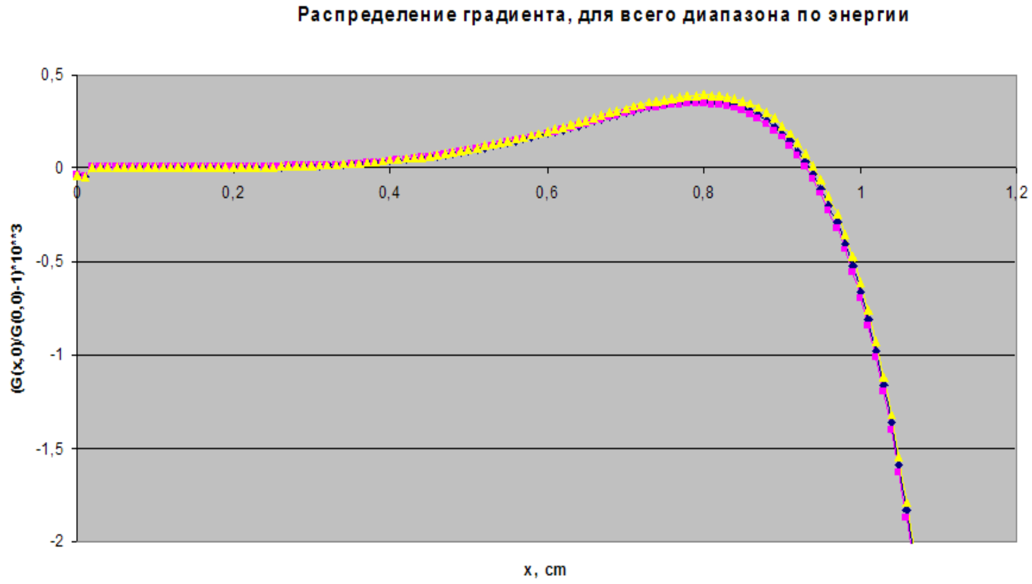

Fig. 4.3.40 Dependence of the gradient of the lens *SEQ0* (*NEQ0*) on the transversal coordinate for gradients of 11 kG/cm, 9 kG/cm and 5.3 kG/cm.

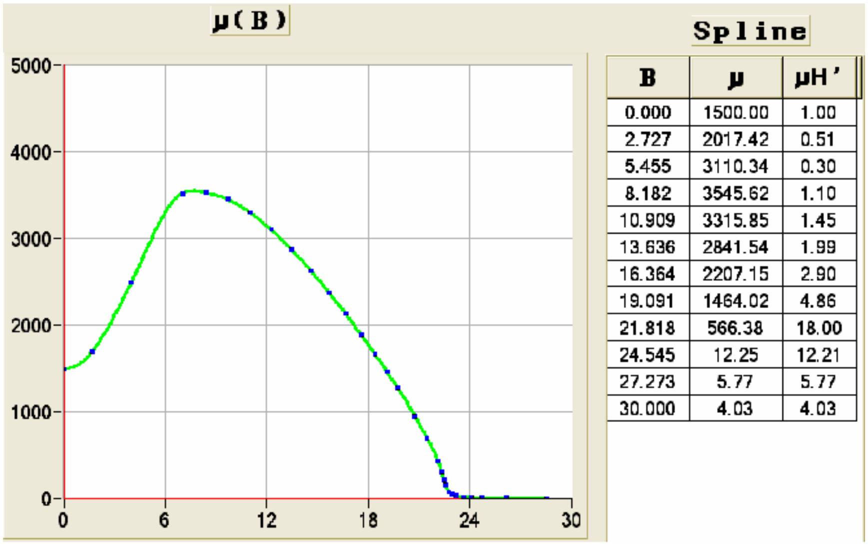

B	μ	μH'
0.000	1500.00	1.00
2.727	2017.42	0.51
5.455	3110.34	0.30
8.182	3545.62	1.10
10.909	3315.85	1.45
13.636	2841.54	1.99
16.364	2207.15	2.90
19.091	1464.02	4.86
21.818	566.38	18.00
24.545	12.25	12.21
27.273	5.77	5.77
30.000	4.03	4.03

Fig. 4.3.41 Magnetization curve of the permendure for the yoke of the FF lens.

The excitation coil of the lens is wound of superconducting *NbT* wire of a 1.20×0.75 mm rectangular cross section, manufactured by *Oxford Instruments*. The coil consists of two layers of 7 turns in each. The minimum bend radius is about 7 mm. The coil is wound in a simple flat shape as shown in Fig.4.3.42 and then bent into a saddle shape and made monolithic.

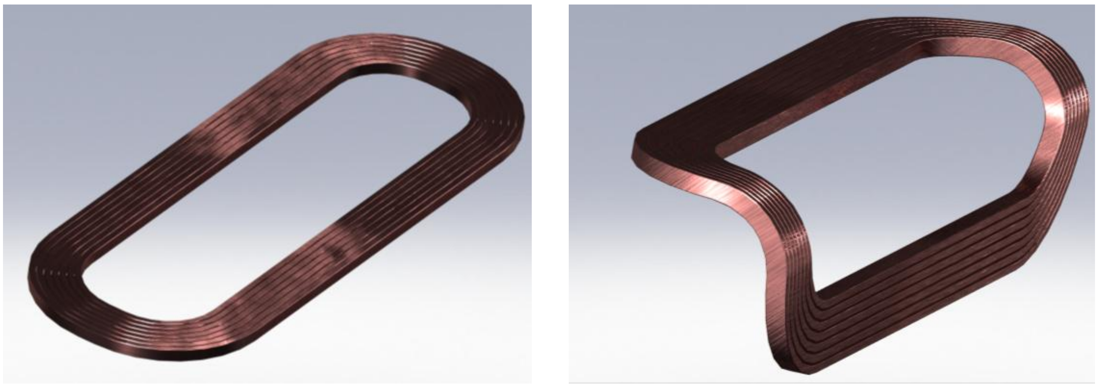

Fig. 4.3.42 Fabrication of the superconducting coil.

The design of the second (focusing) lens *SEQ1 (NEQ1)* in the final doublet is similar to that of the first lens; the gradient of the first lens is less, but the aperture is larger. Computation of the magnetic field shows that it is possible to obtain a gradient differing from the ideal one by $\Delta G / G_0 < 10^{-3}$ within the operation aperture R = 22 mm.

REFERENCES

1. Karl L. Brown, SLAC-PUB-4159
2. E.D. Courant, H.S. Snyder, Annals of Physics 3, 1-48 (1958)
3. Karl L. Brown, SLAC-PUB-3381
4. Bogomyagkov, S. Glukhov, E. Levichev, P. Piminov. Effect of the sextupole finite length on dynamic aperture in the collider final focus, http://Arxiv.Org/Abs/0909.4872
5. K. L. Brown and R. Servranckx, “First And Second Order Charged Particle Optics”, AIP Conf. Proc. 127, 62 (1985)
6. E.Levichev, P.Piminov. Algorithms for Chromatic Sextupole Optimization and Dynamic Aperture Increase. EPAC06-WEPCH085, EPAC’06, Edinburgh, Scotland, 26-30 Jun 2006

4.4 Beam-beam effects and luminosity

For flat ($\sigma_y << \sigma_x$) electron-positron beams colliding at an arbitrary horizontal angle θ, the luminosity and the shifts of the betatron tunes are determined by the following formulas [2, 3]:

$$L = \frac{\gamma}{2er_e} \cdot \frac{I \cdot \xi_y}{\beta_y},$$

$$\xi_x = \frac{N_p r_e}{2\pi\gamma} \cdot \frac{\beta_x}{\sigma_x^2 (1+\phi^2)}, \qquad \xi_y = \frac{N_p r_e}{2\pi\gamma} \cdot \frac{\beta_y}{\sigma_x \sigma_y \sqrt{1+\phi^2}},$$

$$\phi = \frac{\sigma_z}{\sigma_x} \cdot tg\left(\frac{\theta}{2}\right).$$

Here I is the total beam current, N_p is the number of particles in the bunch, ϕ is the Piwinski angle. Thus, it is clear that increasing the luminosity requires raising the total current and ξ_y as well as reducing the vertical beta function at the IP. In so doing, it is necessary to keep in mind that

1) Increasing the total current at the expense of the bunch amount (making the inter-bunch distances smaller) may be restricted by the beam interaction effects at parasitic IPs;
2) N_p is restricted by the collision effects (ultimate ξ) and the electromagnetic interaction of the beam with the vacuum chamber, which imposes limitations on the minimum bunch length;
3) At attempts to make $\beta_y < d$, where d is the length of the region of beam interaction ($d \approx \sigma_z$ for small ϕ), the ultimate ξ_y and luminosity will decrease due to the *hour-glass* effect.

All this makes a substantial increase in the luminosity impossible with the traditional methods.

In March 2006, the Italian physicist Pantaleo Raimondi suggested a fundamentally new scheme of beam collision [1] known as the Crab Waist scheme. Its main feature is a large Piwinski angle ($\phi \geq 10$), obtained by reducing σ_x at the IP (small emittance and β_x), so that the crossing angle θ is still small, about 50 ÷ 60 mrad. In this case, the size of the beam intersection region d becomes much smaller than the bunch length: $d \approx \sigma_z / \phi$ for $\phi >> 1$, which allows an abrupt reduction in β_y and gives a huge gain in the luminosity for the same total current. Additional advantages of this scheme are a small space charge parameter ξ_x and the absence of problems with parasitic IPs because of moving the beams far apart the in terms of σ_x.

Another fundamental feature relates to the "crab" sextupoles which are located on both sides of the IP, in places with a certain betatron phase advance. These sextupoles rotate the vertical "waist" of the beam at the IP, which is reflected in the name of the scheme. This rotation gives a small (5 ÷ 10%) gain in the luminosity due to geometrical factor, but their main effect is the strong suppression of the betatron and synchro-betatron coupling resonances [4, 5]. The ultimate value of the parameter ξ_y increases 2-3 times!

This scheme was first tried at the Italian Φ-factory DAΦNE, which increased its luminosity three times; a good agreement between the experimental data and the numerical simulations was achieved [6,7]. Now the CW scheme is the base of the project of the Italian Super B factory [8] and the Japanese Super KEKB factory.

At large ϕ, the expressions for the shift of the betatron tunes can be rewritten as follows:

$$\xi_x = \frac{2N_p r_e}{\pi\gamma} \cdot \frac{\beta_x}{(\theta\sigma_z)^2}, \qquad \xi_y = \frac{N_p r_e}{\pi\gamma} \cdot \frac{\beta_y}{\theta\sigma_z\sigma_y}.$$

It can be seen that a simultaneous increase in N_p and the bunch length leaves ξ_y unchanged and no problems with the high bunch current arise because its length is also growing.

On the other hand, it should be remembered that this scheme requires a fairly specific magnetic structure of the storage device. For example, there is a problem of obtaining a required dynamic aperture (including the energy acceptance), small emittances at high beam currents, etc. As a result, the maximum ξ_y may turn out to be determined not by the collision effects, as is usually the case, but by other factors.

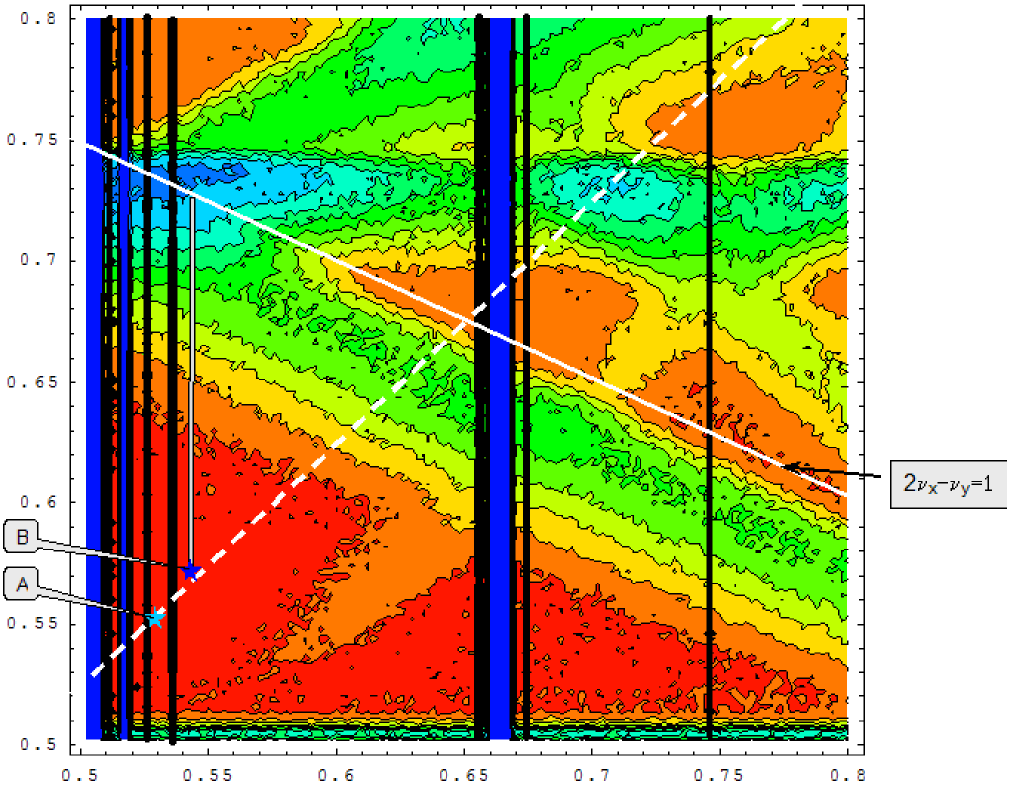

Fig. 4.4.1 Luminosity as a function of the betatron tunes for $\xi_y = 0.12$. Low and high luminosity is shown with the dark blue/black and red colors, correspondingly.

To study the BB effects in the Crab Waist scheme, identify the main factors limiting the luminosity, and choose the working point, a numerical simulation was carried out with the LIFETRAC code. A simplified model of the ring was used (a linear structure without betatron coupling). The rated vertical emittance was obtained at the expense of artificially imposed vertical noise. The results of the simulation – luminosity as a function of unperturbed betatron tunes – are shown in Fig.4.4.1. In the red region, the luminosity is in the range of $(1.0 \div 1.1) \cdot 10^{35}$ cm^{-2} s^{-1}. Of strong resonances limiting the good area we should note the horizontal synchro-betatron resonances (mainly the synchrotron satellites of the half-integer resonance), which are shown with the vertical blue and black stripes, as well as the low-order coupling resonance of $2\nu_x - \nu_y = 1$, which is shown with the white line. Since the shift of the horizontal tune ξ_x is very small at a large Piwinski angle (the spread of the tunes in the beam being even much smaller [9]), the beam-occupied region in the tune diagram («footprint») has the form of a narrow vertical stripe. This means that the horizontal synchro-betatron resonances do not restrict the luminosity but only the choice of the working point. The luminosity is limited by the resonance of $2\nu_x - \nu_y = 1$. The upper edge of the footprint (small betatron amplitudes) must remain below this resonance, which thus sets limits on ξ_y for every operating point. Therefore, to obtain the maximum luminosity it is necessary to move left and down along the dotted line, towards the half-integer resonance. For example, at the point (0.528, 0.550) (marked *A* in Fig.4.4.1), you can easily get ξ_y= 0.3, which is 2.5 times greater than the calculated value! In this case, the actual betatron tune shift $\Delta\nu_y$ will of course be less, about 0.19, which corresponds precisely to the distance from the resonance. In the simulation, this increase in ξ_y was achieved by simply raising the bunch current. In so doing, the horizontal emittance grew by 20% due to the collision effects; the vertical emittance, by 40%, the specific luminosity, 2.35 times and the "tails" of the equilibrium distribution remained around 10 σ_x and 15 σ_y.

On the other hand, the nonlinearities of the magnetic lattice of the storage ring taken into account, the spread of the horizontal betatron tunes will be more than just ξ_x. Therefore the choice of a working point cramped between two strong synchro-betatron resonances may be nonoptimal. Point *B* (0.545, 0.570) looks more attractive. Here the ultimate $\xi_y \approx 0.24$, and the corresponding footprint is shown in Fig.4.4.1 with the gray strip, which begins at this point and bears against the resonance line $2\nu_x - \nu_y = 1$.

Fig.4.4.2 shows the results of simulation for this operating point with different bunch currents. It can be seen that the vertical size and the specific luminosity vary only slightly with ξ_y increasing from 0.12 to 0.24, with a sharp jump following.

Increasing the bunch current in the simulation helps one to understand where the limits on the luminosity due to the BB effects are. However, in practice, the maximum bunch current will be limited by other factors: the bunch length, the power of the injector, etc. Another way to increase ξ_y is to reduce the vertical emittance, which also looks problematic since it will lead to a significant decrease in the lifetime of the beams, which is determined by the scattering on the colliding bunch and the intra-bunch scattering (Touschek effect).

ξ_y	0.12	0.18	0.24	0.30
Density	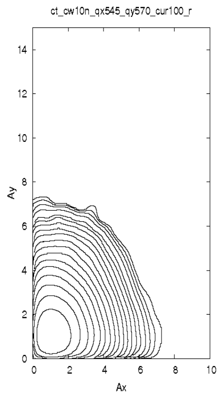	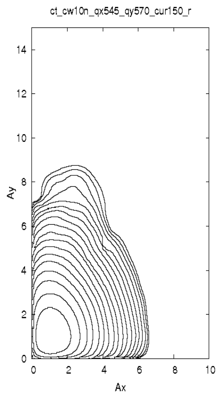	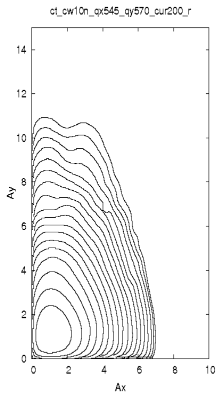	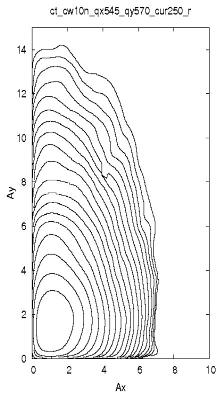
ϵ_y/ϵ_{yo}	1.12	1.16	1.30	2.23
L_c/L_{co}	1.00	0.99	0.96	0.85

Fig. 4.4.2 The equilibrium beam distribution in the plane of normalized betatron amplitudes, the vertical emittance, and the specific luminosity in dependence on ξy for the working point (0.545, 0.570). The distribution density on adjacent lines of the level differ *e* times. L_{co} is the specific luminosity for the nominal parameters (ξ_y = 0.12).

Besides, the choice of the operating point is determined not only by the BB effects but also by the nonlinear structure of the storage ring. The calculations show that, because of the strong nonlinear chromaticity, the dynamic aperture for particles with non-equilibrium energy is small near the half-integer resonance. Therefore it is necessary to raise the betatron tunes. If there is no need to increase the rated ξ_y, which already provides a luminosity of 10^{35} $cm^{-2}s^{-1}$, the choice of the betatron tunes becomes much wider: any red dot (see Fig.4.4.1) to the right and above point *B*. The final choice will be made after the end of the optimization of the dynamic aperture.

We can conclude that for the calculated parameters, the collision effects will not have a significant influence on the beam dynamics. The calculated value $\xi_y = 0.12$ is small and allows varying the operating point in a fairly wide range. If it can be moved closer towards the half-integer resonance, the ultimate ξ_y grows. This opens up the possibility of obtaining higher luminosity.

REFERENCES

1. P. Raimondi, Status of the SuperB Effort, presentation at the 2nd Workshop on Super B Factory, LNF-INFN, Frascati, March 2006
2. P. Raimondi and M. Zobov, DAΦNE Technical Note G-58, April 2003;
3. D. Shatilov and M. Zobov, ICFA Beam Dyn. Newslett. 37, 99 (2005)
4. P.Raimondi, D.Shatilov, M.Zobov, “Beam-Beam Issues for Colliding Schemes with Large Piwinski Angle and Crabbed Waist”, LNF-07-003-IR, Feb. 2007, e-Print: physics/0702033.
5. P.Raimondi, D.Shatilov, M.Zobov, “Suppression of beam-beam resonances in Crab Waist collisions”, Proc. of EPAC08, Genoa, Italy, 23-27 Jun. 2008.
6. M.Zobov et al., “Test of crab-waist collisions at DAFNE Phi factory”, Phys.Rev.Lett.104:174801,2010.
7. M.Zobov, “Beam-Beam Interaction in Novel, Very High Luminosity Parameter Regimes”, Proc. of IPAC10, Kyoto, Japan, 23-28 May 2010.
8. M.Bona et al., “A High-Luminosity Asymmetric e+e- Super Flavor Factory. Conceptual Design Report”, SLAC-R-856, INFN-AE-07-02, LAL-07-15, May 18, 2007, e-Print: arXiv:0709.0451.
9. D.Shatilov, E.Levichev, E.Simonov, “Aplication of Frequency Map Analysis to Beam-Beam Effects Study in Crab Waist Collision Scheme”, arXiv:1002.3733.

4.5 Longitudinal polarization at the IP

Spin-polarized electrons arise on the photocathode of the source with energy of 100 keV to 200 keV and then are accelerated to the energy required in the experiment, 1 GeV to 2.5 GeV. A spin manipulator of the source can set any desirable direction of the electron spin at the point of their injection into the ring. It remains to arrange such a closed spin trajectory along the ring circumference that the spin is directed longitudinally at the point of the electron-positron collision.

4.5.1 Closed spin orbit. Spin rotators.

We suggest installing 5 spin rotators – Siberian snakes [1] – on the electron storage ring, each snake rotating the spin through 180^0 around the longitudinal axis of the accelerator coordinate system. Each snake consists of two SC solenoids separated by a mirror-symmetrical optical system of 7 quadrupole lenses, see Fig.4.5.1. The total integral of the field of the two solenoids is

$$\int Bdl = \pi B\rho = 26 \ \mathrm{T\cdot m}, \quad \text{if} \quad \mathrm{E=2.5\ GeV}$$

The transport matrix of the spin rotator, including the solenoids, must comply with the following two conditions: 1) zero 2x2 off-diagonal blocks, 2) spin transparency. Both these requirements are met for a full Siberian snake if [2]

$$\mathrm{T_x} = -\mathrm{T_y} = \begin{pmatrix} -\cos(2\varphi) & -2r\sin(2\varphi) \\ (2r)^{-1}\sin(2\varphi) & -\cos(2\varphi) \end{pmatrix} = \begin{pmatrix} 1 & 0 \\ 0 & 1 \end{pmatrix}$$

where φ is the angle of spin rotation by one solenoid. For a full snake $\cos(2\varphi) = -1$. If $\varphi < \pi/2$, the snake is called partial. Unfortunately, it yields to a full one and will not be considered here.

A method of compensation of the solenoid-introduced betatron coupling via inserting an optical system meeting the condition $T_x = -T_y$ between the solenoids was proposed in [3]. A big advantage of this method is no need to use any skew-quadrupoles. In this scheme the solenoid field may vary in a wide range without changing the strength of the quadrupole lenses, including their complete switching off, the coupling remaining zero in this case. Though, if one wants to leave the advance of the betatron phases unchanged throughout the insert, the field gradients in the lens still have to be slightly corrected. The main advantage is that there is no need to rotate the lenses around the longitudinal axis as it is with some alternative schemes of compensation of coupling also considered in [3].

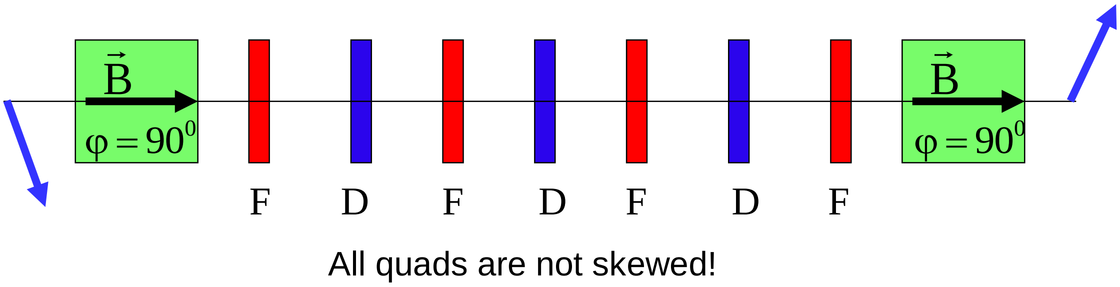

Fig. 4.5.1 Optical scheme of the spin rotator – the Siberian snake rotating the spin through 180^0 around the axis of the solenoids.

With an odd number of the snakes the spin in the arcs of the ring lies in the median plane and takes exactly the longitudinal direction in the middle of the arcs between the snakes. It is presented schematically in Fig.4.5.2, where the equilibrium direction of the spins – a closed spin trajectory – in the ring with the three snakes evenly placed in azimuth is shown.

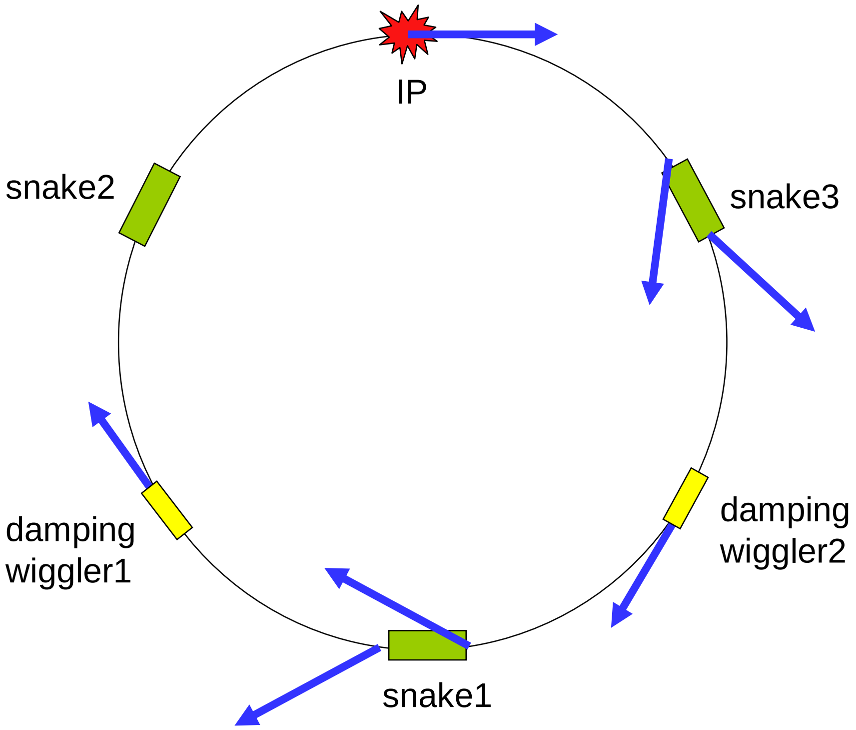

Fig. 4.5.2 The equilibrium closed spin trajectory in the ring with three Siberian snakes. The depolarizing influence from the damping wigglers is minimal if they are situated in those places where the spin is longitudinal.

4.5.2 Radiative relaxation of spins

The larger the number of the snakes installed on the ring, the greater the depolarization time reached. The depolarization time increases proportionally to the square of the number of the snakes. We chose five snakes providing perfect preservation of the electron beam polarization across the energy range. At low-energy operation it is possible to use a smaller number of snakes. The analytical estimates of the azimuth-averaged squared modulus of the vector of the spin-orbit coupling for a ring with n_{snk} Siberian snakes give the following result:

$$\left\langle \vec{d}^2 \right\rangle = \vec{d}^2(0) + \frac{\pi^2}{3}\frac{\nu^2}{n_{snk}^2}$$

$$\vec{d}^2(0) = \frac{\pi^2}{4}\sin^2\frac{\pi\nu}{n_{snk}}$$

Here $\vec{d}$ is the spin-orbit coupling vector, $\vec{d}^2(0)$ is the squared modulus of it at the minimum point, $\left\langle \vec{d}^2 \right\rangle$ is its value averaged over the arc length, and $\nu = E(\mathrm{MeV})/440.652$ is the spin frequency. The azimuthal dependence of $\vec{d}^2(\theta)$ for the cases of $n_{snk} = 1$ and $n_{snk} = 3$ for the electron energy $E = 1$ GeV is presented in Fig.4.5.3. Knowing the behavior of $\vec{d}$ in the ring, it is easy to calculate the time of the radiation spin relaxation as well as the equilibrium degree of radiation polarization. They are determined from the known formulas by Derbenev and Kondratenko [4]:

$$\xi_{\mathrm{rad}} = -\frac{8}{5\sqrt{3}} \frac{\left\langle |\mathrm{r}|^{-3}\, \vec{\mathrm{b}}\left(\vec{\mathrm{n}}-\vec{\mathrm{d}}\right)\right\rangle}{\left\langle |\mathrm{r}|^{-3}\left(1-\frac{2}{9}(\vec{\mathrm{n}}\vec{\mathrm{v}})^2+\frac{11}{18}\vec{\mathrm{d}}^2\right)\right\rangle}$$

$$\tau_{\mathrm{rad}}{}^{-1} = \frac{5\sqrt{3}}{8}\lambda_e r_e c\gamma^5 \left\langle |\mathrm{r}|^{-3}\left(1-\frac{2}{9}(\vec{\mathrm{n}}\vec{\mathrm{v}})^2+\frac{11}{18}\vec{\mathrm{d}}^2\right)\right\rangle$$

Here r is the radius of curvature of the orbit in the dipole magnets, $\vec{b}$ is the unit vector directed along the field in these magnets, $\vec{n}$ is the unit vector of the equilibrium spin direction, $\vec{v}$ is the unit vector directed along the velocity, and the rest designations are standard.

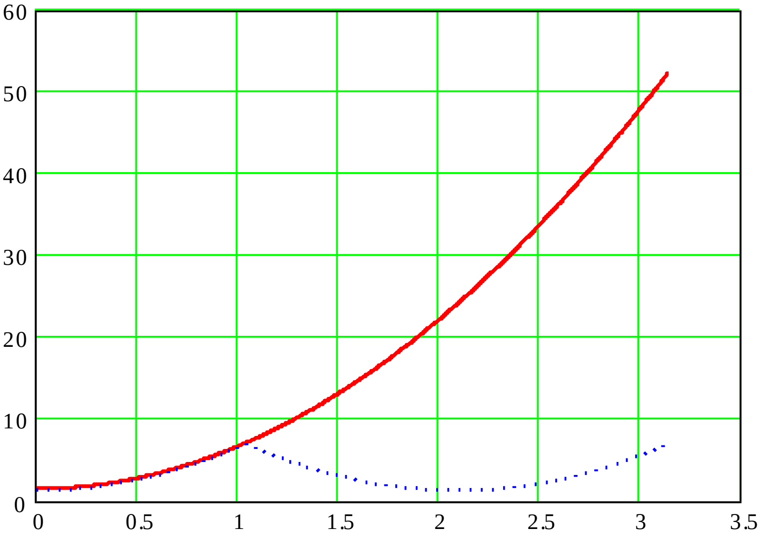

Fig.4.5.3 Azimuthal dependence of the squared modulus of the vector of the spin-orbit coupling at the energy $E = 1\,\mathrm{GeV}$ with one and three (dark blue dots) Siberian snakes.

At the $c\tau$-factory the wigglers are supposed to be used for the regulation of the radiative damping decrements, namely, to maintain the damping time of around 30 ms in the entire energy range of the complex. At low energy the wigglers are turned on for the maximum field, while at the maximum energy near 2.5 GeV the wigglers are completely turned off. When calculating the time of depolarization in the storage ring, it is necessary, of course, to consider the influence of the wigglers on this process. As seen in Fig.4.5.4, the contribution of the damping wigglers strongly depends on the place of their location. If they stand in such segments of the ring where the modulus of the spin-orbit coupling is minimal (in the middle of the arc between the two wigglers), their effect is negligible. If they are distributed evenly over the ring, their influence is quite palpable.

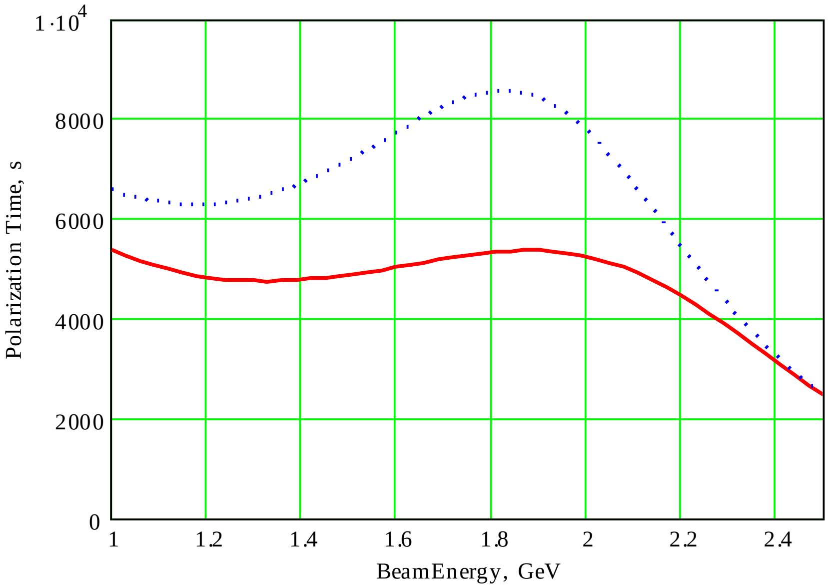

Fig.4.5.4 Dependence of the time of spin relaxation on the electron energy in the variant with five Siberian snakes. The solid curve corresponds to the uniform placement of the wigglers over the ring, and the dots show the preferable variant of placing the damping wigglers at points with the minimum modulus of the spin-orbit coupling.

4.5.3 Time-averaged degree of polarization

With the Siberian snakes on the ring, the equilibrium degree of radiative polarization of the beams almost vanishes. This is a positive moment because a definite sign of beam polarization may lead to systematic errors in the analysis of the spin asymmetry of the processes of interest. It is planned to randomly inject several (up to a few hundreds) bunches of polarized electrons into different separatrices and mark all the recorded events with the number of the separatrix they correspond to. The loss of particles occurring mainly due to the bremsstrahlung on the counter beam, of course, must be made up for with the fresh-polarized electrons. As a result, some equilibrium polarization degree determined by the balance of particles surviving in the ring for different times will establish gradually. It is easy to show that the equilibrium polarization degree is equal to

$$\xi = \xi_{beam} \frac{\tau_{rad}}{\tau_{beam} + \tau_{rad}} + \xi_{rad} \frac{\tau_{beam}}{\tau_{beam} + \tau_{rad}}$$

Here $\xi_{beam} = 90\%$ is the degree of polarization of the fresh beam; $\xi_{rad} \approx 0\%$ is the degree of the radiative self-polarization of electrons in the ring; $\tau_{beam} = 1000$ sec is the lifetime of the particles in the ring; τ_{rad} is the time of the radiative polarization of the spins. Fig.4.5.6 presents the plots of the time-averaged degree of electron beam polarization for 1, 3, and 5 snakes. These results were obtained analytically and confirmed by computations with the ASSPIRIN program [5,6]. It is seen from the figure that the variant with 5 snakes ensures a polarization degree of about 80% across the accelerator energy range.

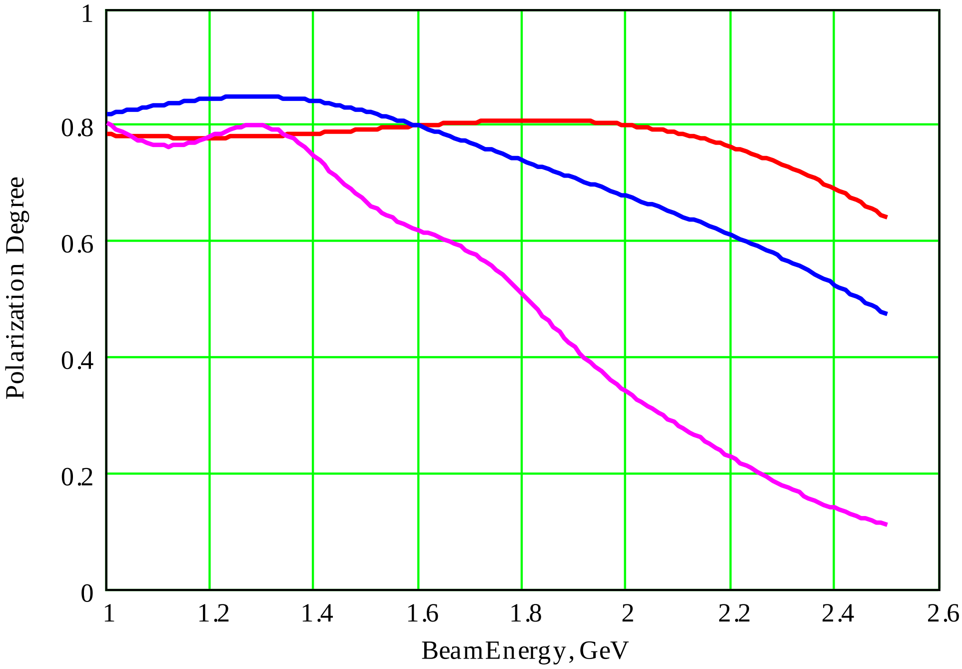

Fig.4.5.6 Time-averaged degree of electron polarization in the ring of the c-tau factory for 1 (magenta), 3 (blue), and 5 (red) snakes.

4.5.4 Technical aspects of the realization of the spin rotators

A set of two superconducting solenoids and seven quadrupole lenses should be created for each of the spin rotators. One solenoid is 2 m long and has a maximum field of 6.5 Tesla and a 4-cm aperture. It seems that a solenoid with such parameters can be cooled with a three-stage cooler and placed in just a vacuum cryostat without liquid helium. Such experiments using indirect cooling of small superconducting devices are currently under way.

The total length of the Siberian snake is about 10 meters, or about 1.5% of the entire perimeter. All the quadrupole lenses have the same specifications as the main lenses of the ring.

We have investigated the issue of the field of tolerances for the deviation of the gradients of the lenses from the nominal values. No too severe restrictions on the precision of control over the currents of the lenses were found. In fact, deviations of the field in the lenses and solenoids of up to 10% lead to no substantial increase in the vertical emittance.

REFERENCES

1. Ya.S.Derbenev et al. “Radiative Polarization: Obtaining, Control, Using”, Part.Acc. 8, 115, 1978.
2. I.A.Koop, A.V.Otboyev, P.Yu.Shatunov, Yu.M.Shatunov.”Orbit and Spin transparent Siberian Snake and Spin Rotator with Solenoids”, SPIN2006, Nagoya, Japan, 2006.
3. A.A.Zholents and V.N.Litvinenko, “On the Compensation of Solenoid Field Effects by Quadrupole Lenses”, DESY-L-TRANS-289, Mar 1984. 9pp. Translation of Novosibirsk preprint IYF-81-80 (translation).
4. Ya.S.Derbenev, A.M.Kondratenko, “Polarization kinematics of particles in storage rings”, Sov.Phys.JETP 37:968-973,1973, Zh.Eksp.Teor.Fiz.64:1918-1929,1973.
5. V.I. Ptitsyn , Ph.D. Thesis, Novosibirsk, BINP, 1997 (in Russian).
6. V.I. Ptitsyn, (Brookhaven), Yu.M. Shatunov, (Novosibirsk, BINP), S.R. Mane, (Convergent Computing, Shoreham, NY). “Spin response formalism in circular accelerators”. Published in Nucl.Instrum.Meth.A608:225-233,2009.

4.6 Beam life time

The life time of the beams depends strongly on the particle loss due to their scattering on the counter beam at the IP (Fig.4.6.1). This influence is proportional to the luminosity of the collider

$$\frac{dN}{dt} = -\sigma \cdot L\,,$$

where σ is the cross section of the process and L is the luminosity. Naturally, the role of this influence increases with the luminosity.

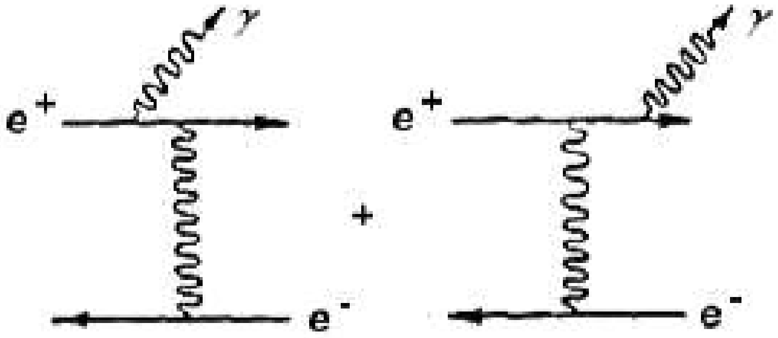

Fig. 4.6.1 Inelastic scattering of the particles of the colliding beams.

If the luminosity is considered constant, the dependence of the number of the particles on the time may be estimated approximately as

$$N(t) \approx N_0 e^{-\Delta t \frac{\sigma \cdot L}{N_0}}\,.$$

It is necessary to distinguish between elastic scattering, $e^+e^- \to e^+e^-$, and single bremsstrahlung from one particle in the field of another particle, $e^+e^- \to e^+e^-\gamma$. The cross section of the elastic process that leads to loss of a particle if the angle of its deviation exceeds the acceptance of the accelerator is in this case more than one order of magnitude smaller than the bremsstrahlung cross section.

A standard quantum electrodynamics (QED) calculation of the E_γ-differential cross section of single bremsstrahlung gives the following:

$$d\sigma_{cl} = \frac{16\alpha}{3} r_0^2 \frac{dy}{y}\left[1 - y + \frac{3}{4}y^2\right]\left[\ln\left(\frac{4\gamma^2(1-y)}{y}\right) - \frac{1}{2}\right],$$

where $y = E_\gamma / E_b$, E_b is the beam energy, and r_0 is the classical electron radius. Small momentum transfers corresponding to large impact parameters contribute to single bremsstrahlung. This makes the process cross-section sensitive to various macroscopic effects. As was shown in experiments on VEPP-4, the restriction of the impact parameters by the transverse dimension of the beam is the most important.

Single bremsstrahlung can be considered as the scattering of virtual photons accompanying an electron on a counter electron. Virtual photons with an energy ω fill a disk of the radius $\rho \sim \gamma / \omega$. The main contribution to the bremsstrahlung cross-section comes from the photons with the energy $\omega \sim E_\gamma / 4\gamma^2$, for which the effective "disk" has a characteristic radius

$$\rho \sim \frac{4\gamma^2}{E_\gamma} \approx 4 \text{ mm} \qquad \text{at} \qquad E_\gamma / E_b = 0.01.$$

Since the transverse beam size is <<4 mm, not all virtual photons encounter electrons, and a standard QED calculation gives an overestimated cross section. The impact parameters of the process were allowed for correctly in [1, 2], and the results of these studies are used below to estimate the lifetime of the beams at the $c\tau$-factory. The single-bremsstrahlung cross-section obtained in the standard manner and subject to the amendments is shown in Fig.4.6.2.

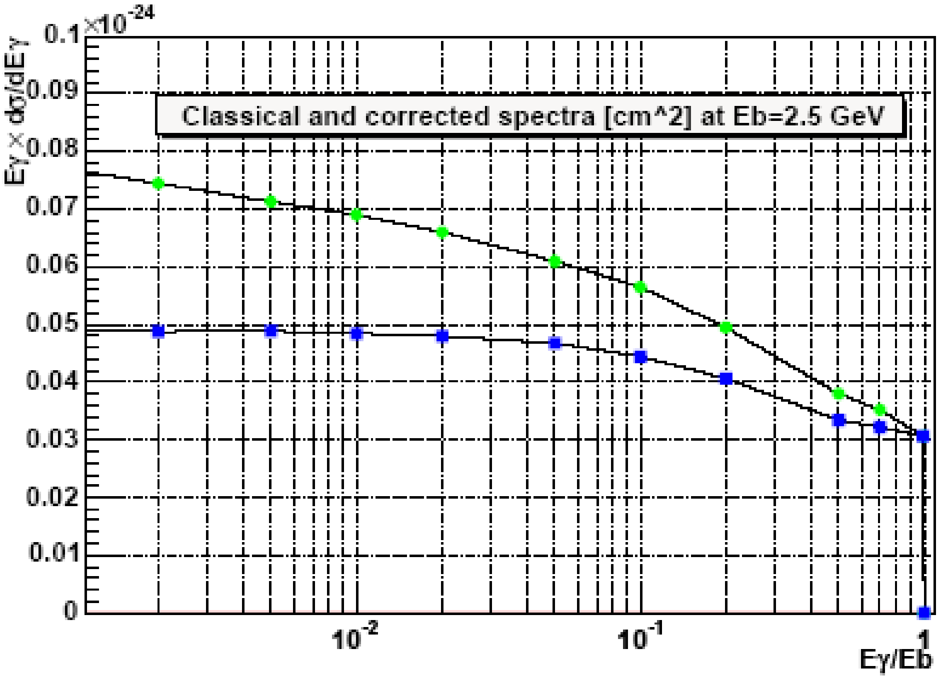

Fig. 4.6.2 Bremsstrahlung cross-section (to one side) at $E_b = 2.5\,\text{GeV}, \sigma_y = 0.39$ μm and $\sigma_x = 14$ μm. The upper curve is the result of a standard QED calculation; the lower one was obtained with the impact parameters taken into account.

The rate of the particle loss and the beam life time determined by single bremsstrahlung, calculated for the $c\tau$-factory parameters subject to the restriction of the impact parameters are shown in Fig.4.6.3. The minimum life time in the energy range of ~1.8÷2.5 GeV is 1600 seconds.

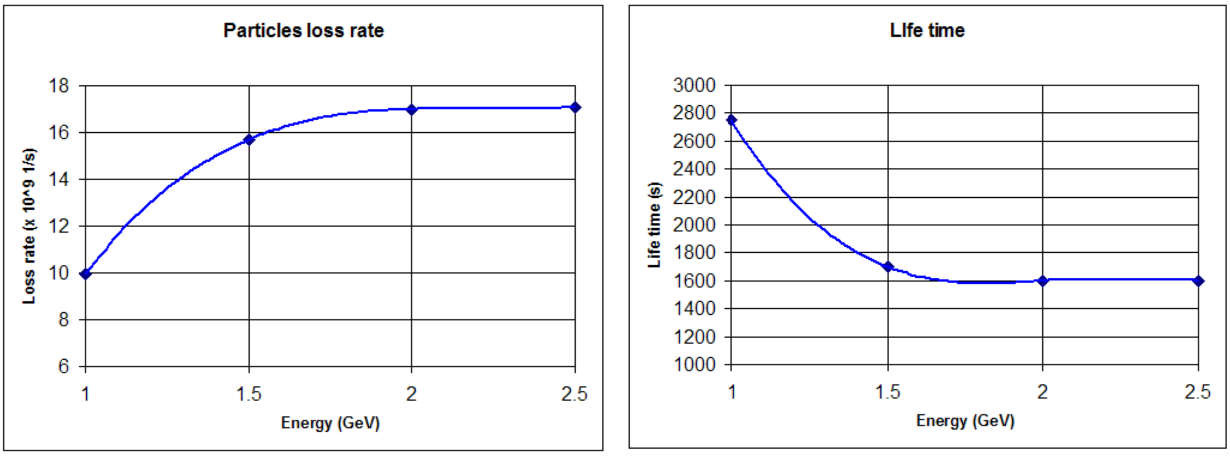

Fig. 4.6.3 Particle loss (left) and beam life time (right) for single bremsstrahlung.

For low beam emittance and the fairly large bunch intensity it is expected that the intra-bunch scattering of particles (Touchek effect), which is determined as [4]

$$\tau_T^{-1} = \frac{1}{N}\frac{dN}{dt} = \frac{Nr_0^2 c}{8\pi\sigma_x\sigma_y\sigma_z}\frac{\lambda^3}{\gamma^2}D(\xi),$$

where λ is the energy aperture

$$\xi = \left(\frac{\Delta E/E}{\gamma}\right)^2 \frac{\beta_x}{\varepsilon_x},$$

and the $D(\xi)$ function is determined as [3]

$$D(\xi) = \sqrt{\xi}\left(\ln\left(\frac{1}{1.78\xi}\right) - \frac{3}{2}\right)$$

will be one more important effect influencing the life time of particles at the $c\tau$-factory.

The energy aperture, the size of which influences the “Touchek” life time very much, is chosen as the least of the RF acceptance and the energy dynamical aperture, the latter being determinative in this case.

The life time determined by the intra-bunch scattering was modeled for a realistic accelerator structure using a modified Piwinsky algorithm [5]. The results of the modeling at energy of 2 Gev are presented in Fig.4.6.4.

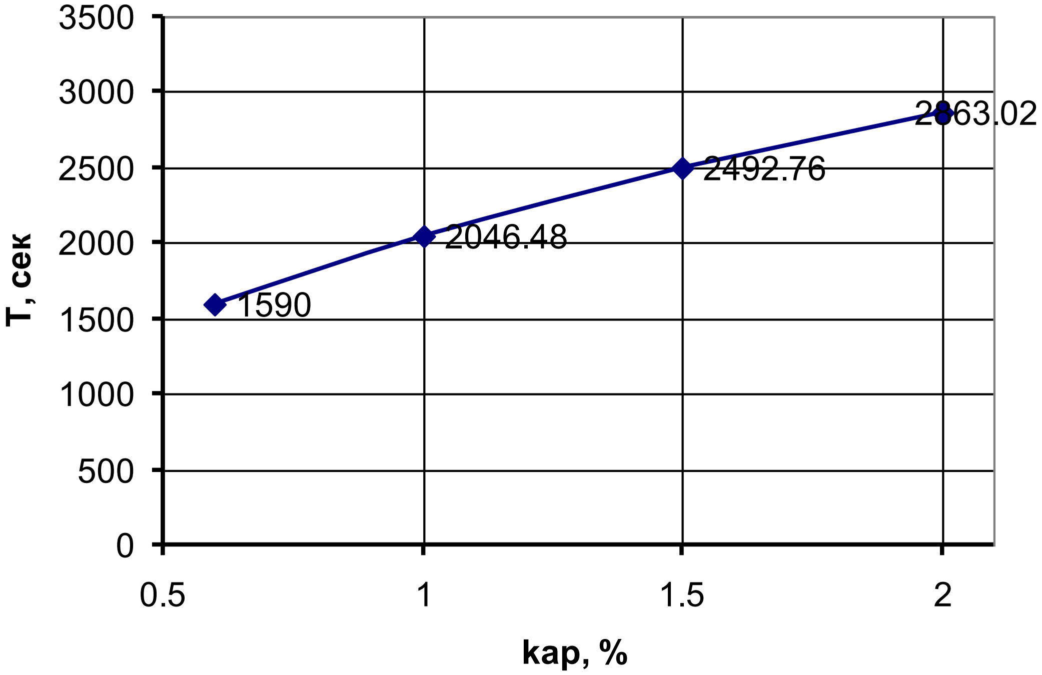

Fig. 4.6.4 Life time determined by the intra-bunch scattering as a function of the betatron coupling for energy of 2 GeV.

REFERENCES

1. V.N.Bayer et al., Yadernaya Fizika 36 (1982), 163. (in Russian)
2. G.K.Kotkin et al., Yadernaya Fizika 42 (1985), 925. (in Russian)
3. J. Le Duff, Proc. CERN Accelerator School, 2nd Advanced Accel. Physics Course, Berlin, 114 (1987).
4. H.Bruck, “Circular particle accelerators”, LA-TR-72-10, Los Alamos, NM, p.323.
5. A. Piwinski, in Handbook of Accelerator Physics and Engineering, edited by A. Chao and M. Tigner (World Scientific, Singapore, 1999), p. 125; K.Kubo, S.Mtingwa and A.Wolski, Phys. Rev. ST Accel. Beams 8, 081001 (2005).

4.7 Collective effects

4.7.1 Collective effects

The interaction of an intense beam of charged particles with the electromagnetic fields induced by it in a vacuum chamber (wake-fields) leads to various collective effects in the beam dynamics. These effects depend on the beam intensity and manifest themselves with a large number of particles in the beam. The most significant result of the collective effects is the instability of beam motion. When the resonance conditions are met, small deviations in the beam position or energy can increase because of the beam interaction with the wake-fields. Such positive feedback leads to instability of the oscillations and, consequently, beam loss or degradation.

In the frequency domain, the beam interaction with the components of the vacuum chamber through the wake-fields is described with the frequency-dependent coupling impedances. The presence of sections with narrow-band impedance (e.g. the parasitic higher modes of the accelerating cavities) in the accelerator may give rise to multi-bunch instability, and the broadband impedance can cause single-bunch instability of the beam. The foundations of the theory of collective effects, instabilities, and coupling impedances are given in [1, 2, 3].

The vacuum chamber of accelerator as a whole is usually represented as a broadband impedance obtained by summing the broadband impedances of all the components of the chamber. The broadband impedance can be assumed additive since the wake-fields decay rapidly, and the interference of the beam-excited wake-fields in different components of the vacuum chamber can be ignored in practice. The value of the total broadband impedance is used to estimate the single-bunch stability of the beam motion and is a criterion of the quality of the vacuum chamber design and manufacturing.

For estimating the maximum allowable coupling impedances of the collider to design, it would be useful to consider the experience of the existing B-factories – KEKB and PEP-II. It makes sense to compare the parameters of the storage rings, the beam energy of which is close to energy of 2.5 GeV, which was chosen for the $c\tau$-factory. Those are the KEKB LER with energy of 3.5 GeV and PEP-II LER with energy of 3.1 GeV. The energy of the KEKB HER and PEP-II HER storage rings is 8 GeV and 9 GeV, respectively, which is significantly higher than the design energy of the $c\tau$-factory under consideration.

The main parameters of KEKB LER, PEP-II LER and $c\tau$-factory that are of interest for the analysis of the collective effects as well as the results of the instability estimates are presented in Tables 1 and 3 (see Attachment).

4.7.2 Beam lengthening

The beam-induced electromagnetic fields change the shape of the accelerating RF field that affects the beam, which results in the distortion of longitudinal distribution of the particles and beam lengthening, while the energy spread does not change. The beam lengthening caused by the potential well distortion is described with the following equation:

$$\left(\frac{\sigma_s}{\sigma_{s0}}\right)^3 - \frac{\sigma_s}{\sigma_{s0}} + I_b \frac{\alpha \operatorname{Im}\left(Z_\parallel / n\right)_{\text{eff}}}{\sqrt{2\pi}\,\frac{E}{e}\nu_s^2}\left(\frac{R}{\sigma_{s0}}\right)^3 ,$$

where I_b is the beam current, $\sigma_{s0} = \dfrac{c\alpha}{\nu_s\omega_0}\dfrac{\sigma_E}{E}$ is the bunch length at a zero current, $\dfrac{\sigma_E}{E}$ is the relative energy spread, R is the mean radius of the accelerator, α is the momentum compaction factor, ω_s is the synchrotron frequency (in units of the revolution frequency ω_0). The effective impedance $\left(Z_\parallel / n\right)_{\text{eff}}$, which is often used to estimate the beam stability, is the weighted normalized impedance $Z_\parallel / n$ averaged over the beam frequency spectrum [7]. There is an approximate relation between the low-frequency broad-band impedance and the effective one, which depends on the rms bunch length. For short bunches, if the rms bunch length $\sigma_t = \sigma_s / c$ is by far less than $1/\omega_c$, where $\omega_c = c/b$ is the characteristic frequency of the impedance (b is the characteristic transverse dimension of the vacuum chamber), we have $\left(Z_\parallel / n\right)_{\text{eff}} \approx \omega_c\sigma_t\left(Z_\parallel / n\right)_{\text{BB}}$, while for long bunches, i.e. if $\sigma_t > 1/\omega_c$, it may be considered that $\left(Z_\parallel / n\right)_{\text{eff}} \approx \left(Z_\parallel / n\right)_{\text{BB}}$.

If the beam current exceeds a threshold value, the interaction of the beam with the longitudinal impedance leads to microwave instability of the longitudinal motion. Above the instability threshold, increase in the beam current is accompanied by growth both in the longitudinal dimension and in the beam energy spread. For a relativistic beam, the peak value of the threshold bunch current I_p can be estimated using the following formula [8,9]:

$$I_p \le \frac{\alpha}{\left|Z_\parallel / n\right|}\frac{E}{e}\left(\frac{\Delta p}{p}\right)^2_{FWHM},$$

where $\dfrac{\Delta p}{p} = \dfrac{\gamma^2}{\gamma^2 - 1}\dfrac{\Delta E}{E}$ is the width of the particle distribution throughout the longitudinal momentum, which is equal to the energy spread $\dfrac{\Delta E}{E}$ for relativistic beams. For a bunch with Gaussian density distribution and the rms length ω_s, the relation of peak bunch current I_p and the average current I_b is:

$$I_p = \frac{\sqrt{2\pi}R}{\sigma_s} I_b .$$

The average threshold current of the microwave instability is determined by the following expression [47]:

$$I_b \le \frac{\sigma_{s0}}{R}\frac{\sqrt{2\pi}\alpha\dfrac{E}{e}}{\left|Z_\parallel / n\right|_{\text{eff}}}\left(\frac{\sigma_E}{E}\right)^2 . \tag{4.7.1}$$

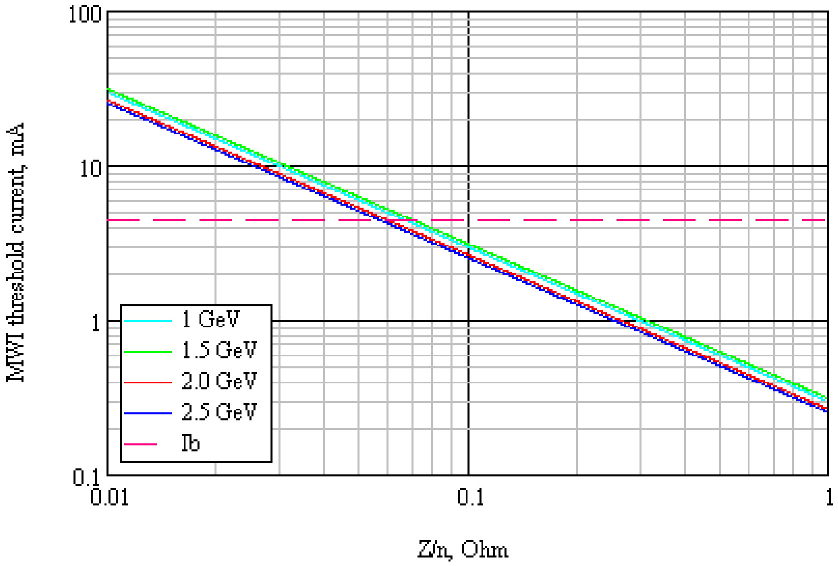

Fig. 4.7.1 The average threshold current of microwave instability

Fig.4.7.1 shows microwave instability threshold current versus the normalized longitudinal impedance. It can be seen that the design bunch current of 4.4 mA will not exceed the instability threshold at normalized impedance less than 70 milliohms. For comparison, the KEKB LER threshold current calculated by formula (4.7.1) using parameters from Table 1 is 0.1 mA (the working bunch current is 0.5 mA); the PEP-II LER threshold current is 3 mA (the bunch current is 1.3 mA).

Above the threshold of microwave instability, the bunch lengthening as a function of the current is described for a relativistic electron or positron beam with the Gaussian distribution of linear density by the following cubic equation [42, 43]:

$$\left(\frac{\sigma_s}{R}\right)^3 = I_b \frac{\alpha}{\sqrt{2\pi}\frac{E}{e}\nu_s^2}\left(\left|\frac{Z_\parallel}{n}\right|_{\text{cr}} + \left|\frac{Z_\parallel}{n}\right|_{\text{eff}}\right),$$

where $\left|\frac{Z_\parallel}{n}\right|_{\text{cr}}$ is the impedance value at the critical frequency $\omega_c = c/b$, which mainly determines the turbulent bunch lengthening. Fig.4.7.2 shows the plots of the bunch length as a function of the bunch current for three values of the normalized longitudinal impedance at energy of 2 GeV and the fixed accelerating voltage U_{RF}=0.99 MV. It should be noted that the KEKB LER bunch stretching is about 20% at the working current.

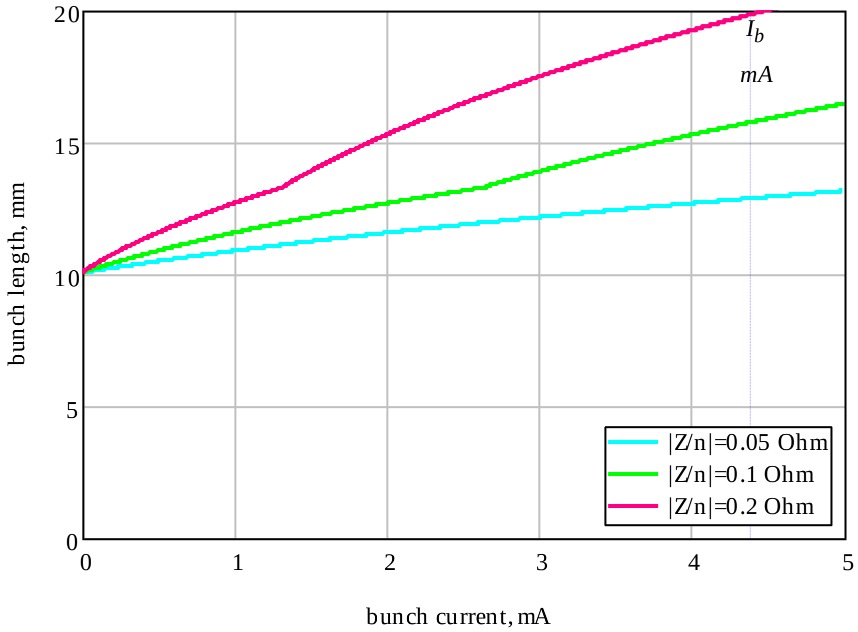

Fig. 4.7.2 Bunch lengthening as a function of the current.

If it is necessary to keep the longitudinal beam size at any current, the accelerating RF voltage should be increased in order to compensate the bunch lengthening, see Fig.4.7.3. One can see the undesirability of exceeding considerably the microwave instability threshold because it leads to a significant increase in the RF voltage required for the bunch lengthening compensation.

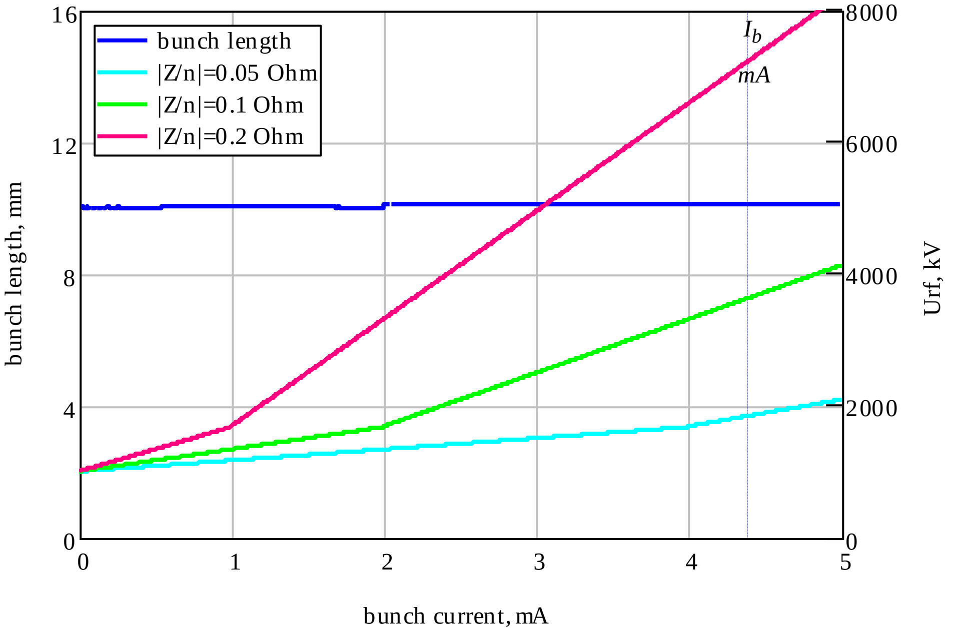

Fig. 4.7.3 Compensation of the bunch lengthening, *E*=2 GeV.

4.7.3 Coherent energy loss

The real part of longitudinal impedance causes coherent loss of the beam energy that is in quadratic dependence on the beam charge [2]:

$$\Delta E = -k_{\parallel} q^2 . \tag{4.7.2}$$

The coefficient of proportionality $k_\parallel$ is called the longitudinal loss factor. It depends on both the properties of the vacuum chamber that are characterized by the impedance $Z_\parallel$ and on the longitudinal beam density distribution λ:

$$k_\parallel = \frac{1}{\pi}\int_0^\infty \mathrm{Re}\, Z_\parallel(\omega)\left|\lambda(\omega)\right|^2 d\omega\,,$$

where $Z_\parallel(\omega)$ is the total broadband longitudinal impedance of the chamber and $\lambda(\omega)$ is the Fourier transform of the beam density distribution $\lambda(t)$. Similarly to the loss caused by synchrotron radiation, the coherent energy loss is compensated in the accelerating RF cavities at each beam turn.

Fig.4.7.4 shows the graphs of the coherent energy loss as a function of the beam current at 2 GeV , the fixed accelerating voltage U_{RF} =0.99 MV (a) and at the fixed bunch length σ_s =10 mm (4.7.1).

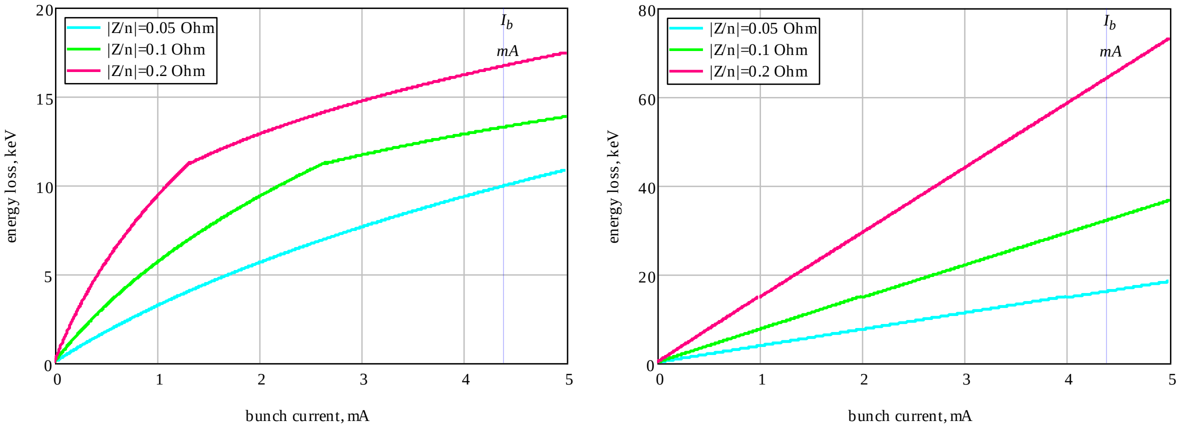

a) U_{RF}=0.99 MV б) σ_s=10 mm

Fig. 4.7.4 Coherent energy loss, *E*= 2GeV.

4.7.4 TMC instability (fast head-tail)

The resonant interaction between the beam and the short-lived transverse wake-fields, which is characterized by the transverse broadband impedance, causes the instability of the transversely-coupled modes (transverse mode coupling, TMC, or fast head-tail). The wake fields induced by the head part of the bunched beam affect the particles of its tail (head-tail-effect). Due to the synchrotron oscillations, the head and the tail of the beam periodically interchange; when the resonance conditions are met, there occurs an unlimited increase in the amplitude of betatron oscillations, which causes losses of the beam particles till the threshold intensity.

For a vacuum chamber of circular cross section, the relation of longitudinal and transverse dipole impedances is described by the following formula (a consequence of the Panofsky-Wenzel theorem):

$$Z_\perp = \frac{2R}{b^2}\frac{Z_\parallel}{n}\,,$$

where *b* is the chamber radius. This formula can also be used for rough estimates in case of a chamber of variable cross section if *b* is set equal to the average half-height of the chamber.

The interaction of the beam with the reactive part of transverse impedance leads to the coherent shift of betatron tunes. At low currents this shift depends linearly on the beam current [1]:

$$\frac{\Delta \nu_\beta}{\Delta I_b} = \frac{\sqrt{2\pi}R}{\sigma_s}\frac{\langle \operatorname{Im} Z_\perp \beta \rangle}{8\pi \frac{E}{e}}, \qquad (4.7.3)$$

where $\langle \operatorname{Im} Z_\perp \beta \rangle$ is the total broadband reactive impedance weighted by the beta function. The coherent shift of the vertical betatron tune of the $c\tau$-factory, computed by formula (4.7.**3)**, is $\Delta\nu_y/\Delta I_b = -0.36\ \mathrm{A}^{-1}$ at $E = 2$ Gev, $Z_\parallel / n = 0.1$ Ohm, and $Z_\perp = 39$ kOhm. For comparison, the coherent shift of the vertical betatron tune of the KEKB LER is $\Delta\nu_y/\Delta I_b = 4.2\ \mathrm{A}^{-1}$ (measurement) and of the PEP-II LER, $\Delta\nu_y/\Delta I_b = 0.23\ \mathrm{A}^{-1}$ (calculation).

The threshold current of the TMC instability can be estimated from the coherent shift of the betatron tune in (4.7.3):

$$I_b \le \frac{\sigma_s}{\sqrt{2\pi}R}\frac{8\pi \frac{E}{e}\nu_s}{\langle \operatorname{Im} Z_\perp \beta \rangle}, \qquad (4.7.4)$$

Fig.4.7.5 shows the graphs of the threshold current of the TMC instability, (4.7.4), in dependence on the normalized longitudinal impedance under the assumption that the transverse impedance is proportional to the longitudinal one, in accordance with the Panofsky-Wenzel theorem. For the KEKB LER the threshold current is $I_{\mathrm{th}} = 1.5$ mA at $Z_\perp = 99$ kOhm, for the PEP-II LER $I_{\mathrm{th}} = 32.6$ mA at $Z_\perp = 22.5$ kOhm.

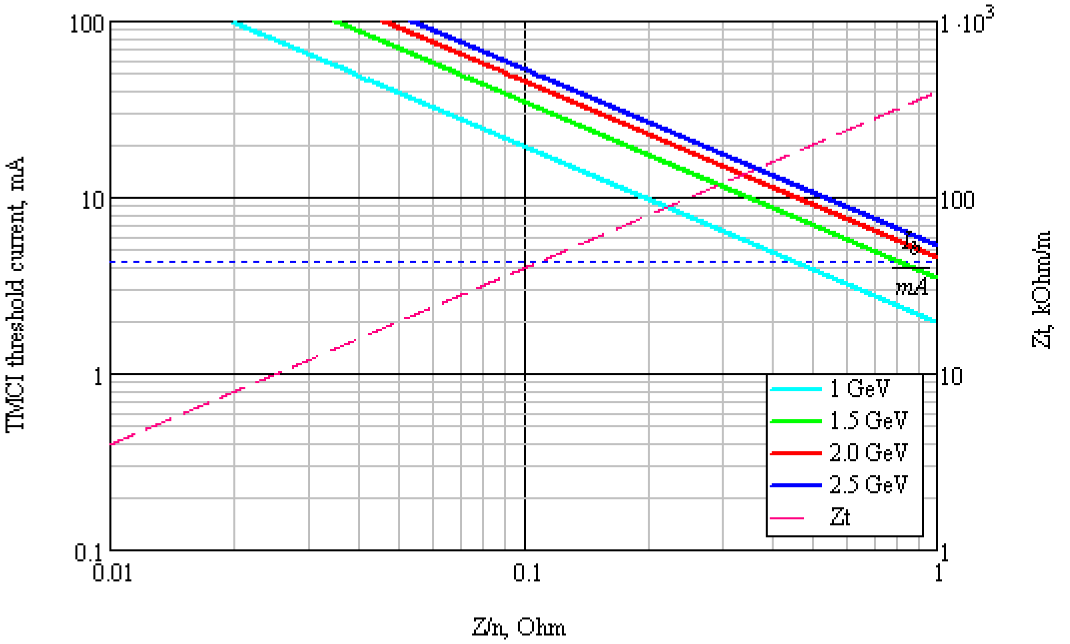

Fig. 4.7.5 . The threshold current of the TMC instability.

4.7.5 Longitudinal multi-bunch instability

The interaction of the beam with the high-order modes (HOMs) of the accelerating RF cavities (narrowband impedance) leads to excitation of long-lived wake-fields, the influence of which on next bunches may cause longitudinal instability in the multi-bunch mode [11, 12, 13]. If N_b bunches are uniformly distributed over the perimeter of the accelerator, the *n*th oscillation mode is excited when the resonance condition

$$\omega_r^{HOM} = \left(pN_b + n + \nu_s\right)\omega_0 ,$$

is met, where p is an integer and ν_s is the synchrotron tune. The impedance of every longitudinal mode can be written as

$$Z_{\parallel}(\omega) = \frac{R_s^{HOM}}{1 + iQ\left(\frac{\omega}{\omega_r^{HOM}} - \frac{\omega_r^{HOM}}{\omega}\right)} ,$$

Since the impedance of each high-order mode is characterized by the corresponding resonance frequency ω_r^{HOM}, shunt resistance R_s^{HOM} and quality factor Q, the instability rise time should be estimated separately for each mode:

$$\frac{1}{\tau} = \frac{\alpha N_b I_b}{4\pi\nu_s \frac{E}{e}} \cdot R_s^{HOM}\omega_r^{HOM} . \tag{4.7.5}$$

Here I_b is the current of one bunch.

For the motion to be stable, the characteristic time of the radiation damping of the longitudinal oscillations must be less than the rise time of (4.7.5) for any mode in the operating range of the beam current. Taking the radiation damping into account, we can formulate the stability condition limiting the $R_s^{HOM}\omega_r^{HOM}$ value for any HOM of the RF cavities:

$$R_s^{HOM}\omega_r^{HOM} \le \frac{1}{\tau_s}\frac{4\pi\nu_s \frac{E}{e}}{\alpha N_b I_b} \cdot .$$

For the $c\tau$-factory, $R_s^{HOM}\omega_r^{HOM} \le 10^{13}$Ohm at E = 2 GeV, N_b = 390, and I_b = 4.4 mA

4.7.6 Transverse multi-bunch instability

The transverse narrow-band impedance of the high-order modes of RF cavities may cause the transverse multi-bunch instability, the rise time of which can be estimated using a formula similar to (4.7.5) [12]:

$$\frac{1}{\tau} = \frac{\beta_{RFC}\omega_0 N_b I_b}{4\pi \frac{E}{e}} \cdot R_{s\perp}^{HOM} ,$$

where $R_{s\perp}^{HOM}$ is the shunt resistance of the transverse mode and β_{RFC} is the beta function at the cavity location. The resonance condition for the nth oscillation mode excitation looks as follows:

$$\omega_r^{HOM} = \left(pN_b + n + \nu_\beta\right)\omega_0 , \tag{4.7.6}$$

Taking the radiation damping into account, we can also formulate the stability condition limiting the $R_{s\perp}^{HOM}$ value for any high-order mode of the cavities:

$$R_{s\perp}^{HOM} \le \frac{1}{\tau_\perp}\frac{4\pi \frac{E}{e}}{\beta_{RFC}\omega_0 N_b I_b} .$$

For the $c\tau$-factory $R_{s\perp}^{HOM} \le 13$ kOhm at E = 2 GeV, N_b = 390, I_b = 4.4 mA

Besides the high-order modes of the RF cavities, the transverse multi-bunch instability may be excited due to beam interaction with the resistive impedance of the vacuum chamber walls (resistive wall) at the frequencies (4.7.6). The instability rise time can be estimated as follows [14]:

$$\frac{1}{\tau}=\frac{\langle\beta\rangle\omega_0 N_b I_b}{4\pi\frac{E}{e}}\sum_{p=-\infty}^{\infty}\mathrm{Re}\,Z_{\perp rw}(\omega_{np}),$$

The frequency dependence of the resistive-wall impedance of a cylindrical vacuum chamber with a radius *b* and a length *L* is described by the following expression:

$$Z_{\perp rw}=\frac{\pi^2}{12}(1+i)\frac{L}{2\pi}\frac{Z_0\delta_s}{b^3},$$

where $Z_0 = 120\pi$ Ohm is the free space impedance and $\delta_s=\sqrt{\frac{2\rho}{\mu\omega}}$ is the skin depth. Thus, the low-frequency impedance is the most dangerous as concerns the beam stability. For the $c\tau$-factory the minimum time of the rise time of transverse multi-bunch instability is estimated as $\tau \approx 30$ ms at the frequency $(\nu_y+1)f_0\approx 12$ MHz at $E = 2$ GeV, $N_b = 390$, and $I_b = 4.4$ mA

REFERENCES

1. Chao A. Physics of Collective Beam Instabilities. New York: Wiley, 1993.
2. Zotter B.W., Kheifets S.A. Impedances and Wakes in High-Energy Particle Accelerators. Singapore: World Scientific, 1998.
3. Dikansky N.S., Pestrikov D.V. Physics of intensive beams in storage rings. Novosibirsk: Science, 1989. (in Russian)
4. Zotter B., Potential-Well Bunch Lengthening", CERN SPS/81-14 (DI), 1981.
5. Clarke J.A., Bunch Lengthening Thresholds on the Daresbury SRS, CCL Daresbury Laboratory, 1995.
6. Chao A.W., Tigner M., Handbook of Accelerator physics and Engineering, World Scientific, 2006.
7. Sacherer F. IEEE Trans. Nucl. Sci, NS-24 (1977) p. 1393.
8. Keil E., Schnell W. // CERN ISR-TH-RF 69/48 (1969).
9. Boussard D., CERN-Lab II/RF/75-2, 1975.
10. Boussard D. Observation of Microwave Longitudinal Instabilities in the SPS // CERN II/RF/Int.75-2 (1975).
11. Wiedemann H. Particle Accelerator Physics II, Springer-Verlag, 1995.
12. Fabris A., Pasotti C., Svandrlik M., Coupled Bunch Instability Calculations for the ANKA Storage Ring, Proc. of EPAC-98, Stockholm, Sweden, 1998.
13. Dobbing G.S., Wolski A., Instability Threshold Calculations for DIAMOND, Proc. of EPAC-2000, Vienna, Austria, 2000.
14. Ohmi K. Beam Instabilities // International Symposium “Forty Years of Lepton Colliders” (COLLID04) Novosibirsk, Russia, 2004.

4.8 Stabilization of the beam parameters and the feedback systems

4.8.1 Goals of stabilization

Ensuring the efficient operation of lepton colliders and synchrotron light sources always imposes high demands on the stability of beam parameters. The disturbing factors, the influence of which may reduce the effectiveness of the accelerator include: field deviation in the magnets, alignment errors, seismic vibration, thermal expansion of the magnets and of the accelerating RF cavities, the temperature drift of parameters as well as other dynamic effects. Completely self-automated control of such key beam parameters as the orbit, betatron tunes, coupling factor, chromaticity, energy, etc. with continuous correction of the perturbation introduced by the above factors becomes essentially an integral part of the control systems of modern accelerators.

The diversity of the modern feedback systems results from the variety of requirements to the feedback parameters in accelerators of different types. Let consider the basic principles of construction of systems for stabilization of beam parameters [1]. Requirements to the stability depend on the properties and quality of beams used in experiments. The beam stability in the collider is a necessary condition for the luminosity optimization in high energy physics experiments. Just as in synchrotron radiation sources [2], the orbit stabilization is necessary to minimize the emittance and to provide stable beam convergence at the IPs. Besides the orbit, the feedback system is used to stabilize the betatron tunes so that to prevent crossing of the betatron resonances during acceleration, which may cause loss of beam particles.

Various disturbances affecting the beam orbit, betatron tunes, betatron coupling, chromaticity and energy can be divided into three groups according to their sources:

External perturbations: changes in the ambient temperature and the atmospheric pressure; mechanical movement of soil caused by seismic activity, tidal waves and human activity (industry, transport). These disturbances are transmitted into the particle beam mainly through the quadrupoles, the beam focusing in which depends on the transverse displacements.

2. Intrinsic perturbations in the accelerator: variation of fields in the magnets, the noise caused by the flows of cooling fluids, the vibration of air pumps, the eddy currents.

3. Failures of individual elements, which are important for large machines, where failure of one of tens or even hundreds of correcting magnets can stop the experiment for the time of repair.

The characteristic time scale of the perturbations may be long-term (a few months to several days), medium (days or hours) or short-term (hours to milliseconds). The applicability of feedbacks correcting slow beam perturbations is eventually limited by the thermal drift, the noise and the systematic errors of the measuring and correcting circuits. Because of the beam sensitivity to the thermal drift, in the modern machines it is necessary to stabilize not only the orbit but also the temperature of the experimental hall, the accelerator tunnel, the vacuum chamber and the cooling water within ± 0.1 °C.

External disturbances, beam parameters and the strength of the correctors are functions of time. Therefore, designing feedback systems is often accompanied by a separate analysis of the scheme for correction of deviations of beam parameters from the desired values for a given constant perturbation (space domain) and of time-dependent (time domain) processes describing the operation of the system in real time. Such a separation allows making the system operation more flexible, especially at possible failures of individual elements when quick adjustment of the feedback parameters is required.

4.8.2 Correction algorithms

For most accelerators, the influence of the correcting elements on such parameters as orbit, betatron tune, betatron coupling, chromaticity and energy can be considered linear in the first approximation; the matrix formalism can be used for calculating the correction. The relation of the measured beam parameters and the corrective action in the linear approximation is described with the following matrix equation:

$$\vec{x} = \mathbf{R}\vec{f}^{\,3}, \tag{4.8.1}$$

where $\vec{x} = (x_1, \ldots, x_N)$ is the beam parameter vector measured with *N* pickups; $\vec{f} = (f_1, \ldots, f_N)$ is the vector of *M* corrective actions; **R** is the response matrix, the elements R_{ij} of which describe the response of the *i*th pickup to a variation in the strength of the *j*th corrector. So, in case of correction of a closed beam orbit, $\vec{x}$ is the set of orbit deviations measured with beam position monitors and $\vec{f}$ are the currents of the dipole magnet correctors.

A space-domain algorithm of correction is being developed to compute the strengths of the correctors $f_s = \lim\limits_{t \to \infty} \left[f_1(t), \ldots, f_M(t) \right]$ that minimize the deviation of the beam parameter *r* at a given constant perturbation:

$$r = \left\| \vec{x} - \vec{x}_0 \right\| = \left\| R\vec{f}_s \right\| < \varepsilon ,$$

where **R** is the response matrix; $\vec{x}$ is the vector of the actual measured values; $\vec{x}_0$ is the target vector. The vector norm is defined as follows:

$$\left\| \vec{x} \right\| = \frac{1}{N} \sqrt{\sum_{i=1}^{N} x_i^2} \ .$$

It follows from (4.21) that the correction algorithm essentially consists in the inversion of the response matrix **R**. However, in practice the matrix **R** is often singular or almost singular, so one of the most widely used algorithms is the singular value decomposition (SVD). The response matrix can be written as $\mathbf{R} = \mathbf{U}\lambda\mathbf{V}^T$ and the inverse matrix, as $\mathbf{R}^{-1} = \mathbf{V}\lambda^{-1}\mathbf{U}^T$; where **U** is the $m \times n$ full unitary matrix; λ is the diagonal matrix consisting of the eigenvalues of the matrix **R**; and **V** is an orthogonal matrix, the columns of which are the eigenvectors of the matrix **R**. To eliminate singularities at the calculation of $\mathbf{R}^{-1}$, the λ_k^{-1} values corresponding to small eigenvalues λ are set equal to zero. The number of the eigenvalues used to compute the inverse matrix $\mathbf{R}^{-1}$ is chosen as a compromise between the accuracy and reliability of the correction algorithm: a larger number of eigenvalues provides a better convergence, but at the same time the correction process becomes more sensitive to the measurement errors and the noise of the electronics. In addition, the response matrix used for the correction can deviate from the real matrix of the magnet lattice, and therefore the correction process may consist of several consecutive iterations.

4.8.3 Computation of the transfer functions

Analysis of the time-domain processes occurring in the beam parameter stabilization system allows optimizing the system operation in real time. A typical scheme of a closed single-input-single-output (SISO) automatic control system is presented in Fig.4.8.1.

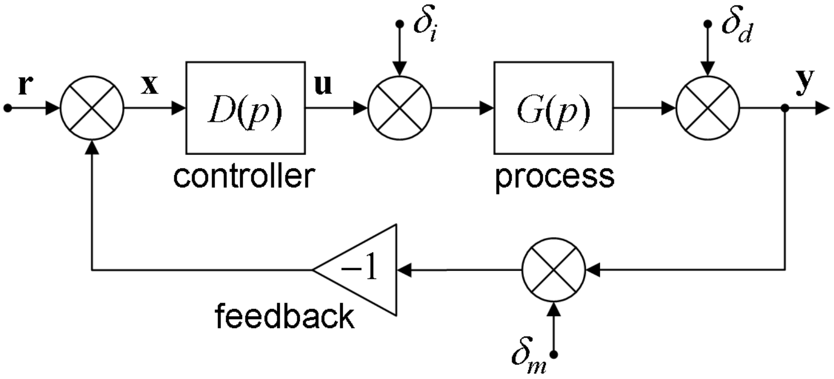

Fig.4.8.1 First-order automatic control system

The controlled process and the control device (controller) are characterized by the frequency-dependent transfer functions $G(p)$ and $D(p)$, respectively, where p is the complex Laplace frequency. The stability of the system and its sensitivity to perturbations and noise are determined by the following functions:

$$\begin{aligned} T(p) &\equiv \frac{y}{r} = \frac{D(p)G(p)}{1+D(p)G(p)} \\ S_d(p) &\equiv \frac{y}{\delta_d} = \frac{1}{1+D(p)G(p)} \\ S_i(p) &\equiv \frac{y}{\delta_i} = \frac{G(p)}{1+D(p)G(p)} \\ S_u(p) &\equiv \frac{u}{\delta_d} = \frac{D(p)}{1+D(p)G(p)} \end{aligned} \tag{4.8.1}$$

where $T(p)$ is the full (nominal) transfer function; $S_d(p)$ is the nominal sensitivity, which determines the perturbation suppression by the feedback; $S_i(p)$ is the sensitivity to input perturbations; $S_u(p)$ is the sensitivity of the control system. The state variables are also denoted in Fig.4.8.1: **r** is the target of correction; **y** is the variable to control; **x** is the error signal; **u** is the correction action; δ_m is the measurement noise; δ_i and δ_d are the perturbations at the input and output of the process, respectively.

The classic computation of feedback is based on the study of zeros of the denominator in equations (4.8.1) using, for example, the Nyquist stability criterion in the following formulation: a closed-loop system is stable if the hodograph of the transfer function $D(p)G(p)$ of the open-loop system does not include the (-1, 0i) point in the complex plane. If an open-loop system is unstable, for the closed-loop system stability it is necessary and sufficient that the hodograph of the transfer function $D(p)G(p)$ of the unstable open-loop system includes the point with the coordinates (-1, 0i) $n/2$ times, where n is the number of the roots of the characteristic equation of the open-loop system with a positive real part. In this case a number of conditions must be observed, such as providing the necessary bandwidth, minimizing the mavericks during the regulation, providing a wide dynamic range of corrective actions as well as achieving maximum reliability in relation to the measurement errors and the model inaccuracies.

Typically, the feedback systems to stabilize the beam parameters in accelerators are developed and put into operation independently of one another, and the study of their interdependence and the reduction of parasitic relationships are often neglected. Nevertheless, for the systems to work stably and reliably it is necessary to take into account the possible cross-talk coupling between several parallel and possibly nested feedback loops at the design stage.

A typical cross-talk coupling is inherent, for example, to the systems for stabilization of the orbit and betatron tunes: although beam orbit stabilization at the micron level inhibits the undesirable effects associated with the orbit deviation in the magnets and has a positive effect on the beam lifetime, it also imposes substantial limitations on other systems, in particular, those intended to stabilize the betatron tunes and the chromaticity, the measurement of which requires excitation of the beam jitter and, in case of chromaticity, even a change in the longitudinal momentum.

4.8.4 Orbit stabilization

Beam trajectory stability is essential for efficient operation of particle accelerators. Identification and minimization of noise sources at the accelerator design stage can significantly improve the situation. However, in many cases the required level of stability of the trajectory can only be achieved by using feedback systems. In particular, it is impossible to do without fast feedback in cases when the most severe conditions are imposed on the short-term (milliseconds - seconds) and medium-term (minutes - days) beam stability [3].

The main cause of beam trajectory distortion on the short-term and mid-term scales is usually a mechanical displacement of the magnets, especially quadrupoles, caused by vibrations of the soil, thermal effects, coolant motion, etc. Other sources of trajectory instability are oscillations of the supply current, which contain the harmonics of the mains frequency as well as stray electrical and magnetic fields.

In a typical feedback scheme intended to stabilize the beam trajectory, the input signals are supplied by a set of beam position pickups, and the corrective action is carried out using magnetic dipole correctors or electromagnetic kickers. The regulators are usually programmable signal processors of various types. In a local scheme, three or four magnetic correctors are used to create a local compensated effect stabilizing the position and angle of the electron beam at a desired point without affecting the rest of the orbit. A global feedback scheme which includes all the beam pickups and all the correcting dipole magnets is most often used to minimize the standard deviation of the orbit from a golden one, though other correction strategies are also possible.

The correction algorithm is usually based on the inversion of the response matrix, which relates the beam position at the locations of the pickups to the currents of the magnetic correctors. The inversion is executed by the method of expansion of the matrix in eigenvalues. This method allows us to represent a system of an arbitrary number of pickups and correctors interrelated via the response matrix in the transformed space, where each pickup is connected with one virtual corrector through a single coefficient. These coefficients correspond to the eigenvalues of the diagonal response matrix in the transformed space, which allows passing from the original MIMO system to a set of independent SISO feedback loops for each of the transformed channel of correction. The dynamics of each channel are determined by the low-frequency characteristic of the corrector, mainly by the eddy currents in the magnet yoke and the walls of the vacuum chamber. Another important parameter is the total delay time of the system, determined by the time of measurement and data processing and transmission. The typical delay time of modern feedback systems [4, 5, 6] is in the order of several hundreds of nanoseconds. Thus, each correction channel can be quite accurately described via a model consisting of a first-order low-pass filter and a delay line.

A proportional-integral-differential controller (PID controller) is most commonly used as a control element. With a feedback operating frequency of up to 10 kHz the optimal choice of the PID controller parameters allows effective stabilization of the beam orbit in the frequency band of 100-150 Hz. The bandwidth in local loops of a fast feedback system can be extended using correctors without magnetic cores, while a slower global feedback system usually includes all the available standard orbit correctors.

The stable components of the perturbation spectrum such as the mains frequency and its harmonics can be effectively suppressed with special narrowband feedback loops. Since filters tuned to different frequencies are decoupled, they can operate in parallel. Moreover, since the perturbations introduced by the harmonics of the mains frequency usually change very little in time, they can be suppressed even if the perturbation frequency exceeds the frequency limit of a system with open feedback system.

In systems for fast orbit stabilization, data are processed using different computing platforms such as field-programmable gate arrays (FPGA), digital signal processors (DSP) and general-purpose computers with real-time operating system, which are integrated in the control system of accelerator complex. Ethernet with modified low-level drivers is often used in fast communication networks.

4.8.5 Fast feedback systems

At present, most accelerator facilities are equipped with fast feedback systems for the turn-by-turn suppression of the transverse and longitudinal instabilities of beam motion.

The development of digital technology allows creating bunch-by-bunch feedback systems, which control the motion of each bunch in the multi-bunch mode [7, 8, 9]. All digital feedback systems are similar to one another in their design. The flowchart of a multi-bunch feedback system is shown in Fig.4.8.2. Electrostatic or stripline pickups, the signals of which are processed by analog hybrid circuits outputting signals proportional to the horizontal and vertical coordinates of the beam and its intensity, are used as the beam position sensors. These signals are then detected and digitized. The digital data are processed either by field-programmable gate arrays (FPGA) or by a digital signal processor (DSP), which calculates the strength of the pulse kicker, which impacts on the beam. Filters with finite impulse response, FIR-filters, are widely used for signal processing.

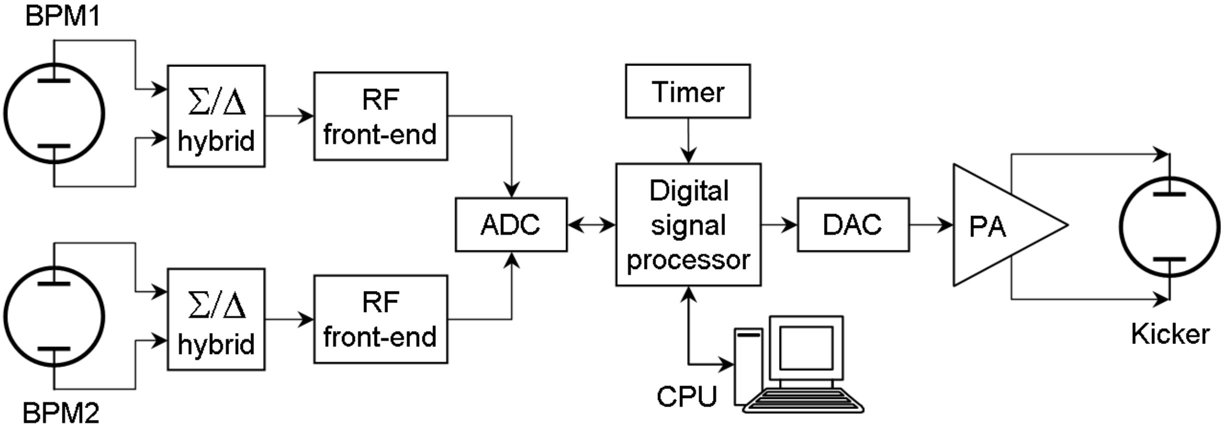

Fig.4.8.2 Scheme of a digital feedback system.

It should be noted that the use of stripline pickups and kickers with the directivity allows simultaneous stabilization of the electron and positron bunches circulating in opposite directions, the same striplines used for both types of particles [10].

Using two pickups allows calculating the transverse beam position and momentum at each turn. In the linear approximation, the coordinate transformation by the section of magnet lattice between the pickups looks as follows:

$$x_2 = x_1\sqrt{\beta_2/\beta_1}\left(\cos\Delta\phi_{12} + \alpha_1 \sin\Delta\phi_{12}\right) + x'_1\sqrt{\beta_2\beta_1}\sin\Delta\phi_{12}, \qquad (4.8.2)$$

where $x_{1,2}$, $x'_{1,2}$, $\beta_{1,2}$, $\alpha_{1,2}$ are the values of the position, momentum, and the lattice functions at the first and second pickup, respectively; φ_{12} is the betatron phase advance in this section. Conversion of (4.8.2) allows expressing the transverse momentum of the beam center of mass at the azimuth of the first pickup via the x_1 and x_2 positions measured by both the pickups. Applying a similar conversion, we obtain the beam position x_K and momentum x'_K in the kicker.

$$x_K = x_1 C_{1K} + \frac{x_2 - x_1 C_{12}}{S_{12}} \qquad x'_K = \frac{1}{\beta_K}\left[-x_1(\alpha_K C_{1K} + S_{1K}) \frac{x_2 - x_1 C_{12}}{S_{12}} (C_{1K} - \alpha_K S_{1K}) \right], \tag{4.8.3}$$

Here

$$C_{1K} = \sqrt{\beta_K / \beta_1} \cos \Delta\phi_{1K}\ , \qquad S_{1K} = \sqrt{\beta_K / \beta_1} \sin \Delta\phi_{1K}\ ,$$

$$C_{12} = \sqrt{\beta_2 / \beta_1} \cos \Delta\phi_{12}\ , \qquad S_{12} = \sin \Delta\phi_{12}\ , \qquad (4.8.4))$$

φ_{1K} is the betatron phase advance in the section between the first pickup and the kicker; β_K and α_K are the lattice functions at the azimuth of the kicker.

The kicker voltage is calculated as follows:

$$V_{kick} = \frac{E}{e}\frac{d}{L}\left(\mathrm{Re}\, K_{FB} x'_K + \mathrm{Im}\, K_{FB} \frac{x_K}{\beta_K} \right), \tag{4.8.5}$$

where ReK_{FB} and ImK_{FB} are the coefficients of the resistive and reactive feedback, respectively; E is the beam energy; L is the kicker length; d is the distance between the plates.

So, the signal processing should consist in the following operations:

- setting the feedback coefficients ReK_{FB} and ImK_{FB};
- measuring the beam position in the x_1 and x_2 pickups;
- calculation of the beam position and momentum in the kicker by formulae (4.8.3) and (4.8.4);
- calculation of the kick amplitude by formula (4.8.5).

Note that all the values in the formulae except x_1 and x_2 are computed beforehand, and the signal processor is used for fast computation of expressions of the $ax + by$ type. Fig.4.8.3 presents an example of computer simulation of the feedback in the Matlab-Simulink environment.

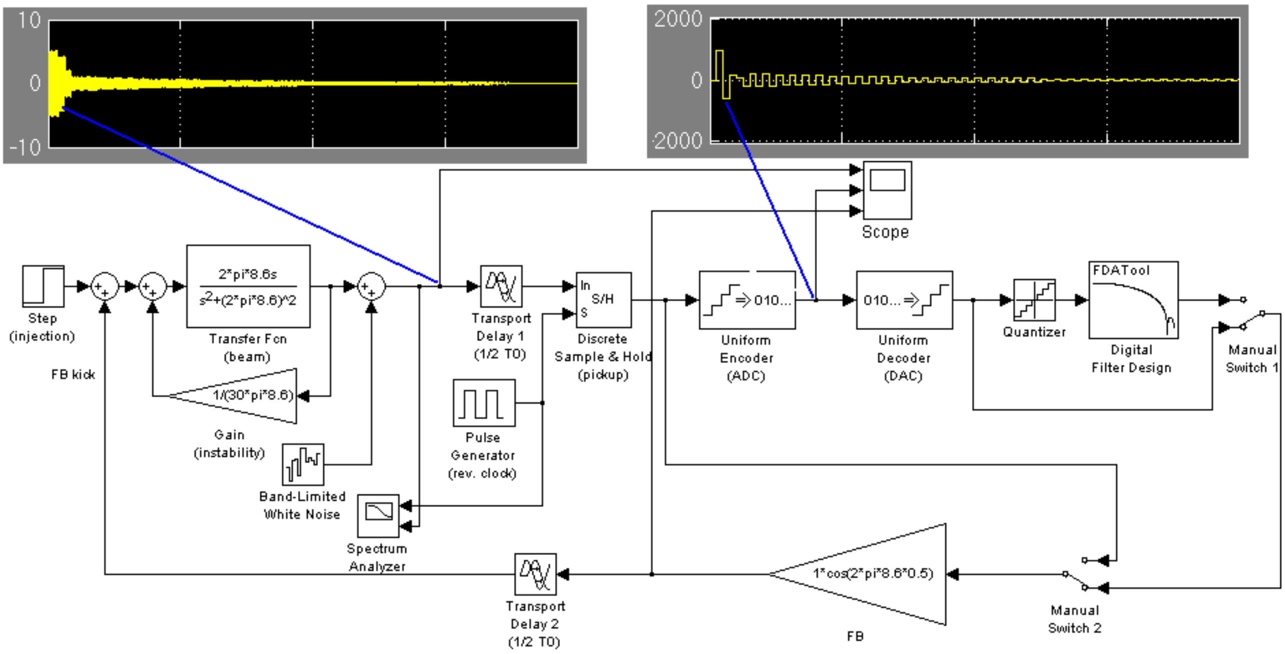

Fig.4.8.3 Computer simulation of feedback system.

In the longitudinal feedback systems, the input signal is the deviation of the beam phase from the equilibrium one and broadband cavities are used as kickers [11, 12].

The technique of direct digitization of the RF signal of beam position pickups has developed recently [13]. Direct digitization allows transferring the signal to the low-frequency region and detecting the signal without complex analog electronics. This simplifies the system and reduces its cost as well as makes its setting more convenient.

REFERENCES

1. Ohmi K. Beam Instabilities // International Symposium “Forty Years of Lepton Colliders” (COLLID04) Novosibirsk, Russia, 2004.
2. Steinhagen R.J. Real Time Feedback on Beam Parameters // Proc. of APAC 2007. Indore, India, 2007.
3. Boege M. Achieving Sub-micron Stability in Light Sources // Proc. of EPAC 2004. Lucerne, Switzerland, 2004.
4. Bulfone D. Overview of Fast Beam Position Feedback Systems // Proc. of EPAC 2008. Genoa, Italy, 2008.
5. Masuzawa M., Flanagan J.W., Funakoshi Y., Oide K. IP Orbital Feedback for Collision Tuning at KEKB // Proc. of EPAC 2000. Vienna, Austria, 2000.
6. Hendrickson L., Gromme T., Grossberg P. et al. Slow Feedback Systems for PEP-II // Proc. of EPAC 2000. Vienna, Austria, 2000.
7. Abbott M.G. Performance and Future Developments of the Diamond Fast Orbit Feedback System // Proc. of EPAC 2008. Genoa, Italy, 2008.
8. Tobiyama M., Kikutani E., Flanagan J. W., Hiramatsu S. Bunch by Bunch Feedback Systems for the KEKB Ring // Proc. of PAC 2001. Chicago, USA, 2001.
9. Weber J., Chin M., Doolittle L. PEP-II Transverse Feedback Electronics Upgrade // Proc. of PAC 2005. Knoxville, USA, 2005.
10. Yao C.-Y., Norum E., Di Monte N. An FPGA-Based Bunch-to-Bunch Feedback System at the Advanced Photon Source // Proc. of PAC 2007. Albuquerque, USA, 2007.
11. Cherepanov V., Dementev E., Levichev E. et al. Transverse Bunch-by-bunch Feedback for the VEPP-4M Electron-positron Collider // Proc. of DIPAC-2007. Venice, Italy, 2007.
12. Arbuzov V.S., Gorniker E.I., Kenjebulatov E.K. et al. Feedback System for Damping of Longitudinal Bunch Oscillations in VEPP-4M Collider // Proc. of RuPAC 2006. Novosibirsk, Russia, 2006.
13. Yujong Kim, Busch W., Wang M. et al. New Generation Digital Longitudinal Feedback System for Duke FEL and HIGS Facilities // Proc. of PAC 2007. Albuquerque, USA, 2007.
14. Nakamura T., Kobayashi K., Zhou Z. Bunch by Bunch Feedback by RF Direct Sampling // Proc. of EPAC 2008. Genoa, Italy, 2008.

ATTACHMENT

Table 1. Parameters of KEKB, PEP-II and the C-τ-factory

	KEKB LER	KEKB HER	PEP-II LER	PEP-II HER	C-tau BINP
Energy, GeV	3.5	8.0	3.1	9.0	2.0
Circumference, m	3016.26	3016.26	2199.3	2199.3	766.6
Bunch, length, mm	4	4	11	11	10
Energy spread	$7.1\cdot10^{-4}$	$6.7\cdot10^{-4}$	$8.1\cdot10^{-4}$	$6.1\cdot10^{-4}$	$8.4\cdot10^{-4}$
Bunch-to-bunch distance, m	0.59	0.59	1.26	1.26	1.77
Horizontal emittance, nm	18	18	50		8
Vertical emittance, nm	0.36	0.36	2		0.04
Synchrotron frequency	0.01-0.02	0.01-0.02	0.03	0.05	$9.3\cdot10^{-3}$
Betatron tune (hor.)	45.52	47.52	36.57	24.57	47.54
Betatron tune (ver.)	45.08	43.08	34.64	23.64	30.57
Average beta function (hor.), m	10	10	10.84	14.5	15
Average beta function (ver.), m	10	10	9.95	13.84	15
Momentum compaction factor	$(1\text{-}2)\cdot10^{-4}$	$(1\text{-}2)\cdot10^{-4}$	$1.31\cdot10^{-3}$	$2.41\cdot10^{-3}$	$9.07\cdot10^{-3}$
Bending radius, m	16.3	104.5			8.25
Bending magnet length, m	0.915	5.86			0.454
RF voltage, MV	5-10	10-20	5.12	18.5	0.99
RF frequency, MHz	508.887	508.887	476	476	500
RF harmonic number	5120	5120	3492	3492	1300
Revolution frequency, kHz	99.4	99.4	136.3	136.3	391
Radiation damping time (long.), ms	43/23	23	40	37	15
Energy loss to SR, MeV/turn	0.81/1.5	3.5	0.87	3.57	0.343
Total radiation power, MW	2.1/4.0	3.8			0.586
Particles per bunch	$3.3\cdot10^{10}$	$1.4\cdot10^{10}$	$6\cdot10^{10}$	$2.7\cdot10^{10}$	$7\cdot10^{10}$
Bunch current, mA	0.52	0.22	1.3	0.59	4.4
Bunch peak current, A	158	67	104.5	47	134
Total beam current, A	2.6	1.1	2.1	1.0	1.71
Vacuum chamber	Cu [1] Ø94 mm[2] NEG inserts	Cu racetrack[3] 104×50mm^2 Ø50mm NEG stripes	Straight sections: stainless steel Ø94mm arcs: Al ellipt. 95×59 mm^2 +antechamber	1300 m: copper, 900 m: stainless steel	copper-plated aluminum 100×50 mm^2

[1] – low photodesorption coefficient, high thermal conductivity, possibility of shielding the X-rays.
[2] – in order to avoid the resistive-wall multi-bunch instability.
[3] – in order to minimize the gap in the dipole magnets.

Table 2. Estimates for the instabilities at KEKB, PEP-II and the C-τ factory

	KEKB LER	KEKB HER	PEP-II LER	PEP-II HER	C-tau BINP
Microwave instability $I_{th} = \frac{\sqrt{2\pi}\sigma_{s0}}{R} \frac{\alpha}{Z/n} \frac{E}{e} \left(\frac{\sigma_E}{E} \right)^2$	I_{th}=7.4·10^{-6} B/(Z/n) I_{th}=0.1 mA @ Z/n=72·mOhm I_{b}=0.52 mA	I_{th}=1.5·10^{-5} B/(Z/n) I_{th}=0.2 mA @ Z/n=76·mOhm I_{b}=0.22 mA	I_{th}=2.1·10^{-4} B/(Z/n) I_{th}=3 mA @ Z/n=71·mOhm I_{b}=1.3 mA	I_{th}=2.2·10^{-4} B/(Z/n) I_{th}=9 mA @ Z/n=76·mOhm I_{b}=0.59 mA	I_{th}=2.7·10^{-4} B/(Z/n) I_{th}=2.7 mA @ Z/n=100·m□ I_{b}=4.4 mA
Bunch lengthening	~20%	~20%			~50%
TMC instability $\frac{\Delta\nu}{\Delta I} = \frac{\sqrt{2\pi}R}{\sigma_{s0}} \frac{< Z_\perp \beta >}{8\pi\, E/e}$ $I_{th} = \frac{\sigma_{s0}}{\sqrt{2\pi}R} \frac{4\pi\nu_s}{< Z_\perp \beta >} \frac{E}{e}$	$\Delta\nu_y/\Delta I_b$=3.4 A^{-1} (design) (0.38 - CDR) I_{th}=1.5 mA@ Z_{T}=99 kOhm $\Delta\nu_y/\Delta I_b$ =4.2 A^{-1} $\Delta\nu_y/\Delta I_b$ =1.5 A^{-1} (measured.)	$\Delta\nu_y/\Delta I_b$ =0.44 A^{-1} (design) I_{th}=11.4 mA@ Z_{T}=29 kOhm	$\Delta\nu_y/\Delta I_b$ =0.23 A^{-1} (design) I_{th}=32.6 mA@ Z_{T}=22.5 kOhm	$\Delta\nu_y/\Delta I_b$ =0.1 A^{-1} (design) I_{th}=98.2 mA@ Z_{T}=20 kOhm	$\Delta\nu_y/\Delta I_b$ =0.36 A^{-1} (design) I_{th}=13.1 mA @ Z_{T}=39 kOhm
Longitudinal multi-bunch instability – HOMs of the RF cavities	60 ms	150 ms			
Transverse multi-bunch instability – RF HOMs of the RF cavities	30 ms	80 ms			
Transverse multi-bunch instability – resistive-wall CBI	~5 ms (suppressed by the feedback)		hor.: 1.41 ms ver.: 0.92 ms feedback damping time of 0.31 ms	hor.: 5.56 ms ver.: 3.85 ms	hor.: 170 ms ver.: 8.6 ms
Multi-bunch instability – ions		~1 ms (2D modeling) feedback is needed	Solenoids with a field of 30 G are used		
Multi-bunch instability – electron clouds	>0.4 ms Solenoids+feedback				

Chapter 5

Injection system

5.1 Injection into the cτ-factory

Injection into the $c\tau$-factory is carried out from the linear accelerator located in the tunnel at a height of 1200 mm from the floor. The linac tunnel floor is at the 158.82 m mark; the floor of epy technical straight section of the $c\tau$-factory is at the 162.85 m mark (in the urban coordinate system). The level difference is 4 m. The transfer line begins at a distance of +3 m from the 33rd axis of the 13th building (on the outer boundary of the lead-in tunnel).

5.1.1 Transfer line geometry

Beams are brought normally to the technical straight section of the $c\tau$-factory. Fig. 5.1 shows the electron transfer line; the positron transfer line is its symmetric reflection relative to the vertical axis of the figure. 9° bending magnet *M1X* moves the beams apart in opposite directions in a horizontal plane. Nine successive magnets M2X-M10X, lying in a horizontal plane and bending the beam through 9°, bring the injected particles to the axis of the storage ring.

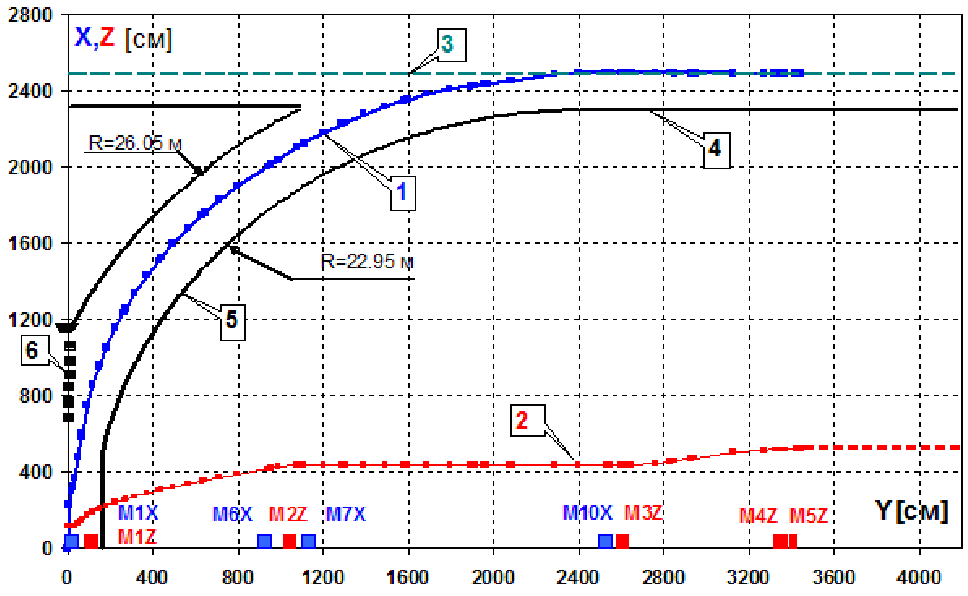

Fig. 5.1 Beam geometry in the injection line. Legend: (1) beam trajectory in horizontal, (2) beam trajectory in vertical, (3) axis of the injection (technical) straight section of the $c\tau$-factory, (4) wall of the tunnel of the technical straight section, (5) wall of the tunnel of the transfer line, (6) support columns of the injection tunnel.

Beams are elevated in the tunnel with the help of vertical magnets *M1Z-M2Z* (Fig. 5.2). The usage of magnets with a turned median plane is complicated in this case for the following reasons: (1) the floor in the elevation channel is already made under a rather large angle of 13°, (2) it is very difficult to zero the dispersion functions in horizontal and in vertical using magnets with a turned median plane, (3) oscillation coupling at injection should be minimal.

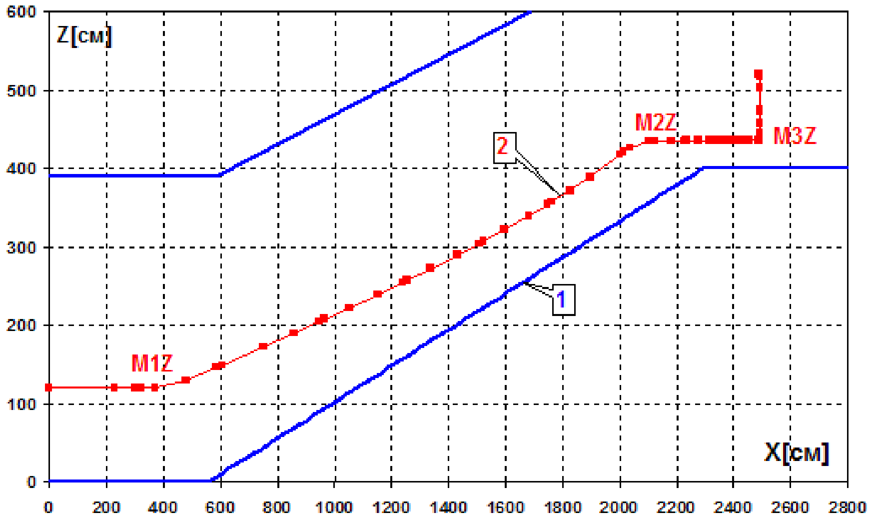

Fig. 5.2 Geometry of the elevation interval. Legend: (1) floor of the elevation channel, (2) beam axis in the vertical plane.

The beam is brought to the straight technical straight section from below and with a -800-mm vertical offset relative to the median plane of the storage ring. Then magnet *M3Z* elevates the beam in vertical and two successive magnets *M4Z* and *M5Z* bring it in the median plane at the distance ΔX = + 15 mm from the equilibrium orbit.

Magnets *M2X-M10X* and *M1Z-M3Z* are identical in design, have the effective length L = 110 cm and the maximum field H = 11.93 kG. The magnet pole width and the pole gap are tentatively assumed to be 100 mm and 16 mm, correspondingly. The pole width in magnet *M1X* is about 280 mm, in order to ensure the required field quality. Magnet *M4Z* is a septum with a current blade 30 mm thick. The length of the magnet is 144 cm, the field is 7.8 kG, and the bending angle is 7.8°. *M5Z* is a Lambertson septum magnet, with a thin magnetic blade (1 mm thick). The length of the magnet is 50 cm, the field is 3.5 kG, and the bending angle is 1.2°.

All magnets have DC supply. We have done calculations for straight magnets with edge focusing, assuming that they are made of stamped iron. However, in principle, the magnetic core of these magnets may be manufactured of solid iron, because a need to retune the field arises only when the energy of the experiment is changed.

Tentative coordinates of the injection point (in the coordinate system as in Fig. 5.2) are as follows: $X \approx$ 24.9 meters (2 meters from the inner wall of the technical straight section), $Y \approx$ 34.4 m (from the center of the straight interval), Z = 1.2 m (the storage rings are at this height from the floor).

БMore accurate coordinates will be obtained after the final determination of the location of the rings and channel in the tunnels.

5.1.2 Injection optics

To implement the radial and vertical achromatic bends and to match the optical functions at the inlet to the storage ring, 16 quadrupole lenses are used in each transfer line (for electrons and positrons). In addition, two lenses are placed at the entrance, in the common part, for matching with the optics of the linac.

The linear accelerator consists of modules 16 meters long. Each module comprises 4 accelerating sections, each 3 m long. Between the sections there are quadrupole lenses, creating the FODO structure as shown in Fig. 5.3.

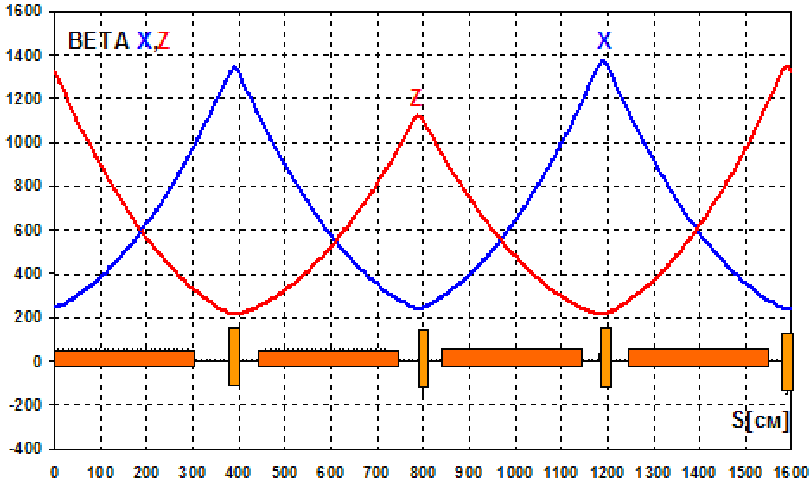

Fig. 5.3 FODO structure of the linac (a 16-meter module consisting of 4 sections and ensuring 200 MeV acceleration is shown).

Figs. 5.4 and 5.5 show the dispersion and beta functions of the transfer line.

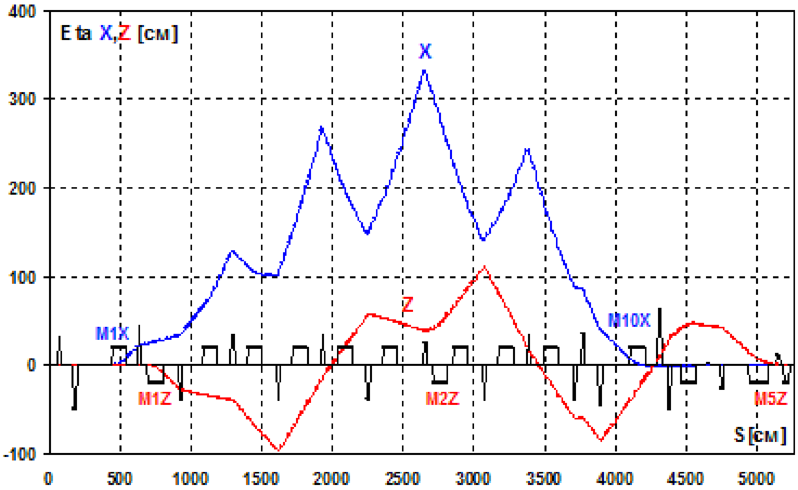

Fig. 5.4 Horizontal and vertical functions of the transfer line.

The radial injection of electrons (positrons) in the technical straight section of the $c\tau$-factory is performed using a special insert device with an increased horizontal beat function as shown in Fig.5.6.

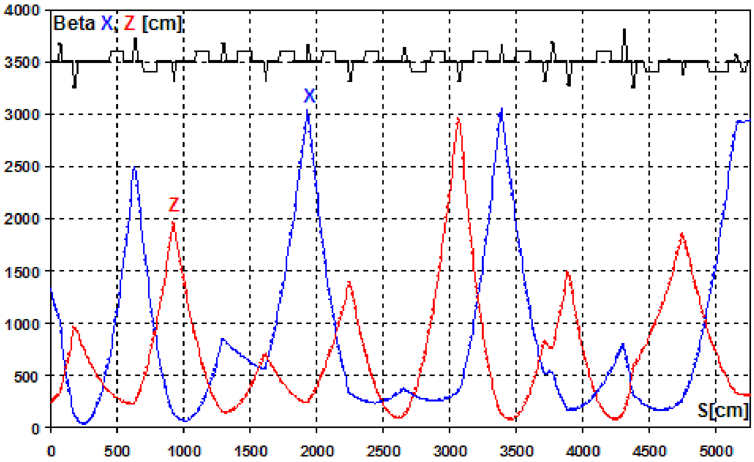

Fig. 5.5 Betatron functions of the transfer line.

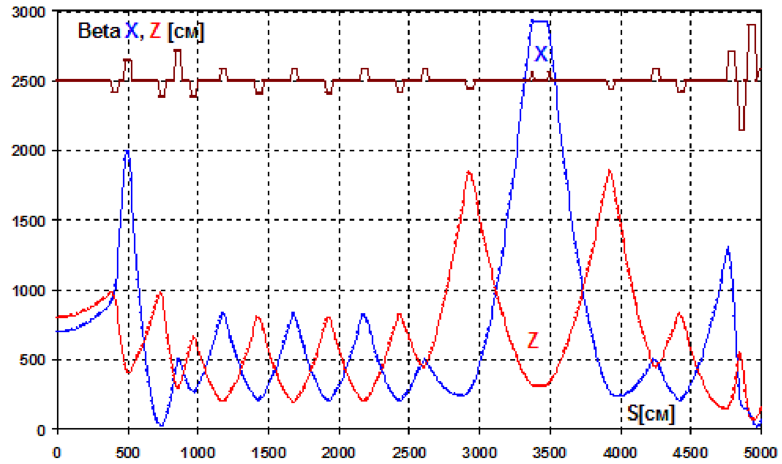

Fig. 5.6 Injection insert device in the regular structure of the technical straight section (the azimuth is ~3300 – 3500 cm).

In the injection azimuth, which is between the two focusing lenses, the betaron functions are $\beta_x = 2940$ cm and $\beta_z = 300$ cm. The horizontal betaron phase advance in the injection insert interval is $\Delta\nu_x = 0.65$, which makes it possible to place a pre-inflector and an inflector here.

The scheme of radial injection is presented in Fig.5.7, where the parameters of the elements involved in the injection are also shown. We apply a conventional scheme using two septum magnets: *S1* with a thick ($d \approx 30$ mm) blade and *S2* with a thin (d = 1mm) blade.

Between lenses *QF* there is a Lambertson septum magnet, which bends the beam in vertical. The small thickness of the blade of the septum magnet is achieved due to placing its yoke in the vacuum chamber of the storage ring and its coil outside. Besides, its field is rather small, $H_x = 3.5$ kG.

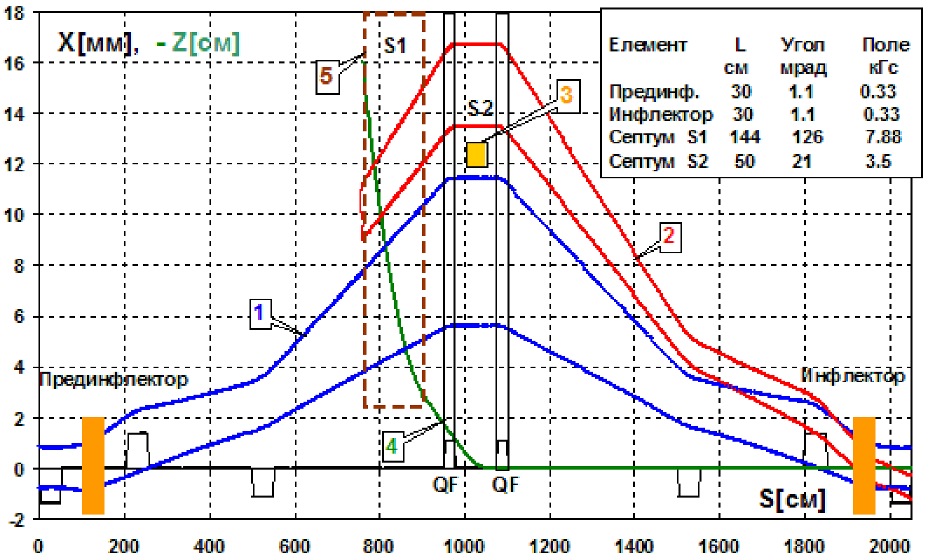

Елемент	L см	Угол мрад	Поле кГс
Прединф.	30	1.1	0.33
Инфлектор	30	1.1	0.33
Септум S1	144	126	7.88
Септум S2	50	21	3.5

Fig. 5.7 Scheme of radial injection. Legend: (1) the stored beam after the inflector impact ($\pm 6\sigma_x$, $\varepsilon_x = 8$ nm-rad), (2) the injected beam ($\pm 3\sigma_x$, $\varepsilon_x = 10$ nm-rad), (3) the blade of second septum magnet *S2* ($d = 1$ mm), (4) the beam trajectory in vertical at the entry, (5) the boundary of first septum magnet *S1*.

The bending angle of the magnet is chosen so that the beam vertical coordinate at the exit of *S1* be $\Delta z > 30$ mm. Septum magnet *S1* has a C-shaped yoke. The outer field coil of the magnet covers the gap and thus forms a current screen. A radial corrector is placed before septum magnet *S1* and in the focal plane of lens *QF*. The corrector deflects the beam by an angle of 2.4 mrad, so in the *S2* azimuth the injected beam has only a coordinate shift $\Delta x = 15$ mm.

For single injection of beam to the equilibrium orbit, the field in the inflector has to be increased up to $H = 0.58$ kG.

5.1.3 Storage ring acceptance and parameters of injected beams

The acceptances of the storage rings in vertical and in horizontal are determined by the geometrical aperture of the final focus lenses. In units of beam standard dimensions they are $A_x = 23\sigma_x$ and $A_z = 60\sigma_z$. In absolute terms, $A_x = 4250$ nm-rad and $A_z = 180$ nm-rad.

The electron beam accelerated from the photo gun to the full energy in the linac will have the following parameters: $\varepsilon_x = \varepsilon_z = 10$ nm at $E_{inj} = 1$ GeV and $\varepsilon_x = \varepsilon_z = 5$ nm at $E_{inj} = 2.5$ GeV; the energy spread $\sigma_E \leq 1\cdot 10^{-3}$.

For the positron beam from the storage/cooler ring at the energy $E = 510$ MeV we have $\varepsilon_x = 23$ nm-rad and $\varepsilon_z = 5$ nm-rad. After acceleration in the linac, the emittance decreases adiabatically: $\varepsilon_x = 11$ nm, $\varepsilon_z = 2.5$ nm at $E_{inj} = 1$ GeV and $\varepsilon_x = 4.6$ nm, $\varepsilon_z = 1$ nm at $E_{inj} = 2.5$ GeV. The energy spread of positrons from the storage/cooler ring will be $\sigma_E = 5\cdot 10^{-4}$ and the bunch length at the exit from the storage ring will be $\sigma_S = 3$ mm. After acceleration in the linac at the acceleration field wavelength $\lambda = 10$ cm, the energy spread in the beam because of the bunch phase length will increase by one order. In this case, the efficiency of the capture of such beam into the storage ring of the $c\tau$-factory will not exceed 60÷70%.

To reduce the positron energy spread after the pre-acceleration in the linac, it is necessary to compress the positron bunch 2÷3 times before its injection into the linac. For this purpose it is necessary to install a section of a 15 ÷20 MeV linear accelerator in the positron extraction line, after the 90° bend. The beam energy spread will increase 4÷5 times at the exit of the section, and the bunch length will decrease after the achromaticity interval for descent to the tunnel with the longitudinal dispersion function $\eta_S \approx 50$ cm. After these manipulations, the energy spread at the entry to the storage ring of the $c\tau$-factory will be $\sigma_E = 1\div 2\cdot 10^{-3}$, and the bunch length will be $\sigma_S \approx 0.5$ cm (the bunch will become longer after passing the transfer line to the $c\tau$-factory, where $\eta_S \approx 250$ cm).

5.1.4 Injection scheme and requirements to the beam parameter stability

Injection and storing take place in a radial plane. The injection point is in 34.4 from the middle of the technical straight section and between the two focusing lenses, where $\beta_x \approx 30$ m, $\beta_z \approx 3$ m, and $\alpha_x = \alpha_z = 0$.

The beam is brought to the lens from below. Then the Lambertson septum magnet brings the beam to the median plane in 16 cm from the equilibrium orbit (Fig.5.8). The distance between the injected beam and the stored one (after the latter has been impacted by the pre-inflector) is 6.5 mm in the azimuth of the septum magnet. The inflector puts the stored beam in the equilibrium orbit, and the injected beam experiences residual oscillations with amplitude of 6.5 mm.

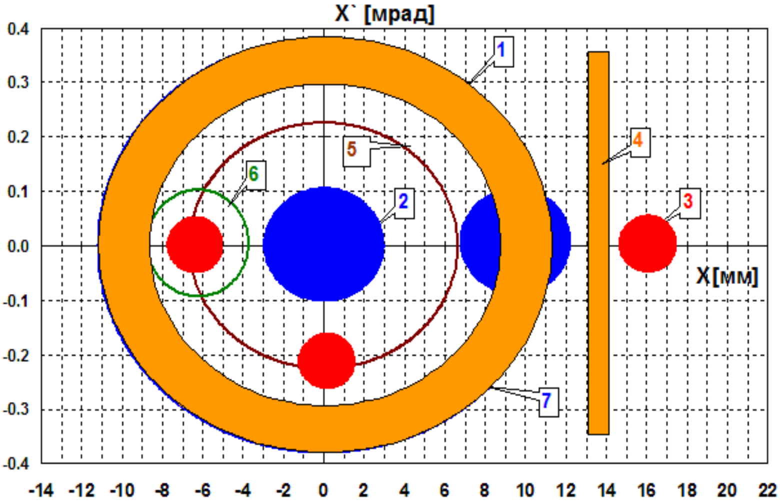

Fig. 5.8 Scheme of the radial injection and storing of beam in the $c\tau$-factory. Legend: (1) boundary of the radial acceptance of the ring A_x = 0.425 cm·mrad (25σ_x), (2) stored beam emittance, containing 6σ_x (ε_x = 8 nm), (3) injected beam, containing 95 % particles of 3σ_x (ε_x = 10 nm), (4) blade of the septum magnet (1 mm), (5) amplitude of the oscillations of injected beam after the impact from the pre-inflector (6.5 mm), (6) effective acceptance to capture the injected portion (A_{eff} = 270 nm), (7) collimator for 18σ_x (background killer) behind the inflector.

The phase advance between the pre-inflector and the septum magnet is $d\nu_x$ = 0.25; that between the inflector and the pre-inflector is $d\nu_x$ = 0.5. Ensuring a storing efficiency close to 100% imposes rather tight requirements on the vertical and horizontal position of beam at injection. From Fig.5.9, which schematically presents the efficient acceptance for beam capture and the beam itself, it follows that the requirements for a 100% injection coefficient are $\Delta x < \pm1.5$ mm and $\Delta x' < \pm0.04$ mrad.

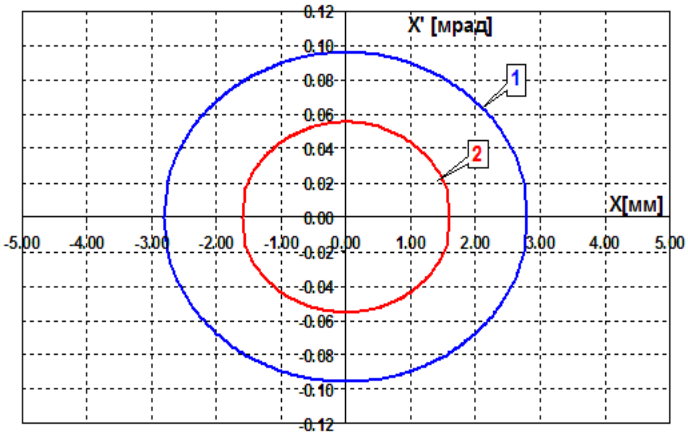

Fig. 5.9 Horizontal acceptance (A_{xeff} = 270 nm) for the injected beam (1) and the injected beam boundary containing 95% of particles for the emittance ε_x = 10 nm.

Not less stringent requirements are imposed on the position of the injected beam in vertical.

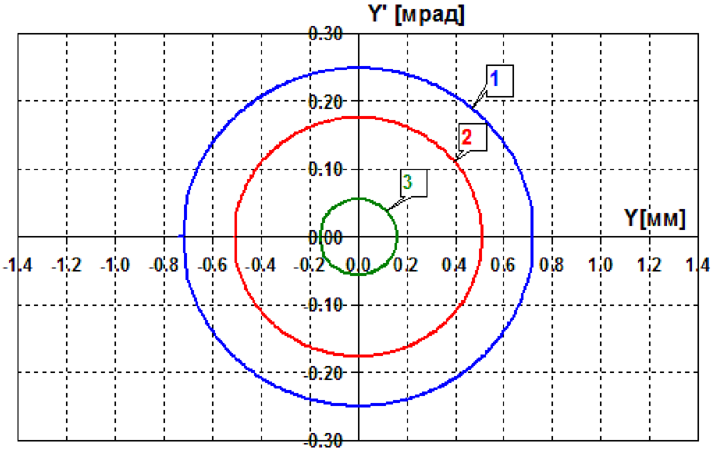

Fig. 5.10 Vertical acceptance (A_{zeff} = 180 nm, β_z = 3 m) for the injected beam (1) and the injected beam boundary, containing 95% of particles for a 100% coupling and the emittance ε_z = 10 nm.

For a 100% injection the requirements to the vertical coordinate stability and the injection angle must be as follows:

- ε_z = 10 nm $\Delta z = \pm 0.2$ mm $\Delta z' = \pm 0.075$ mrad
- ε_z = 1 nm $\Delta z = \pm 0.56$ mm, $\Delta z' = \pm 0.20$ mrad

The above requirements to the stability of the coordinate and angular position of the beam at injection allow estimating a requirement to the magnet power supply stability.

$\Delta H/H = 4\cdot 10^{-5}/1.57 = 2.5\cdot 10^{-5}$ for 90° bends. However, since these magnets are powered in series and the bends are achromatic, the power supply stability requirement decreases to about $1\div 2\cdot 10^{-4}$. For separately-powered magnets, like the 8° septum magnet with current blade, $\Delta H/H = 7.5\cdot 10^{-5}/0.139 = 5\cdot 10^{-4}$. For the inflector with $\varphi = 1.85\cdot 10^{-3}$ (at single injection), $\Delta H/H = 4\cdot 10^{-2}$.

Subject to possible simultaneous drifts, the requirements to the field stability of $\Delta H/H \le 1 \div 2\cdot 10^{-4}$ in the permanent magnets and of $\Delta H/H \le 1\cdot 10^{-2}$ in the pulsed inflector and pre-inflector appear quite feasible.

5.2 Polarized electron source

This project of polarized electron source is substantially based on the successful experience with such device made in the 1990s at BINP SB RAS in cooperation with the Institute of Semiconductor Physics SB RAS and NIKHEF (Amsterdam) [40, 41, 42, 43, 44]. The Amsterdam source was applied to experiments on the study of the inner structure of polarized nuclei via the scattering of polarized electrons on the nuclei of the inner target in the AmPS storage ring. Unlike the AmPS source, where a laser drew a rather long-duration electron pulse (2.1 μs, 15-50 mA, 1 Hz, polarization degree as high as 80%, 100 keV) from the photocathode, in the new source it is necessary to accelerate a single bunch of $5\cdot 10^{10} - 1\cdot 10^{11}$ electrons with a duration of 2 ns or less. Later the electron current pulse is to be compressed to an even shorter bunch suitable for direct acceleration up to energy of 2.5 GeV in a pulsed S-band linac operating with a repetition rate of 50 Hz.

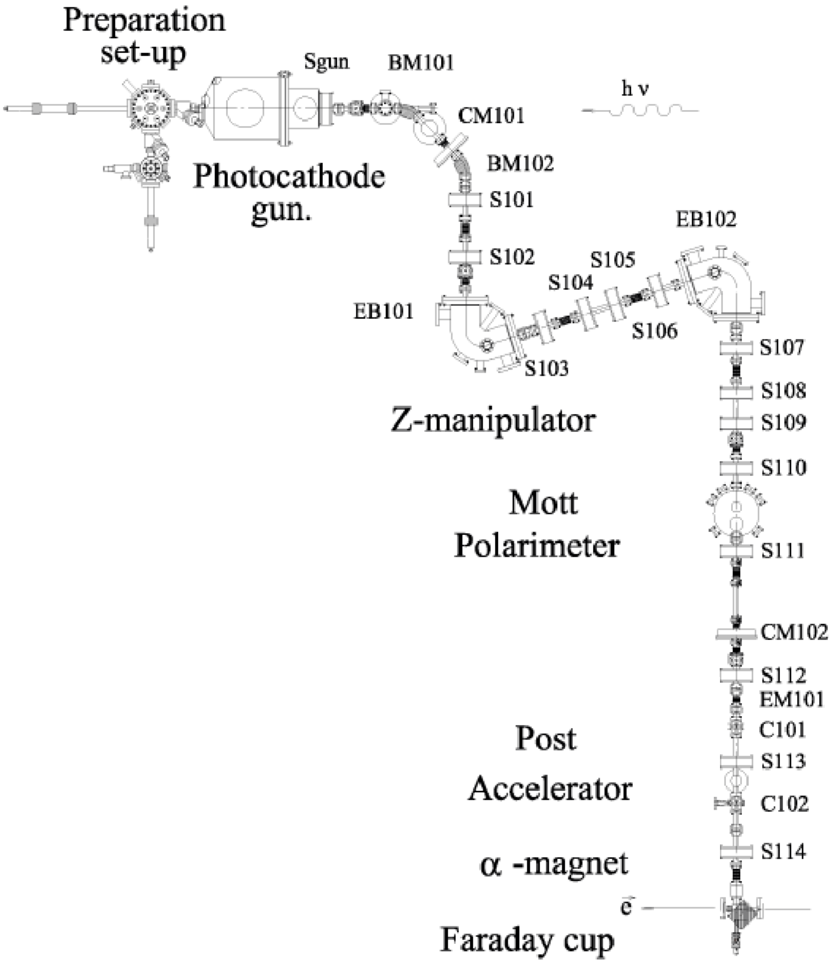

Fig. 5.11 Detailed scheme of the source of polarized electrons.

In spite of some difference in the tasks, the general arrangement of the source for the $c\tau$-factory practically repeats the AmPS source scheme (Fig.5.11). Now we proceed to the discussion of the most important units and problems of the future source.

5.2.1. Photocathode

Photocathodes in the source created for NIKHEF were structures of InGaAsP and GaAs crystalline layers [40]. Judging by our measurements, the degree of polarization was 80% in best samples. The cathodes, the system for their preparation and the laser optics were designed and manufactured at the Institute of Semiconductor Physics SB RAS at the laboratory directed by A.S. Terekhov.

In recent years, the technology of manufacturing of GaAs photocathodes used for generation of polarized electron beams has advanced significantly [45]. Almost all their options have been improved, see Table 5.1. So, the degree of electron polarization in the best photocathodes has increased up to 92% and the possibility of its further increase up to 97% has been discussed. The quantum efficiency of photocathodes has reached 0.85%.

Best photocathodes are now produced in St. Petersburg by the research team led by Professor Yu. Mamaev. These photocathodes have passed a comprehensive test at the SLAC laboratory in Stanford. They not only showed a high degree of polarization and good quantum efficiency but also demonstrated a quite acceptable lifetime. The project of the source for the ILC is also being developed on their base.

Table 5.1. Comparative characteristics of the best photocathodes [6].

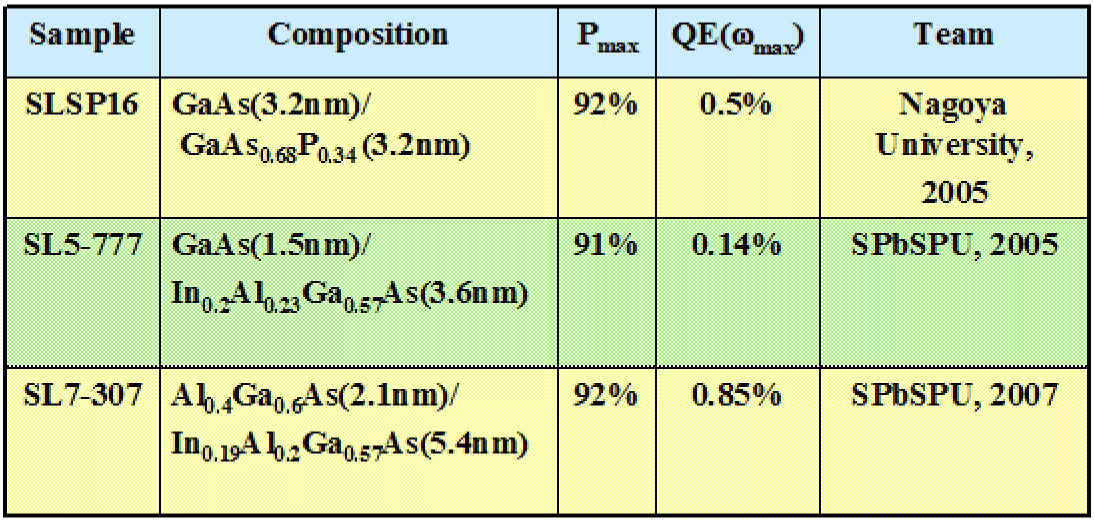

Sample	Composition	P_{max}	$QE(\omega_{max})$	Team
SLSP16	**GaAs(3.2nm)/ $GaAs_{0.68}P_{0.34}$ (3.2nm)**	**92%**	**0.5%**	**Nagoya University, 2005**
SL5-777	**GaAs(1.5nm)/ $In_{0.2}Al_{0.23}Ga_{0.57}As$(3.6nm)**	**91%**	**0.14%**	**SPbSPU, 2005**
SL7-307	**$Al_{0.4}Ga_{0.6}As$(2.1nm)/ $In_{0.19}Al_{0.2}Ga_{0.57}As$(5.4nm)**	**92%**	**0.85%**	**SPbSPU, 2007**

A modern photocathode is a multilayer semiconductor structure with alternating periods of a crystal lattice grown on a relatively thick GaAs substrate. The mechanical stress induced by alloying the alternating layers of the main semiconductor with atoms of indium, aluminum and other elements creates sufficiently large splitting of the energy levels of electrons with different spin direction in the valence band. This splitting of the levels J = 3/2, m =- 3/2 and J =3/2, m =-1/2 exceeds 60 meV in the best samples, which allows rather selective emission of electrons with only one spin direction into the conduction band, Fig. 5.12 [46].

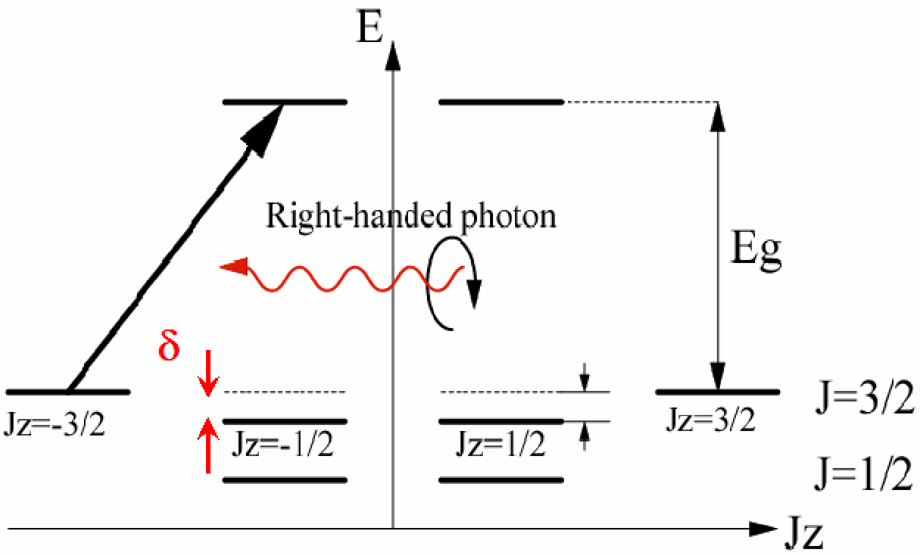

Fig. 5.12 Valence band splitting and scheme of transitions to the conductance band.

Details of the technology of photocathode preparation are outside the scope of this review. What we are interested in is the quality of this product. The graph in Fig. 5.13 shows the quantum yield and polarization vs. the wavelength of the light used [45]. One can see from the data that the maximum degree of polarization, 92%, is achieved at 825 nm.

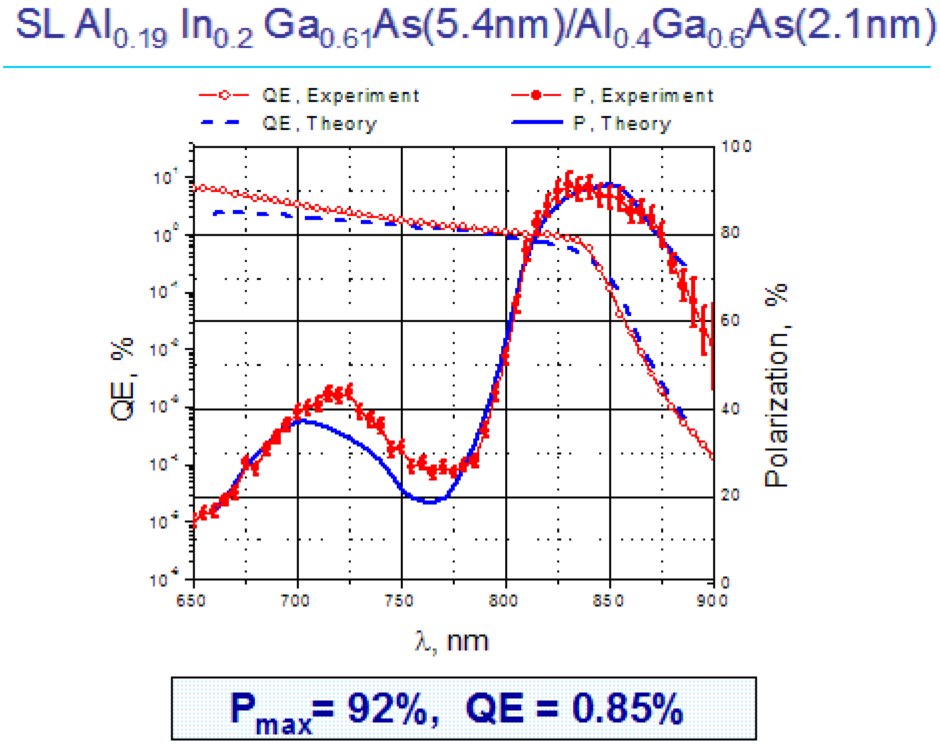

Fig. 5.13 Quantum yield and polarization degree vs. the light wavelength.

5.2.2. HV unit

The main requirement to the high voltage chamber of the photo gun is that is must ensure ultra-high vacuum, at a level of 10^{-11} mbar. The idea of using a double vacuum chamber with a 10^{-8} mbar insulating vacuum encompassing the insulators of the accelerating tube was successfully tested for the Amsterdam source. Fig. 5.14 shows a diagram of such a double vacuum chamber.

A negative voltage pulse of -100 kV about 500 microseconds in base was applied to the accelerating tube. The beam pulse duration was determined by the light flash duration. For the c-tau source, the light pulse duration should be shorter than 2 nsec.

The low pulse rate of the accelerating voltage by more than three orders of magnitude reduced the time of bombing the photocathode with dark currents, which are always present in high-voltage devices, which, in turn, allowed us to increase the lifetime of the cathodes up to one month. With a constant voltage across the accelerating gap, the lifetime of the cathode did not exceed 2-3 days.

The accelerating gap of the AmPS guns was 65 mm. The maximum field strength on the cathode surface did not exceed 17 V/cm. The photocathode diameter was equal to 12 mm, and the spot size could vary from 1 to 7 mm.

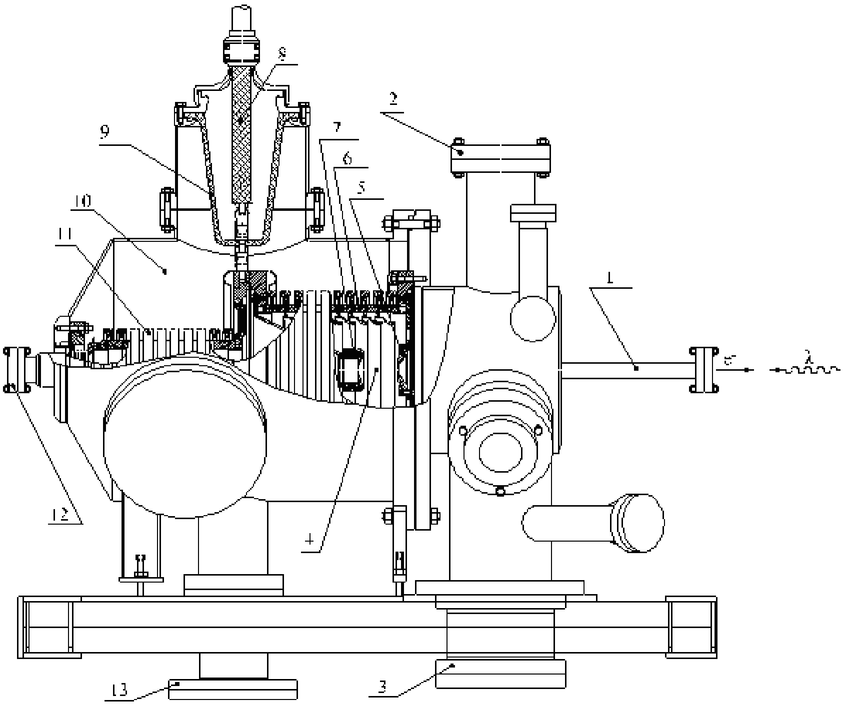

Fig. 5.14. Photo gun: 1- extraction line and the window for laser radiation input, 2,3, 13 – vacuum pumping ports, 4 – acceleration gap, 5 – anode, 8 – HV cable, 6 – insulator of the accelerating tube, 11 – second insulator of the accelerating tube, 10 – protective vacuum case, 12 – flange for interfacing the preparation and loading chambers with the unit.

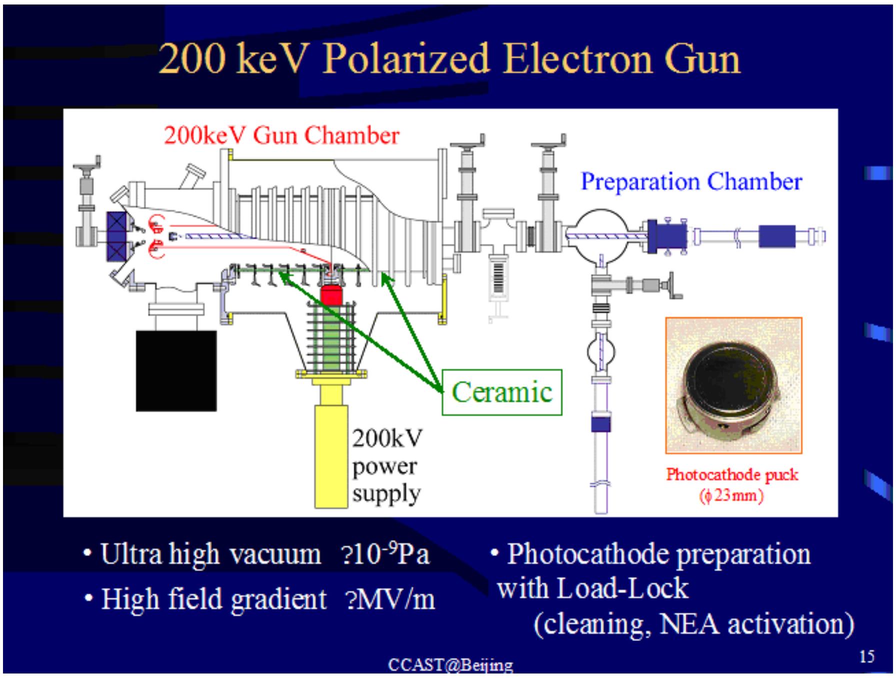

200 keV Polarized Electron Gun

- Ultra high vacuum ?10^{-9}Pa
- High field gradient ?MV/m
- Photocathode preparation with Load-Lock (cleaning, NEA activation)

CCAST@Beijing

15

Fig. 5.15 Scheme of the HV unit of the polarized electron source for the University of Nagoya, Japan [46].

Generation of a shorter beam pulse in the c-tau source will obviously require a significantly higher rate of acceleration as compared with the AmPS source. For instance, in the source under development at the University of Nagoya within the framework of the ILC project, the acceleration rate has been increased up to 29.7 kV cm on the photocathode surface [46]. In this case, a constant accelerating voltage of -200 kV is applied to a very small gap of 35 mm,

Fig. 5.15 and Fig. 5.16. In this source, dark currents are suppressed using molybdenum as a material for the cathode electrodes and titanium as a material for the anode. Studies conducted at the University of Nagoya show the attainability of maximum field strengths of up to 1300 kV/cm for molybdenum-titanium pairs of electrodes [47]. In general, the high-voltage unit of the University of Nagoya with the preparation and loading chambers bases on the same principles that were used earlier for the AmPS source. However, the cathode in it is better screened from weak electrical discharges that occur along the ceramic insulators. Besides, magnetic lense with a longitudinal magnetic field is made as close to the photo-cathode as possible. This measure improves the matching of the beam emittance with the electron-optical path of the channel. All of these innovations as well as the new photocathodes produced in St. Petersburg will be used in the project of the source for the c-tau factory.

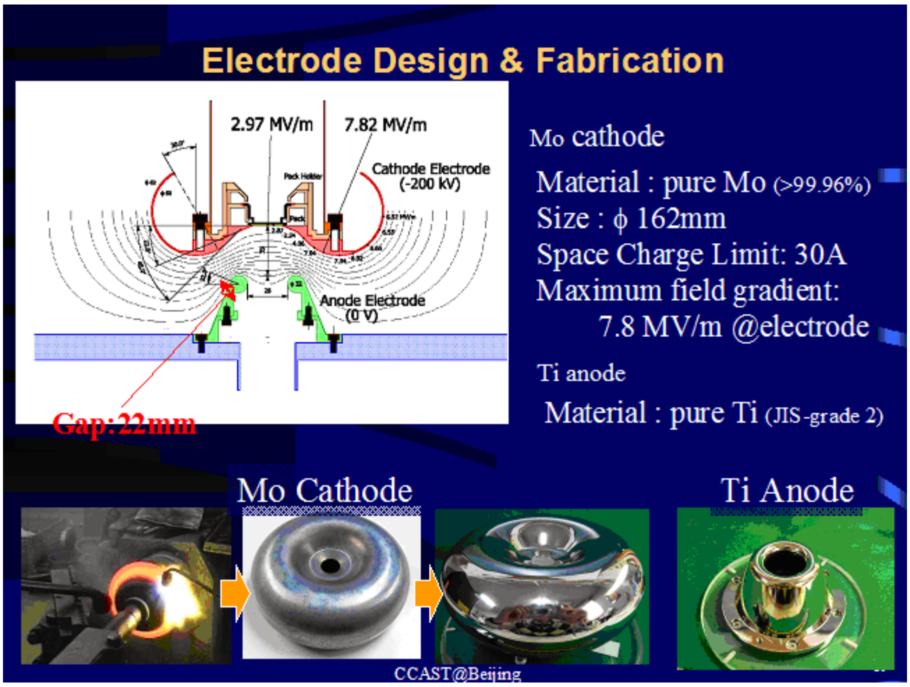

Electrode Design & Fabrication

Mo cathode

Material : pure Mo (>99.96%)
Size : ϕ 162mm
Space Charge Limit: 30A
Maximum field gradient:
7.8 MV/m @electrode

Ti anode

Material : pure Ti (JIS-grade 2)

Mo Cathode

Ti Anode

CCAST@Beijing

Fig. 5.16 Geometry of the acceleration interval of the source for the University of Nagoya [46].

5.2.3. Activation of the cathodes

The cathode is subjected to chemical etching in hydrochloric acid (15-20 seconds), in a nitrogen atmosphere in a fume hood. Then it is washed with methanol and dried. After that, the cathodes are inserted into frames and placed in a special sealed container on the top of the hood. The container can comprise up to three cathodes at once. The nitrogen-filled container with the cathode is transferred to the upper port of the loading chamber, also filled with pure nitrogen. Then oil-free turbo-pumps and magnetic-discharge pump out the loading chamber with the cathodes inside it to 10^{-8} mbar. After that, the cathodes are transported through a sluice to the preparation chamber, where they are placed on a carousel, up to 4 cathodes at once. The cathodes are always transported by magnetic manipulators. The chambers are separated by a gate with metal sealing.

The procedure of photo-cathode activation occurs in the preparation chamber under a vacuum of 10^{-11} mbar, maintained with an ion pump with titanium getter and NEG ribbon. The carousel is rotated, and the cathode in the frame is moved into position in front of the plate of the heater. Infrared radiation of the heater gradually warms up the cathode up to $600^0 C$. In so doing, the pressure should not rise above 10^{-8} mbar. A temperature of $600^0 C$ is maintained for one hour in order to evaporate the contaminated surface layer of different arsenic compounds. After that, the cathode is slowly cooled to room temperature.

Then, in order to reduce the potential barrier for electron emission, deposition of alternating cesium and oxygen atoms is performed. This procedure is called "Yo-Yo". The thickness of each elementary layer is about 0.1 of a monolayer. Cesium is deposited first. 12-15 pairs of layers are applied, till the saturation of the photocurrent collected on a special collector. In the process of cesium application, the cathode is continuously illuminated with a halogen lamp.

The activation over, the quantum yield is measured using a helium-neon laser at several power levels. A good InGaAsP cathode usually shows a 10-14% yield at the wavelength of this laser.

The old cathode is taken off and put to the carousel for subsequent reactivation. As a rule, 2-3 reactivations reduce the cathode quality insignificantly. The new cathode is placed on the cathode unit and tested at several wavelengths of a titanium-sapphire laser.

5.2.4. Magneto-optical system. Spin rotator

There is a lens with an axially symmetric longitudinal magnetic field set immediately at the gun exit. The configuration of the lens field is chosen in view of the influence of the space charge effect on the trajectory of the electrons. For an intense nanosecond bunch the influence of this effect must be considered and, if possible, compensated. From the results of the simulation and measurement of the normalized emittance at the University of Nagoya [46], its value does not exceed $\varepsilon_{x,y} = 10\pi \cdot mm \cdot mrad$. These measurements were made for $q = 5nC$ and a bunch duration of 1 nsec.

Then the magnetic field bends the beam through 90^0 or a slightly less angle in order to separate the light beam and the electron one. However, in principle, it seems possible to input the laser beam along an oblique trajectory, in which case no magnetic bend is required. The latter variant needs additional elaboration. Note that magnetic bends of a nonrelativistic electron beam have practically no influence on the spin, in the sense that the spin is rotated in the same way as the velocity vector.

Next, there are two ways to rotate the spin perpendicular to the velocity vector. In the Amsterdam source we used an electric field to bend the beam through 110^0. In so doing, the spin was almost not rotated and exactly perpendicular to the velocity. Then the solenoid rotated the spin around the longitudinal axis into the upright position, and the spin remained vertical after experiencing a reverse rotation by the electric field. If the solenoids between the bends were included in a configuration with a zero integral of the longitudinal field, the two electric rotations compensated each other, and the spin remained longitudinal. By adjusting the value of the longitudinal field integral, it was possible to obtain any desired orientation of the spin. This type of spin rotator is called Z-shape manipulator because of its shape in the plan.

Another variant is using the so-called Wien filter. It is a straight section with crossed electric and magnetic fields. Their effects on the velocity vector are mutually compensated, and in this case the spin is rotated around the magnetic field direction through an angle proportional to the integral of the magnetic field. The main advantage of using the Wien filter is the absence of linkage with a strictly defined energy of electrons

5.2.5. Mott polarimeter

After passing the spin rotator, the beam has a spin orientation normal to the velocity, e.g. a vertical one, see Fig.5.11. Its scattering on gold atoms through an angle of 120^0 is noticeably asymmetrical, which is usually applied to measurement of the polarization degree. Details of the polarimeter structure and particularities of its operation can be found in [41, 43].

5.2.6. Beam bunching, pre-acceleration and injection to the linac

In the AmPS source, the beam was bunched; then two cavities, which were supplied with part of the power of the 1st klystron of the large linac, accelerated it to energy of 400 keV [42]. Then the so-called alpha-magnet injected the beam to the linac axis with the help of a magnetic rotation through 270^0. Such a rotation has several advantages as compared with rotation through 90^0. It can be made achromatic and focusing in both transverse coordinates. In addition, it has a certain bunching effect, which is opposite in sign to the drift gap. In the version with unpolarized electron source, the alpha-magnet was turned off to pass the beam from the straight direction.

5.2.7. Main parameters

In conclusion, Table 5.2 presents a list of the main subsystems of the polarized electron source.

Table.5.1 Main subsystems of the polarized electron source.

Glove box for photocathode etching
Loading chamber
Preparation chamber
Magnetic manipulators
Photo gun + 100 kV pulsed power supply (0.2 ms pulse, 50 Hz)
Ultra-high vacuum system (pumps, heaters, NEG, sensors): $p < 10^{-11}$ mbar
Ti-Sapphire drive laser + optics
Z-shape spin-manipulator
100 keV beam line
Mott polarimeter
Sub-harmonic pre-buncher + pre-accelerator
Alpha-magnet
Faraday cup

The main design parameters of the source of polarized electrons for the c-tau factory are shown in Table 5.3. It should be noted that many of the characteristics of the beam are determined not so much by the photo gun quality as such but by its subsequent transformation in the process of bunching and pre-acceleration. In particular, the value of emittance is not reliably predictable at this stage.

Table.5.2 Parameters of the source of polarized electrons for the c-tau factory.

Beam polarization	80-90%
Polarization lifetime in ring	3000-4500 s
Cathode voltage (pulsed, 02 ms, 50 Hz)	-100 kV
Photocathode type	AlInGaAS/AlGaAS SL with strained QW, SPbSPU
Laser type	Ti-Sapphire
Laser wavelength	700-850 nm
Laser energy in pulse	10 mkJ

Pulse duration	2 ns
Repetition rate	50 Hz
Number of electrons/pulse	3×10^{10} (5 nC)
Normalized beam emittance, rms	10-30 mm-mrad
Photocathode quantum efficiency	up to 0.5 %
Photocathode recesiation time	200-600 urs (depends on laser power)

5.3. Production of intense positron beams at the injection complex

5.3.1. Introduction

There are two processes known to be practically suitable for production of positrons: (a) β+ decay of radioactive isotopes and (b) production of electron-positron pairs when a relativistic photon passes in the field of atom nucleus. Positron sources based on the β+ decay are not well suited for experiments with colliding electron-positron beams because of the relatively low intensity of particle production as well as the complexity of the collection of produced positrons into short narrowly focused bunches the modern accelerators work with. In the accelerator technology, the process of production of electron-positron pairs in an electromagnetic shower is used for the production of positrons. An electromagnetic shower can be obtained via directing a high-energy electron beam on a target. Electrons lose their energy in the target and emit relativistic bremsstrahlung photons. These photons produce high-energy electron-positron pairs in the field of the nuclei, which pairs emit new photons. The avalanche multiplication of particles occurs until the electrons and positrons slow down so that the energy loss due to bremsstrahlung equals the ionization losses. This critical energy for different substances can be roughly estimated by the formula [30, p. 213]

$$E_c = \frac{800\ \text{МэВ}}{\mathrm{Z}+1.2}, \tag{5.1}$$

where Z is the number of protons in an atom of the material of the target.

Modern positron sources based on particle production in electromagnetic shower [1, 2] operate on a principle which was first implemented in Stanford in the 1950s [3]. Fig. 5.17 shows the general scheme of such a source. The electron beam of linear accelerator, focused on a target of a material with a high atomic number, generates an electromagnetic shower. Shower-produced positrons leave the target with a large angular and energy spread (Figure 4.18), so only a small fraction (typically <10%) of these particles can be focused and accelerated in the second linear accelerator. The beginning of this accelerator is placed in a solenoidal magnetic field that ensures retention of positrons near the axis of the accelerating structure until they acquire a longitudinal momentum sufficient for using quadrupole lenses for alternate-sign focusing in the rest of the accelerator.

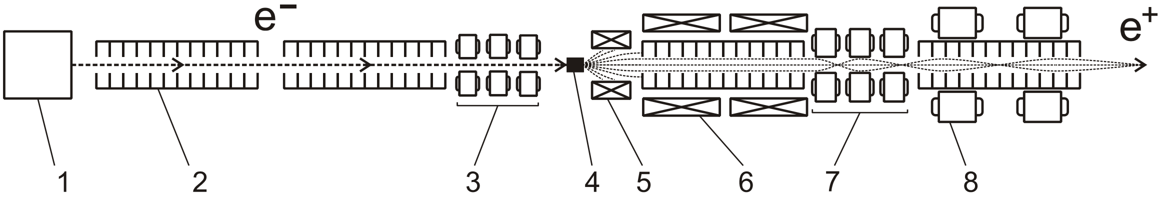

Fig. 5.17. Scheme of a typical source of positrons for the acceleration technology. 1 — electron source, 2 — accelerating RF structure, 3 — quadrupole lenses focusing electrons on the target, 4 — conversion target, 5 — the matching device, 6 — solenoid comprising the first structure for positron acceleration, 7, 8 — quadrupole lenses.

The number of positrons in the maximum of the electromagnetic shower produced by an electron with energy E is given by the following expression [9, p. 197]:

$$N_{e^+} \approx \frac{0{,}15}{\sqrt{\ln(E/E_c) - 0{,}37}} \cdot \frac{E}{E_c}, \tag{5.2}$$

This dependence is close to linear for a broad energy range (see Fig.5.9), that is why the positron source efficiency is usually measured with the following value:

$$Y = \frac{1}{E} \cdot \frac{N_+}{N_-}, \tag{5.3}$$

which is called the positron yield. Here N_- is the number of positrons coming to the target; N_+ is the number of accelerated positrons. Modern facilities give the positron yield $Y = 0{,}02 \div 0{,}06$ GeV^{-1} (see Table 5.3).

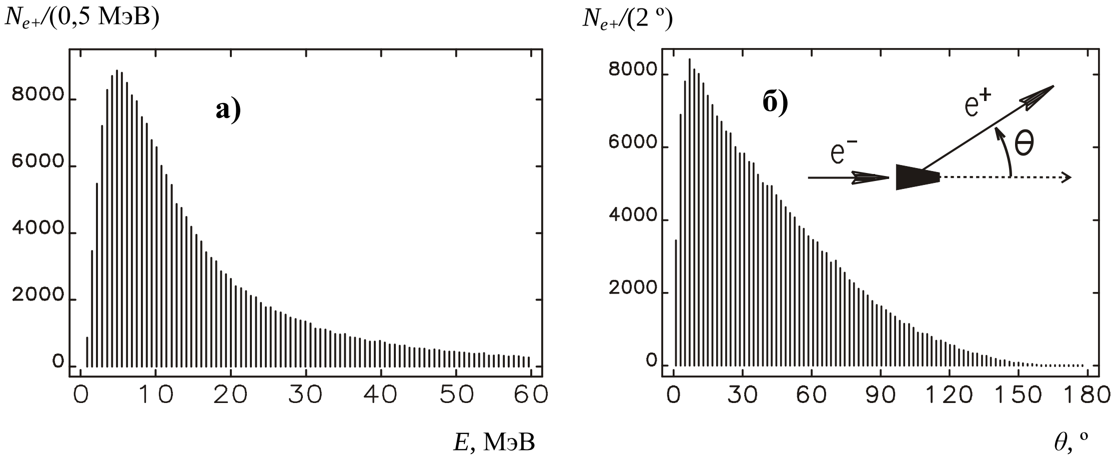

Fig. 5.18. Energy (a) and angular (b) spread of positrons coming out of the conversion target. The spectra were obtained using the GEANT code [16] (the number of electrons coming to the target is $2 \cdot 10^5$; the electron energy is 280 MeV; the tantalum target length is 12 mm). The total number of positrons coming out of the target is $2{,}4 \cdot 10^5$ (the disagreement with the formula is explained by the fact that approximately half of the shower-produced positrons annihilate inside the target). The spectra are in weak dependence on the primary electron beam.

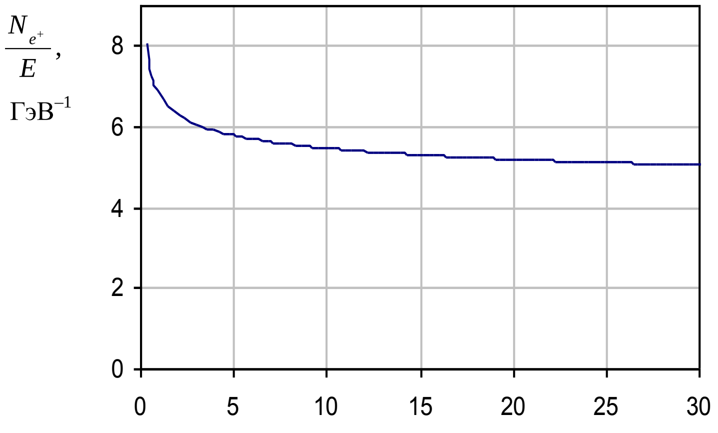

Fig. 5.19. Dependence of the N_{e^+}/E value on the energy calculated by formula (5.2).

Table 5.3. Parameters of the positron sources. Abbreviations: flux concentrator (FC) and quarter-wave transformer (QWT). Parameters that were not found in literature and thus were calculated from indirect data are marked with asterisk.

Facility name	**PEP-II**	**KEKB**	**DAFNE**	**BEPC**	**DORIS**	**LIL**
Research center	SLAC	KEK	LNF	IHEP	DESY	CERN
Country	USA	Japan	Italy	China	Germany	Switzerland
Frequency of the accelerating RF structures, MHZ	2856	2856	2856	2856	2998	2998
Frequency of the complex, Hz	120	50	50	12.5	50	100
Energy of e^- on the target, GeV	33	3.7	0.19	0.14	0.4	0.2
e^- per bunch	$5 \cdot 10^{10}$	$6 \cdot 10^{10}$	$1.2 \cdot 10^{10}$*	$5.4 \cdot 10^{9}$*	$3.1 \cdot 10^{9}$*	$3 \cdot 10^{9}$*
Field in the solenoid, T	0.5	0.4	0.5	0.35	0.4	0.36
e+ energy after solenoid, MeV	120	100	120*	100	🟩	90
Material of the target	W-25Re	W	W-25Re	W	W	W
Type of the matching device	FC	QWT	FC	FC	QWT	QWT
Parameters of matching device	$B = 6$ T $L = 10$ cm	$B = 2$ T $L = 4.5$ cm	$B = 5$ T $L = 12$ cm	$B = 2.6$ T $L = 12$ cm	$B = 1.8$ T $L = 4.5$ cm	$B = 0.83$ T $L = 4.4$ cm
Positron yield after the linac, 1/GeV	0.054*	0.023	0.053	0.014	0.025	0.0295
Energy of the storage ring, GeV	1.15	3.5	0.51	1.3	0.45	0.5
Energy acceptance of the storage ring, $(\Delta E/E) \cdot 100\%$	2 %	0.5 %	3%	1%	1%	2 %
Positron production, 1/s	$\sim 8 \cdot 10^{12}$*	$\sim 10^{11}$* $(2 \cdot 10^{11}$*)	$\sim 2 \cdot 10^{10}$*	$\sim 2.5 \cdot 10^{8}$*	🟩	$\sim 2.2 \cdot 10^{10}$*
Information sources	[17, 18, 19]	[20, 21]	[22, 23, 24]	[25, 26]	[27, 28]	[27, 29]

The VEPP-5 injection complex is intended to provide relativistic electrons and positrons for elementary particle physics experiments on colliding electron-positron beams. Particular attention in the development of the positron source was placed on the magnetic system for collection of positrons after the conversion target. As a result, a pulsed axial magnetic lens with magnetic field of fairly high quality (with a small field transverse component deflecting the particles from the accelerator axis) was created, which ensured a fairly high positron yield ($Y \approx 0{,}1$ GeV^{-1}) of the positron source at a relatively modest cost of the installation construction. The BINP-developed source allows producing $5 \cdot 10^{8}$ positrons in one pulse.

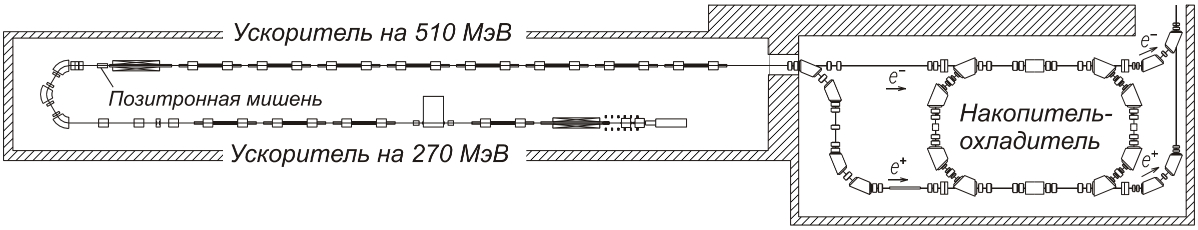

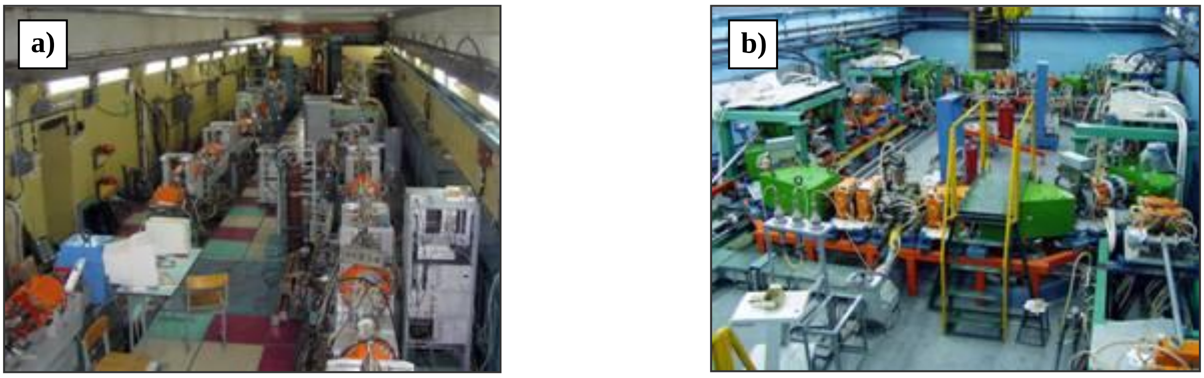

Fig. 5.20. VEPP-5 injection complex. a) linear accelerators, b) storage/cooler ring.

These positrons are accelerated to energy of 70 MeV in the first accelerating section after the target. The electron beam coming to the target contains $2{\cdot}10^{10}$ electrons with energy of 270 MeV.

Table 5.4. Design objectives for the pre-injector

Final energy of beams	510 MeV
Electrons per pulse	$2{\cdot}10^{10}$ e^-
Positrons per pulse	$5{\cdot}10^{8}$ e^+
Pulse repetition rate	50 Hz
Energy spread of	
electron beam	± 1 %
positron beam	± 3 %
Emittance of	
electron beam	~ 10^{-5} rad·cm
positron beam	~ 10^{-4} rad·cm
Working radio frequency	2856 MHz
Pulse power of klystron	≈ 60 MW
Number of klystrons	4 pcs.
Total power consumption	600 kW

Table 5.5. Design objectives for the storage/cooler ring

Beam energy	510 MeV
Perimeter	2740 cm
Radio frequency	700 MHz
Time of radiation damping	18 ms (τ_z)
Beam output parameters	
number of particles	$2{\cdot}10^{10}$ e^+ or e^-
energy spread	± 0,07 %
longitudinal size	4 mm (σ_z)
horizontal emittance	$2{,}3{\cdot}10^{-6}$ rad·cm
vertical emittance	$0{,}5{\cdot}10^{-6}$ rad·cm
Total power consumption	800 kW

5.3.2. VEPP-5 injection complex

The VEPP-5 injection complex (Fig.5.20) is a modern source of relativistic electrons and positrons under construction at Budker Institute of Nuclear Physics for operation of facilities on colliding electron-positron beams. The basis of the injection complex is the pre-injector, i.e. two linear accelerators for energy of 270 MeV and 510 MeV. After rotation through 180° in a magnetic field, electrons from the first accelerator come to the conversion target and produce positrons, some of which are then accelerated up to 510 MeV in the second accelerator. A pre-injector operation mode in which only electrons are accelerated is also possible. In this case, individual electron bunches are sent past the target to the second linear accelerator, which is arranged so that to accelerate electrons from 270 MeV to 510 MeV.

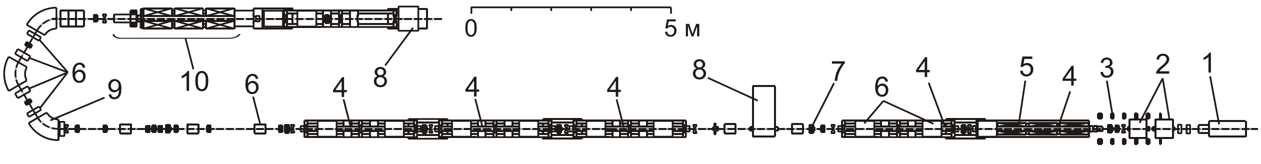

Fig. 5.21. Scheme of the positron injection source of the VEPP-5 complex. 1 — electron gun, 2 — subharmonic buncher, 3 — focusing coil, 4 — acceleration structure, 5 — solenoid coil, 6 — quadrupole lens, 7 — corrector, 8 — spectrometer, 9 — bending magnet, 10 — conversion system.

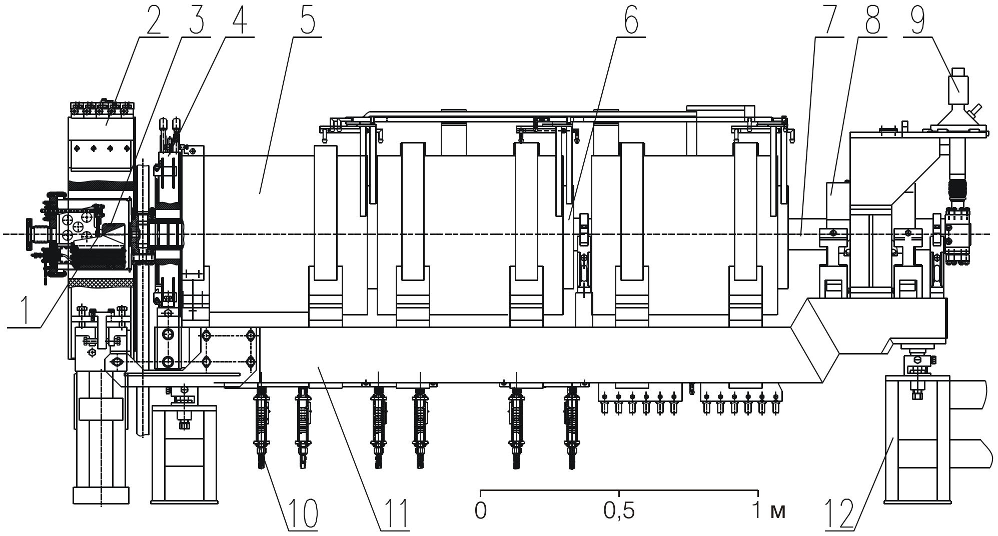

Fig. 5.22. Conversion system. 1 —conversion target, 2 —coil of the convertor, 3 —matching device, 4 — matching coil, 5 — outer coil of the solenoid, 6 — inner coil of the solenoid, 7 — acceleration structure, 8 — quadrupole lens, 9 — vacuum pump, 10 — cooling water meter, 11 — stand for the solenoid, 12 — support.

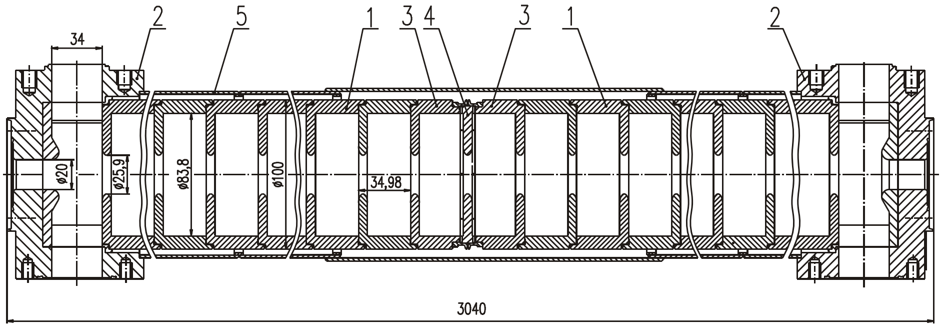

Fig. 5.23. Acceleration RF structure of the VEPP-5 injection complex. 1 — regular acceleration cell, 2 — wave-type transformer, 3 — transition (connection) acceleration cell, 4 — connecting diaphragm, 5 — water jacket.

Apart from the linear accelerators, the injection system includes a cyclic particle storage ring. After the linac, the electron or positron beams are injected into the storage ring, where they are moving along a closed trajectory in a magnetic field. After a certain number of turns, next portion of particles from the linear accelerator is added to the circulating bunch. When a required number of particles are collected, the beam is extracted to consumers. Since the coefficient of positron yield is small, most time the storage ring has to work with these particles. Electrons can also be injected into the storage ring, and they will move in the opposite direction (see Fig. 5.20). The design of the storage ring does not provide simultaneous accumulation of both types of particles moving in opposite directions.

Particles in the storage ring execute betatron oscillations relative to the equilibrium orbit, which consists of circular arcs in the bending magnets and linear segments in the straight sections between them. The straight sections of the orbit comprise quadrupole lenses that ensure sustainability of the betatron oscillations. Moving in the field of the bending magnets of the storage ring, a charged particle is emitting the so-called synchrotron radiation, which results in a radiation reaction force directed against the vector of the particle momentum. The average energy loss of particles by radiation is compensated in the storage ring by means of the RF cavity operating at a frequency that is a multiple of the rotation frequency of the beam in the equilibrium orbit. The electric field in the cavity is directed along the equilibrium orbit, and therefore fills only the loss of the longitudinal component of momentum. As a result, after a lot of turns the radiation reaction force leads to a gradual decrease in the transverse components of the particle momentum and in the amplitude of betatron oscillations [31, p. 197, 5]. In the accompanying system moving with the average speed of the beam, the chaotic particle velocity decreases, in other words, the beam is being "cooled". The equilibrium phase-space volume of the beam is mainly determined by the quantum fluctuations of synchrotron radiation [32, p. 123, 5]. The maximum intensity of the circulating bunch is limited by the coherent instabilities arising from the interaction of electromagnetic fields of the bunch with the RF cavity, inhomogeneities of the vacuum chamber, the inlet and outlet devices, etc. [33, p. 231].

The time of radiative damping of the transverse components of the particle momentum in the storage ring can be estimated as [5]

$$\tau \sim \frac{m^4 c^7}{e^4} \cdot \frac{1}{EB^2}, \tag{5.4}$$

where E is the particle energy, B is the magnetic field value in the bending magnets of the storage ring, m is the electron mass, e is the electron charge, c is the light speed. A more exact formula must allow for the degree of orbit filling by the bending magnetic field. For the storage/cooler ring of the VEPP-5 injection complex, the time of radiation damping is approximately 20 ms, which corresponds to $2 \cdot 10^5$ turns of the beam.

Reduction in the phase-space volume of the beam under the influence of synchrotron radiation is crucial for the accumulation of particles. A new portion of particles from the linear accelerator is added to the circulating beam by a pulsed electric field, the action time of which is less than the orbital period of the beam in the storage ring. The radiation losses being negligible for such a short period of time, the Liouville theorem can be applied to the process of injection of particles into the storage ring [39, p. 188, 1]. According to this theorem, the phase-space volume occupied by the particles must remain the same after the merging of the two beams. Consequently, if new portions of particles are injected into the same circulating bunch with time intervals shorter than the time of radiation damping, the phase-space volume of the beam in the storage ring and the amplitude of betatron oscillations will grow until the particle start leaving the beam, falling on the walls of the vacuum chamber of the storage ring. Since the aperture of the vacuum chamber is limited by the pole gaps of the magnetic elements of the storage ring, high beam intensity can be achieved only through radiative damping, when new portions of particles are added to the vacated areas of the phase space. Thus, the productivity of the injection complex is inversely proportional to the time of radiation damping.

The considerations of minimizing the time of radiation damping apart, parameters of experiments on high energy physics also influence the choice of the working energy and magnetic structure of the storage ring. For example, the working energy of the storage/cooler of the VEPP-5 injection complex is chosen equal to 510 MeV for using the beams let out of the ring without additional acceleration for the production of φ-mesons with a mass of 1019 MeV/s^2.

Cooling the beams before their injection into the main circular accelerator that executes collisions between electrons and positrons (collider) is often applied for several reasons. Accumulation and cooling of the particles directly in the collider is in principle possible since the time of beam accumulation and cooling is much smaller than the time of beam life in the cyclic accelerator. However, injecting a beam of a large phase-space volume requires a correspondingly large aperture of the vacuum chamber of the accelerator and, therefore, it is often advantageous to use a relatively small preliminary storage/cooler ring, which allows reducing the aperture of the vacuum chamber in the subsequent electron-optical system, and, consequently, the size and cost of the magnetic elements. Besides, the loss of electrons and positrons on the walls of the vacuum chamber of the collider is a source of background events in the detector. A sharp increase in the beam size at the moment of injection leads to a corresponding increase in the level of this background, which is undesirable because it can result in failure of the sensitive recording equipment of the detector.

5.3.3. Positron source of the VEPP-5 injection complex

5.3.3.1 Electron linear accelerator

Acceleration of electrons and positrons is carried out in waveguide structures on a traveling wave (Fig. 5.23). The structure is based on the disk-loaded constant-impedance structure, through which the electromagnetic wave with a phase velocity equal to velocity of light in vacuum is passed. The representative value of the longitudinal component of electric field in the accelerating structure is ~ 10 MV/m. Already on the first ten centimeters of the way, electrons or positrons, gaining the energy in the field of such magnitude, obtain the velocity close enough to the velocity of light and, further, move synchronously with a traveling wave.

High-power klystron UHF amplifiers of a decimeter range are used to create high tension electric fields in accelerating structures. At the VEPP-5 injection complex, the majority of structures provide an average rate of acceleration equal to 18 MeV/m. Two structures, which are accelerating the particles with low initial energies (one structure is located after the electron source, the second — after the conversion target), are supplied with a higher UHF-power, therefore, the average rate of acceleration in these structures is 25 MeV/m.

The parameters of accelerating structure require the electron source capable of producing the electron beams suitable for capture in accelerating phase of wave: the required beam energy is ~ 100 keV, the length ~ 1 cm. There are two approaches to creation of electron sources for accelerators on a traveling wave: it is possible to gain the required electron bunch via short-laser-pulse irradiation of the photocathode with the extraction electric field applied to it [30, p. 419]; or via compression in the longitudinal direction of a longer beam gained in the source on the basis of the thermo-emission cathode. The thermo-emission electron source with the subsequent time-of-flight bunching system is used at the injection complex.

Basic elements of the bunching system are RF-cavities and free sections. At passing through the cavity, particles gain different energy depending on its longitudinal position in the bunch. The phase of injection is chosen to provide the deceleration of the head particles and acceleration of the rear ones – in this case the bunch is compressed in the longitudinal direction in the free section. At the longitudinal compression, the electron bunch starts to extend in the transverse direction due to its own charge. To suppress this effect, solenoidal focusing is used at beam bunching and the movement in the first accelerating section.

To decrease the total length of the installation, electron and positron accelerators are located in parallel to each other, and the particles in them move in opposite directions (see Fig. 5.21). Before the conversion target, the electron beam is turned in magnetic field by 180˚. The isochronic scheme of achromatic turn, where, in the first order, beam energy spread does not lead to increase in its transverse and longitudinal size, is used. The elongation of electron and, hence, positron beam is undesirable, as it results in the increase of energy spread in the accelerated positron beam that complicates its injection into the cooling storage ring.

To the present time, the electron linear accelerator of the VEPP-5 injection complex is created and successfully tested at the designed parameters at 270-MeV energy (Fig. 5.21) as the conversion system (Fig. 5.22).

5.3.3.2 Conversion target

To manufacture fixed conversion targets, refractory heavy metals - tantalum, tungsten and rhenium, 73rd, 74th and 75th numbers in periodic table, respectively, are usually used. These metals possess a large nuclear charge and, hence, correspond to low critical energy $E_c \approx 10$ MeV. Besides, the given metals and also their alloys possess high mechanical strength and high fusion temperature - this is important as the conversion target should withstand repeated hits of an intensive electron beam. As a result of sharp thermal expansion of a material under the influence of an electron beam, the shock wave, which can have the intensity sufficient for target destruction is formed in a conversion target. It is experimentally determined that metal targets on the basis of tungsten-rhenium alloy are capable of a long-term withstanding the hitting of an electron beam with the energy density (per target unit area) of up to $2 \cdot 10^{12}$ GeV/mm^2 [12].

At the VEPP-5 injection complex, the electron beam focused on 1-mm area corresponds to the energy density of $0{,}27$ GeV $\cdot\ 2 \cdot 10^{10} \approx 5 \cdot 10^9$ GeV/mm^2. Thus, in our case, the electron beam intensity is definitely less than the maximum permissible one. The average power produced in the target is also insignificant: at the electron beam pulse frequency equal to 50 Hz, it is necessary to remove approximately 30 W of heat power from a target.

At next-generation electron-positron colliders, such as the international linear collider ILC being now under design, the positron source productivity is required to be higher by several orders. In this case the average heat power produced in the target results in the necessity to use a rotating wheel or a stream of liquid metal as a conversion target.

At the VEPP-5 injection complex, the target material is chosen to be tantalum (radiation length $X_0 \approx 4$ mm). The cone-shape tantalum target with the minimum diameter of 2,5 mm and the length of 12 mm is fixed in the holder, which can move in the longitudinal direction by ± 2 mm from the position shown in Fig. 5.25 by means of a tie-rod. The target has also a special slot, through which the electron beam can be injected into the positron accelerator. In this case, before the target, the beam is parallel-shifted by 2 mm downwards with the help of two magnets.

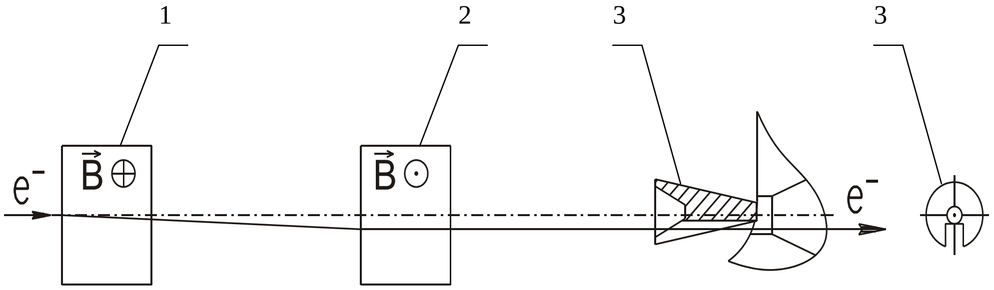

Fig. 5.24. System of parallel shift of electron beam. 1, 2 — magnets, 3 — conversion target

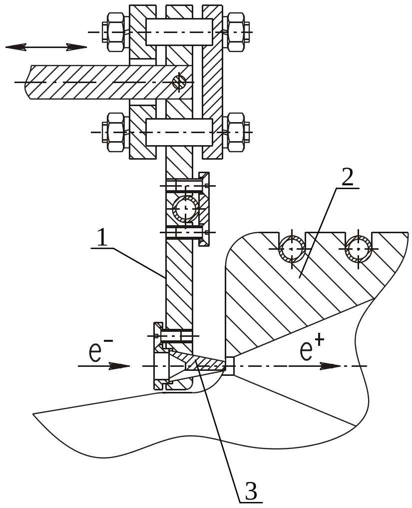

Fig. 5.25. The design of the target holder. 1 — movable target holder, 2 — pulsed magnetic lens (the flux concentrator), 3 — conversion target

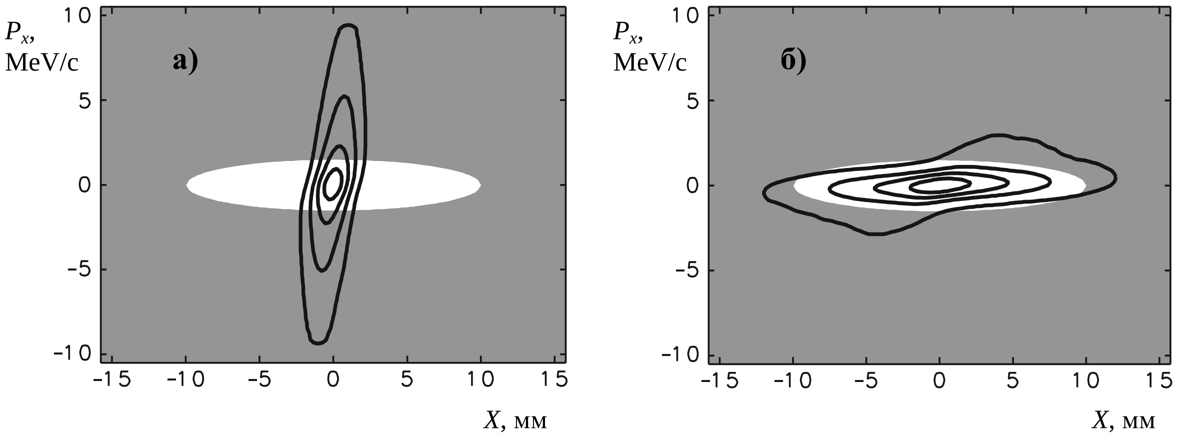

Fig. 5.26. Positron beam phase portraits represented by lines of constant density: a) after the conversion target, b) after the matching device. Grey color shows the area of P_x–X plane inaccessible for acceleration. The images are obtained by modeling the passage of positrons through axially-symmetrical magnetic field, an approximating field of the matching device of the injection complex:

$$B(z,r=0)=\frac{B_t}{1+gz},\ \text{где}\ g=\frac{1}{L}\left(\frac{B_t}{B_w}-1\right),\ B_t = 10\ \text{Т},\ B_w = 0{,}5\ \text{Т},\ L = 8\ \text{см}.$$

5.3.3.3 Solenoidal focusing of positrons

The pulse transverse component of the major part of positrons, which are coming out a target, does not exceed 15 MeV/c (Fig. 5.27).

The RF-structure changes the transverse pulse of accelerated particles slightly; therefore positron trajectory inside the structure placed in the solenoid in the transverse plane will be a Larmor circle. Magnetic field of ≈ 10 T is necessary to provide fitting of Larmor orbit of the positron produced near the axis with transverse pulse of 15 MeV/c into the accelerating section with the aperture radius of 1 cm. The generation of such fields in a sufficient enough volume is possible via the superconducting magnets, the usage of which in conversion system is complicated due to a strong radiation background. The constant solenoidal field generated by the magnets with water-cooled windings is limited by the value ≈ 0,5 T. Maximal transverse pulse of positrons in such field at the chamber aperture diameter of 2 cm is equal to 1,5 MeV/c.

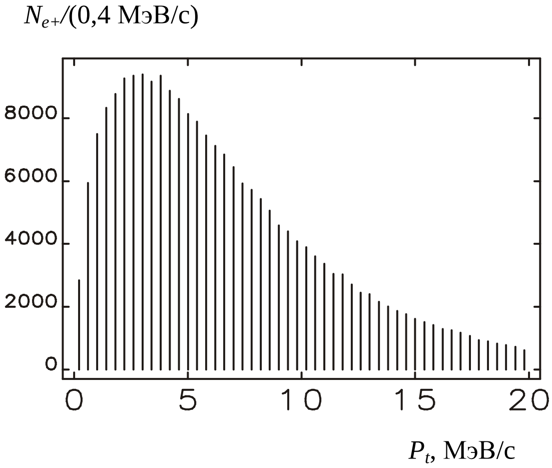

Fig. 5.27. Distribution of the transverse component of pulse of the positrons, which were produced in the conversion target**.** The spectrum is obtained by means of GEANT code [16] (quantity of the electrons hitting the target — $2\cdot10^5$, electron energy — 280 MeV, length of a tantalum target — 12 mm). The total number of the positrons extracted from the target — $2.4\cdot10^5$.

As the size of an electromagnetic shower at the target exit is usually several times less than the diameter of accelerating section aperture, there is a possibility in principle to reduce angular spread of positrons through expansion of a beam up to the diameter of accelerating section aperture via using magnetic focusing in accordance with Liouville theorem. The magnetic lens performing the described transformation of phase volume, i.e. focusing positrons before accelerating structure is called the matching device.

The principle of operation of the matching device is illustrated in Fig. 5.26, where phase portraits of the positron beam before the matching device and after it are represented on the accelerating structure acceptance background. By the acceptance in Fig. 5.26 we mean the projection of phase volume accessible for particle acceleration in plane P_x—X. I.e., if the particle gets to this area, it still should meet some conditions for other coordinates to be captured in the accelerating structure, but if the particle does not get inside the white ellipse — then it is surely lost on the walls of accelerating structure.

There are three main types of matching devices: the quarter-wave transformer, the magnetic flux concentrator and a plasma or lithium lens [1]. In all these devices, the pulsed magnetic field of a large magnitude is used. In a plasma lens, particles are focused by the azimuthal magnetic field appearing in the medium through which the electric current runs in parallel to a beam axis. The quarter-wave transformer is a short pulsed solenoid. The conversion target is placed at the beginning of this solenoid and its length and a magnetic field are chosen so that the transverse pulse of positrons could be compensated by the hit, which the particles gain at the solenoid exit. The basic drawback of both - the lenses with an azimuthal magnetic field and the quarter-wave transformer - is selectivity of these devices on particle energy. The quarter-wave transformer and the plasma lens focus positrons well only in a narrow part of the spectrum near the maximum.

In the matching device based on the magnetic flux concentrator, focusing of particles is used in a decaying magnetic field. The positron beam in this device extends in the magnetic field, which decays from the maximum value near the conversion target to the minimum one in the accelerating structure. The advantage of the given device is in a lesser dependence of its focusing properties on the energy of positrons. At the VEPP-5 injection complex, this type of the matching device is used; its general layout is represented in Fig. 5.28. Calculation and optimization of parameters of the concentrator were carried out by means of numerical simulation [38, 37]. In this case, optimization key parameters are the length and the maximum magnetic field in the device.

For the first time the magnetic flux concentrator was applied for gathering of positrons at Stanford linear accelerator (SLC) [6]. At first implementations of this device its length was 60 ÷ 80 cm and the maximum field - about 3 T [10, 11]. The adiabatic condition is satisfied at positron movement in such field: magnetic field change on a step of Larmor spiral is much less than the magnitude of a field. Thus, the device was called an adiabatic matching device.

Later, shorter concentrators of flux were used to focus the positrons as the effect of beam elongation due to the difference of lengths of positrons trajectories is manifested in them more slightly. Here, though the adiabatic condition for the majority of positrons is already not fulfilled, the matching device of this type is often traditionally called adiabatic or quasi-adiabatic.

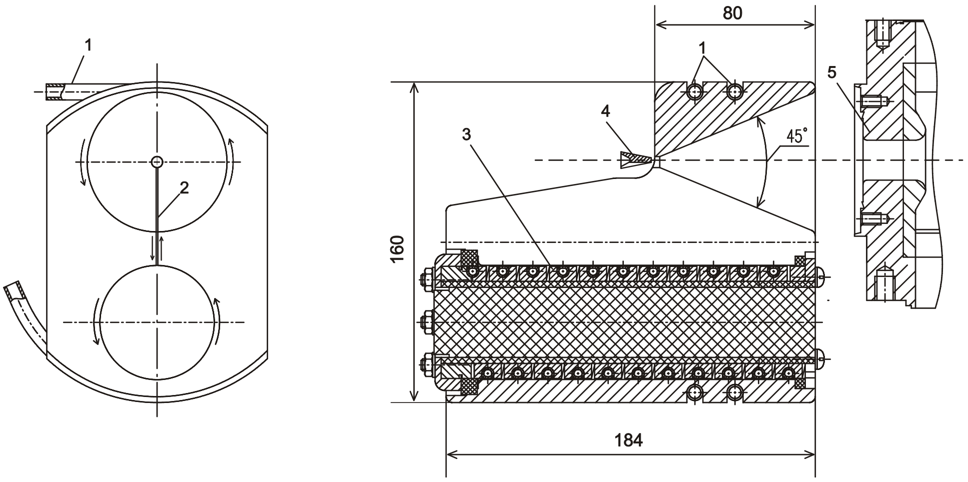

Fig. 5.28. The layout of the magnetic flux concentrator used in the positron source of the VEPP-5 injection complex. Arrows mark surface currents. 1 — water-cooling tubes; 2 — a slot between a conic cavity and a cavity of a primary winding (slot width — 0,2 mm; in the drawing the width of a slot is represented in inexact scale, since otherwise both edges of a cut merge); 3 — the pulsed coil (a primary winding); 4 — a conversion target, 5 — the beginning of the accelerating structure

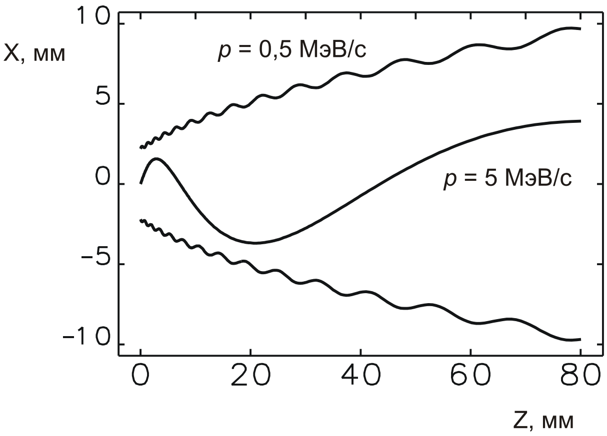

Fig. 5.29. The trajectories of positrons in a decaying field of the magnetic flux concentrator. The magnetic field decays from 10 T at Z = 0 down to 0,5 T at Z = 80 mm under the law

$$B(z,r=0)=\frac{B_t}{1+gz},\ \text{where}\ g=\frac{1}{L}\left(\frac{B_t}{B_w}-1\right),\ B_t = 10\ \text{T},\ B_w = 0{,}5\ \text{T},\ L = 8\ \text{cm}$$

Fig. 5.28 represents the concentrator of a magnetic flux used in the positron source of the VEPP-5 injection complex. The device is the transformer, whose primary winding is the pulsed solenoid, and secondary one — the massive copper case with two cut-out cavities. As pulse duration is 20 microseconds, the current runs in a thin skin-layer of conductors (~ 0,5 mm). The magnetic flux, created by a primary winding, is closed on the upper cavity where the required longitudinal profile of magnetic field can be obtained due to the conic geometry.

Fig. 5.29 shows characteristic trajectories of positrons in a magnetic field approximating the decaying field of the magnetic flux concentrator used at the VEPP-5 injection complex. Positrons with the energy of few MeV forming the major part of spectrum make only 1—2 turns in this field.

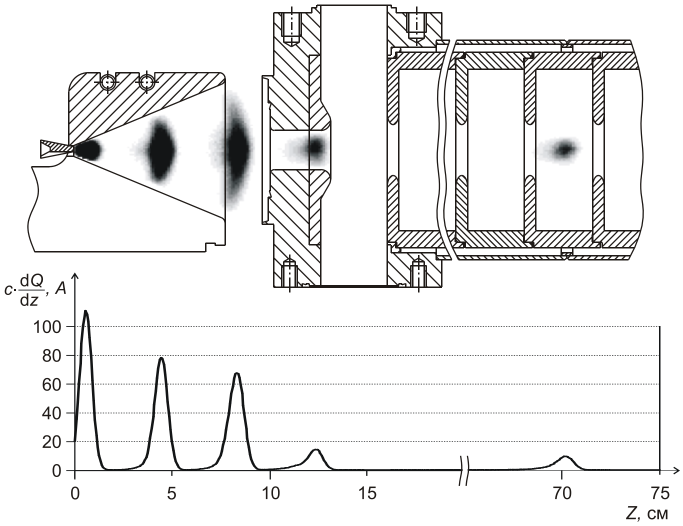

Fig. 5.30. Portraits of the positron beam at different moments of time (numerical simulation)

At creation of the magnetic flux concentrator, three basic problems related to mechanics, energy properties and optics of this pulsed magnet should be solved. Mechanics problem: the effect of electro-dynamic forces in magnet elements, first of all, in its conductive parts. The problem of mechanical fixing of winding turns becomes challenging due to impossibility of using organic insulation at intensive fluxes of ionizing radiation. Here, only ceramic insulation can be used, and only for those winding elements, which are in a weaker field and under the condition of guaranteed absence of vibrations or at the restriction of vibrations to the admissible value that excludes deterioration of ceramics-metal pair.

Elimination of the above-mentioned loosening of mechanical structure during operation is practically impossible, as these elements are, as a rule, located in vacuum, and in intensive fluxes of ionizing radiation, therefore, they are strongly activated. This condition can exclude possibility of access to these elements even after switching-off of the radiation source.

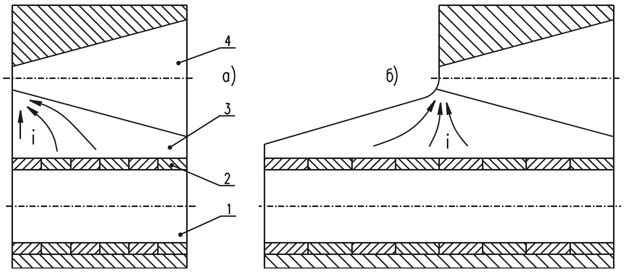

Fig. 5.31. Distribution of currents *(i)* along one of the surfaces of the slot (3) connecting the cavity of a primary winding (1) and the cavity of the flux concentrator (4). The length of a primary winding (2) is equal to the length of a conic cavity. b) The elongation of a primary winding allows the reduction of parasitic effect of the longitudinal components of currents.

Along with providing the necessary parameters of the longitudinal magnetic field, it is necessary to reduce to the minimum the axially-asymmetrical field component, which originates, first of all, due to the leak of the flux from a conic cavity of the magnet through essentially necessary slot on the edge of this cavity. Decaying profile of magnetic field (Fig. 5.31- a) inside the conic cavity, required for focusing of positrons, corresponds to strongly non-uniform distribution of current on the internal surface of a cone. This results in current deviation on the surface of a slot from the radial direction, i.e. to appearing of the currents with the component directed along a cone axis. To reduce parasitic effect of these current components, a primary winding is twice longer than a conic cavity of the concentrator (Fig. 5.31-b). Such elongation of a primary winding allows the reduction of parasitic effect of the longitudinal components of surface currents.

Main parameters of the magnetic flux concentrator are the following:

• The maximum value of magnetic field	10 T,
• Total current of the magnet conic cavity	120 kA,
• The maximum voltage of the capacitor storage	1,2 kV,
• Power consumption of the capacitor storage	90 J,
• Pulse duration of current	26 microseconds,
• Frequency of work	50 Hz,
• Average power consumption	4 kW.

5.3.3.4 Stand testing of the magnetic flux concentrator

After development and manufacturing of the pulsed magnet, its stand testing with proper pulse generator has been carried out. Magnetic measurements were performed by means of the inductive sensor supplied with the RC-integrator [7]. Fig. 5.32 represents distribution of the longitudinal and transverse magnetic field in the magnet cone.

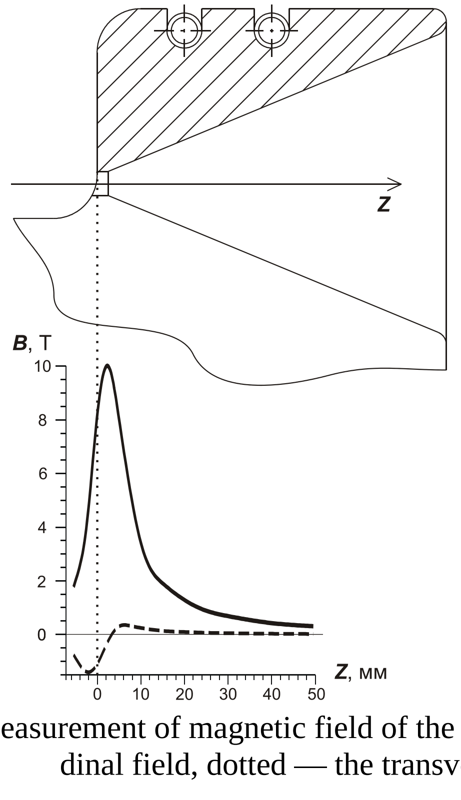

Fig. 5.32. Results of measurement of magnetic field of the concentrator. A solid line — longitudinal field, dotted — the transverse field.

The magnet has worked at the stand about 10^7 cycles without any faults or change of its parameters.

The conversion target placed in a strong pulse magnetic field, considerably warms up, however, the cooling provided by a design of the target holder ensures the heating of an end face of the target not more than 100°C. Magnetic field perturbation at an end face of such "semitransparent" (thickness of skin layer ≈ 1 mm) for pulsed magnetic field target also appeared to be insignificant. Magnitude of pulsed field decreases only by 2÷3 % at a distance of 1 mm from the target end face.

5.3.3.5 Quadrupole focusing of positrons

Quadrupole focusing is economically more favorable than solenoidal one as it does not require creation of magnetic field in the whole volume of the vacuum chamber; but the beam focused by quadrupole lenses should be monochromatic enough. Quadrupole focusing is usually used in the positron sources at beam average energy more than 100 MeV when energy spread is ≈ 20 %.

To pass to focusing by quadrupole lenses without particle losses is possible only in the case when the quadrupole channel acceptance matches the beam emittance at the solenoid exit. The acceptance of quadrupole channel can be estimated as

$$A \approx \frac{r^2}{L_q} p, \tag{5.5}$$

where r is radius of the vacuum chamber aperture, L_q — distance between the centers of quadrupoles, p — an average momentum of positrons. By acceptance we mean here the phase area in co-ordinates (x, p_x) or (y, p_y). This estimation is close to an exact value in the case when change of energy of positrons between two lenses is small in comparison with their energy at the solenoid exit.

The solenoid can be can passed through by the positrons, the transverse momentum of which is less than the value

$$P_{t,\max} = reB_w, \tag{5.6}$$

where e — positron charge, B_s — magnetic field in the solenoid. For parameters of the VEPP-5 injection complex, $P_{t,\max} \approx 1{,}5$ MeV/sec. The area of phase plane (x, p_x), accessible for acceleration of particles inside the long solenoid, is restricted by an ellipse with the area

$$A_s = \pi r P_{t,\max}. \tag{5.7}$$

The filling of this ellipse by positrons depends on parameters of the matching device. Fig. 5.33 represents the distribution of positrons on planes (x, p_x), which corresponds to the parameters of the VEPP-5 injection complex.

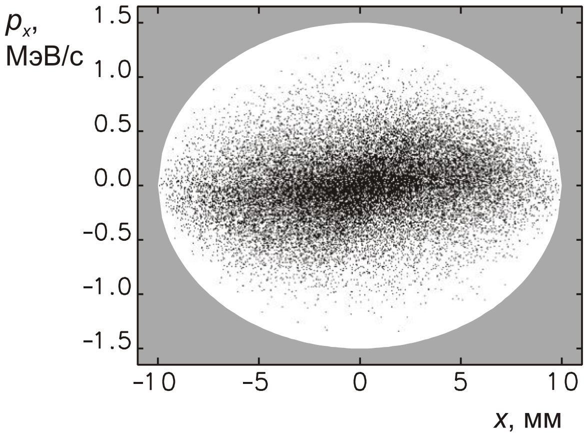

Fig. 5.33. The phase portrait of the positron beam at the end of the solenoid (numerical simulation). The solenoid acceptance is shown by a white oval.

According to Fig. 5.33, a beam at the end of the solenoid occupies the entire accessible aperture; and the distribution of particles is twice narrower than the accessible interval from– $P_{t,\,\max}$ to $P_{t,\,\max}$ on the axis of pulses (see Fig. 5.34). The similar situation with slight changes is characteristic for all matching devices and reflects the fact that the closer is the positron transverse momentum to restriction $P_{t,\,\max}$, the easier for this particle to hit walls of a vacuum chamber in the solenoid. From the distributions shown in Fig. 5.33 and Fig. 5.34, it follows that 90 % of positrons occupy on a phase plane the area twice smaller than the area estimated by the expression (5.7).

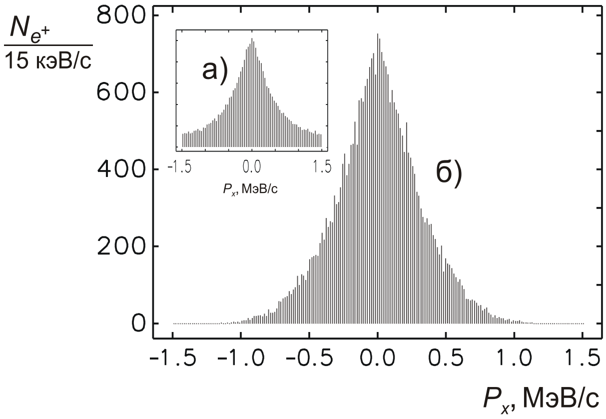

Fig. 5.34. Distribution of the number of positrons vs horizontal momentum: a) at the beginning of the solenoid b) at the end of the solenoid

Thus, the equation for energy of transition between solenoidal and quadrupole focusing, at which the loss of positrons is less than 10 %, is as follows:

$$\frac{r^2}{L_q} \approx \frac{\pi}{2} \cdot \frac{rP_{t,\,\max}}{E_{tr}/c}, \tag{5.8}$$

where E_{tr} is transition energy. Hence, we express E_{tr}

$$E_{tr} \approx \frac{\pi}{2} \cdot \frac{L_q}{r} \cdot cP_{t,\,\max} = \frac{\pi}{2} \cdot B_s L_q ec. \tag{5.9}$$

At the VEPP-5 injection complex, the distance between the lenses, which are located in the accelerating sections, L_q = 1,7 m (see Fig. 5.35); field in solenoid B_s = 0,5 T; hence, $E_{tr} \approx$ 400 MeV.

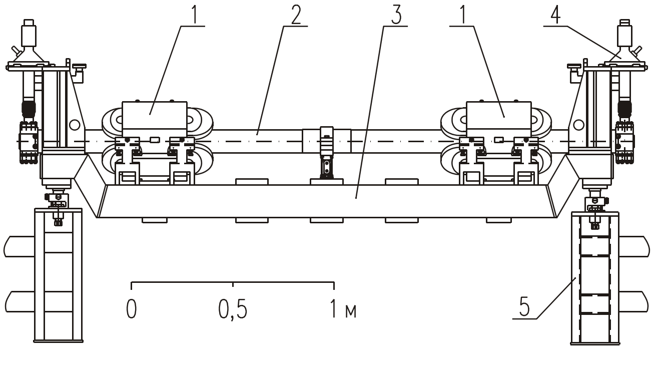

Fig. 5.35. Accelerating structure with quadrupole lenses. 1 — quadrupole lens, 2 — accelerating structure, 3 — support, 4 — vacuum pump, 5 — support stand

Currently, at the injection complex, $E_{tr} \approx 70$ MeV; this results in high losses of positrons (about 2/3 from the number of those passed through the solenoid). In the future, increase of the length of the conversion system solenoid and installation of additional quadrupole lenses to double the yield of positrons are planned.

Fig. 5.36 shows the minimum sizes of the positron beam which can be provided by quadrupole focusing in the positron accelerator of the injection complex (without restriction on the vacuum chamber aperture). As seen from Fig. 5.36, the beam transverse size becomes smaller than its initial size in the solenoid only at the end of the linear accelerator where the energy of positrons is over 400 MeV; this corresponds to the estimations performed earlier.

Fig. 5.37 shows how the number of positrons decreases with the beam movement along the accelerator due to the losses of positrons on vacuum chamber walls.

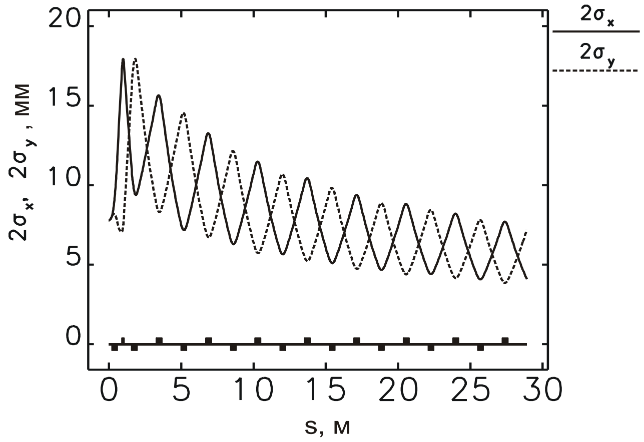

Fig. 5.36. The minimized transverse sizes of the beam in the positron accelerator of the injection complex (without taking into account restriction on the vacuum chamber aperture). Calculations are made in ELEGANT code [13]. Quadrupole lenses are shown by rectangles at the bottom of the diagram

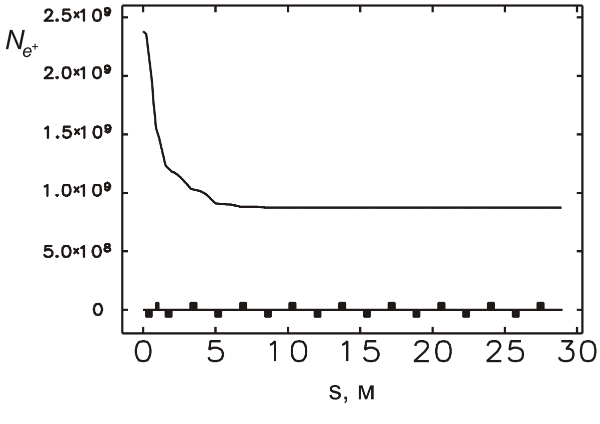

Fig. 5.37. Quantity of positrons vs the beam position along the linear accelerator of the injection complex (from the conversion system solenoid to the injection channels of the cooling storage ring). Simulation is made by ELEGANT code [13]. Quadrupole lenses are shown by rectangles at the bottom of the diagram.

5.3.3.6 Injection of the positron beam into the cooling storage ring

The characteristic feature of the cooling storage ring, as well as of many cyclic accelerators, is its rather small energy acceptance, i.e. the maximum permissible energy spread in the injected beam. For the cooling storage ring of the VEPP-5 injection complex, the maximum deviation of particle energy from the equilibrium one is $\Delta E/E_0 = \pm 0{,}012$.

The energy spread of the positron beam at the end of the linear accelerator is defined by the ratio of beam length and wave length of the accelerating RF-field. Usually this energy spread is more than maximum permissible spread for the storage ring, therefore, an additional matching device — debuncher-monochromator is used at many installations before injection of positrons into the storage ring. This device provides a turn of the positron beam in plane *E* — *s* (energy — longitudinal coordinate), thus, reducing the energy spread via increasing the beam longitudinal size.

Fig. 5.38 represents the scheme of debuncher-monochromator operation at the VEPP-5 injection complex.

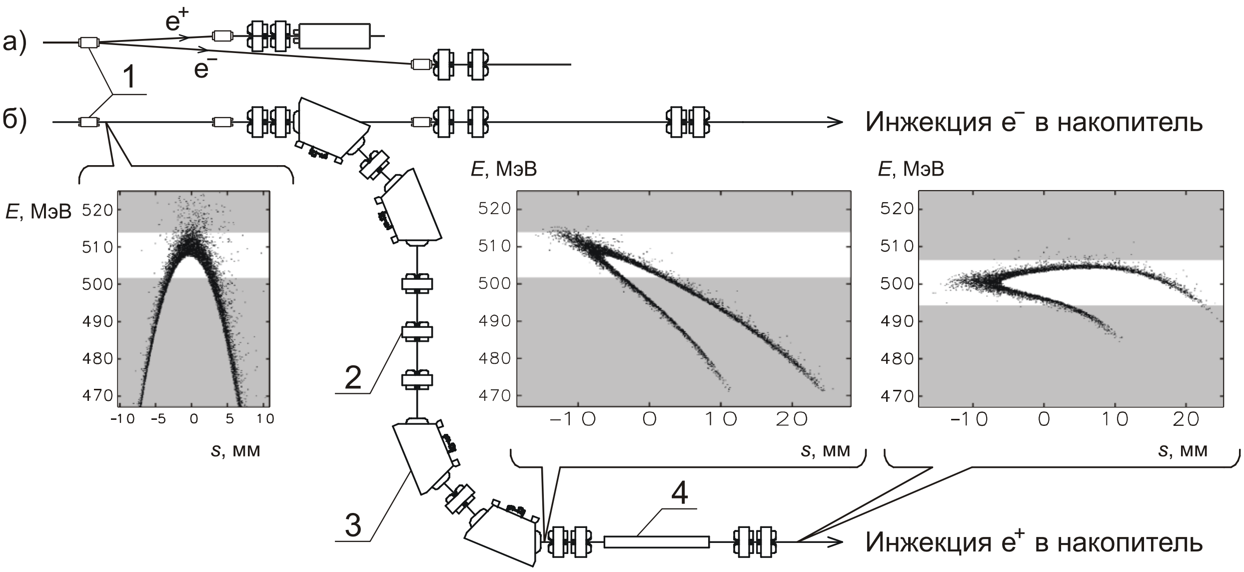

Fig. 5.38. a) Scheme of separation of positrons and electrons before injection into the cooling storage ring (side view). B) Scheme of positron beam debuncher-monochromator (top view). 1 — dipole magnet separating electrons and positrons in a vertical plane; 2 —quadrupole lens; 3 — bending magnet; 4 — accelerating structure. The inserts show the portraits of the positron beam on plane *E* — *s* (energy — longitudinal coordinate) in various points of the channel. White strip denotes the energy acceptance of the cooling storage ring

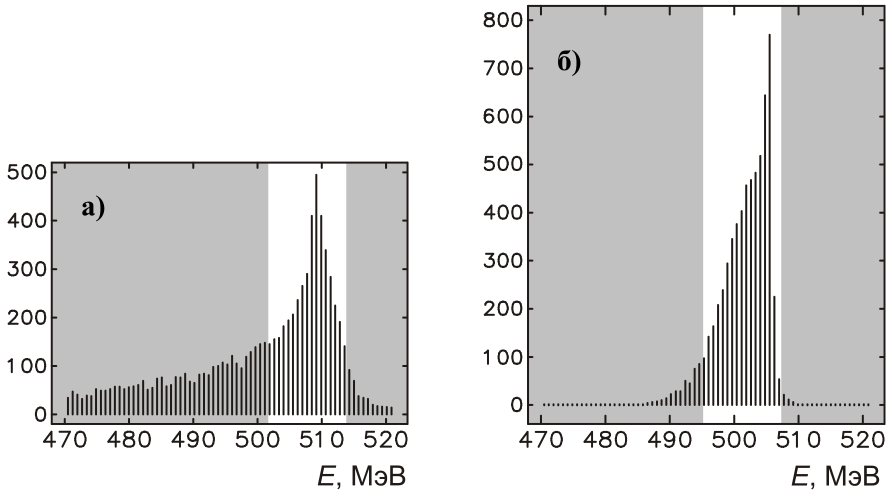

Fig. 5.39. Estimated spectrum of the positron beam: a) at the end of the linear accelerator, b) after the debuncher-monochromator. White strip denotes energy acceptance of the cooling storage ring.

It is supposed to direct positrons to the storage ring through the channel consisting of four 45-degree bending magnets. The particles of a higher energy move in the field of bending magnets along the trajectory with a larger radius and get to the tail-end of a beam; thus, the particles with a lower energy get to the head-part of the beam. The energy spread in the beam, arranged in such manner, can be partially reduced via passing a beam through the accelerating structure close to a zero phase of electric field. Fig.5.39 represents estimated spectra of the positron beam before and after the debuncher-monochromator.

The calculations show that usage of debuncher-monochromator at the VEPP-5 injection complex will allow increasing the number of the positrons captured into the storage ring by 1,5 times.

5.3.3.7 Results of the experiments, measurement of the yield factor of Y positrons

To determine yield factor of *Y* positrons, measurements of all three values of the formula (5.3) have been performed: E, N_- and N_+.

Measurement of electron beam charge before the conversion target was made via using the Faraday cup. The Faraday cup is made of tungsten, its length is 70 mm, width and height are 20 mm. Simulation in GEANT code [16] shows that charge absorption in the cylinder is 94 % (the cylinder of total absorption could not be used because of a free-space deficiency). To prevent the current of secondary electron emission from a cylinder surface, a 300V-voltage, being positive relative to the vacuum chamber, is applied to the cylinder. Electron beam charge was calculated using the oscillogram of the current coming from the Faraday cup.

Electron energy was measured after the bending magnet using the beam image on a sliding luminescent screen (see Fig. 5.40).

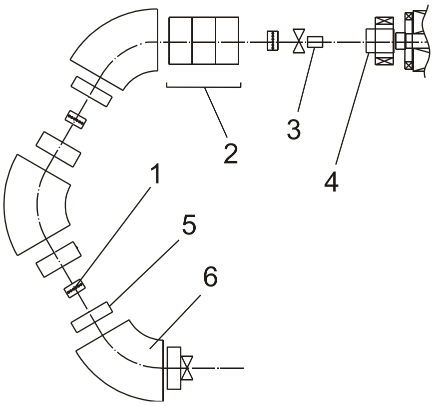

Fig. 5.40. Isochronous beam turn before the conversion system. 1 — luminophor flag, 2 — focusing triplet, 3 — Faraday cup, 4 — conversion system, 5 — lens, 6 — bending magnet. Quadrupole lens 5 is switched off during measurement of electron beam energy.

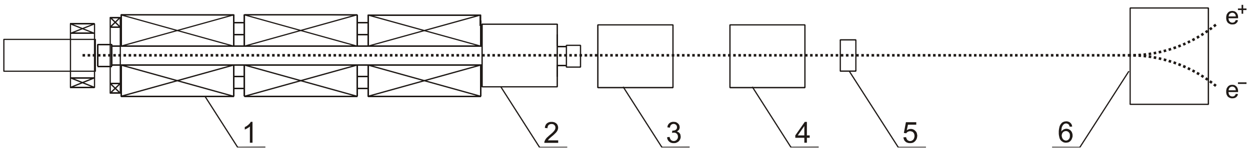

Fig. 5.41. The installation used for measurement of positron yield factor. 1 — conversion system solenoid, 2, 3, 4 — quadrupole lenses, 5 — beam position corrector, 6 — magnet-separator

To measure the quantity of the positrons produced by the conversion system, it is necessary to separate positrons from the electrons, which are accelerated in the adjacent phases of the RF-structure traveling wave. The rectangular dipole magnet was used for this purpose (magnet-separator in Fig. 5.41).

Three quadrupole lenses are placed between the conversion system solenoid and the magnet-separator for beam focusing. The results of calculation of positron losses in the vacuum channel from the solenoid to the end of the magnet-separator are shown in Fig. 5.42.
The simulation showed that, at optimum values of magnetic field gradient in lenses, not more than 80 % of positrons from the number of positrons accelerated in completely assembled positron accelerator can pass through the channel used for measurements (Fig. 5.43). Thus, measurement of the positron beam charge after the magnet-separator should not give unreasonably exaggerated estimation of the efficiency of the whole injection complex.

S

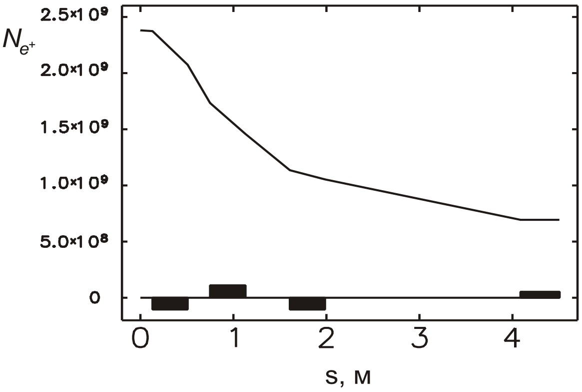

Fig. 5.42. Quantity of positrons vs beam position along the vacuum channel of the experimental installation. Three quadrupole lenses and a magnet-separator are shown by rectangles at the bottom of the diagram. Simulation was made by ELEGANT code [13].

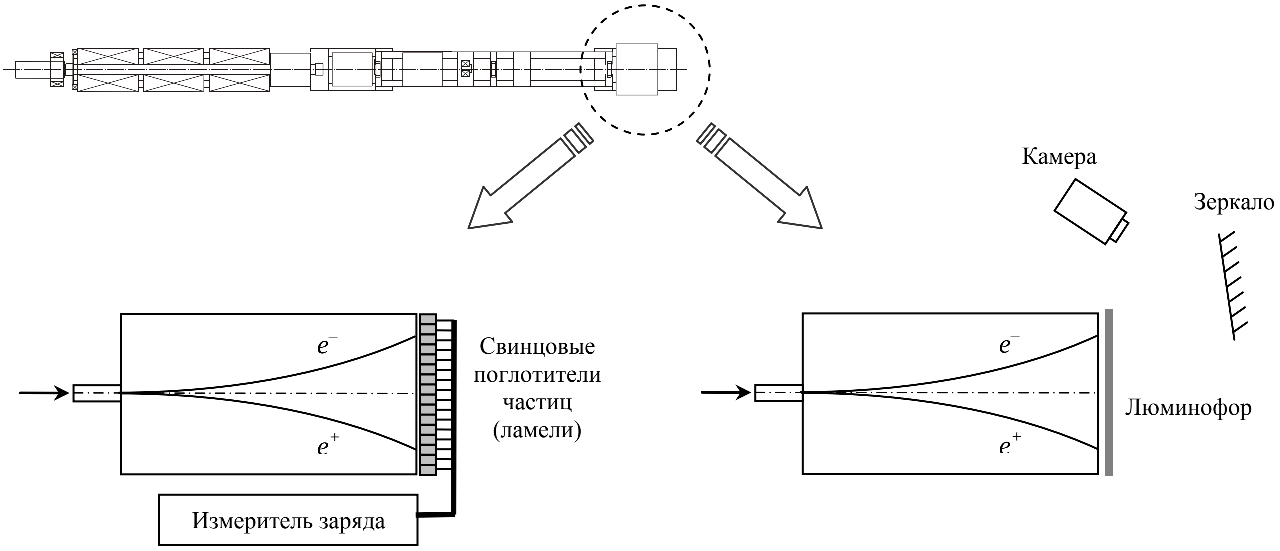

Fig. 5.43. Systems of particle registration.

To measure the charge and average energy of the positron beam, the sectioned receiver consisting of 16 lead sections (lamellas) was installed after the dipole magnet-separator. Section width is 10 mm, length is 50 mm. Sections are isolated from each other by a glass-fiber laminate. The incident beam is completely absorbed in the receiver. Measurement of the charge got on a lamella is made by the device consisting of 32 charge-sensitive amplifiers, commutated on ADC in turn. Measurement was made from each lamella separately, and then the bunch charge was computed by summation. Fig. 5.44 shows the dependence of the number of positrons on the field maximum in the matching device at different energies of the electron beam hitting the target.

At 265-MeV electron energy, the quantity of the positrons registered after the magnet-separator is $5\cdot10^8$. The number of electrons before the target measured by means of the Faraday cup is $1{,}8\cdot10^{10}$. Thus, the conversion ratio (5.3) for the given system is $Y \approx 0{,}1$ GeV^{-1}.
To measure spatial particle distribution in a beam, the luminescent screen has been installed after the magnet-separator instead of lead absorbers. Light flash on luminescent screen induced by beam hit was registered by means of the CCD-camera synchronized with the accelerator operation. Fig. 5.45 represents the image registered by the camera.

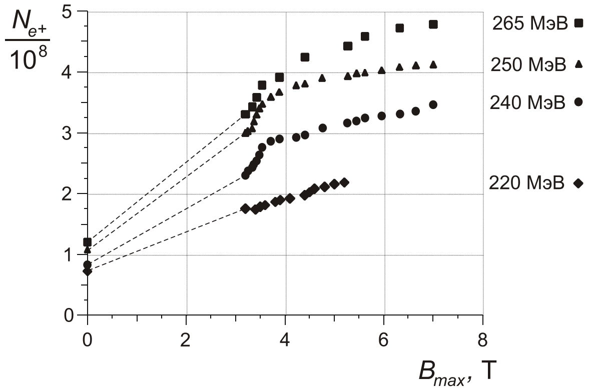

Fig. 5.44. Number of the accelerated positrons vs the concentrator magnetic field value for different energies of electron beam.

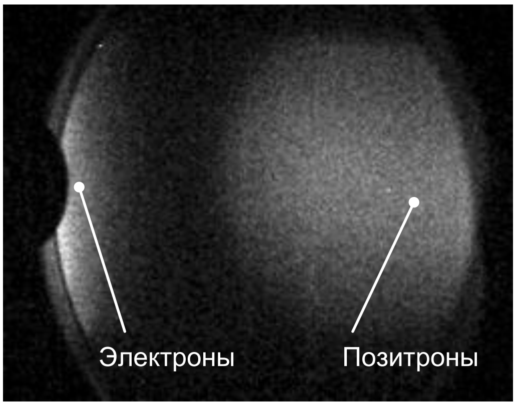

Fig. 5.45. The image on the luminescent screen.

5.3.4. Conclusion

Tests of conversion system of the VEPP-5 injection complex have shown that the given installation is capable of producing up to $5\cdot10^8$ positrons per a pulse. Losses of positrons at injection into the cooling storage ring according to the estimations should be approximately a half of this number, therefore, the possible total yield of the injection complex at operation frequency of linear accelerators of 50 Hz can be expected to be up to 10^{10} positrons per second.

The main advantage of the VEPP-5 injection complex over analogous installations, as seen from Table 1, is the matching device of the improved design, which provided the optimal magnetic field value for positron focusing, without violating the axial symmetry of this field.

The disadvantages are: small length of the solenoid providing focusing of positrons at the beginning of the accelerator and a small number of quadrupole lenses, these results in unavoidable losses of positrons at beam passing through transition area between solenoidal and quadrupole focusing. One more constructive deficiency of the positron system is absence of the magnetic system separating positrons from electrons at the beginning of the accelerator (after the solenoid). The electron bunch, being behind the positrons by half-length of RF wave, will fly through the whole accelerator till the cooling storage ring complicating the adjustment of the installation. The magnets for separating electrons were not provided at the injection complex to save the space for the linear accelerator of positrons.

Future increase of the complex productivity is possible in several directions: via improvement of magnetic focusing of positrons, increase in intensity and energy of a primary electron beam. The elongation of the conversion system solenoid and also installation of additional quadrupole lenses at accelerating sections can exclude the losses of positrons after the solenoid (Fig. 5.37) and double or triple the output of positrons. Usage of an updated electron source can provide the increase of the number of electrons (approximately by 3 times, up to $6\cdot 10^{10}$) in a beam hitting the target (further increase in electron beam intensity is restricted by the effects of RF-field distortion under the influence of the electromagnetic fields radiated by a beam into the accelerating structure). Besides, there is a possibility for a 1,5-time increase of the electron beam energy via installation of additional accelerating structures. Thus, 10^{11} positrons per second, is, probably, the ultimate productivity, which can be provided by the VEPP-5 injection complex.

5.4 The linear accelerator

The linear accelerator (LA) of $c\tau$-factory is intended to provide effective injection of electrons and positrons into collider at the energy of performing the experiments up to maximum E = 2.5 GeV. The accelerating waveguide structures on a traveling wave, which are already used at BINP at the VEPP-5 injection complex, are planned to be applied at $c\tau$-factory LA.

Vertical and a horizontal acceptance of $c\tau$-factory is determined by geometrical aperture of the lenses of final focus and is $A_x = 23\sigma_x$ and $A_z = 60\sigma_{z,}$ or, in absolute values A_X = 4250 nm-rad and A_Z = 180 nm-rad.

Positron beam emittances at the exit of the cooling storage ring at energy E = 510 MeV are equal to ε_x = 23 nm-rad, ε_z = 5 nm-rad. After acceleration in the linac, the emittances will decrease adiabatically and will be: ε_x = 11 nanometers-rad, ε_z = 2.5 nm-rad at $E_{inj} = 1\,\mathrm{GeV}$ and ε_x = 4.6 nanometers-rad, ε_x = 1 nm-rad at $E_{inj} = 2.5\,\mathrm{GeV}$.

The electron beam, which is accelerated from a photo-gun to a full energy in linac, will have: ε_x = z ε= 10 nm-rad at $E_{inj} = 1\,\mathrm{GeV}$, and ε_x = z ε= 5 nm-rad at $E_{inj} = 2.5\,\mathrm{GeV}$ with power spread $\sigma_E \leq 1\cdot 10^{-3}$.

The cooling storage ring emits positrons with power spread $\sigma_{E0} = 5\cdot 10^{-4}$. The length of a bunch at the storage ring exit is $\sigma_{s0} =$ 0.3 cm. After additional acceleration in the linac with the wave length λ = 10 cm, beam energy spread, due to the phase extent of a bunch, will increase by an order. Efficiency of injection of such beam into the storage ring of $c\tau$-factory will not be above 60÷70%.

To decrease the energy spread of positrons after additional acceleration in the linac, a bunch of positrons, before injection to the linac, should be compressed by 2÷3 times. For this purpose, a section of the linear accelerator of 15÷20 MeV should be installed in the extraction positron channel, after 90°-turn (hall №.2). At the section exit, the energy spread in a beam will be increased by 4÷5 times, and after passing the achromatic section of descent to the tunnel, with the longitudinal dispersion function $\eta_s \approx$ 50 cm, the bunch length will decrease. After these manipulations, the energy spread at the entry of the of $c\tau$-factory storage ring will be $\sigma_E = 1\div 2\cdot 10^{-3}$, and the bunch length - $\sigma_s \approx 0.5$ cm (the bunch will become longer after passing the injection channel to the $c\tau$-factory where $\eta_s \approx 250$ cm).

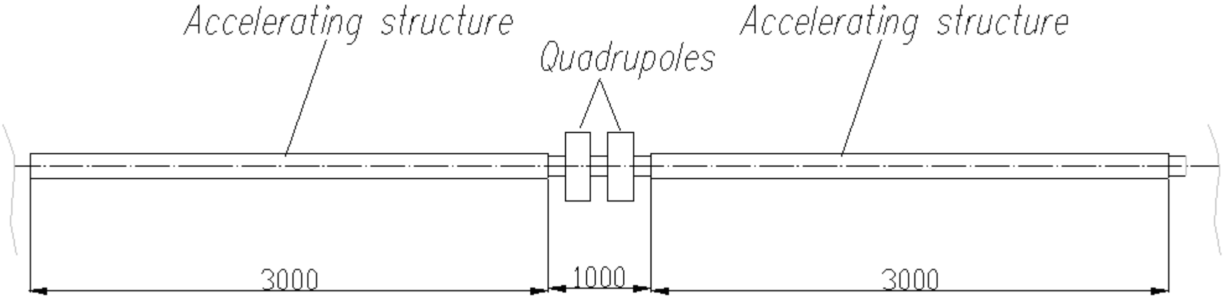

Fig. 5.46. Schematic view of the accelerator module.

Thus, the linear accelerator, which should accelerate positrons up to energy of 2 GeV and the electrons, produced by the source of polarized electrons, up to 2.5 GeV is necessary. The structures on a traveling wave are suggested to be used as the accelerating structures. They are the disk-loaded waveguide structure with constant impedance, phase shift on a cell of 2π/3 and phase velocity of the main accelerating harmonic equal to the velocity of light. Positrons get to a regular part of the accelerator, which consists of the accelerating structure and OFODO cell, therefore, are not considered separately.

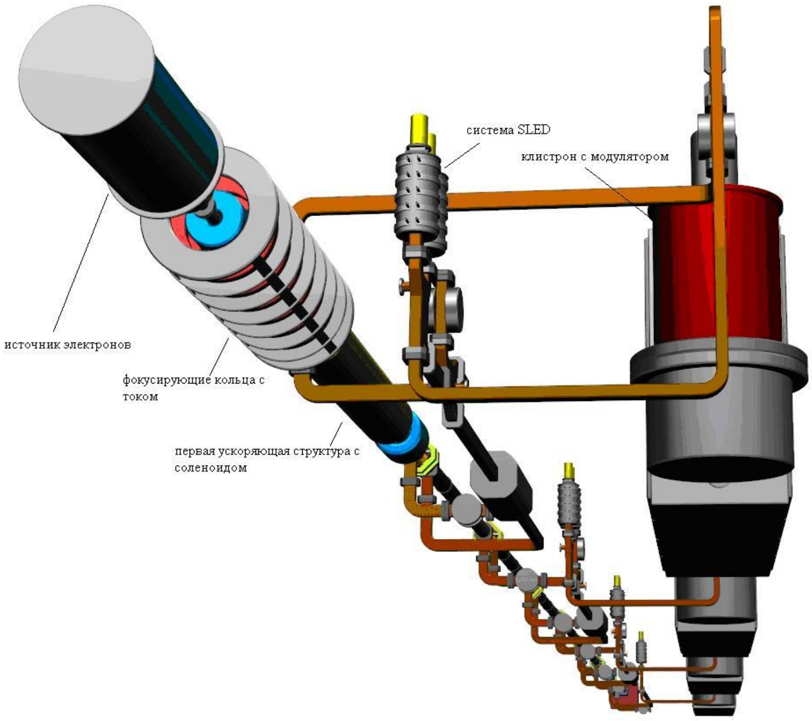

Fig. 5.47. General view of the electron accelerator.

The general scheme of the accelerator will consist of the modules (Fig. 5.46), which include one klystron with the modulator, power compression system SLED-type of SLED-type, two accelerating structures and two waveguide loads. Between the structures, it is necessary to provide the gap, in which OFODO cell, beam diagnostics system and a vacuum gate-valve should be placed. The general view of the accelerator is represented in Fig. 5.47.

After the source of polarized electrons, the beam has the energy $W \approx 100\,\text{keV}$ and duration $t_b \approx 2$ nanoseconds. To increase the quantity of accelerated particles and to decrease the energy spread in a beam, the bunching system should be placed between the electron source and the first accelerating module. The given system will consist of the subharmonic cavity and the buncher on the main frequency of the accelerator $f_0 = 2856\,\text{MHz}$.

For the longitudinal compression of electron bunch of 2-nanosecond length, a subharmonic buncher should possess the period twice larger than the beam length, i.e. 4 nanoseconds. Thus, the frequency is equal to 250 MHz. It is rational to make the cavity with the frequency below the necessary one, so that the wave half-period in it were slightly larger than the beam length, for example $f_S \approx f_0/12 = 238$ MHz. To provide the decrease of the beam longitudinal size by ~6 times before injection to the buncher at the main frequency, a free section is necessary after the cavity. The length of the section will be determined after calculation of particle dynamics, and is estimated to be up to 1.5 m.

The buncher on the main frequency can be produced as a three-cell cavity with an oscillation mode π used for a long time at the VEPP-5 pre-injector. The advantage of such cavity is in the fact, that at the exit, its bunch is already bunched and is ready for injection into the accelerator.

Also, for the electron accelerator, the focusing system placed after the electron source is very important. As Coulomb repulsion forces will increase at beam compression after the subharmonic cavity, the increase of magnetic field, in which a beam should move, is necessary. Such increase of the field can be formed by means of the rings with current, which are placed correctly. Besides, while passing the first accelerating structure, the beam should always be in solenoidal magnetic field.

5.4.1. RF system of the linear accelerator

5.4.1.1. Klystron

Klystron TH 2128 C/D, Thales-produced, is suggested to be used as RF power source. Average power of such klystron is 10 kW, this corresponds to repetition frequency of 50 Hz at 4-microsecond pulse duration. Its parameters and view are represented in Table 5.7 and Fig. 5.48, respectively.

Table 5.7. Main parameters of TH 2128 C/D Klystron

RF frequency	2856 MHz
Peak output power	45.5 MW
Average power	10 kW
RF pulse duration	4 microseconds
Gain	54 dB
Efficiency	43 %
Max. input power	200 W
Bandwidth	10 MHz
Cathode voltage	315 kV
Beam current	335 A
Cathode heating voltage	30 V
Cathode heating current	24 A

Fig. 5.48. View of the klystrons of TH 2100-series (at the left) and the modulator K2-3

Modern pulsed high-voltage power supply of the given klystron is produced by the several companies. For example, the equipment produced for such klystrons by the Swedish company “ScandiNova Systems” (http://www.sc-nova.com/) – modulators K2-1/K2-3 (Table 5.8).

Table 5.8. Parameters of the modulators of K2-series (ScandiNova Systems)

Parameter	Unit	K2-1	K2-2	K2-3
Pulse output RF power of klystron	MW	35	40	45
Average output RF power of klystron	kW	1.6	1.6	1.6
Pulse power of modulator	MW	74.3	91.5	100.5
Average power of modulator	kW	4.3	5.0	5.1
Pulse voltage	kV	270	300	314
Pulse current	A	275	305	320
Pulse repetition frequency	Hz	1-10	1-10	1-10
Pulse duration	μsec	4.5	4	3.5
Uniformity of pulse flat part	%	± 1	± 1	± 1
Pulse shape repeatability	%	± 0.2	± 0.2	± 0.2

The given modulator (Fig. 5.48) is the complete solution of providing a regular work of the klystron. It includes all necessary components for this device: the high-voltage charger, PFN, solid-state high-voltage switches, the pulsed high-voltage transformer, klystron heating power supply, control, diagnostic and interlock systems.

5.4.1.2. SLED system

The power compression SLED-type system is applied at the VEPP-5 pre-injector (Fig. 5.49). The parameters of such system are represented in Table 5.9.

Table 5.9. Main parameters of the power multiplication system

Cavity diameter, D	196 mm
Cavity height, H	346.6 mm
Operation frequency, f_0	2856 MHz
Tuning range, Δf ($\Delta f/\Delta H$)	±5 MHz (2.75 MHz /mm)
Unloaded Q-factor, Q_0	53200
Coupling coefficient with supplying waveguide, β	5.84
Time constant, τ_0	5.93 microseconds
The loaded time constant$T_C = \tau_0/(1+\beta)$	0.87 microseconds
Time of phase reversal (180^0)	3 microseconds
Klystron pulse duration	3.5 microseconds
Voltage multiplication factor K_0	2.67

Fig. 5.49 also shows a typical dependence of RF power at the exit of the power compression system on time. The values of corresponding parameters of power compression system (of SLED-type) are represented in the Table 5.9. Difference of real dependence from the ideal one is connected with finiteness of fronts of the klystron RF-pulse, a nonzero time of phase reversal and with resistance losses in the compression system.

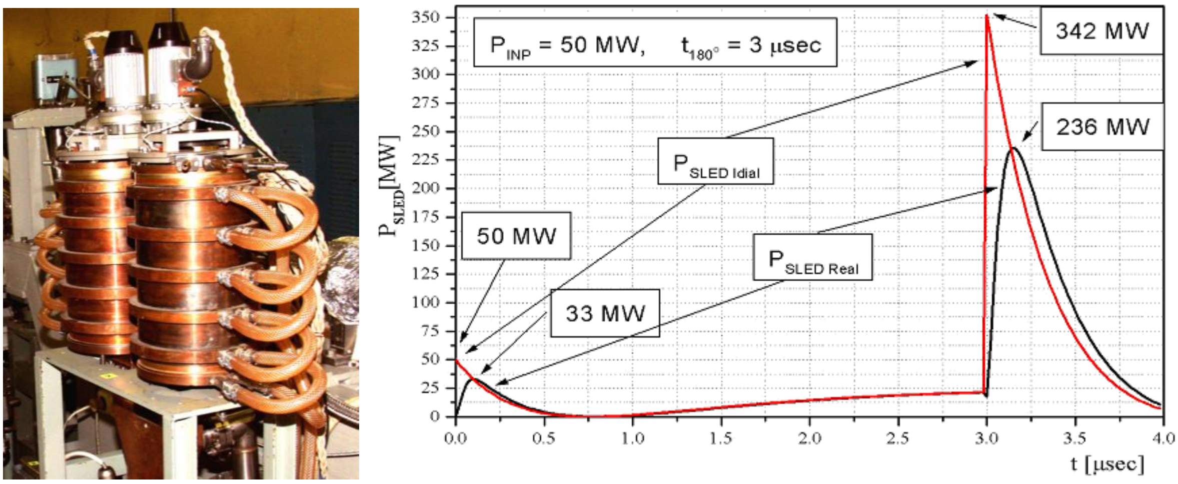

Fig. 5.49. SLED power multiplication system produced in BINP SB RAS (at the left). RF power at the SLED system exit vs time for ideal (red curve on the right) and real (black curve) cases.

5.4.1.3. *Bunching system*

The bunching system for the beam from the source of polarized electrons is represented as two cavities-bunchers and a free space between them.

The first cavity, which is a sub-harmonic buncher, operates with an oscillation mode E_{010} at frequency $f_S \approx f_0/12 = 238$ MHz. It should compress a beam approximately by 6 times before injection into the buncher at the main frequency of the accelerator. A free section of 1.5-m length should be provided between two cavities for beam bunching.

The second cavity is made as a three-cell cavity with oscillation mode π. Its view is represented in Fig. 5.50. Fig. 5.51 shows the electric field distribution on the cavity axis.

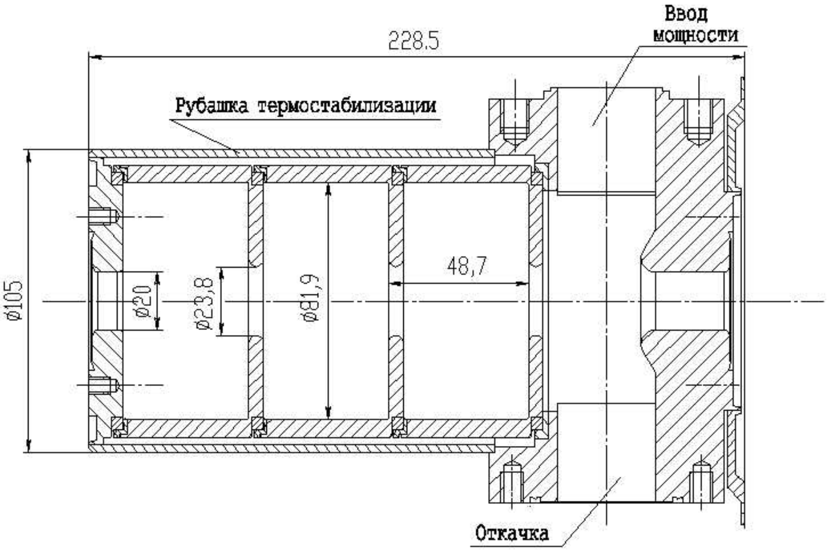

Fig. 5.50. The cavity-buncher at the main frequency of 2856 MHz

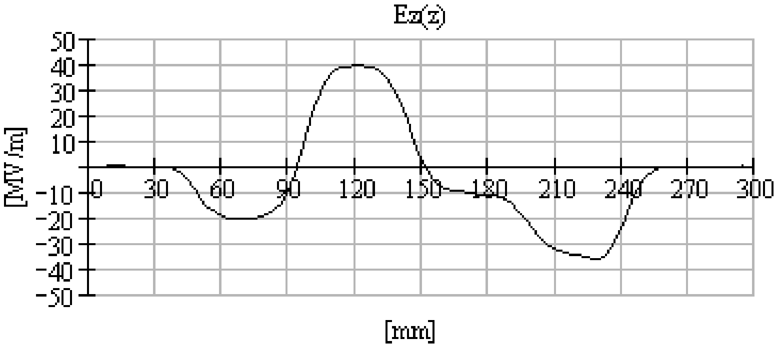

Fig. 5.51. Electric field strength on the cavity-buncher axis at the main frequency with the stored energy of 1 J

5.4.1.4. Accelerating section

The operation scenario of the linear accelerator of *S*-range on a traveling wave with the power compression system is as follows: RF power pulse, analogous to the pulse in Fig. 5.49, is divided between the necessary quantity of accelerating structures (AS), and through phase shifters comes to their inputs. Electric field strength reaches the maximum value at the very beginning of the structure, at the moment, when the maximum power after multiplication system starts passing through the AS. If this strength exceeds a certain value, then RF breakdowns originating in this case in the beginning of the structure will result in a beam loss. For our AS design the maximum strength of accelerating electric field obtained experimentally is ≤ 40 MV/m. Then, RF power is spread along the structure with a group velocity and in the time interval equal to the time of filling the structure starts to enter the matched load. This very moment is optimal for acceleration of the electron bunch.

Table 5.10. AS main parameters

Operation frequency	2855.5 MHz
Operation mode of oscillations	$2\pi/3$
Length, L	2.93 m
Unloaded Q-factor, Q_0	$1.32\cdot10^4$
Group velocity, V_{gr}	$0.021\cdot C$
Shunt impedance	51 MOm/m
AS unloaded constant, $\tau_0 = 2\cdot Q_0/\omega$	1.47 μs

AS field damping factor , $\alpha = 1/(\tau_0 \cdot V_{gr})$	0.108 1/m
Damping parameter αL	0.316
AS Filling time, $T_f = L/ V_{gr}$	0.465 μs
Period	34.98 mm
Inner diameter of the cell cavity	83.8 mm
Iris aperture diameter	25.9 mm
Iris thickness	6 mm
Overvoltage coefficient	1.7

In our case one klystron and one power compression system SLED feed two accelerating sections. Section parameters are given in the Table 5.10. Total gained energy in ideal variant without taking into account a beam from one section is 70 MeV (Fig. 5.54). As it is seen from the scheme in Fig. 5.53, field strength in the first cell of the section is close to critical 40 MV/m. Thus, the acceleration gradient of 23 MeV/m is actually maximal for stable operation of the accelerator. The proposed correct energy of the beam after one accelerating section is about 65 MeV. In this case, the field strength in the first cell will be below 40 MV/m (about 35 MV/m), but acceleration rate – 21 MeV/m. Taking into account imperfection of the structures, realistic rate of acceleration will be ≈17 MeM/m. If interval between the sections is 1 meter, then one accelerating module will occupy 7 m and provide the energy of 102 MeV. Fig. 5.52 represents a sketch of the BINP-developed accelerating structure.

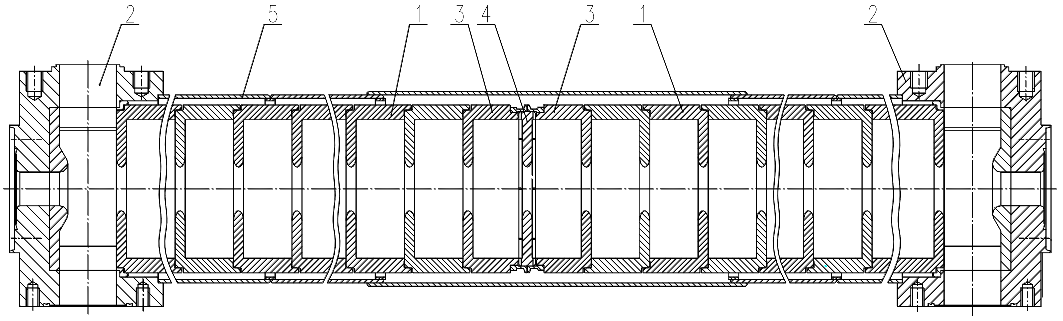

Fig. 5.52. Accelerating structure: regular accelerating cell (1), transformer of a wave-type (2), transitive (connecting) accelerating cell (3), connecting diaphragm (4), cooling jacket (5).

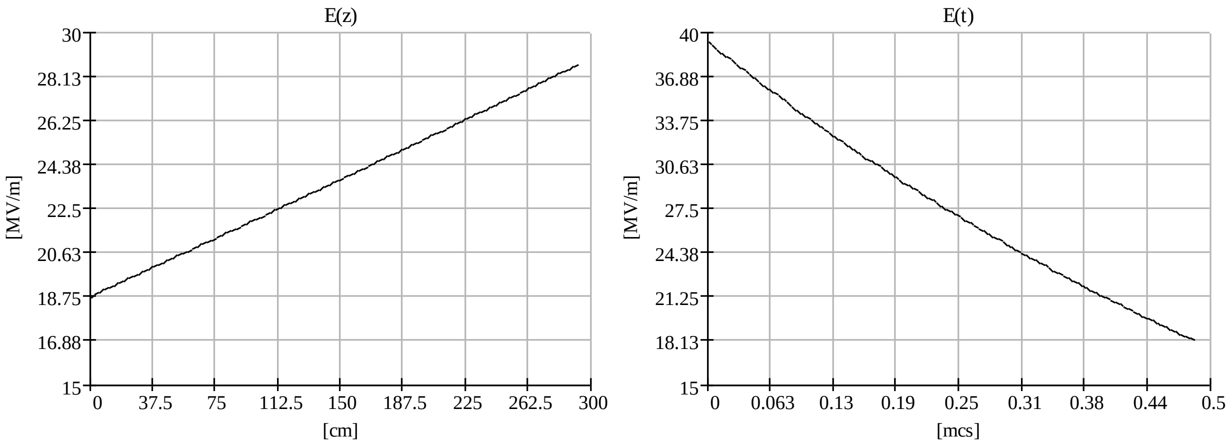

Fig. 5.53. Distribution of electric field strength along the structure (at the left) and dependence of electric field strength in the first cell on time (at the right).

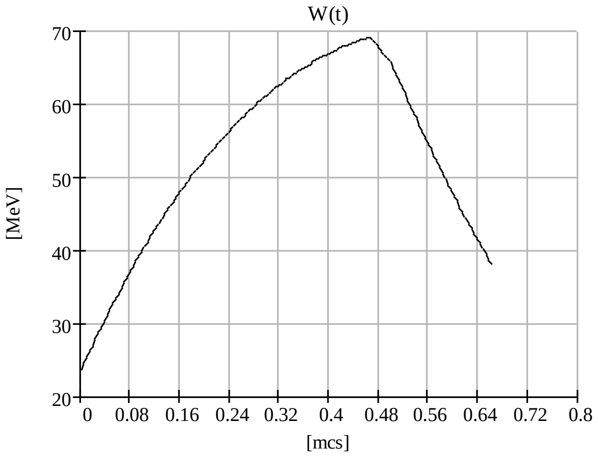

Fig. 5.54. Energy gained by a beam vs time of injection into the AS (time is counted after phase reversal in SLED system)

5.4.2. Beam focusing system

After the sub-harmonic cavity, there is the electron beam longitudinal compression, at which Coulomb repulsion force increases. Thus, the beam should move in increasing axial magnetic field. Such field can be obtained, for example, by means of the rings with current. Their supposed view and field distribution are represented in Fig. 5.55 and Fig. 5.56, respectively.

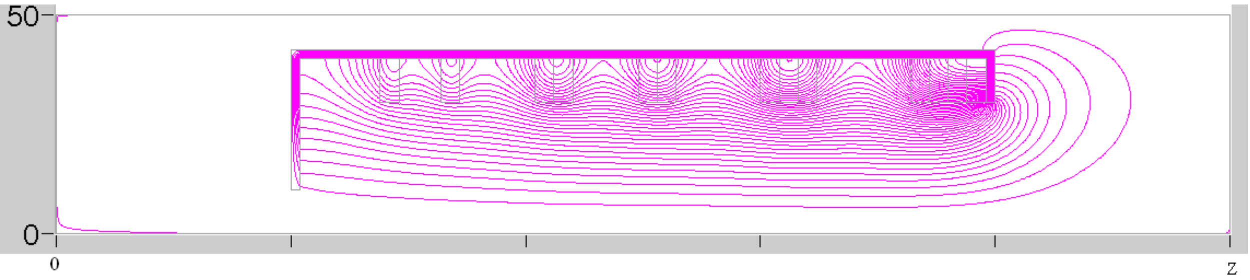

Fig. 5.55. Rings with current and the distribution of magnetic field lines.

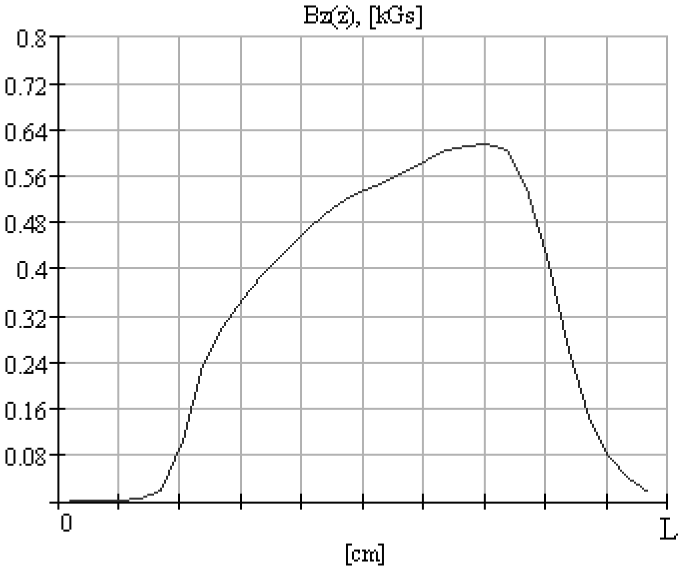

Fig. 5.56. Distribution of magnetic field of the rings with current.

At passing the first accelerating structure, the beam should move in magnetic field of solenoid. The solenoid is desirable to be iron-free to provide a "softer" injection of the beam into the structure. Calculation of particle dynamics should determine the field value, the preliminary value is not more than 3 kGs.

5.4.3. RF load

BINP-developed cavity RF load consists of two low-Q cavity structures connected with a rectangular waveguide (cross-section - 72×34 mm) through the apertures in a wide wall. Plunger is placed at the end of the waveguide, opposite the entry. The distance between the connection apertures and the plunger corresponds approximately to half-length of electromagnetic wave in the waveguide. The magnetic field from the side of supplying waveguide and inside each cavity assemblage around the connection apertures has the maximum value. Usage of two connection apertures allows the raise of electric strength of the structure due to the decrease of electric field strength on the aperture surface and the decrease of the average power level dissipated at each aperture. The operation mode for each assemblage is analogous to mode E_{020} of the cylindrical cavity. The general view of the load is shown in Fig. 5.57.

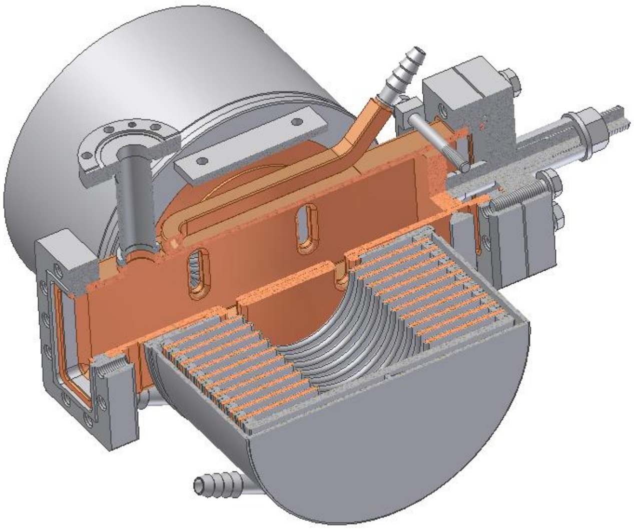

Fig. 5.57. Design of the load for the maximum pulse and average power.

The main parameters of RF loads of three types are represented in Table 5.11.

Table 5.11. Main parameters of RF loads.

Load type	Low	Average	High
Level of absorbed power (MW)	1	60	120
Cavity diameter (mm)	180	182	184
Aperture size (mm)	39	39	39
Cavity height (mm)	5	5	5
Disk thickness (mm)	-	5	5
Quantity of cavities in assemblage	1	5	11
Bandwidth at SWRv level of 1.21 (MHz)	2.2	2.5	2.5
Loaded Q factor	200	180	180

5.4.4. Conclusion

The basic element of the linear accelerator is the accelerating module of 7-m length. For a stable operation mode the acceleration gradient is desirable to be about 17 MeV/m. In this case, the gain of beam energy after such module will be 102 MeV. To gain the energy of 2 GeV, 20 modules with total length of 140 m are necessary. For the energy of 500 MeV, 5 modules and 35-m length are necessary. Besides, the bunching system with a free interval of about 1.5 m should be placed between the source of polarized electrons and the first accelerating section. The schematic view of the electron accelerator to energy of 500 MeV is represented in Fig. 5.58.

Positrons come to the accelerator from the pre-injector with 500-MeV energy, therefore, they should be accelerated up to energy of 2 GeV (Fig. 5.59).

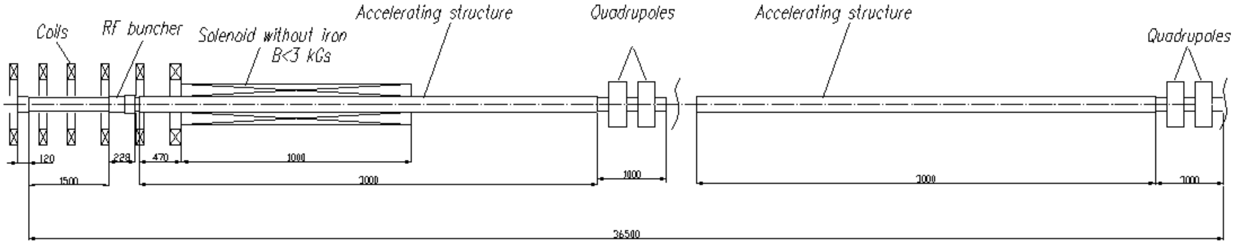

Fig. 5.58. Schematic view of the beginning of the electron accelerator.

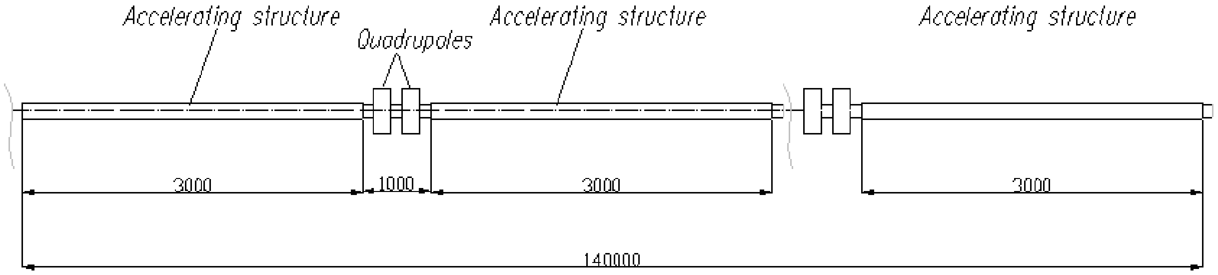

Fig. 5.59. Schematic view of 2-GeV accelerator.

References

1. R.Chehab. Positron Sources. Proc. CERN Accelerator School, General Accelerator Physics, Geneva, 1994, p.643
2. H.-H. Braun “Positrons for Accelerators”, Ph.D. thesis, Zurich University, 1992.
3. D. Yount and J. Pine “Production of Positrons with the Stanford Mark III accelerator”, Nucl. Inst. and Meth. 15, pp 45-50, 1962.
4. A.A.Kulakov, P.V.Martyshkin «Development of the positron source on the basis of linear accelerators», BINP preprint № 99-26.
5. A.N.Skrinsky, V.V. Parchomchuk «Methods of cooling the charged particle beams», Physics of elementary particles and atomic nucleus, 1981, vol. 12, ed. 3.
6. R. H. Helm, “Adiabatic Approximation for Dynamics of a Particle in the Field of a Tapered Solenoid”, SLAC-4, 1962.
7. G.Knopfel. Superstrong pulsed magnetic fields. "Mir", Moscow, 1972.
8. [Lapik2001] R.Lapik, P.Martyshkin. Capture Efficiency of High Field Flux Concentrator. PAC-2001, 2001.

9. C. Leroy, P.-G. Rancoita. Principles of Radiation Interaction in Matter and Detection. World Scientific, 2004
10. The Stanford two-miles accelerator. Ed. by R. B. Nearl, New-York-Amsterdam: W. A. Benjamin, Inc. 1968.
11. R. Chehab, G. L. Meur, B. Mouton, M. Renard. An adiabatic matching device for the Orsay linear positron accelerator. LAL/RT/83-03 March 1983.
12. S. Ecklund, Positron Target Materials Tests, SLAC-CN-128, 1981 г.
13. M. Borland, "elegant: A Flexible SDDS-Compliant Code for Accelerator Simulation",
14. Advanced Photon Source LS-287, September 2000.
15. Klaus Gruppen «Detectors of elementary particles», Novosibirsk 1999
16. http://cern.ch/geant4
17. R. Pitthan et al., "SLC Positron Source-Simulation and Performance", IEEE Particle Accelerator Conf., San Francisco, CA, 1991, in Particle Accel.Conf: IEEE 1991:2098-2100 (QCD183:P3:1991).
18. HIGH-YIELD POSITRON SYSTEMS FOR LINEAR COLLIDERS. By J.E. Clendenin (SLAC), SLAC-PUB-4743, April 1989. Published in Proceedings of the 1989 Particle Accelerator Conference, March 23 - 27, 1989, Chicago, IL. p. 1107.
19. RECENT IMPROVEMENTS IN THE SLC POSITRON SYSTEM PERFORMANCE. By P. Krejcik, W.J. Corbett, Stanley D. Eeklund, P. Emma, T.H. Fieguth, Richard H. Helm, A.V. Kulikov, T. Limberg, H. Moshammer, M.C. Ross, R. Siemann, W.L. Spence, M.D. Woodley (SLAC). SLAC-PUB-5786, Mar 1992.3. Contributed to 3rd European Particle Accelerator Conf., Berlin, Germany, Mar 24-28, 1992.
20. Abe, et. al., "The KEKB injector linac", Nucl. Instr. and Methods A, Vol. 499, pp. 167-190 (2003).
21. T. Kamitani, et. al, KEKB INJECTOR LINAC STATUS AND FUTURE UPGRADE, Proceedings of EPAC 2002, Paris, France
22. Sannibale, et al, DAΦNE Linac Commissioning Results, Frascati, April 4, 1997. Note: BM-2.
23. R. Boni, F. Marcellini, F. Sannibale, M. Vescovi, G. Vignola: "DAFNE Linac Operational Performances", Proceedings of the European Particle Accelerator Conference, Stockholm (Sweden), 22-26/6/1998, p. 764.
24. M.A. PREGER, et al., PERFORMANCE AND OPERATION OF THE DAFNE ACCUMULATOR, Proceedings of the European Particle Accelerator Conference, Stockholm (Sweden), 22-26/6/1998, p. 415.
25. X. Yu, Y. Chen, X. Wang, M. Liu, OPERATION STATUS OF THE BEIJING ELECTRON-POSITRON COLLIDER, Proceedings of APAC 2004, Gyeongju, Korea
26. G. X. Pei et al., Design Report of the BEPCII Injector. Linac, IHEP-BEPCII-SB-03-02, November 2003.
27. J. Clendenin, et. al., "Compendium of Scientific Linacs", CERN/PS 96-32 (DI), 1996
28. A. Frebel and G. Hemmie, "PIA, the Positron Intensity Accumulator for the PETRA Injection", IEEE Transactions on Nuclear Science, Vol. NS-26, No. 3 (June 1979).
29. New optics of the LEP injector linac for positron production. C. Bourat, H. Braun, L. Rinolfi (CERN) . Jun 1994. Prepared for 4th European Particle Accelerator Conference (EPAC 94), London, England, 27 Jun - 1 Jul 1994. Published in London 1994, EPAC 94, vol. 1, 704-706
30. Alexander Wu Chao, Maury Tigner. Handbook of accelerator physics and engineering. Singapore: World Scientific, 1999
31. Kolomensky A, Lebedev A. Theory of cyclic accelerators. Moscow: PhysMathLit, 1962
32. Sands M. The physics of electron storage rings. An introduction. SLAC, 1979
33. Brook G. Cyclic charged-particle accelerators. Moscow: AtomIzdat, 1970

34. Burshtejn E. L, Voskresensky G.V. Linear accelerators of electrons with intensive beams. Moscow: AtomIzdat, 1970
35. Wangler T. Principles of RF Linear Accelerators. New York: John Wiley & Sons, 1998
36. R.M.Lapik, P.V.Martyshkin, S. V.Shijankov, A. M. Jakutin. System of the elektron-positron conversion of the VEPP-5 injection complex. BINP preprint №2005-50
37. R. M. Lapik, P. V. Martyshkin. The Capture Efficienty of High Field Flux Concentrator. Proceedings of the 2001 Particle Accelerator Conference
38. A. A. Kulakov, P. V. Martyshkin. VEPP-5 Positron Source Simulations. Proceedings of the 1996 European Particle Accelerator Conference
39. L.D.Landau, E. M.Lifshits. The theoretical physics. T.1 Mechanics. Moscow: "Science", 1988
40. Yu. B. Bolkhovityanov et al., SPIN96 Proceedings, 4, 700 (1997).
41. B.L.Militsyn. “A pulsed polarized electron source for nuclear physics experiments”, Proefschrift (Ph.D. Thesis), Universiteit Eindhoven, Eindhoven (1998).
42. I.Koop et al. “Polarized electrons in AmPS”, NIM-A427, 36-40 (1999).
43. B.L.Militsyn et al., “Beam optical system of the polarized electron source of the Amsterdam pulse stretcher AmPS”, NIM-A427, 46-50 (1999).
44. I.A.Koop. “Longitudinally polarized electrons in AmPS storage ring”, doctoral thesis, Novosibirsk, 2000.
45. L.G.Gerchikov, SPU, St.Petersburg, Russia. “Optimization of Semiconductor Superlattice for Spin-Polarized Electron Source”, PESP2008 - workshop on sources of polarized electrons and high brightness electron beams.
46. M.Yamamoto, Nagoya University. “High polarization and low emittance electron source for ILC”, CCAST workshop on TeV physics and the LHC, Beijing, 2006.
47. F.Furuta et al., NIM-A 538(2005), 33-44.

Chapter 6

Infrastructure

The Super $c\tau$ factory will be situated at the territory of the Budker Institute of Nuclear Physics. It will include both the partially existing injection complex and a new tunnel of the main accelerator ring and a few new buildings as shown in Fig. 6.1.

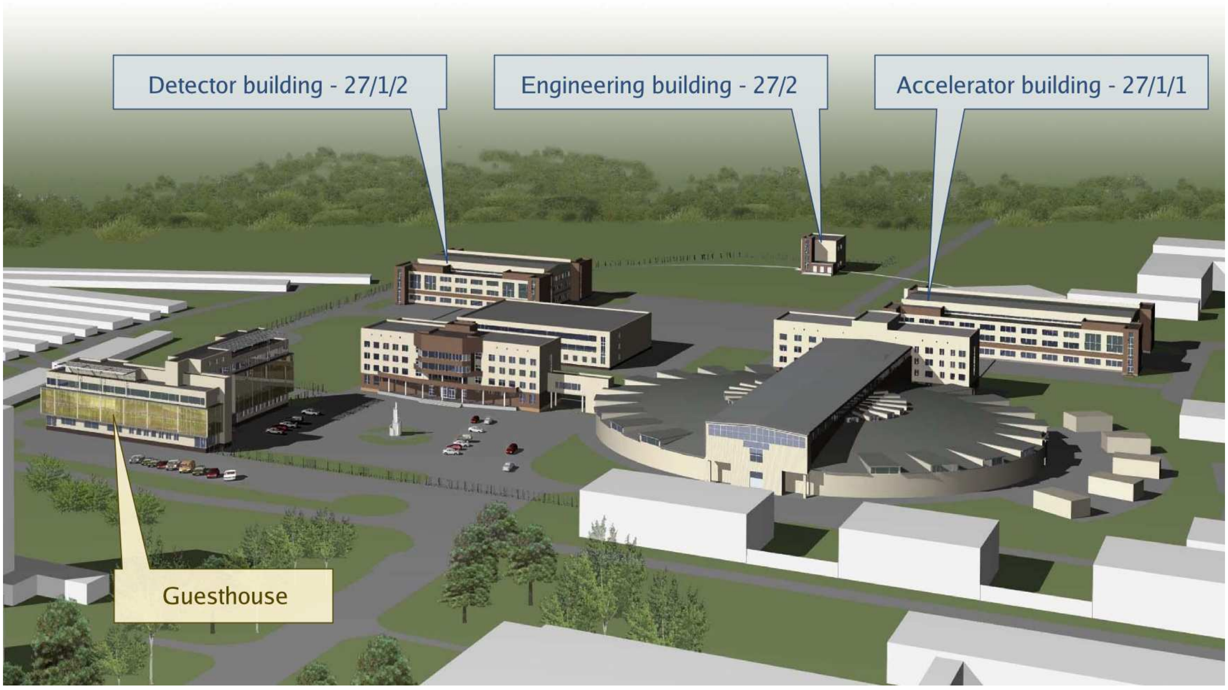

Figure 6.1: Plan of the future experimental facilities at BINP. Buildings related to Super $c\tau$ factory are marked with balloons.

The accelerator rings of about 800 m in circumference will be placed in the tunnel of 4×3 m^2 cross-section at a depth between 9 and 17 m.

The building for the detector (27/1/2) with the area of $54 \times 48\,\mathrm{m}^2$ will house the detector hall of $30 \times 23 \times 18\,\mathrm{m}^3$, a loading area to facilitate the transport of heavy parts of the detector, technical rooms and rooms for personell. The detector will be mounted on the rails so that it can be moved in and out of the beam line area. A crane (30 t) spans the whole inner building area.

The accelerator building (27/1/1) has the similar size as the detector building. It will house power supplies of the beam lines, the RF system and service systems of the collider.

The artistic view of the detector/accelerator building is shown in Fig. 6.2.

Figure 6.2: Detector/accelerator building.

Two buildings (27/2 and 27/3) with the area of $18 \times 12\,\mathrm{m}^2$ will be built ot top of the centers of accelerator arcs for the technological purposes (ventilation, water and electric supply *etc.*). Each building will have 5 m diameter shaft down to the accelerator tunnel.

Chapter 7

Cost

The cost and manpower estimation is based on the experience of BINP physicists in the detector and the accelerator construction and operation.

The multiyear history of particle physics experiments in our institute is based on several dedicated and general purpose detectors such as OLYA, CMD–1, CMD–2, ND, MD–1 which were working on VEPP–2, VEPP–2M, VEPP–4 e^+e^- colliders. At the present time two colliders are in operation – VEPP–2000 and VEPP–4M. Three detectors are taking data – SND, CMD–3 and KEDR.

The Budker INP participates in many international collaborations. Novosibirsk physicists took part in the design, the construction and the operation of ATLAS, BaBar, Belle detectors. BINP actively participates in newly suggested experiments such as Belle–II in Japan, SuperB factory in Italy and others.

For the detector part cost estimates are broken into "Labor" and "Cost" categories where "Labor" is a manpower needed in man-months and "Cost" is materials and services (M&S) to be purchased. For the rest "Cost" is the total cost including manpower and M&S.

		Labor, mm	**Cost, kEuro**
	Super $c\tau$ factory		**327300**
1	**Detector**	**2851**	**77300**
1.1	**Vertex Detector**	**144**	**200**
1.2	**Drift Chamber**	**304**	**2500**
1.2.1	System engineering	24	50
1.2.2	Endplates	22	650
1.2.3	Inner cylinder	10	200
1.2.4	Outer cylinder	8	100
1.2.5	Wires	10	300
1.2.6	Feedthroughs	19	450
1.2.7	Endplate systems	8	400
1.2.8	Assembly and Stringing	170	250
1.2.9	Gas System	18	50

1.2.10	Testing	15	50
1.3	**FARICH**	**344**	**17250**
1.3.1	Photodetectors (1.3M)	120	14150
1.3.2	Radiator (Focusing Aerogel)	170	2050
1.3.3	Cooling system	24	700
1.3.4	Mechanical support	24	250
1.3.5	Calibration system	6	100
1.4	**Calorimeter**	**600**	**29750**
1.4.1	Crystals ($\sim$40t CsI)	300	25400
1.4.2	Photodetectors	200	3650
1.4.3	Support structure	100	700
1.5	**Muon system**	**225**	**4300**
1.5.1	Detectors	100	350
1.5.2	Gas System	75	350
1.5.3	Flux Return	50	3600
1.6	**Magnet**	**250**	**4350**
1.6.1	Superconducting solenoid	100	3250
1.6.2	Cryogenics	150	1100
1.7	**Electronics**	**420**	**7150**
1.7.1	Vertex Detector	12	200
1.7.2	Drift Chamber	12	350
1.7.3	FARICH	288	4150
1.7.4	Calorimeter	60	1000
1.7.5	Muon system	12	200
1.7.6	Trigger	12	450
1.7.7	Infrastructure	24	800
1.8	**Computing**	**564**	**11800**
1.8.1	R&D + prototypes	216	700
1.8.2	Computing	24	2200
1.8.3	Network	12	1200
1.8.4	HPC storage	48	2450
1.8.5	Tape storage	24	2250
1.8.6	Data Center 1 infrastructure	120	2200

1.8.7	Data Center 2 infrastructure	120	800
2	**Accelerator complex**		**200000**
2.1	**Collider**		**149000**
2.1.1	Magnetic system + Power supplies		85000
2.1.2	Damping wigglers		6000
2.1.3	Siberian snake solenoids		5000
2.1.4	Vacuum system		35000
2.1.5	RF system		10000
2.1.6	Feedbacks		1000
2.1.7	Diagnostics		4000
2.1.8	Control system		3000
2.2	**2.5 GeV Linac**		**50000**
2.3	**Polarized Electron Injector**		**1000**
3	**Buildings Construction and Site Utilitues**		**50000**
3.1	Building 27/1/1 (accelerator)		6000
3.2	Building 27/1/2 (detector)		5500
3.3	Buildings Engineering Support		4500
3.4	CTF tunnel		15000
3.5	Injector building and linac tunnel		6000
3.6	Electricity support (power transformers 3x5 MW, 5 km cable ..)		5000
3.7	Water cooling systems (towers 3x5 MW, 16 pumps, 5 km pipes, equipments…)		6000
3.8	Ventilation		2000